

THE IDENTIFICATION AND
INTERPRETATION OF MICROBIAL
BIOGEOMAGNETISM

Thesis by

Robert Evans Kopp

In Partial Fulfillment of the Requirements for the

Degree of

Doctor of Philosophy

CALIFORNIA INSTITUTE OF TECHNOLOGY

Pasadena, California

2007

(Defended April 12, 2007)

© 2007

Robert E. Kopp

All Rights Reserved

ACKNOWLEDGEMENTS

The efforts of many people, both inside and outside of Caltech, have allowed me to complete this dissertation. My advisor, Joe Kirschvink, played a particularly critical role. Over the last five years, he has been extraordinarily generous with his time, thoughts, and resources. Nearly as soon as I arrived in Pasadena in July 2002, I left to spend a month with Joe traveling through the Paleoproterozoic in South Africa and Canada. He has since taken me to explore the early Precambrian in Western Australia and the late Precambrian in South Australia and sent me to China to investigate the record of the Permo-Triassic extinction there. Such global travels have not only helped me understand many of the great geological questions of geobiology; by exposing me to different nations and different economic situations, they have played a major role in shaping my motivations for my future work. Joe has also been exemplary in the classroom in exciting students about the Earth sciences and has provided me with abundant opportunities to develop my own teaching skills. My favorite student evaluation from an Earth history class I helped Joe teach in 2006 reads, “Kopp and Kirschvink are a fascinating pair. The class is almost worth taking just to hear them banter.” Joe is trusting, open, and in many ways selfless with respect to his students, and I am deeply appreciative of it.

This work would not have been possible without my collaborators and co-authors, particularly Ben Weiss, Adam Maloof, Cody Nash, Tim Raub, David Fike, Atsuko Kobayashi, Hojatollah Vali, and Nic Beukes, who have all taught me much and in many cases have served as welcoming hosts as well. Munir Humayun eight years ago helped guide me into geological and planetary sciences. Dianne Newman and Andreas Kappler taught me almost everything I know about microbiology. John Eiler let me experience the gritty side of isotope geochemistry during my first year as a graduate student. George Rossman has been a constant source of probing questions and interesting magnetic samples. John Grotzinger, first as an instructor in the Agouron Institute Geobiology summer course and later as a professor at Caltech, has immensely expanded my appreciation of sedimentology. David Morrow, Ryan Petterson, Rebecca Adler, Spider Vetter, Andrew

Matzen, and numerous other friends and colleagues have provided me with critical support at key points during my graduate career.

Without Angelo Di Bilio, I would have been unable to conduct electron spin resonance experiments at Caltech, which would have made it impossible for me to do most of the work described in this dissertation. Bruce Brunschweig and the Beckman Institute have made it possible for me to do low-temperature magnetic experiments at Caltech. Numerous Geological and Planetary Sciences Division staff members, particularly Jean Grinols, Carolyn Porter, Tess Puig, Marcia Hudson, Jim O'Donnell, and Tony Diaz, have been immensely helpful over the last five years.

My life would be greatly lacking if I had lived the last five years exclusively within academia. The Caltech Tai Chi Club and its two instructors, Peter Mugglebee and David Nakomoto, have been a pillar of my life in Pasadena. The Pasadena Young Democrats have provided me with an outlet for my civic interests, and I would like to thank Asa Hopkins in particular for working with me to try to bring some of those civic interests to Caltech.

I have been fortunate to have spent the last several years close to members of my extended family: my cousins Harold, Eileen, and Rachel Brown, my uncle Richard Kornblith, and my aunt Lisa Kornblith. Moreover, I consider myself blessed that my first year in southern California I was able to get to know well an extraordinary woman, my great-aunt Hermione Brown, whose drive, intelligence, and warmth will live with me for the rest of my life.

My parents, my sister Emily, my grandmother Violet Raum, and numerous aunts, uncles, and cousins have been unfailingly supportive during my time at Caltech (and, indeed, during my entire life), as has my brother-in-law Wagner. Though they were not able to see me complete college or graduate school, my grandparents Lester Kornblith, Barbara Kornblith, and Arnold Raum, as well as Faye McPhee, made it possible for me to reach this point.

When I applied to Caltech, the Division offered me a Gordon and Betty Moore Foundation Fellowship and, with more wisdom than they could have realized, decided to name it after Harrison Brown. Harrison Brown, a late professor of geochemistry at Caltech, had begun

his career at the University of Chicago, and, after completing my undergraduate degree, I followed his path from the Midway to the Arroyo Seco. Brown was, however, not only a University of Chicago expatriate; he was also deeply concerned about global poverty and sustainability and heavily involved in civic affairs. His career as both an Earth scientist and a public intellectual has come to serve as an example to me.

In addition to the Moore Foundation, my work has been funded by a graduate research fellowship from the National Science Foundation and by grants from the Agouron Institute and the National Aeronautics and Space Administration.

The chapters of this dissertation were each the collaborative work of many different people.

Chapter 1: This chapter was co-authored with Joe Kirschvink. Mark Hounslow, Hojatollah Vali, and Atsuko Kobayashi graciously provided TEM images. We thank Jared Leadbetter, Adam Maloof, Cody Nash, Dianne Newman, and Lael Vetter for helpful discussion.

Chapter 2: This chapter was co-authored with Ben Weiss, Adam Maloof, Hojatollah Vali, Cody Nash, and Joe Kirschvink. We thank John Grotzinger for access to the Bahamian samples, J. Ewing for field assistance in the Bahamas, George Rossman, Sam Kim, Tim Raub, and two anonymous reviewers for helpful discussion, Bruce Brunschweig and Angelo Di Bilio for technical assistance with the MPMS and EPR spectrometer, respectively, and the Beckman Institute for funding the use of the MPMS. Ben Weiss was supported by the NASA Mars Fundamental Research and NSF Geophysics Programs, Adam Maloof and Cody Nash by the Agouron Institute, Hojatollah Vali by the Natural Sciences and Engineering Research Council of Canada, and Joe Kirschvink by NASA Exobiology grant NAG5-10618 and the NASA Astrobiology Institute.

Chapter 3: This chapter was co-authored with Cody Nash, Atsuko Kobayashi, Ben Weiss, Dennis Bazylinski, and Joe Kirschvink. We thank Angelo Di Bilio for assistance with the EPR spectrometer, Arash Komeili for assistance with the mutagenesis, and Mike Jackson, David Griscom, and an anonymous reviewer for helpful comments. The Beckman Institute provided support for the use of the MPMS. Joe Kirschvink and Cody Nash were supported by the Agouron Institute and the NASA Astrobiology Science and Technology Instrument

Development program. Atsuko Kobayashi was partially supported by funds from a New Energy and Industrial Technology Development Organization fellowship. Dennis Bazylinski was supported by US National Science Foundation grant EAR-0311950. Ben Weiss was supported by the NASA Mars Fundamental Research and NSF Geophysics Programs.

Chapter 4: This chapter was co-authored with Adam Maloof, John Grotzinger, David Fike, Tanja Bosak, Hojatollah Vali, Pascale Poussart, Ben Weiss, and Joe Kirschvink. This project was supported by an Agouron Postdoctoral Fellowship to Adam Maloof, and Agouron Institute grants to John Grotzinger and Joe Kirschvink. We appreciate keen field observations from John Abelson, Chris Guthrie, Peter Johnson, Jim Dahlberg and Elsebet Lund and logistical support from Joan Kobori. We thank Angelo Di Bilio for support with the EPR spectrometer and David Mohrig and John Woodruff for stimulating discussions. Amy Myrbo and Anders Noren at the Limnology Research Center (University of Minnesota) provided us with coring equipment and a wealth of practical knowledge. This work would not have been possible without the genius of Roberta Bennett-Calorio, field assistance from Jay Ewing, the able seamanship of Bradley Mackey, and logistical support from Agent Nixon of the Andros Island Police and Jeff Birch and the staff of Small Hope Bay Lodge.

Chapter 5: This chapter was co-authored with Tim Raub, Dirk Schumann, Hojatollah Vali, and Joe Kirschvink. We thank David Evans, Mark Pagani, Alexei Smirnov, Ellen Thomas, and Karl Turekian for comments, and Gerry Dickens for spurring my initial interest in the magnetically anomalous PETM sediments. NASA and the Agouron Institute provided support for this work through grants to Joe Kirschvink.

Appendix I: This chapter was co-authored with Joe Kirschvink, Isaac Hilburn, and Cody Nash. We thank Rebecca Adler, Nic Beukes, Bob Blankenship, Jochen Brocks, Hermann Dorland, Andreas Kappler, Jim Kasting, Adam Maloof, Dianne Newman, Shuhei Ono, Alex Sessions, Dawn Sumner, Tim Raub, Ben Weiss, and three anonymous reviewers for advice and discussion, Ryuji Tada for help with fieldwork in the Huronian, A. Pretorius and Assmang Limited for access to Nchwaning Mine, and Paul Hoffman for communicating

this manuscript. Partial funding was provided by the Agouron Institute and by a NASA Astrobiology Institute cooperative agreement with the University of Washington.

Appendix II: This chapter was co-authored with Joe Kirschvink. The refinement of the sample changer has been supported by a continent-wide consortium of faculty, consisting of David Evans (Yale), Ben Weiss (MIT), Scott Bogue (Occidental College), and John Holt (UT–Austin). Numerous students in and visitors to the Caltech lab helped debug the system. Chris Baumgartner’s skills as an electrical engineer were critical in building the current incarnation of the system upon the earlier help of Victor Nenow. Former Caltech students Gaylon Lovelace, Hiroshi Iishi, Bryce Engelbrecht, Tim Raub, and Isaac Hilburn played key roles in constructing the early versions of the sample changer and software.

ABSTRACT

Microbial activity plays a major role in the sedimentary iron cycle. Some microbes gain energy by reducing or oxidizing iron and thus induce changes in the sedimentary iron mineral assemblage. Magnetotactic bacteria engage in controlled, intracellular precipitation of magnetic iron minerals. These biological transformations are frequently a major influence on the magnetic properties of sediments. Understanding the biogeochemical iron cycle therefore facilitates the interpretation of sedimentary paleomagnetism; conversely, magnetic tools provide a non-destructive and rapid way of analyzing the biogeochemical iron cycle in modern and ancient environments.

Ferromagnetic resonance (FMR) spectroscopy, a form of microwave spectroscopy, provides a rapid means of assessing internal fields generated in magnetic particles by interparticle interactions and particle anisotropy. It can therefore assess particle shape, arrangement, and heterogeneity. Because magnetotactic bacteria typically produce chains of crystals with narrow distributions of size and shape, FMR spectroscopy is well suited as a screening tool for identifying fossil magnetotactic bacteria (magnetofossils).

Application of FMR and other techniques to modern carbonate sediments of the Triple Goose Creek region, Andros Island, Bahamas, reveals the contributions of magnetotactic bacteria, iron metabolizing bacteria, and sulfate reducing bacteria to the magnetization of carbonate sediments. In sediments above mean tide level, magnetofossils dominate sediment magnetism. Although stable remanent magnetization is preserved throughout the sediments, the quantity of biological magnetite diminishes by an order of magnitude in the iron reduction zone. Below this zone, the development of a sulfate reduction interval can lead to the authigenesis of magnetic iron sulfides. Supratidal portions of shallowing-upward parasequences in carbonate rocks therefore likely provide the most accurate record of syndepositional paleomagnetism.

Anomalous magnetic properties of clay deposited in the Atlantic Coastal Plain, New Jersey, during the Paleocene/Eocene Thermal Maximum (PETM) led previous authors to speculate that an extraterrestrial impact triggered the PETM. Reexamination of the clay using FMR

and transmission electron microscopy reveals instead that the clay hosts abundant magnetofossils. The first identification of ancient biogenic magnetite using FMR indicates that the anomalous magnetic properties of PETM sediments were not produced by an impact, but instead reflect paleoenvironmental changes along the western North Atlantic margin.

TABLE OF CONTENTS

CHAPTER 1: INTRODUCTION.....	1
1.1 Introduction.....	1
1.2 Ecology of magnetotactic bacteria.....	2
1.3 Traits and identification techniques for magnetotactic bacteria.....	8
1.4 Fossil record of magnetotactic bacteria.....	19
1.5 Magnetofossil taphonomy.....	27
1.6 Magnetofossils as an archive of environmental change	28
1.7 Summary.....	32
CHAPTER 2: CHAINS, CLUMPS, AND STRINGS.....	36
2.1 Introduction.....	36
2.2 Samples	41
2.3 Methods	44
2.4 Results	48
2.5 Discussion.....	63
2.6 Conclusions.....	65
CHAPTER 3: FERROMAGNETIC RESONANCE SPECTROSCOPY FOR ASSESSMENT OF MAGNETIC ANISOTROPY AND MAGNETOSTATIC INTERACTIONS	67
3.1 Introduction.....	67
3.2 Methods	70
3.3 Models.....	74
3.4 Results	79
3.5 Discussion.....	92
3.6 Conclusion	96
3.7 Selected notation	97
CHAPTER 4: SEDIMENTARY IRON CYCLING AND THE ORIGIN AND PRESERVATION OF MAGNETIZATION IN PLATFORM CARBONATE MUDS, ANDROS ISLAND, BAHAMAS	98
4.1 Introduction.....	98
4.2 Geological setting.....	99
4.3 Methods	103
4.4 Results	107
4.5 Discussion.....	120
4.6 Conclusions.....	125
CHAPTER 5: A MAGNETOFOSSIL SPIKE DURING THE PALEOCENE/EOCENE THERMAL MAXIMUM.....	127
5.1 Introduction.....	127
5.2 Samples	128

5.3 Characterization of magnetic particles.....	130
5.4 Environmental implications	134
5.5 Conclusions.....	135
EPILOGUE.....	138
APPENDIX I: THE PALEOPROTEROZOIC SNOWBALL EARTH.....	140
I.1 Introduction	140
I.2 Geological setting	141
I.3 Mass-independent fractionation of sulfur	142
I.4 The appearance of local oxygen.....	143
I.5 An ecological stoichiometry model of planetary oxygenation	147
I.6 Timescale for methane greenhouse collapse	149
I.7 Implications of the possible late evolution of cyanobacteria.....	151
I.8 Biomarker counterevidence for Archean oxygen	152
I.9 Indirect counterevidence for Archean oxygen	154
I.10 Future directions	156
I.11 Summary	157
APPENDIX II: AN AUTOMATIC SAMPLE CHANGER FOR RAPID, PRECISE, AND HIGH-SENSITIVITY ACQUISITION OF PALEOMAGNETIC AND ROCK MAGNETIC DATA.....	159
II.1 Introduction	159
II.2 Hardware and software	161
II.3 Operations	163
II.4 Automatic error checking.....	165
II.5 Measuring weak samples.....	166
II.6 Alternating field demagnetization and rock magnetic experiments..	167
II.7 Assessment of systematic errors	168
II.8 Conclusions	169
APPENDIX III: NOTES ON THE USAGE OF THE BRUKER EMX-300 FOR FERROMAGNETIC RESONANCE SPECTROSCOPY	170
APPENDIX IV: GUIDE TO ELECTRONIC MATERIAL.....	172
BIBLIOGRAPHY	173

LIST OF FIGURES

Figure 1-1: Schematic representation of chemical gradients, the typical optimal growth positions of different types of magnetotactic bacteria, and diagenetic fate of magnetite.	3
Figure 1-2: Oxidation/reduction potential of maghemite/magnetite, greigite/mackinawite, and ferrihydrite/Fe ⁺² couplets at pH 7 and pH 8 plotted against Fe(II) activity.	6
Figure 1-3: Single-domain stability field of magnetite as a function of shape factor (width/length ratio) and length..	10
Figure 1-4: Schematic representation of particle size distributions.	11
Figure 1-5: TEM images of magnetite-producing magnetotactic bacteria exhibiting different magnetosome crystal morphologies.....	12
Figure 1-6: Example coercivity spectra and FMR spectra	14
Figure 1-7: TEM images of magnetofossils.....	20
Figure 2-1: Synthetic FMR spectra	40
Figure 2-2: Definitions of basic FMR parameters.	46
Figure 2-3: Measurements of intact and altered AMB-1.....	49
Figure 2-4: Measurements of synthetic magnetite.....	54
Figure 2-5: Semi-log plots of the FMR parameters of the synthetic magnetite and AMB-1 samples against k_{ARM}/IRM	56
Figure 2-6: Transmission electron micrographs of Pt-C replica of synthetic magnetite powder TMB-100 diluted at 6,000 ppm in sucrose.....	57
Figure 2-7: Summary of FMR parameters.....	59
Figure 2-8. Measurements through Andros Island core C51.....	60
Figure 2-9. Representative FMR spectra of Oligocene-Miocene deep-sea muds from DSDP Leg 73 Site 522 and silts from the Pleistocene Wilson Creek Formation of Mono Basin.....	62
Figure 2-10. The factor α for model spectra. α is plotted for synthetic spectra with first-order uniaxial anisotropy specified by B_{an}	64

Figure 3-1: Angles used in the derivation of the resonance conditions.....	75
Figure 3-2: Transmission electron micrographs of MV-1.....	79
Figure 3-3: Transmission electron micrographs of and summary statistics for AMB-1 strains.	80
Figure 3-4: FMR spectra of MV-1.	83
Figure 3-5: FMR spectra of AMB-1 wild-type, <i>mnm13</i> and <i>mnm18</i>	83
Figure 3-6: Rock magnetic measures of selected samples.	87
Figure 3-7: FMR parameters compared to rock magnetic parameters for the samples discussed in this paper.	93
Figure 3-8: Plot of ΔB_{FWHM} against A for the samples discussed in this paper	95
Figure 4-1: Bathymetry of the Great Bahama Bank.	100
Figure 4-2: Panchromatic Quickbird image of Triple Goose Creek.	101
Figure 4-3: Stratigraphic columns and profiles of magnetic and ferromagnetic resonance parameters through algal marsh cores C129, C139, and C149, and microelectrode data from C130 and C148.....	108
Figure 4-4: Stratigraphic columns and profiles of magnetic and ferromagnetic resonance parameters through levee crest core C160 and mangrove pond core C165, and mm-scale oxygen profiles through <i>Scytonema</i> and <i>Schizothrix</i> mats.	109
Figure 4-5: Crossplots of $ \Delta B_{FWHM} $ and total ferromagnetic resonance absorption against the FMR asymmetry parameter A	111
Figure 4-6: Smoothed and unsmoothed FMR derivative absorption spectra for C139 samples from 49 cm above and 24 cm below MTL.....	114
Figure 4-7: TEM images of superparamagnetic magnetite particles within an organic matrix from above MTL in C139, single-domain stoichiometric magnetite particles from surface samples at C6, and elongate magnetic iron sulfide particles resembling greigite from 20 cm below MTL in C149.....	116
Figure 4-8: Representative vector component diagrams showing AF-demagnetization behavior of TGC carbonate samples.....	118
Figure 4-9: Equal-area stereonet projections of paleomagnetic directions from surface and core samples	119
Figure 4-10: Redox zones of cores determined from changes in ferromagnetic material	121

Figure 4-11: Schematic representation of the biogeochemical processes affecting the magnetic properties of Triple Goose Creek sediments.....	122
Figure 5-1: Map of New Jersey drill sites.....	128
Figure 5-2: Fine quartz sand fraction, $\delta^{13}\text{C}_{\text{inorganic}}$, ratio of saturation remanence magnetization to saturation magnetization, saturation magnetization, FMR parameters α , A , ΔB_{FWHM} , and g_{eff} , and example FMR spectra for upper Paleocene to lower Eocene strata, ODP Leg 174AX, Ancora, New Jersey.....	130
Figure 5-3: FMR parameters ΔB_{FWHM} and A for PETM clay and underlying and overlying sediments.....	131
Figure 5-4: Fine quartz sand fraction, $\delta^{13}\text{C}_{\text{inorganic}}$, total FMR absorption, rock magnetic parameters, and IRM acquisition coercivity spectra for upper Paleocene to lower Eocene strata, ODP Leg 174AX, Ancora, New Jersey.....	132
Figure 5-5: Coercivity spectra from Ancora samples in late Paleocene silty clay, PETM clay, and early Eocene silty clay, determined from the derivative of IRM acquisition curves.....	132
Figure 5-6: ARM acquisition curves for Ancora samples in late Paleocene silty clay, PETM clay, and early Eocene silty clay, determined in a 100 mT alternating field.....	133
Figure 5-7: TEM images of well-preserved single-domain magnetite crystals from the PETM clay with shapes characteristic of bacterial magnetite.....	134
Figure 5-8: Length and shape factor (width/length ratio) of magnetite particles from magnetic separates of Ancora sample at 168.81 m depth.....	134
Figure I-1: Proposed correlation of the Huronian Supergroup and the upper Transvaal Supergroup.....	145
Figure I-2: Modeled O_2 production at different levels of P and Fe flux into the photic zone and at varying C burial efficiency and C/Fe ratio..	148
Figure II-1: Block diagram of the sample changer system.	163
Figure II-2: Paleomagnetic and rock magnetic data from a weakly magnetic Permian carbonate specimen, Kyushu.....	166
Figure II-3: Error analysis of measurements run on the Eugene Shoemaker Memorial Magnetometer in 2006.....	169

LIST OF TABLES

Table 1-1.	Proposed magnetofossil robustness criteria.....	17
Table 1-2.	Magnetofossil reports from pre-Pleistocene localities with stratigraphic context	34
Table 1-3.	Magnetofossil reports from pre-Pleistocene localities with limited or no stratigraphic context	35
Table 2-1.	Summary of FMR and magnetic parameters of bacterial samples.....	50
Table 2-2.	Summary of 77 K FMR parameters of bacterial and synthetic magnetite samples	51
Table 2-3.	Summary of FMR and magnetic parameters of synthetic magnetite samples	52
Table 2-4.	Summary of parameters of environmental samples	61
Table 3-1.	Measured ferromagnetic resonance parameters.....	81
Table 3-2.	Ferromagnetic resonance spectral fits.....	82
Table 3-3.	Room temperature rock magnetic parameters	88
Table 3-4.	Low temperature magnetic properties.....	91
Table 5-1.	FMR and rock magnetic parameters for upper Paleocene to lower Eocene strata, ODP Leg 174AX, Ancora, New Jersey.	137
Table I-1.	Midpoint potentials of relevant redox couplets	144

GUIDE TO ACRONYMS

AF	Alternating field	MD	Multidomain
ARM	Anhyseritic remanent magnetization	MDH	Magnetite dissolution horizon
BCM	Biologically controlled mineralization	MHTL	Mean high tide level
BIF	Banded iron formation	MIF	Mass independent fractionation
CRM	Chemical remanent magnetization	MP	Mangrove pond
DRM	Detrital remanent magnetization	MPMS	Magnetic Properties Measurement System
EDS	Electron diffraction x-ray spectroscopy	MTL	Mean tide level
EPR	Electron paramagnetic resonance	NRM	Natural remanent magnetization
FMR	Ferromagnetic resonance	OATZ	Oxic/Anoxic Transition Zone
FWHM	Full width at half maximum	PETM	Paleocene/Eocene Thermal Maximum
HAM	High algal marsh	SD	Single-domain
IAM	Inland algal marsh	SEM	Scanning electron microscopy
IGRF	International Geomagnetic Reference Field	SP	Superparamagnetic
IRM	Isothermal remanent magnetization	SPH	Sulfide precipitation horizon
LAM	Lower algal marsh	TGC	Triple Goose Creek
LC	Levee crest	TEM	Transmission electron microscopy

Chapter 1

INTRODUCTION*

The identification and biogeochemical interpretation of fossil magnetotactic bacteria

1.1 Introduction

Traditionally, paleobiology has focused on studying the products of biologically-controlled mineralization (BCM), the process of inducing minerals to precipitate following a template established by organic molecules (LOWENSTAM, 1981). Such products are clear indications of the existence and nature of past life. A fossil shell, for instance, is an unequivocal biosignature that conveys information about the paleoenvironment of its formation and hints to the evolutionary complexity of the organism that created it. BCM is rare, however, in microbes. Thus, the study of ancient microbes usually relies upon alternative techniques, each with distinctive strengths and weaknesses: techniques such as the study of stromatolites and carbonaceous microfossils, the interpretation of organic biomarker compounds and isotopic signatures, and the phylogenetic analysis of genomic data.

Though many prokaryotes precipitate carbonate, sulfide, or oxide minerals as extracellular metabolic byproducts, magnetotactic bacteria are among the few prokaryotes to engage in BCM (BLAKEMORE, 1975). These bacteria are defined by the ability to precipitate intracellular crystals of ferrimagnetic minerals, specifically magnetite and greigite, and have been found from several divisions of the Proteobacteria (DELONG et al., 1993; MARATEA and BLAKEMORE, 1981; SIMMONS et al., 2004) and from the Nitrospira (SPRING et al., 1993; SPRING and SCHLEIFER, 1995). Like fossil shells, bacterial magnetite and greigite bear the signs of natural selection's optimizing influence. They can therefore be identified in sediments, where they are given the name magnetofossils. Like the presence of more conventional fossils, the presence of magnetofossils reflects environmental conditions, specifically conditions that facilitate magnetotactic bacteria growth and magnetofossil

* Co-authored with Joseph L. Kirschvink.

preservation. Magnetofossils are therefore a largely untapped proxy for ancient biogeochemistry.

1.2 Ecology of magnetotactic bacteria

1.2.1 Magnetotaxis and redox zonation

Magnetotactic bacteria produce magnetite or greigite crystals within membrane-bound vesicles called magnetosomes (BAZYLINSKI and FRANKEL, 2004; GORBY et al., 1988; KOMEILI et al., 2006; KOMEILI et al., 2004; MATSUNAGA and OKAMURA, 2003). The crystals provide the bacteria with a net magnetic moment, which they employ for magnetotaxis, movement directed by the local magnetic field. Many magnetotactic bacteria grow preferentially under specific, narrow redox conditions (Figure 1-1). Magnetite producers are often microaerophiles or nitrate-reducers found in the suboxic conditions of the oxic-anoxic transition zone (OATZ) (BAZYLINSKI and MOSKOWITZ, 1997). SIMMONS et al. (2004) found that, in Salt Pond, Massachusetts, magnetite producers were particularly concentrated at the top of OATZ, where oxygen diffusing from above and iron diffusing from below produce a peak in particulate Fe(III) abundance. There are exceptions to this typical distribution, however. Some magnetite producers can grow under aerobic conditions (e.g., SCHÜLER and BAEUERLEIN, 1998), but they do not produce magnetite at high oxygen levels. At least one magnetite producer, *Desulfovibrio magneticus* RS-1, is a strictly anaerobic sulfate reducing bacterium (SAKAGUCHI et al., 2002; SAKAGUCHI et al., 1993), although it is only weakly magnetotactic and may use its magnetosomes for an alternate purpose (PÓSFAL et al., 2006).

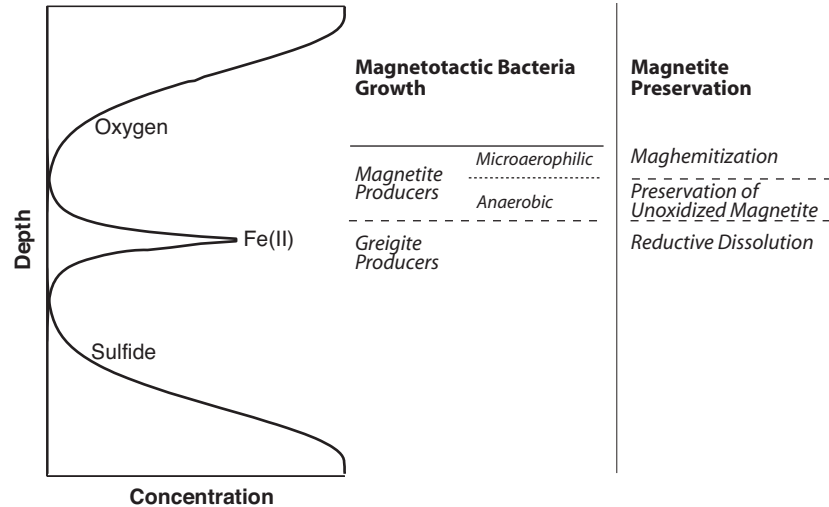


Figure 1-1: Schematic representation of chemical gradients, the typical optimal growth positions of different types of magnetotactic bacteria, and diagenetic fate of magnetite. Redox gradients can exist over scales from millimeters to meters.

Greigite producers prefer more reduced conditions and are often strictly anaerobic sulfate reducers. SIMMONS et al. (2004) found that greigite-producing multicellular magnetotactic prokaryotes (MMPs) grew in greatest abundance near the dissolved Fe(II) concentration peak at the base of the OATZ, while other greigite producers grew in deeper, more sulfidic waters. One sulfate-reducing greigite bacterium, found in microbial mats associated with methane-seep carbonate concretions in the Black Sea, is a member of a syntrophic partnership engaged in anaerobic oxidation of methane (REITNER et al., 2005). A magnetotactic bacterium found in Pettaquamscutt River Estuary, Rhode Island, produces both greigite and magnetite, with a greater proportion of greigite particles produced under more reducing conditions (BAZYLINSKI et al., 1995).

In environments with sharp redox gradients, magnetotaxis likely provides magnetotactic bacteria with a selective advantage by allowing them to search in one dimension instead of in three dimensions for optimal geochemical conditions (KIRSCHVINK, 1980a). The cells' magnetic moment causes them to align passively with the local magnetic field. Redox gradients are often nearly vertical, and, except at the geomagnetic equator, the geomagnetic field has a vertical component. For cells with moments $> 10^{-15} \text{ Am}^2$, equivalent to that produced by ~ 17 cubic magnetite crystals with 50 nm edge lengths, $> 90\%$ of the cell's

velocity is directed along magnetic field lines (FRANKEL and BLAKEMORE, 1989). However, because other gradient organisms thrive in spite of performing three-dimensional biased random walks to find optimal conditions, additional functions for the magnetosomes have been proposed, including iron storage (CHANG and KIRSCHVINK, 1989) and energy storage (VALI and KIRSCHVINK, 1991). The discovery of membrane-bound iron oxide inclusions in the non-magnetotactic, iron-reducing bacterium *Shewanella putrefaciens* (GLASAUER et al., 2002) lends credence to these suggestions.

1.2.2 Magnetotaxis as a way to short-circuit diffusion

For most organisms living at sharp redox gradients, metabolism is limited by the diffusive fluxes of nutrients, but, as reviewed by SCHULZ and JØRGENSEN (2001), several species of large colorless sulfur bacteria have found ways of bypassing diffusive limitations. These microaerophilic or nitrate-reducing organisms employ two distinctive strategies: (1) overcoming diffusive limitation of electron donors and acceptors through various approaches to motility, and (2) storage of intracellular electron donor and acceptor reserves as a buffer against external variability. *Thioploca*, for instance, forms elevator-like sheaths many centimeters long, within which filaments swim up and down (JØRGENSEN and GALLARDO, 1999). The sheaths provide it with direct paths between electron-donor rich and electron-acceptor rich environments. *Thioploca* can accumulate nitrate in storage vacuoles at concentrations as high as 0.5 M when at the more oxidized end of their shafts, then use the nitrate to oxidize sulfide when at the more reduced end. Conversely, they can also partially oxidize sulfide to form elemental sulfur granules as an electron donor reserve.

Magnetotaxis performs a function analogous to that of the sheaths of *Thioploca*: namely, enabling the magnetotactic bacteria to swim rapidly and directly between electron donor rich and electron acceptor rich regions. Moreover, as in the colorless sulfur bacteria, sulfur globules have been found in a number of magnetotactic bacteria (COX, 2002; MOENCH, 1988; SPRING et al., 1993); as SPRING et al. (1993) suggested, these globules may act as electron donor reserves. Some magnetotactic bacteria also contain additional energy storage compounds, such as polyphosphate granules and polyhydroxyalkanoates (KEIM et al., 2005). Following VALI and KIRSCHVINK (1991), we suggest that the magnetosome crystals themselves may act as intracellular storage batteries, becoming partially oxidized while the

bacterium is in oxidizing waters and reduced back to stoichiometric magnetite while the bacterium is in reducing waters.

Like magnetite and greigite, maghemite ($\gamma\text{-Fe}_2\text{O}_3$) is a ferrimagnetic mineral that can have a cubic closed-packed spinel structure. Magnetite, which forms a solid solution with maghemite, can transform to maghemite topotactically, leaving its anionic framework (DAVIS et al., 1968) and magnetic orientation (VALI and KIRSCHVINK, 1989) intact. Thus, redox cycling would not significantly hinder a magnetite crystal's navigational utility. Although the ferrous sulfide mackinawite, which has been reported in the magnetosomes of greigite-producing magnetotactic bacteria (PÓSFAL et al., 1998b), is non-magnetic, it similarly shares a common cubic close-packed anionic framework with greigite and has been observed to transform topotactically into greigite.

Assuming that magnetotactic bacteria have a mechanism for coupling the energy generated to adenosine triphosphate production, the magnetosomes could be used as an electrochemical battery in either of two ways: as a way of boosting the energy produced by respiration or as a self-sufficient catabolic iron cycle. Both approaches extract energy from the Fe(II) concentration gradients of the redoxcline. In natural waters, [Fe(II)] reaches as high as $\sim 300 \mu\text{M}$ under suboxic conditions, and $< 100 \text{ nM}$ under oxic and sulfidic conditions (e.g., LEHTORANTA, 2003; O'SULLIVAN et al., 1997).

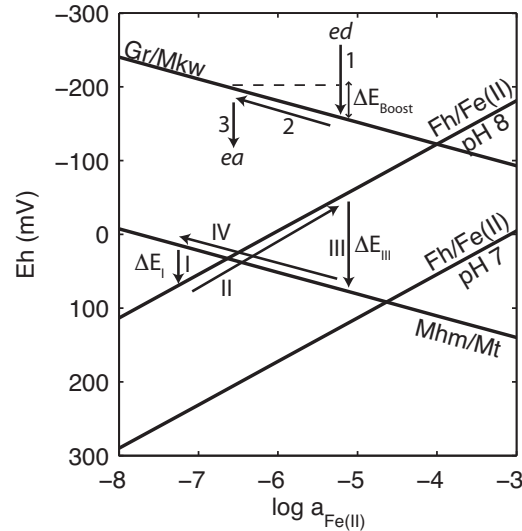


Figure 1-2: Oxidation/reduction potential of maghemite/magnetite, greigite/mackinawite, and ferrihydrite/Fe⁺² couplets at pH 7 and pH 8 plotted against Fe(II) activity. Arrows 1-3 show a pathway for a bacterium using magnetosome redox cycling to boost the energy provided by external electron donors and acceptors: (1) The bacterium transfers electrons from a donor (*ed*) to a greigite magnetosome crystal, partially reducing the crystal to mackinawite. (2) The bacterium swims to a region of lower Fe(II) activity. (3) The bacterium transfers electrons from mackinawite to an external acceptor (*ea*). The redox potential boost over direct transfer from *ed* to *ea* is shown by ΔE_{Boost} . Arrows I-IV show a closed-cycle magnetosome battery: (I) The bacterium transfers electrons from a magnetite magnetosome crystal to an internal ferrihydrite store, producing Fe⁺² and tapping a redox potential of ΔE_{I} . (II) The bacterium swims to a region of higher Fe(II) activity. (III) The bacterium transfers electrons from Fe(II) to the partially oxidized magnetosome crystal, generating ferrihydrite and tapping a redox potential of ΔE_{III} . (IV) The bacterium returns to a region of lower Fe(II) activity. (Calculated using thermodynamic constants from DREVER, 1997; MAJZLAN et al., 2003).

In the first mechanism (Figure 1-2, arrows 1-3), a bacterium would use an external electron donor in high-Fe, suboxic waters to reduce partially oxidized magnetosome crystals, swim to low-Fe oxic or sulfidic waters, and use an external electron acceptor to re-oxidize the crystals. Cycling the magnetosome crystals in this fashion effectively increases the difference in redox potential between the electron donor and the electron acceptor by ~30 mV for each order-of-magnitude change in Fe(II) activity. The additional potential generates an energetic boost of ~6 kJ/mol per 2 e⁻ transfer for each order-of-magnitude change.

In the second mechanism, a properly “charged” magnetotactic bacteria could temporarily survive in a reductant-depleted and oxidant-depleted environment through a self-sufficient, closed-loop Fe cycle (Figure 1-2, arrows I-IV). A bacterium swimming between water with $\sim 0.1 \mu\text{M Fe(II)}$ and water with $\sim 100 \mu\text{M Fe(II)}$, both at pH 8, could generate $\sim 51 \text{ kJ/mol}$ per $2e^-$ transfer from each cycle. A bacterium could drive a similar closed-loop cycle by coupling magnetosome redox cycling to redox cycling of intracellular sulfur globules.

In order for either use of the magnetosome as a battery to be a feasible metabolic activity, the energy gained from the reaction must be at least comparable to that spent in swimming through the redoxcline. By Stokes’ law, the cost to a $\sim 1 \mu\text{m}$ diameter bacterium of moving 1 cm at a reasonable velocity of $20 \mu\text{m/s}$ is $\sim 4 \times 10^{15} \text{ J}$ (BERG, 1993). A typical bacterium with 20 magnetosomes, approximated by cubes with an edge length of $\sim 50 \text{ nm}$, has about 5×10^{17} moles of magnetite.* If the magnetosomes were fully oxidized, then the breakeven point would occur when the oxidation reaction released $\sim 80 \text{ J}$ per mole magnetite oxidized ($\sim 240 \text{ J/mol}$ per $2e^-$ transfer), considerably less than the $\sim 6\text{-}18 \text{ kJ/mol}$ per $2 e^-$ transfer boost available. These estimates ignore the low efficiency of flagellar propulsion, estimated to be a few percent (PURCELL, 1997), the tortuosity of the bacterium’s path through sediments, which will reduce swimming efficiency by up to $\sim 30\%$ (ULLMAN and ALLER, 1982), and the likelihood that the magnetosome crystals are only partially oxidized. Nevertheless, a magnetosome battery is thermodynamically feasible across centimeter length scales comparable to those of redox gradients in sediments like those inhabited by many magnetotactic bacteria (e.g., SPRING et al., 1993).

The feasibility of a magnetosome battery can also be analyzed by considering the growth rate of an organism using intracellular magnetite as an electron donor for carbon fixation, as in the simplified reaction:



* At least one species of magnetotactic bacteria, *Magnetobacterium bavaricum* (SPRING et al., 1993), has up to 1,000 magnetosomes per cell and could therefore produce considerably more energy per battery cycle.

By mass balance, 46.4 g magnetite must be reduced to produce 1 g of biomass (“CH₂O”). For a cell that contains 2 wt% Fe as magnetite, this means that the magnetite must be cycled ~2300 times per replication. For a reasonable bacterial doubling time of two weeks, this requires a cycling time of ~9 minutes. A bacterium cycling its battery across a ~1 cm redox gradient must therefore swim at ~20 $\mu\text{m/s}$, in line with the observed swimming speed of magnetotactic bacteria (SEONG and PARK, 2001).

If correct, the magnetosome battery hypothesis would explain why magnetotactic bacteria live predominantly near sharp redox gradients and why some bacteria (e.g. SPRING et al., 1993) produce many more magnetosomes than are necessary for magnetotaxis. It also suggests that magnetotaxis might have been an evolutionary exaptation, a metabolic pathway adapted after its initial evolution for sensitivity to the geomagnetic field. Our calculations demonstrate the feasibility of the hypothesis, which could be tested through examination of the oxidation state of magnetite from magnetotactic bacteria across natural gradients and in gradient culture, as well as through microbial growth experiments and genetic investigation of the magnetite biomineralization pathway.

1.3 Traits and identification techniques for magnetotactic bacteria

1.3.1 The fingerprint of natural selection

In the modern world, Fe is often a scarce nutrient, its availability limited by the insolubility of iron under oxic conditions. Because natural selection has not eliminated magnetosome production, magnetotactic bacteria must gain some adaptive advantage from the sequestration of this precious resource in magnetosomes. Natural selection should therefore favor traits that maximize the efficiency with which the bacteria employ Fe. Since magnetotaxis, requires that the cells’ magnetic moments are strong enough that the magnetic aligning effect dominates thermal agitation, selection should favor traits that maximize the moment produced per atom of Fe used.

The most fundamental characteristic of biologically controlled mineralization is that it occurs under biological control. Magnetosome crystals are produced within membrane-bound vesicles in a process orchestrated by a mechanism that genetic studies are just starting to reveal (BAZYLINSKI and FRANKEL, 2004; KOMEILI et al., 2006; KOMEILI et al.,

2004; MATSUNAGA and OKAMURA, 2003; SCHEFFEL et al., 2006). Biochemical regulation allows magnetotactic bacteria to produce crystals with three broad categories of adaptive traits: (1) narrow size and shape distributions, (2) chain arrangement, and (3) chemical purity and crystallographic perfection. Several aspects of these traits were previously discussed by THOMAS-KEPRTA et al. (2000). Some of these traits can be partially assessed at a bulk level through the techniques of rock magnetism and ferromagnetic resonance (FMR) spectroscopy (see Chapters 2 and 3), while others traits require detailed electron microscopy to identify.

1.3.2 Size and shape distributions

Magnetosome crystals typically exhibit species-specific, narrow distributions of size and shape factor (length/width ratio) (e.g., ARATÓ et al., 2005; DEVOUARD et al., 1998; KIRSCHVINK and LOWENSTAM, 1979). Almost all magnetotactic bacteria produce crystals that, at least in the arrangement that naturally occurs in the cell, act as single-domain (SD) particles (Figure 1-3). While the moments of smaller, superparamagnetic (SP) particles are buffeted by thermal noise and those of larger, multidomain (MD) particles are reduced by the formation of domains with moments aligned in different directions, in single-domain particles the entire crystal contributes to producing a stable net magnetization. Natural selection would predict such an outcome in organisms that are capable of controlling the microenvironment in which the crystals form and that gain a selective advantage from their magnetic moment.

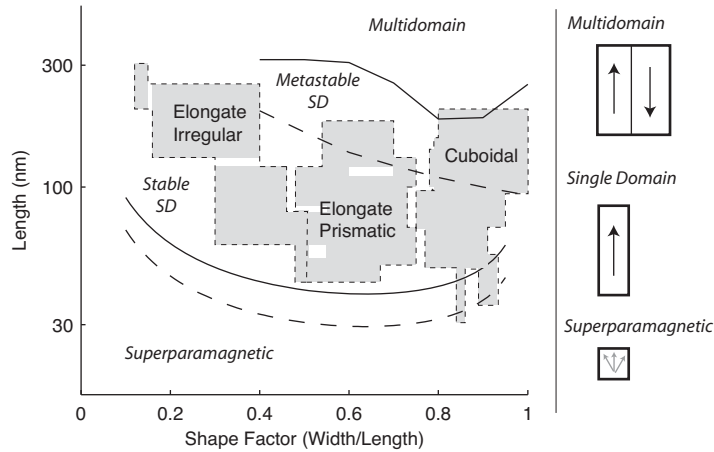


Figure 1-3: Single-domain stability field of magnetite as a function of shape factor (width/length ratio) and length. Diagrams on the right schematically represent the arrangement of magnetic moments in two domain, single-domain, and superparamagnetic particles. The lower, SD/superparamagnetic boundary is determined for rectangular parallelepipeds with unblocking times of 100 s (dashed line) and 4.5 Gy (solid line) following BUTLER and BANERJEE (1975) and DIAZ-RICCI and KIRSCHVINK (1992). Because the calculation ignores magnetocrystalline anisotropy, it overestimates the minimum SD length at shape factors close to 1. The dashed upper boundary of the stable SD field and the solid upper boundary of the metastable SD field are taken from the micromagnetic models of WITT et al. (2005) for characteristic magnetosome crystal shapes. Shaded regions mark size and shape of crystals from magnetotactic bacteria (ARATÓ et al., 2005; BAZYLINSKI et al., 1995; DEVOUARD et al., 1998; FARINA et al., 1994; MELDRUM et al., 1993a; MELDRUM et al., 1993b; MOENCH, 1988; SAKAGUCHI et al., 1993; THORNHILL et al., 1994; VALI and KIRSCHVINK, 1991).

Whereas open system chemical growth processes lead to log-normal size distributions, magnetotactic bacteria produce distributions with sharper cutoffs at larger sizes. Cultured bacteria generally produce negatively skewed crystal size distributions, although a few bacteria produce Gaussian size distributions (ARATÓ et al., 2005; DEVOUARD et al., 1998; PÓSFAL et al., 2001) (Figure 1-4).

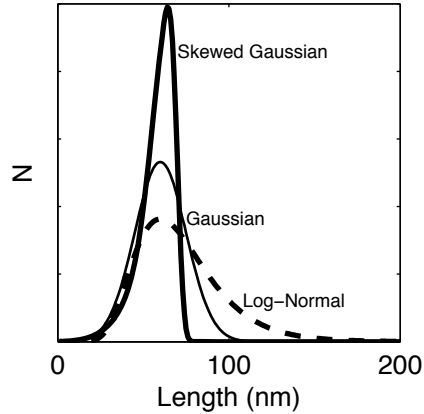


Figure 1-4: Schematic representation of particle size distributions. Most magnetotactic bacteria produce skewed Gaussian distributions, although some produce Gaussian distributions. Open system chemical growth processes give rise to log-normal distributions.

Common magnetosome magnetite morphologies include equidimensional cubo-octahedra, elongate hexaoctahedral prisms, and irregular and elongate tooth, bullet (THORNHILL et al., 1994), and arrowhead (BAZYLINSKI et al., 1995) shapes (Figure 1-5), while common magnetosome greigite morphologies include equidimensional cubo-octahedra and elongate rectangular prisms (BAZYLINSKI et al., 1994). (Cubo-octahedra are frequently labeled as “cuboidal” and elongate hexaoctahedra are frequently labeled as “prismatic,” a convention we adopt for linguistic simplicity. In the literature, where crystals have not been examined closely, cubo-octahedra have sometimes been identified as cubic or octahedral.) The characteristic magnetosome crystal shapes have less sharp edges than do equidimensional octahedral or rectangular parallelepipeds. This “rounding” reduces the outward warping of magnetization at the crystal ends, which produces magnetic “flower” structures in straight-edged particles (KIRSCHVINK, 2001; WITT et al., 2005). It thereby extends the size to which single-domain crystals can grow (WITT et al., 2005). Because the bending of magnetization in flower structures reduces net crystal magnetization, the elimination of sharp edges also directly increases the magnetic moment per iron atom (KIRSCHVINK, 2001).

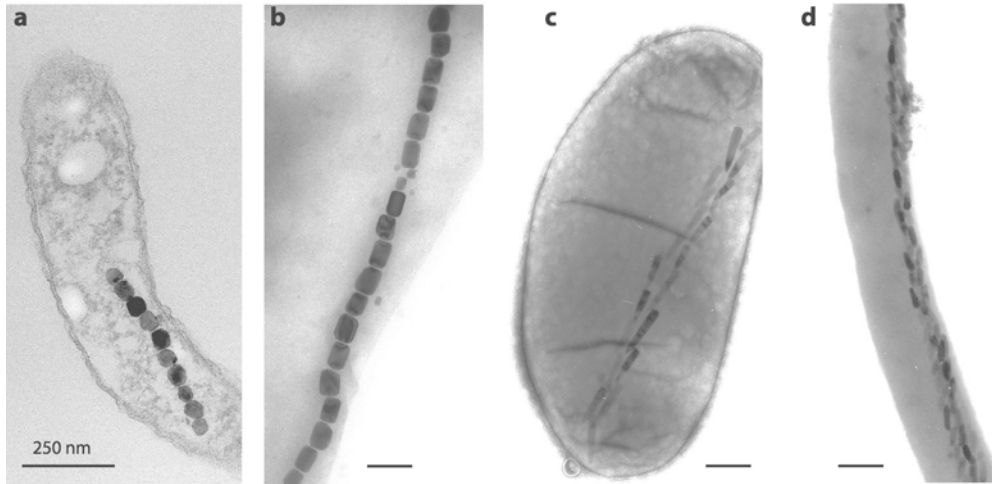


Figure 1-5: TEM images of magnetite-producing magnetotactic bacteria exhibiting different magnetosome crystal morphologies. (a) Cubo-octahedral magnetite in laboratory-grown *Magnetospirillum magnetotacticum* MS-1, (b) hexaoctahedral prismatic magnetite from bacteria living in the sediments of Lake Ammersee, Germany, (c-d) irregular elongate magnetite from bacteria living in the sediments of Lake Chiemsee, Germany. Scale bar is 250 nm in all images. Images courtesy A. Kobayashi (a) and H. Vali (b-d).

Magnetic anisotropy energy causes the magnetization of a domain to align preferentially in certain directions. In SD particles, it therefore controls the particle's coercivity, the field required to remagnetize the particle (see Chapter 3). In equidimensional magnetite and greigite particles, magnetic anisotropy, and thus coercivity, is controlled by the inherent magnetocrystalline anisotropy. In stoichiometric magnetite, magnetocrystalline anisotropy leads to room-temperature bulk coercivities of ~ 15 mT. Increasing the anisotropy of a particle increases coercivity and permits larger particles to remain within the single-domain field. Shape anisotropy increasingly governs magnetic anisotropy for crystals with width-to-length ratios less than ~ 0.9 . A 50 nm long magnetite particle with a width-to-length ratio of 0.5, for instance, has a room-temperature bulk coercivity of ~ 50 mT. At 0 K, an infinitely long magnetite rod would have a bulk coercivity of ~ 150 mT, the maximum possible for magnetite.

In magnetotactic bacteria with elongate magnetite particles, the crystals are typically elongated along a [111] axis (but for exceptions see MANN et al., 1987; TAYLOR and BARRY, 2004; TAYLOR et al., 2001; VALI and KIRSCHVINK, 1991). Because [111] axes are

the magnetocrystalline easy axes, elongation along one of these axes produces a shape anisotropy that complements the magnetocrystalline anisotropy. Greigite crystals are often elongated along a [100] axis (BAZYLINSKI et al., 1995; HEYWOOD et al., 1990; PÓSFAL et al., 1998a), fueling speculation that [100] axes are the greigite magnetocrystalline easy axes (BAZYLINSKI and MOSKOWITZ, 1997).

The most direct method of assessing size and shape factor distributions, but also the most labor-intensive and subject to sampling biases, involves direct measurement of particles in magnetic extracts under transmission electron microscopy (TEM). A variety of magnetic techniques allow the construction of coercivity spectra of samples, which are functions of both size and shape. The characteristically narrow distributions of biologically controlled magnetic minerals can sometimes be observed in the dispersion of the coercivity (EGLI, 2004a) (Figure 1-6). Anisotropy fields play a major role in controlling the width and asymmetry of FMR spectra, which can be used to identify elongate magnetic particles as well as the narrow distributions characterized of biological control (Figure 1-6; also see Chapters 2 and 3).

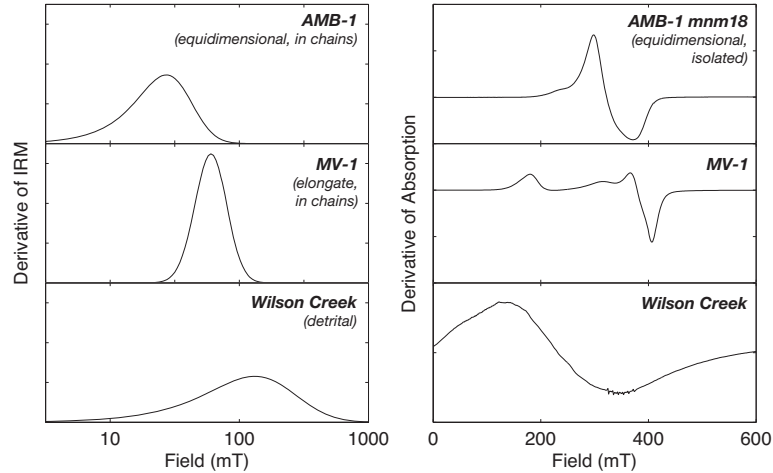


Figure 1-6: Example coercivity spectra (left) and FMR spectra (right). From top to bottom, coercivity spectra are shown for AMB-1 (which produces chains of cuboidal magnetite), MV-1 (which produces chains of elongate prismatic magnetite), and detrital magnetic particles from the Wilson Creek Formation of Mono Basin, California. Comparison of the AMB-1 and MV-1 spectra demonstrates the effect of elongation on particle coercivity, while comparison of the bacterial and detrital spectra illustrates the narrower coercivity distribution of biologically controlled magnetite. FMR spectra are shown for AMB-1 mutant *mnm18*, which predominantly produces isolated equidimensional magnetite particles, MV-1, and Wilson Creek sediments. Whereas magnetocrystalline anisotropy causes the spectrum of *mnm18* to be slightly asymmetric in the high-field direction, the stronger anisotropy produced by particle elongation and chain arrangement causes the spectrum of MV-1 to be much broader and strongly low-field extended. The detrital magnetic particles of the Wilson Creek sediments, being more heterogeneous in size, shape, and arrangement, produce an extremely broad but fairly symmetric spectrum.

1.3.3 Chain arrangement

In most magnetotactic bacteria, the magnetosomes are maintained aligned in one or more chains by a cytoskeletal structure (KOMEILI et al., 2006), an organic sheath (KOBAYASHI et al., 2006), and anchoring proteins (SCHEFFEL et al., 2006). The chain axis is typically aligned with the easy axes of the individual particles (DUNIN-BORKOWSKI et al., 2001). The chain serves the same basic physical function as particle elongation: It increases the stability of the state in which particle moments are aligned along the chain axis by enhancing magnetic anisotropy. Whereas mutant AMB-1 producing isolated particles of nearly equidimensional magnetite have a room-temperature bulk coercivity of ~13 mT, AMB-1 producing short chains of equidimensional particles have a room-temperature coercivity of ~25 mT (see Chapter 3).

Linear strings of magnetic particles can also be produced by physical processes (see Chapter 2). Biologically produced chains are distinguished by being composed of particles from a size and shape factor distribution characteristic of magnetotactic bacteria and having few branch points. If the particle size distribution of the magnetic crystals is known, sampling statistics can assess the probability that the crystals within a chain are not a random sub-sample of the distribution. Chains with these traits are highly suggestive of a biological origin. Techniques for identifying these chains are therefore key to developing the fossil record of magnetotactic bacteria.

TEM imaging of magnetic extracts is currently the only technique for producing high-resolution images of chains. Magnetic extraction, however, involves disrupting the matrix containing the magnetic particles, and the extraction process provides a good mechanism for physically forming strings of particles. Thus, short chains found in extracts are ambiguous as to their origins; only long chains with characteristic magnetofossil traits are indicative of biological origin. Scanning electron microscopy (SEM) permits imaging particles in situ (FRIEDMANN et al., 2001; MAHER et al., 1999) but lacks the resolution needed to characterize particle shape and so is only useful for magnetofossil identification when combined with TEM of extracts (e.g., Figure 1-7c, d).

For unoxidized magnetite, the Moskowitz test, which compares the thermal demagnetization behavior of low temperature saturation remanence magnetizations acquired after cooling in zero field and that acquired after cooling in a strong field, can also indicate the presence of chains (MOSKOWITZ et al., 1993; WEISS et al., 2004a). At the Verwey transition, which occurs at 125 K in stoichiometric magnetite, magnetite shifts from having cubic symmetry at higher temperatures to having uniaxial symmetry at lower temperatures. Magnetite chains exhibit relatively greater demagnetization of the field-cooled remanence upon warming through the Verwey transition than do other arrangements of magnetite. The effect likely results from the influence of the chain structure on the selection of an elongation axis during cooling below the Verwey temperature (MOSKOWITZ et al., 1993). However, the physics underlying this observation (CARTER-STIGLITZ et al., 2002; CARTER-STIGLITZ et al., 2004) is only partially understood, and the test is subject to false negatives generated by limited particle oxidation.

Ferromagnetic resonance spectroscopy is sensitive to the magnetic anisotropy produced by particle chains, as well as the homogeneity that distinguishes biological chains from physical strings (see Chapters 2–3 and Figure 1-6). It is rapid and insensitive to particle oxidation, and thus is currently the best bulk technique capable of screening samples for the presence of likely magnetofossil chains.

1.3.4 Chemical purity and crystallographic perfection

In general, magnetite produced by magnetotactic bacteria is nearly pure iron oxide, with concentrations of trace elements like Ti, Al, and Cr significantly lower than in most abiotic magnetite (THOMAS-KEPRTA et al., 2000). Such purity is expected based both on selection for efficiency in the use of Fe, as trace elements reduce the magnetic moment of magnetite particles, and on the extensive use of pure iron as a specific metal cofactor in numerous enzymatic systems. Some bacteria do produce magnetite that is slightly oxidized; the Verwey transition can be reduced from the 125 K of stoichiometric magnetite to temperatures as low as ~100 K, which indicates up to 0.4% cation depletion (see Chapter 3). Chemical purity can be assessed most accurately by analytical techniques coupled to TEM, such as energy dispersive X-ray spectroscopy (EDS), but can also be assessed in magnetite at a bulk level from shifts in the Verwey transition temperature and Néel temperature. However, these transition temperatures are also affected by diagenetic oxidation.

With the exception of twinning along the [111] easy axis, crystallographic defects also reduce the magnetic moment of magnetite particles. Thus, crystallographic defects are rare in magnetosome magnetite (DEVOUARD et al., 1998). The absence of such defects can be assessed only by high-resolution TEM.

Greigite magnetosome crystals are often less strictly controlled than magnetite crystals, both chemically and crystallographically. Some greigite-producers can incorporate up to ~10 atomic percent Cu into their magnetosome crystals (BAZYLINSKI et al., 1993; PÓSFAL et al., 1998a). Greigite magnetosome crystals also commonly exhibit planar defects along (222)-type planes, believed to be associated with the conversion of mackinawite into greigite (PÓSFAL et al., 1998a). These differences suggest that greigite precipitation by magnetotactic

bacteria may be less regulated than magnetite precipitation and could hinder identification of greigite magnetofossils.

1.3.5 Scoring magnetofossil identifications

We suggest the following scheme for rating possible magnetofossils:

Context and robustness: Magnetofossil identifications are more reliable if the samples under consideration come from an understood stratigraphic, geochemical, and paleomagnetic context or were collected as part of a broader study aimed at understanding this context. Magnetofossil reports from localities lacking robust paleomagnetic data should be viewed cautiously, as they are more likely to have undergone diagenetic or metamorphic processes that altered primary magnetic carriers, including any possible magnetofossils. Our suggested criteria for considering a magnetofossil identification to be robust are given in Table 1-1. Table 1-2 lists reports of pre-Quaternary magnetofossils from samples collected with contextual information, while Table 1-3 lists reports of pre-Quaternary magnetofossils from grab samples lacking such information. For samples where paleomagnetic information is available, we also report a paleomagnetic quality (PQ) score following the criterion of VAN DER VOO (1990). PQ ranges from zero to seven, where samples with $PQ \geq 4$ are considered robust. For demonstrably remagnetized units, PQ is listed as “*.”

Table 1-1. Proposed magnetofossil robustness criteria

Context	Criteria
<i>Environment analogous to younger magnetofossil-bearing environments; Paleomagnetic data robust</i>	$S \geq 3$; or $S \geq 2$ and $C \geq 3$; or $S \geq 2$ and $C \geq 2$ and ChP
<i>Environment analogous to younger magnetofossil-bearing environments; Paleomagnetic data not robust</i>	$S \geq 3$ and ChP; or $S \geq 3$ and $C \geq 3$; or $S \geq 3$ and $C \geq 2$ and ChP
<i>Environment analogous to younger magnetofossil-bearing environment; Sediments have undergone burial metamorphism or paleomagnetic data remagnetized</i>	$S = 4$ and ChP; or $S \geq 3$ and $Ch \geq 3$ and ChP; or $S \geq 3$ and $Ch \geq 2$ and ChP and CrP
<i>Unique environment</i>	$S = 4$ and $Ch \geq 3$ and ChP and CrP

Single-domain (criterion SD): As a basic requirement, all claims of magnetofossils should be supported by magnetic or electron microscopy evidence indicating the presence of a significant amount of single-domain magnetite, maghemite, or greigite (criterion SD in Table 1-2 and Table 1-3).

Size and shape (score S): Beyond the basic single-domain criterion, we score the size and shape of particles in a sample based on (1) coercivity or FMR spectra indicating narrow distributions of size and shape, (2) TEM evidence for SD particles with truncated edges (cubo-octahedral or hexa-octahedral morphologies, for example), (3) TEM evidence for elongate SD particles (such as hexaoctahedral and irregular elongate particles), and (4) statistical TEM evidence for SD populations with narrow size and shape distributions. Each of these four lines of evidence contributes one point to score S, which ranges from zero to four.

Chains (score C): We grade the quality of chain identification from zero to four. Zero indicates the absence of any evidence for chains, while one indicates that either SEM or low-temperature thermal demagnetization indicates the presence of chains. Two indicates either (a) that FMR indicates the presence of chains or (b) that short chains of ambiguous origin were imaged in the TEM of magnetic extracts. Three indicates either (a) the TEM identification of short chains and FMR data indicating that they are a significant, in situ component of the sample, or (b) the TEM identification of long chains in magnetic extracts. Four indicates the TEM identification of long chains in magnetic extracts combined with SEM or FMR evidence confirming that the chains occur in situ.

Chemical perfection (criterion ChP): Criterion ChP reflects whether the particles are relatively pure and, in particular, Ti-free. Among other techniques, EDS and low-temperature magnetometry can assess purity.

Crystallographic perfection (criterion CrP): Criterion CrP reflects whether high-resolution TEM indicates the absence of crystallographic defects other than twinning around the magnetic easy axis.

1.4 Fossil record of magnetotactic bacteria

1.4.1 Phanerozoic magnetofossils

Magnetofossils are a common contributor to sedimentary magnetism in a variety of Quaternary environments. Magnetite magnetofossils, often partially oxidized to maghemite, have been found as a major magnetic component of lacustrine (DEARING et al., 1998; KIM et al., 2005; OLDFIELD et al., 2003; PAN et al., 2005; PECK and KING, 1996; SNOWBALL, 1994), microbial mat (STOLZ et al., 1989), hemipelagic (DINARÈS-TURELL et al., 2003; HOUSEN and MOSKOWITZ, 2006; STOLZ et al., 1986), pelagic (HESSE, 1994; HILGENFELDT, 2000; LEAN and MCCAVE, 1998; PETERSEN et al., 1986; YAMAZAKI and IOKA, 1997; YAMAZAKI et al., 1991) and carbonate platform (Chapter 4 and MCNEILL, 1990; MCNEILL et al., 1988; SAKAI and JIGE, 2006) sediments. Greigite magnetofossils have not yet been identified in Quaternary sediments.

The pre-Quaternary magnetofossil record, in contrast, is sparse; more magnetofossil-bearing localities have been identified in the Quaternary than in all the rest of Earth history. The most robust pre-Quaternary identifications come from Mesozoic and Cenozoic sediments, although possible magnetofossils have also been found in rocks as old as the late Archean (Table 1-2 and Table 1-3). To date, pre-Quaternary magnetofossils have been identified in carbonate platform sediments, basinal sediments, and continental shelf deposits.

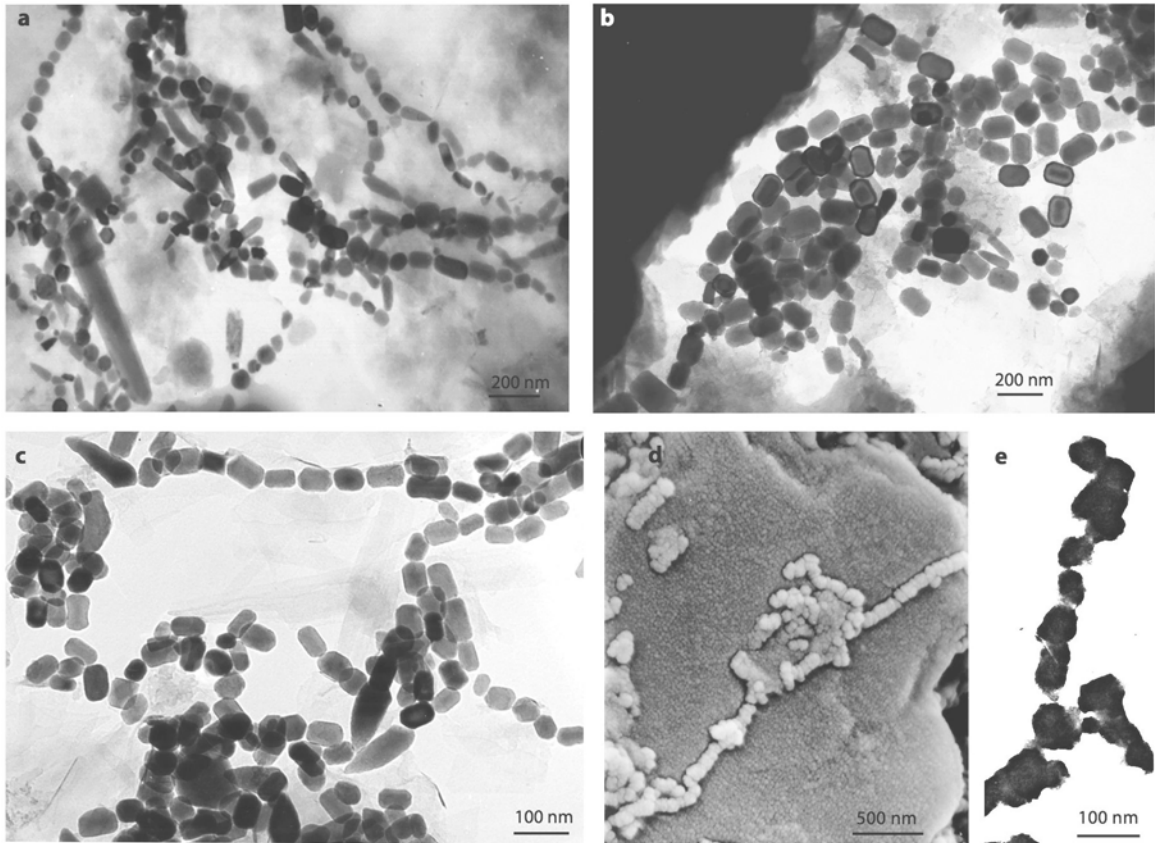


Figure 1-7: TEM images of magnetofossils. (a) Quaternary magnetofossils in a magnetic extract from nannofossil ooze from Ocean Drilling Project Hole 1006D, Santaren Channel, west of the Great Bahama Bank. Cuboidal, prismatic, and bullet morphologies are visible (scale bar = 200 nm). (b) Prismatic Miocene magnetofossils from clay-rich sediments, DSDP Leg 73, Angola Basin, South Atlantic Ocean (scale bar = 200 nm). (c-d) Cretaceous magnetofossils from chalk beds at Culver Cliff, United Kingdom. (c) shows prismatic and irregular elongate magnetosome morphologies in a magnetic extract from Culver Cliff chalk, with some intact chains of prismatic crystal (scale bar = 100 nm), while (d) shows intact magnetite chains imaged in situ with SEM (scale bar = 500 nm). (e) Putative 1.9 Ga magnetofossils from the Gunflint Formation, Ontario, Canada (scale bar = 100 nm). (Images courtesy M. Hunslow (a, c-d) and H. Vali (b). (e) reproduced from CHANG (1988).)

Carbonate platform and atoll sediments. In weakly magnetic Quaternary carbonate sediments, magnetofossils are frequently the primary carrier of syndepositional remanence magnetization, and the limited data available suggest the same is true of ancient carbonate sediments.

Magnetofossils have been robustly identified in Pliocene platform and atoll sediments. In Pliocene to Recent limestones and dolostones from San Salvador Island, Bahamas, TEM investigation of magnetic extracts reveals that the dominant magnetic particles are cuboidal and bullet-shaped SD magnetite crystals, sometimes arranged in short chains (MCNEILL et al., 1988). Similarly, in a core of Pliocene limestones and dolostones of the Mururora atoll, AISSAOUI et al. (1990) found predominantly cuboidal and prismatic SD magnetite particles, mixed with fragments of lithogenic, multidomain titanomagnetite. Coercivity spectra suggested that the single-domain particles dominate the samples' magnetic properties.

Plausible Jurassic (Bathonian-Sinemurian) magnetofossils that marginally fail to meet our robustness criteria have been found in carbonate platform sediments of the Paris and Jura Basins (BELKAALOUL and AISSAOUI, 1997; VALI et al., 1987). In both basins, single-domain magnetite, which constitutes a minor component (~15% in the Paris Basin; "low concentrations" in the Jura) of the bulk magnetic mineralogy, is present in cuboidal and prismatic shapes. Magnetic extracts from the Jura Basin carbonates contain short chains of SD particles (VALI et al., 1987), while the Paris Basin extracts contain pairs and clusters of particles (BELKAALOUL and AISSAOUI, 1997). The Jura samples were collected without paleomagnetic data and VALI et al. (1987) do not report any stratigraphic information that would allow their samples to be tied to other samples from the well-studied Northern Calcareous Alps. The Paris Basin carbonates carry robust paleomagnetic data, and despite the dominance by volume of detrital and authigenic MD magnetite, coercivity data indicate that biogenic SD magnetite is the main remanent magnetization carrier (BELKAALOUL and AISSAOUI, 1997).

Lower Cambrian (Tommotian) limestones of the Pestrosvet Formation, Siberia Platform, similarly contain plausible magnetofossils that marginally fail to meet our robustness criteria. The sediments are well preserved, having experienced no metamorphism, and provide robust paleomagnetic data (KIRSCHVINK and ROZANOV, 1984). Their magnetic properties reflect a dominant role for SD magnetite (CHANG et al., 1987), and TEM investigation reveals that the magnetite particles occur in cuboidal and prismatic shapes. At least in extract, the magnetite crystals occasionally form short chains.

Basinal sediments. Most robust reports of Phanerozoic magnetofossils come from basinal sediments, predominantly unlithified sediments from marine drill cores but also including lithified sediments exposed on land.

In Pliocene to Recent clays from the North Pacific, deposited below the lysocline at depths in excess of 5000 m, YAMAZAKI and IOKA (1997) found that the magnetic mineralogy was a mixture of SD, SP, and PSD magnetite, as well as maghemite and hematite. TEM images revealed that the SD fraction consisted of cuboidal and prismatic crystals, sometimes aligned in chains, while the larger grains were irregularly shaped. Yamazaki and Ioka identified the SD particles as magnetofossils and proposed an aeolian origin for the larger grains.

YAMAZAKI et al. (1991) examined early Miocene siliceous sediments from similar depths in the central equatorial Pacific Ocean. Rock magnetic measurements indicated that SD magnetite was the dominant stable magnetic component of the sediments, and TEM examination revealed crystals with cuboidal, prismatic, and bullet shapes characteristic of magnetofossils.

Several studies have examined magnetofossils in sediments of the Angola Basin, South Atlantic Ocean, collected during Deep Sea Drilling Project (DSDP) Leg 73 at Sites 519, 521, 522, and 523 (Chapter 2 and CHANG and KIRSCHVINK, 1984; PETERSEN et al., 1986; VALI and KIRSCHVINK, 1989). The sediments range in age from Eocene to Quaternary and in composition from nearly pure carbonate ooze to carbonate-poor clays. Magnetic properties indicate that some sediments have a significant amount of MD titanomagnetite, whereas others are dominated by SD magnetite (PETERSEN et al., 1986), often partially oxidized (KIRSCHVINK and CHANG, 1984). Magnetic mineralogy does not correlate with lithology (PETERSEN et al., 1986). TEM images indicate that SD magnetite occurs in cuboidal, prismatic, and bullet shapes and is arranged in small and long chains, clumps, and meshes (PETERSEN et al., 1986; VALI and KIRSCHVINK, 1989). Ferromagnetic resonance spectroscopy of Oligocene-Miocene sediments bearing SD magnetite reveals magnetic properties that are dominated by elongate magnetite particles or magnetite aligned in situ in chains (see Chapter 2). While most of these sediments carry stable remanent magnetizations

(TAUXE et al., 1984), some clay-rich Miocene sediments do not, an observation VALI and KIRSCHVINK (1989) linked to TEM observations of aggregation and partial dissolution of magnetofossils.

The first reported identifications of magnetofossils in consolidated sediments came from the Miocene (Tortonian-Messinian) Potamida clays of Crete, which were deposited in the Kastelli sub-basin at depths of ~600-900 m (MEULENKAMP, 1979; VAN HINSBERGEN and MEULENKAMP, 2006). Initial paleomagnetic work on the Potamida clays found that the intensity of remanent magnetization decreases in sediments deposited during magnetic reversals (VALET and LAJ, 1981). This led KIRSCHVINK (1982) to speculate that magnetofossils carry the magnetization in these sediments and that the decreased magnetization might result from conditions during a reversal that disfavor large populations of magnetotactic bacteria. CHANG and KIRSCHVINK (1985) examined magnetic extracts from the clay under TEM and found cuboidal and prismatic SD magnetite, which they interpreted as magnetofossils, as well as octahedral magnetite that they interpreted as byproducts of bacterial metabolism.

Miocene marls from Łąka, Poland, deposited under brackish conditions in the foredeep of the Western Carpathians, contain greigite particles with a Gaussian size distribution resembling that of crystals produced by multicellular magnetotactic prokaryotes, which led PÓSFAL et al. (2001) to speculate that these particles were produced by magnetotactic bacteria. Though inconclusive, this is the only report of possible greigite magnetofossils.

Continental shelf sediments. Continental shelf deposits have been less frequently investigated than carbonate platform or basinal deposits but are the source of the two most robust identifications of magnetofossils in lithified sediments.

KENT et al. (2003) examined cores through Atlantic Coastal Plain sediments of New Jersey that record the Paleocene-Eocene Thermal Maximum (PETM), the ~220 ky initial Eocene global warming event (ROHL et al., 2000). Sediments that precede and follow the PETM in the cores are glauconitic silts or silty clays and have hysteresis properties suggesting a dominant magnetic contribution from lithogenic input. In contrast, PETM sediments are kaolinite-rich clays, ~3-10 times more magnetic than underlying and overlying sediments,

and have hysteresis properties suggesting that their magnetic mineralogy is dominated by single-domain magnetite. The anomalous magnetic properties do not appear to be lithologically controlled, because they persist for the duration of the PETM despite kaolinite concentrations that range in the most proximal core between ~8% and ~50%. Kent et al.'s TEM examination of clay suspensions found only isolated, equidimensional particles of single-domain magnetite. They therefore concluded that magnetotactic bacteria had not produced the particles and instead proposed that the particles might have been produced as condensates from an impact ejecta plume.

We re-examined the PETM sediments with FMR to check Kent et al.'s observation that the magnetite occurred as isolated, equidimensional particles (see Chapter 5). Whereas FMR properties of silty clays deposited above and below the PETM clay indicate a predominantly detrital magnetic mineralogy, the properties of the PETM clay indicate elongate and/or chain magnetite of biogenic origin. Contrary to Kent et al.'s TEM imaging of clay suspensions, TEM imaging of magnetic extracts reveal the presence of abundant cuboidal, prismatic, and bullet-shaped SD magnetite particles, occasionally in chains. The finding undermines the evidence for an initial Eocene cometary impact but indicates that the Atlantic margin PETM sediments are a rich magnetofossil deposit. Based on the relationship between magnetofossil abundance and sediment oxygen levels discussed later in this article, we interpret the anomalously magnetofossil-rich clay as reflecting reduced oxygen solubility driven by increased temperatures during the PETM, possibly complemented by limited biological productivity along the mid-latitude western Atlantic margin. The result is also the first FMR-driven discovery of magnetofossils and confirms the utility of FMR as a technique for detecting magnetofossils in ancient sediments.

The oldest robust magnetofossils yet found come from Cretaceous (Coniacian-Campanian) chalk deposits of southern England (HOUNSLOW and MAHER, 1996; MAHER et al., 1999; MONTGOMERY et al., 1998). These sediments have been the subject of paleomagnetic, rock magnetic, SEM, and TEM studies. Rock magnetic properties indicate that sediment magnetization is dominated by SD magnetite, occasionally with some hematite. The most abundant magnetite particles are prismatic, but cuboidal and bullet shapes, as well as other elongate irregular morphologies, are also present. The crystals often occur in long chains,

which have been imaged both in magnetic extracts examined under TEM and in situ adhering to clay particles under SEM (Figure 1-7c, d).

Though not a robust magnetofossil identification, BUTLER et al. (1999) found that the magnetization in the microbial limestones and evaporites of the Miocene (Messinian) Calcare di Base, Sicily, was carried by cubic sub-micron magnetite crystals. They interpreted these particles as magnetosome crystals but did not provide detailed descriptions or images.

1.4.2 Putative Precambrian magnetofossils

All putative Precambrian magnetofossils come from carbonate platform sediments, mostly stromatolitic limestones and cherts. This bias is a product of sample selection and does not necessarily reflect the distribution of magnetofossils. The samples studied are all hand samples from outcrops, and the findings are reported with limited contextual information. No Precambrian magnetofossils meet our robustness criteria.

CHANG and KIRSCHVINK (1989) found that limestones from the Ediacaran Nama Group, Namibia, had coercivity spectra dominated by SD magnetite. TEM images of magnetic extracts show cuboidal magnetite that is sometimes arranged in short chains. As with all rocks bearing putative Precambrian magnetofossils, no paleomagnetic data was collected from the Nama Group samples, but MEERT et al. (1997) found that some parts of the Nama Group had been largely remagnetized in the Paleozoic.

CHANG et al. (1989) searched for magnetofossils in a number of silificied Proterozoic stromatolites. The magnetic properties of samples from the Neoproterozoic Bitter Springs Formation, Adelaide Basin, South Australia, indicate a mixture of SD and MD magnetite. TEM investigation shows that SD magnetite occurred in octahedral and cuboidal shapes; no chains were found. Samples from the Mesoproterozoic Vempalle Formation, Cuddapah Basin, India, contain predominantly SD magnetite, which occurred in elongate prismatic shape, but again no chains were found. Samples from the Paleoproterozoic Gunflint Formation, Canada, contain a mixture of SD and MD magnetite, which appears in somewhat corroded cuboidal shapes, sometimes in short chains.

AKAI et al. (1997) conducted no rock magnetic investigations but, based on TEM images alone, identified ~30-50 nm long, elongated, irregular magnetite particles in the acid-insoluble residue of recrystallized and partially silicified stromatolites from the late Archean Meentheena Member, Tumbiana Formation, Fortescue Group, Western Australia. They suggested that these particles were produced by magnetotactic bacteria, although they did not identify chains, examine crystal morphology closely, or report population statistics. Irregular elongated crystals might alternatively be produced by metamorphic alteration of siderite, as has been observed in drill core from lower greenschist grade late Archean siderite of the Ghaap Group, Transvaal Supergroup, South Africa (KIRSCHVINK et al., in prep.).

1.4.3 Putative extraterrestrial magnetofossils

The oldest and most controversial putative magnetofossils come from what is almost certainly the most intensively studied hand sample in the history of the geological sciences, the ~4.5 Ga Martian meteorite ALH84001 (BUSECK et al., 2001; FRIEDMANN et al., 2001; GOLDEN et al., 2004; MCKAY et al., 1996; THOMAS-KEPRTA et al., 2000; THOMAS-KEPRTA et al., 2001; THOMAS-KEPRTA et al., 2002; WEISS et al., 2004b, and many others). A full review of the debate over the biogenicity of magnetite particles in ALH84001 is beyond the scope of this article. Briefly, the magnetic minerals associated with carbonate globules in the basaltic meteorite include stoichiometric SP and SD magnetite, as well as pyrrhotite. There are several different morphological populations of magnetite crystals. ~27% of the magnetite crystals appear chemically pure and assume elongate prismatic shape, ~7% are whiskers with typical inorganic trace impurities, and the remainder take a variety of other shapes. The arguments about biogenicity focus on the prismatic crystals, which THOMAS-KEPRTA et al. (2000) compare to crystals from marine magnetotactic vibrio strain MV-1. GOLDEN et al. (2004) argue that the elongate prismatic crystals from ALH84001 are distinct from those produced by MV-1 and more closely resemble those produced by thermal decomposition of Fe-rich carbonate, a claim disputed by THOMAS-KEPRTA et al. (2004). FRIEDMANN et al. (2001) attempted to identify in situ magnetite chains using SEM with limited success, while WEISS et al. (2004b) used low-temperature magnetometry and FMR spectroscopy to constrain the abundance of any such chains to < ~10% of the volume of magnetite. In addition, KOPP and HUMAYUN (2003) have raised concerns that, even if

magnetofossils are present in association with the carbonate globules, they could have been deposited during the period the meteorite was exposed to surface conditions in Antarctica. However, magnetotactic bacteria have not yet been identified in endolithic or psychrophilic communities, either in Antarctica or on Mars.

1.5 Magnetofossil taphonomy

After a magnetotactic bacterium dies, the magnetic particles it produces can suffer three fates during early diagenesis that affect their utility as fossils: oxidation, chain breakup, and reductive dissolution (Figure 1). Partial oxidation to maghemite, driven by the oxidation and subsequent diffusive loss of Fe^{+2} from the crystal structure (XU et al., 1997), is the least destructive of these fates, as it does not affect the general morphology of the crystals. While it suppresses the Verwey transition (ÖZDEMİR et al., 1993), thereby rendering the Moskowitz chain test (MOSKOWITZ et al., 1993) ineffective, it does not greatly alter ferromagnetic resonance spectra (WEISS et al., 2004a). Although complete oxidation to hematite or goethite destroys magnetofossils, the process is thermodynamically disfavored or kinetically inhibited in many common depositional and early diagenetic settings.

The breakdown of the proteins and lipids that hold the magnetosome crystals within a cell can affect the arrangement of the particles in sediments and potentially destroy the characteristic chain structure. Chains of equidimensional particles, however, will tend to collapse into closed loops that leave the general head-to-tail ($\rightarrow\rightarrow$) dipole arrangement intact (see Chapter 2). Elongate particles are more susceptible to the loss of linearity and tend to collapse into side-by-side dipole arrangement (\rightleftharpoons) (see Chapter 3), but can still be recognized by their distinctive morphologies. At high concentrations, both equidimensional and elongate particles collapse into clumps.

Reductive dissolution is a common fate for fine magnetite particles (e.g., Chapter 4 and HILGENFELDT, 2000; HOUSEN and MOSKOWITZ, 2006; TARDUNO, 1994; VALI and KIRSCHVINK, 1989). Fe(III) is a lower potential electron acceptor than nitrate but a higher potential electron acceptor than sulfide, so once oxygen and nitrate are consumed, organisms turn to Fe(III) , including Fe(III) in magnetite (DONG et al., 2000; KOSTKA and

NEALSON, 1995), as an electron acceptor. If sufficient organic matter is available to fuel microbial metabolism, iron-reducing bacteria will dissolve fine magnetite particles, including magnetofossils. The long-term preservation of magnetofossils thus depends on the race between lithification, which should protect magnetofossils, and the metabolic activities of bacteria living in pore-waters. Although little work has been done investigating the mechanisms and rates of processes that protect magnetofossils from dissolution, increased supply of organic carbon does shift the balance toward the iron-reducing bacteria and against preservation.

Greigite is a metastable mineral and will transform into pyrrhotite or pyrite (BERNER, 1967; MORSE et al., 1987). Nonetheless, greigite can persist for geologically relevant periods of time in sulfide-limited environments. Greigite was first discovered in Miocene lacustrine sediments of the Tropico Group, Kramers-Four Corner area, California (SKINNER et al., 1964), while the oldest greigite described in a published report was formed during early diagenesis in late Cretaceous sediments of the North Slope Basin, Alaska (REYNOLDS et al., 1994). In a meeting abstract, NIITSUMA et al. (2004) described thermomagnetic evidence for greigite from the 2.77 Ga Archean Mt. Roe shale, recovered in an Archean Biosphere Drilling Project core from Western Australia, but NIITSUMA et al. (2005) found no unambiguous evidence of greigite under TEM.

1.6 Magnetofossils as an archive of environmental change

1.6.1 Glacial-interglacial variations in magnetofossil abundance

Coincident with the discovery of the first sedimentary magnetofossils, CHANG and KIRSCHVINK (1984) proposed that magnetofossils might serve as a paleoxygen indicator. At the time, all known magnetotactic bacteria were microaerophiles, so magnetosome magnetite was interpreted as a tracer of the presence of at least small quantities of oxygen. The discovery of the strictly anaerobic, sulfate-reducing, magnetite-producing strain RS-1 (SAKAGUCHI et al., 1993) provided a counter-example, but subsequent work has nonetheless demonstrated a linkage between magnetofossil abundance and paleoenvironmental conditions.

Several studies have found evidence for a climatic influence on magnetofossil populations. In sediment cores from ~4500 m depth in the Tasman Sea, spanning the last ~780 ky, HESSE (1994) found that the abundance of SD magnetite decreased during discrete events coincident with glacial stages. TEM images indicated the magnetite was of bacterial origin. The change in abundance was not controlled by dilution with carbonate but rather reflected a true change in magnetic mineralogy. During the reduced magnetization events, the ratio of equidimensional magnetofossils to elongate magnetofossils also decreased. Because elongate particles have larger surface area-to-volume ratios than equidimensional particles and therefore should be more subject to reductive dissolution, Hesse speculated that the morphological change reflected differences in growth rather than in preservation. A co-occurring reduction in degree of bioturbation and dulling of sediment color indicated that sediment porewaters were more reduced during glacial intervals. Hesse therefore inferred that porewater oxygen depletion, driven either by a drop in bottom water oxygen levels or an increase in organic carbon flux, disfavored magnetotactic bacterial growth and that the bacteria producing elongate crystals favored lower oxygen levels than did bacteria producing equidimensional particles.

Based on TEM imaging of deep-sea surface sediments and sediment trap measurements of organic carbon flux at eight sites in the Pacific Ocean, YAMAZAKI and KAWAHATA (1998) similarly found that the ratio of equidimensional to elongate magnetofossils was higher in areas with lower organic carbon flux. They observed a parallel relationship between organic carbon and magnetofossil morphology in a core through hemipelagic mud in the West Caroline Basin that extended to the Last Glacial Maximum. In the core, the proportion of magnetofossils with equidimensional shapes increased from ~10% to ~50% during the onset of the present interglacial stage, coincident with a decrease in weight percent organic carbon from ~1.4% to ~0.6%.

In a sediment core from 3556 m depth at Chatham Rise, southwest Pacific Ocean, extending from Oxygen Isotope Stage 6 to the present, LEAN and MCCAVE (1998) again identified a decrease in total magnetofossil abundance correlated with increased organic carbon levels during glacial intervals but, in contrast to HESSE (1994) and YAMAZAKI and KAWAHATA (1998), observed an increase in the proportion of equidimensional magnetofossils during

glacial stages. In a core from 488 m depth through hemipelagic sediments of the Sicily Strait, spanning the last ~1 My, DINARÈS-TURELL et al. (2003) likewise found that the total contribution of magnetofossils to sedimentary magnetism was higher in interglacial stages and lower in glacial stages.

Work on Quaternary sediments thus demonstrates an empirical linkage between redox conditions and magnetofossils, with limited evidence suggesting a greater degree of control by ecological factors than by taphonomic factors. Because most magnetite producers live in the upper OATZ, redox changes that expand the OATZ should lead to larger populations of magnetotactic bacteria. In sediments, the size and depth of the OATZ is controlled by a balance between the diffusive supply of oxygen from bottom waters and the consumption of oxygen for organic carbon oxidation (VAN DER LOEFF, 1990). Assuming the organic carbon supply remains sufficient to deplete oxygen, both increased oxygen supply and decreased organic carbon supply to sediments lead to expansion of the OATZ. The relationship between magnetofossil populations and organic carbon content of sediments observed by HESSE (1994) and LEAN and MCCAVE (1998) is consistent with this model. Taphonomic processes could produce a similar correlation, because although some magnetite producers live in the lower OATZ and under sulfidic conditions, such conditions promote the reductive dissolution of fine magnetite particles. Comparative microbiological, geochemical, and magnetic studies of marine sediments with different bottom water oxygen levels and organic carbon supplies would further elucidate and help quantify the magnetofossil paleoredox proxy.

1.6.2 Magnetofossils as a tracer of global oxygen levels

The linkage between paleoredox conditions and magnetofossil patterns keeps alive CHANG and KIRSCHVINK (1984)'s hope that a rich Precambrian magnetofossil record might serve as a tracer of global changes in oxygen level. CANFIELD (1998) proposed that global ocean redox chemistry went through three phases: an anoxic phase in the Archean and earliest Proterozoic, an euxinic phase in the middle Proterozoic, and an oxic phase in the late Proterozoic and the Phanerozoic. Magnetofossil populations and preservation would likely differ among the three regimes.

Studies on Quaternary sediments suggest that, in a predominantly oxic ocean, magnetofossil abundance is inversely correlated with organic carbon burial (HESSE, 1994; LEAN and MCCAVE, 1998; YAMAZAKI and KAWAHATA, 1998). Such studies have been confined to sediments with ≥ 0.4 wt% organic carbon; under conditions so organic poor that oxygen does not become depleted in the sediments, no significant magnetotactic bacteria population should grow. Greigite magnetofossils might be expected to be more abundant in higher productivity sediments but are in need of study.

Modern stratified water bodies like the Pettaquamscutt River Estuary, Rhode Island (BAZYLINSKI et al., 1995), Salt Pond, Massachusetts (SIMMONS et al., 2004), and Lake Ely, Pennsylvania (KIM et al., 2005), provide analog environments for a possible ancient euxinic ocean. Whereas in an oxic water body, the OATZ—and thus the highest density of magnetotactic bacteria—occur in the sediments, in a euxinic water body, the OATZ occurs in the water column. KIM et al. (2005) studied the magnetic properties of sediments from Lake Ely and found that magnetite magnetofossils play a dominant role, with concentrations higher in organic-rich sediments than in organic-poor sediments. However, a steady decline in saturation remanent magnetization from sediments deposited in ~ 1700 CE to sediments deposited in ~ 1300 CE suggests that most of the magnetite may dissolve during diagenesis. KIM et al. (2005) did not find signatures of greigite magnetofossils, but cautioned that sulfide levels in Lake Ely peak at ~ 60 μM . In settings like Salt Pond (SIMMONS et al., 2004), where microbiological studies have found greigite bacteria living in the water column, peak sulfide concentrations exceed 350 μM . It therefore remains unclear whether marine sediments from a euxinic environment would have magnetofossil populations significantly different from oxic environments, although poor preservation might be expected due to higher organic carbon concentrations and consequent diagenetic dissolution.

Understanding the ecology of magnetotactic bacteria in an anoxic ocean where sulfide concentrations are low and iron cycling drives the biosphere (WALKER, 1987) requires a better understanding of the evolution of magnetotaxis than currently exists. In such an ocean, the narrow, suboxic redox environment present in the OATZ today would fill most of the ocean. The navigational value of magnetotaxis for bacteria like the magnetite producers who dwell preferentially at the top of the OATZ would therefore be limited,

though the niche occupied by some greigite bacteria at the bottom of the OATZ would still be present where high-sulfur water masses came in contact with high-iron water masses.

Thus, one might expect that the ability to produce magnetite crystals evolved after the advent of oxygenic photosynthesis and that magnetite magnetofossils trace locally oxic environments. RS-1 appears to provide a counterargument; whether it is a valid counterargument depends upon whether RS-1 independently evolved the ability to produce magnetite after it evolved into a strictly anaerobic sulfate reducer. Alternatively, the ability could have evolved in an ancestor with a different metabolism or have been laterally acquired.

The magnetosome battery hypothesis suggests the possibility that the magnetosome arose first as an iron sulfide-based energy storage mechanism that was later exapted for magnetotaxis and still later adapted for the use of magnetite. Even more speculatively, the primitive, iron sulfide-based magnetosome could be a relict of a protobiotic iron-sulfur world (WACHTERSHAUSER, 1990). Testing these hypotheses requires the construction of a rich magnetofossil record for all of Earth history, as well as a fuller understanding of the diversity of magnetic microbes alive today and the genetic mechanisms underlying biological controlled magnetic mineralization.

1.7 Summary

The existence of magnetotactic bacteria is testimony to the power of evolution, as the intracellular magnetic particles they produce reflect the optimization processes of natural selection. Magnetofossils, the remains of these particles, are therefore distinguishable in sediments from magnetic particles produced by other means and leave a record that extends firmly into the Mesozoic and more ambiguously into the Precambrian.

Most magnetotactic bacteria favor particular redox conditions, and their preservation as fossils also depends upon redox parameters. Thus, the magnetofossil record can serve as a proxy of climate-driven changes in organic productivity and bottom water oxygen and might have utility deep in Earth history as a tracer of ancient oxygen levels. The pre-Quaternary magnetofossil record is, however, currently sparse. Fully utilizing the

magnetofossil proxy will require studies of the mechanisms and evolution of biomineralization in magnetotactic bacteria, investigations of the relationship between magnetotactic bacteria growth, magnetofossil population, oxygen supply, and biological productivity, and the development of a richer magnetofossil record.

Table 1-2. Magnetofossil reports from pre-Pleistocene localities with stratigraphic context

PQ	SD	S	C	ChP	CrP	Age	Locality	Setting	Lithology	Depth	Lithified	Sed. Rate (m/My)	Source
4	+	2	2½	nd	nd	Pliocene	North Pacific	pelagic basinal	clay	> 5000 m	N	0.4-2.7	(YAMAZAKI and IOKA, 1997)
5	+	3	2	nd	nd	Pliocene	San Salvador, Bahamas	carbonate platform	limestone and dolostone	supratidal to euphotic	Y	11-33	(MCNEILL et al., 1988)
5	+	3	0	nd	nd	Pliocene	Mururoa Atoll, French Polynesia	carbonate atoll	limestone and dolostone	euphotic	Y	12-66	(AISSAOUI et al., 1990)
5	+	3	0	nd	nd	Miocene	Potamida Clay, Crete	hemipelagic basinal	claystone	~600-900 m	Y	~40	(CHANG and KIRSCHVINK, 1985)
5	+	½	0	nd	nd	Miocene	Calcare di Base, Sicily	hemipelagic shelf	limestone and evaporite	supratidal to euphotic	Y	~30	(BUTLER et al., 1999)
4	+	4	0	nd	nd	Miocene	Central Equatorial Pacific	pelagic basinal	siliceous ooze and clay	5200-5600 m	N	2-6	(YAMAZAKI et al., 1991)
5/*	+	4	4	+	+	Eocene to Quaternary	Angola Basin, South Atlantic (DSDP Leg 73)	pelagic basinal	clay, marl, and calcareous ooze	3800-4600 m	N	2-9	(KIRSCHVINK and CHANG, 1984; PETERSEN et al., 1986; VALI and KIRSCHVINK, 1989)
nd	+	4	3	+	nd	Eocene (PETM)	Vincentown Fm., Atlantic Coastal Plain, New Jersey	hemipelagic shelf	claystone	euphotic	Y	~25-60	see Chapter 5
5	+	2	4	nd	nd	Cretaceous	Southern England	pelagic shelf	limestone (chalk)	sub-euphotic shelf	Y	30-40	(HOUNSLOW and MAHER, 1996; MONTGOMERY et al., 1998)
5	+	2	0	+	nd	Jurassic	Paris Basin, France	carbonate platform	limestone	euphotic	Y	~30	(BELKAALOUL and AISSAOUI, 1997)
5	+	2	2	nd	nd	Cambrian	Pestrotsvet Formation, Labaia Lena River, Siberia	carbonate platform	limestone	euphotic	Y	5-50	(CHANG et al., 1987)

Table 1-3. Magnetofossil reports from pre-Pleistocene localities with limited or no stratigraphic context

SD	S	C	ChP	CrP	Age	Locality	Setting	Lithology	Source
+	2	2	nd	nd	Jurassic	Northern Calcareous Alps, Austria	carbonate platform	limestone	(VALI et al., 1987)
+	1	2	nd	nd	Ediacaran	Nama Group, Namibia	carbonate platform	limestone	(CHANG and KIRSCHVINK, 1989)
+	2	2	nd	nd	Neoproterozoic	Bitter Springs Fm., South Australia	carbonate platform	stromatolitic chert	(CHANG et al., 1989)
+	2	0	nd	nd	Mesoproterozoic	Vempalle Fm., India	carbonate platform	stromatolitic chert	(CHANG et al., 1989)
+	1	2	nd	nd	Paleoproterozoic	Gunflint Fm., Canada	carbonate platform	stromatolitic chert	(CHANG et al., 1989)
nd	1	nd	nd	nd	Late Archean	Tumbiana Fm., Western Australia	carbonate platform	stromatolitic limestone	(AKAI et al., 1997)
+	2.5	1	+	+	Noachian? Holocene?	ALH84001	Mars? Antarctica?	carbonate globules in basalt	many authors (see text)

CHAINS, CLUMPS, AND STRINGS*

Magnetofossil taphonomy with ferromagnetic resonance spectroscopy

2.1 Introduction

Magnetotactic bacteria are a polyphyletic group of organisms that, uniquely among the bacteria, engage in biologically organized mineralization. They precipitate intracellular crystals of ferrimagnetic iron minerals, either magnetite (Fe_3O_4) or greigite (Fe_3S_4), within membrane-bound organelles called magnetosomes. Although magnetosomes likely have multiple functions (see Chapter 1 and SIMMONS et al., 2006), one major role is the passive alignment of bacterial cells with the geomagnetic field. Magnetotactic bacteria tend to live in regions with well-defined redox gradients. Everywhere except on Earth's geomagnetic equator, the geomagnetic field has a vertical component; by swimming along the field lines, the bacteria reduce a three-dimensional search for optimal chemical conditions to a one-dimensional search (BAZYLINSKI and MOSKOWITZ, 1997; CHANG and KIRSCHVINK, 1989; KIRSCHVINK, 1980a).

Because natural selection can lead magnetotactic lineages to maximize their magnetic sensitivity for the amount of iron used, magnetite crystals produced by magnetotactic bacteria have a number of distinctive traits that facilitate their identification as magnetofossils in sedimentary deposits (THOMAS-KEPRTA et al., 2000). Not all magnetotactic organisms produce magnetite with all of these traits, and abiotic processes can produce crystals with some of them, but the greater the number of traits present, the higher the degree of confidence with which one can identify magnetite as biogenic. The following traits have been identified so far. Magnetite from magnetotactic bacteria is generally chemically pure and lacking in crystallographic defects (but see the relatively rare

* Adapted from R. E. Kopp, B. P. Weiss, A. C. Maloof, H. Vali, C. Z. Nash, and J. L. Kirschvink (2006). Chains, clumps, and strings: magnetofossil taphonomy with ferromagnetic resonance spectroscopy. *Earth and Planetary Science Letters* 247: 10-25, doi:10.1016/j.epsl.2006.05.001.

anomalies described by TAYLOR et al., 2001). It almost always has a narrow size and shape distribution, is stably or meta-stably single-domain, and is arranged in chains of particles. The crystals also tend to have unusual crystal morphologies that increase the single-domain stability field (KIRSCHVINK, 2001; WITT et al., 2005): sometimes elongated along the magnetocrystalline easy axis, and often with truncated crystal edges.

Because magnetotactic bacteria prefer specific chemical environments, their fossils convey information about paleoclimate and paleoecology (EGLI, 2004a; YAMAZAKI and KAWAHATA, 1998). Magnetofossils also have a major advantage over other bacterial fossils: Because the fossils are magnetic, samples likely to contain magnetofossils can potentially be identified using physical techniques rather than time-consuming electron microscopy surveys. Nevertheless, the pre-Quaternary fossil record of magnetotactic bacteria is sparse. The oldest samples with chains of single-domain particles with distinctively biological morphologies are Cretaceous chalks from England (MONTGOMERY et al., 1998), although a few putative Precambrian magnetofossils have also been identified (CHANG and KIRSCHVINK, 1989; CHANG et al., 1989).

Previous attempts to search for magnetofossils in pre-Quaternary sediments with physical techniques have relied on the use of basic rock magnetic procedures designed to identify single-domain magnetite (e.g., CHANG et al., 1989). However, single-domain magnetite may be precipitated or concentrated by abiotic processes and is not unique to magnetofossils. Finding additional characteristic traits would greatly strengthen identifications. New techniques for unmixing coercivity spectra (EGLI, 2003; EGLI, 2004b) allow determination of the degree of variation within populations of magnetic particles, and thus allow detection of the narrow particle size and shape distributions characteristic of magnetotactic bacteria and magnetofossils. Acquiring high-resolution coercivity spectra is a time-intensive process, however. Although the process can be abbreviated for examining stratigraphic variation within a section where the end-member components have been identified (EGLI, 2004a), its time requirements may limit its utility in surveying the deep-time magnetofossil record.

The magnetofossil chain structure and magnetosome crystal elongation should exert distinctive influences on microscale magnetic anisotropy and should therefore be detectable using physical techniques. For instance, MOSKOWITZ et al. (1993) proposed that the relative magnitude of demagnetization upon warming across magnetite's Verwey transition under field-cooled and zero-field-cooled conditions is an indicator of chain structure. While their test did successfully distinguish fresh bacterial magnetite from other sources of magnetite, it is highly susceptible to crystal oxidation and thus to false negatives. In application to sediments, it also needs to be corrected for mixing of materials (EGLI, 2004b).

Isolated, equidimensional magnetite particles are dominated by negative cubic magnetocrystalline anisotropy, such that particle energy is highest when magnetization is aligned along the principal axes of the cubic crystal system and lowest when magnetization is aligned with the family of [111] crystal axes. Positive uniaxial shape anisotropy related to crystal elongation and particle organization in linear chains, in contrast, minimizes magnetostatic energy when the magnetization is aligned parallel to the crystal or chain elongation axis and maximizes magnetostatic energy when the magnetization is orthogonal to the crystal or chain elongation axis. Lowering the magnetostatic energy is equivalent to applying a field along the direction of magnetization, while increasing the energy of a state is equivalent to applying a field against the magnetization. Thus, a physical technique capable of assessing the effective field felt by a particle should be sensitive to chain structure and elongation. Ferromagnetic resonance spectroscopy (FMR) is such a technique (KITTEL, 1948; MORRISH, 1965; SCHLÖMANN, 1958; WEISS et al., 2004a).

FMR is a form of electron spin resonance, also known as electron paramagnetic resonance (EPR) (CALAS, 1988). FMR is based on the Zeeman effect, which causes the energy of an electron with spin aligned with a magnetic field to be lower than that of an electron with spin aligned against the field. The energy splitting is given by $\Delta E = g\beta B$, where g is the spectroscopic g-factor, β is the Bohr magneton ($9.37 \times 10^{-24} \text{ A}\cdot\text{m}^2$), and B is the field felt by the electron. The spectroscopic g-factor is 2.0023 for a free electron and 2.12 for an electron in magnetite (BICKFORD, 1950; CALAS, 1988). The electron can therefore absorb a photon with energy $h\nu = g\beta B$.

In a conventional EPR spectrometer, a sample is placed in a resonating cavity situated inside an electromagnet. A microwave radiation source with limited frequency adjustability (typically X-band, ~9.0-9.8 GHz) generates photons. A detector measures the first derivative of absorption as the electromagnet sweeps the magnetic field strength across a range of values (CALAS, 1988). For a single crystal, the resonant field is shifted to lower values when magnetization is aligned along a magnetically easy direction (e.g., along the [111] crystal axis of magnetite, or along the elongation axis of an elongate crystal or chain) and to higher values when the magnetization is aligned along a hard direction.

Most samples of geological interest are not single crystals, but are composed of particles in a variety of arrangements and orientations with respect to the applied magnetic field. The spectrum of a powder of magnetostatically non-interacting, spherical (isotropic) particles is simply a broadened form of the single crystal spectrum (Figure 2-1a), but for powders of anisotropic particles, the spectrum not only broadens but also develops asymmetry (Figure 2-1, b-e). Consider the case of a powder of elongate magnetite crystals, with elongation axes distributed uniformly in all directions (Figure 2-1c). From simple geometrical considerations, there will be a small number of particles with elongation axes closely aligned with the direction of the applied field, and many more with elongation axes aligned close to the plane perpendicular to the applied field. Those with elongation axes aligned with the applied field will absorb at lower fields than would isotropic particles, while those with elongation axes in the normal plane will absorb at higher fields. Thus, compared to the spectrum of a powder of isotropic particles, the peak absorption will be shifted to higher field values (i.e., lower effective g-factor) but will have a tail asymmetrically extended in the low-field direction. Conversely, a powder of particles with negative anisotropy will have increased effective g-factors and high-field extended asymmetry (Figure 2-1, b and d).

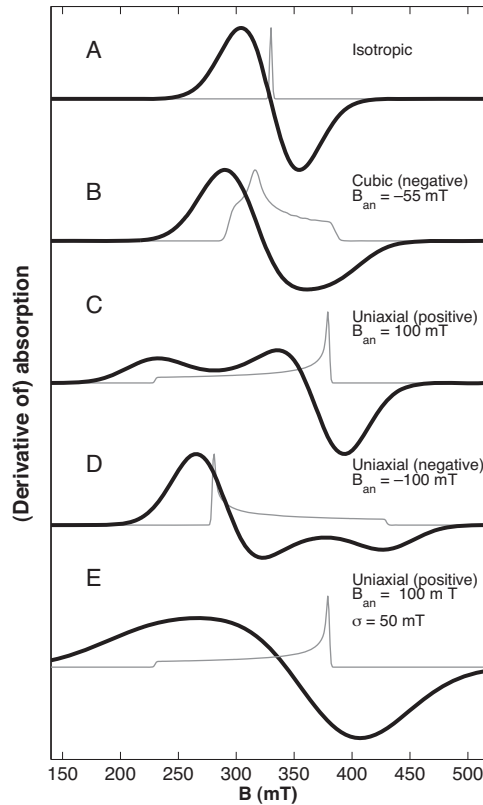


Figure 2-1: Synthetic FMR spectra. Generated with $g = 2.12$, and (a) no magnetic anisotropy, (b) cubic $B_{an} = -55$ mT, as expected for non-interacting cubic magnetite, (c) uniaxial $B_{an} = 100$ mT, (d) uniaxial $B_{an} = -100$ mT, and (e) uniaxial $B_{an} = 100$ mT. For (a-d), $\sigma = 25$ mT; for (e), $\sigma = 50$ mT. Thick lines show derivative spectra and thin lines show integrated absorption spectra with Gaussian broadening lowered to $\sigma = 3$ mT. Sharp spectra with positive uniaxial anisotropy, as in (c), have two local maxima on the low-field side, while sharp spectra with negative uniaxial anisotropy, as in (d), have two local minima on the high-field side; these features can be obscured by spectral broadening, as seen in comparison of (c) and (e).

As can be seen in Figure 2-1, c and d, the derivative spectrum of a powder of particles with uniaxial anisotropy has two peaks on the asymmetrically extended side. The one closer to the zero crossing is associated with the rise to the peak of absorption, while the one farther from the zero crossing is associated with the transition from zero absorption to positive absorption. Samples with more complex anisotropies may have additional peaks. These differences, however, can be obscured by factors that symmetrically broaden linewidth, such as magnetostatic interactions and sample heterogeneity (Figure 2-1e).

WEISS et al. (2004a) found that bacterial magnetite chains have FMR spectra distinct from abiotic magnetite. They postulated that the unique spectra of magnetosome chains result from the positive magnetic anisotropy of the chain structure (Figure 2-1c), which contrasts with the negative cubic magnetocrystalline anisotropy of room-temperature magnetite (Figure 2-1b). They demonstrated, through measurements of laboratory cultures, that intact magnetotactic bacteria have spectra with low-field extended asymmetry, as well as effective g -factors shifted below the standard magnetite value of 2.12 and two local maxima. WEISS et al. (2004a) also showed that lysed (broken) chains do not have the distinct FMR signature of intact chains, which suggests that the chain structure plays a major role in the FMR signature. However, because the crystals in the lysed chains in their experiments were clumped and highly magnetostatically interacting, Weiss et al. were unable to measure the FMR spectra of isolated magnetosomes and thus to demonstrate that the characteristic FMR spectra of magnetosome chains arises from the chain structure rather than from some trait of the individual crystals.

In this paper, we investigate the effects of chain structure and crystal elongation on FMR spectra and the extent to which these features can be mimicked by process other than the growth of chains of magnetite within magnetotactic bacteria. We examined intact and disrupted chains of magnetite from *Magnetospirillum magneticum* strain AMB-1, as well as dilutions of magnetite from lysed AMB-1 and of abiogenic magnetite strung out into linear features. We also examined sediments from a modern carbonate platform in the Bahamas, Oligocene-Miocene clays and calcareous oozes from the Atlantic Ocean, and lacustrine silts and muds from Mono Basin, California, in an attempt to determine whether these features corresponded to those observed in nature.

2.2 Samples

2.2.1 Bacterial cultures

For the lysis experiments, 2 L of *M. magneticum* strain AMB-1 (ATCC strain 700264) were grown to early stationary phase, at $\sim 10^8$ cells/mL, using standard culture conditions (KOMEILI et al., 2004) and then spun down into three subsamples, which were resuspended in 5 mL Tris buffer. Five μ L of β -mercaptoethanol were added to subsample A3. The

samples were frozen at -20°C and then thawed at 5°C . Then, 270 mg of sodium dodecyl sulfate (SDS) were added as a detergent to A3, which was incubated at room temperature for ten minutes. A2 and A3 were subjected to ultrasonication with a Fischer Scientific Sonic Dismembrator 550 for six minutes, with pulses of 0.5 seconds alternated with pauses of 0.5 seconds.

Next, the samples were spun down, frozen, and freeze-dried. Half of A3 was diluted to $\sim 0.1\%$ in powdered sucrose by grinding in an agate mortar and pestle, first for one minute (to form subsample A3b) and then for five minutes (to form subsample A3c). Halves of subsamples A1 and A2 were similarly diluted by grinding for five minutes to form subsamples A1b and A2b.

Based on rock magnetic data and transmission electron microscope images acquired in previous studies from the related magnetotactic bacterium *M. magnetotacticum* strain MS-1 (GORBY et al., 1988; KOBAYASHI et al., 2006), we expect that ultrasonicated AMB-1 contains chains of magnetite crystals liberated from cells but remaining bound by magnetosome membranes. The crystals are likely strung together in composite chains formed by linkage of individual chains from different cells, with some of the chains closed to form loops (see Figure 1 of KOBAYASHI et al., 2006). Closed loops represent the minimum energy configuration for four or more equidimensional magnetite crystals (PHILIPSE and MAAS, 2002).

SDS treatment, in contrast, destroys both cytoplasmic and magnetosome membranes. As a consequence, the crystals in SDS-treated samples collapse into agglomerates with strong three-dimensional magnetostatic interactions. We predict that, when progressively dispersed to lower density, the crystals minimize their energy by transitioning to increasingly linear “stringy” arrangements, with magnetic dipoles oriented in a head-to-tail fashion (PHILIPSE and MAAS, 2002).

2.2.2 *Synthetic magnetite dilutions*

TMB-100 is a synthetic magnetite powder produced by the Toda Industrial Company. The powder contains predominantly equidimensional, octahedral crystals of 80-200 nm

diameter. In concentrated form, the crystals form magnetostatically interacting masses with diameters of several microns (WEISS et al., 2004a).

Aliquots of TMB-100 were mixed in a tube with powdered sucrose. Each mixture was shaken to disperse the magnetite through the sucrose. Undispersed accumulations of magnetite were removed with a small NdFeB magnet. The final mass ratios of magnetite to sucrose were approximately 6%, 6000 ppm, and 400 ppm (for samples T1, T2, and T3 respectively). Subsamples of each mixture were powdered with an agate mortar and pestle for one minute and then for four minutes.

2.2.3 *Sedimentary samples*

Holocene-Recent peritidal carbonate mud samples were collected from a 210 cm core (C51: N 25°1.35' W 78°9.9' in the WGS84 datum) through a levee crest in the Triple Goose Creek region of Andros Island, the Bahamas. The core was extracted using a Livingstone piston corer provided to us by the Limnological Research Center, University of Minnesota. The core was separated into halves and sediment was collected in non-magnetic plastic boxes from interior sediment that had not been in contact with any metal objects. The upper 3 cm of the core is characterized by active microbial mats, containing the morphologically-identified filamentous cyanobacteria *Schizothrix* (HARDIE, 1977). The active microbial mat is underlain by 29 cm of tan, faintly-laminated mud, which is in turn underlain by 178 cm of grey, bioturbated carbonate mud, with variable concentrations of < 1 cm long cerithid gastropod shells.

Samples of Oligocene-Miocene deep-sea clay and calcareous nannofossil ooze from the southern Atlantic Ocean were taken from the Deep Sea Drilling Project site 522, cores 12-20 (44-80 mbsf) (HSÜ et al., 1984). The magnetic mineralogy of these samples, which is dominated by biogenic magnetic, was described by VALI and KIRSCHVINK (1989). Samples were provided by the Ocean Drilling Program (ODP), which is sponsored by the U. S. National Science Foundation (NSF) and participating countries under management of Joint Oceanographic Institutions (JOI), Inc.

Samples of the Pleistocene Wilson Creek Formation of Mono Basin, California (DENHAM and COX, 1971), were collected with permission of the Forest Service in May 2005 at the

formation's type section northwest of Mono Lake (N 38°1.3' W 119°7.5' in the WGS 84 datum). Aside from a few ash layers and sand lenses, the sediments of the Wilson Creek Formation are dominantly laminated (unbioturbated) muds and silts derived from the crystalline rocks of the Sierra Nevada to the west.

2.3 Methods

2.3.1 Rock magnetic measurements

Room temperature magnetic remanence experiments were performed using a 2G Enterprises SQUID magnetometer housed in a magnetically-shielded room. Anhyseritic remanent magnetization (ARM) was acquired in a 100 mT alternating field and a DC biasing field progressively varied in steps from 0 to 1 mT and was then removed by progressive alternating field demagnetization (AF) up to 160 mT. Isothermal remanent magnetization (IRM) at 100 mT was then acquired and removed by AF.

The ARM susceptibility of non-interacting single-domain particles is a function of temperature, particle moment, and particle switching field (EGLI and LOWRIE, 2002). Three-dimensional interparticle magnetostatic interactions significantly reduce ARM susceptibility (CISOWSKI, 1981), so comparison of the ARM susceptibility of similar particles in different arrangements reflects changes in particle arrangement. We report ARM susceptibility as $k_{ARM/IRM}$, the ARM acquired per A/m^2 with a biasing field of 0.1 mT (79.6 A/m) and an alternating field of 100 mT, normalized to the IRM acquired in a field of 100 mT. Typical freeze-dried magnetotactic bacteria (weakly interacting) have $k_{ARM/IRM} = 2.5$ mm/A, while a typical chiton tooth (strongly interacting) has $k_{ARM/IRM} = 0.09$ mm/A.

Low-temperature experiments were performed using a Quantum Design Magnetic Properties Measurement System in the Molecular Materials Resource Center of the Beckman Institute at Caltech. Field-cooled and zero-field-cooled curves were acquired by cooling the sample either in a 3 T field or in zero field to 5 K, respectively, followed by pulsing with a 3 T field and then measuring the remanence magnetization during warming to room temperature in zero field. The combination of field-cooled and zero-field-cooled measurements constitute the Moskowitz test (MOSKOWITZ et al., 1993; WEISS et al., 2004a). The sample was then cycled through low-temperature by pulsing it with a 3 T field at room

temperature and then measuring the remanent magnetization as the sample was cooled to 10 K and then warmed to room temperature.

The results of the low-temperature experiments are reported as the parameters δ_{ZFC} , δ_{FC} , and f_{LTC} . The parameters $\delta = (J_{80K} - J_{150K})/J_{80K}$ assessed for the zero-field-cooled and field-cooled curves respectively, where J_{80K} and J_{150K} are the moments measured at 80 K and 150 K, respectively. A ratio $\delta_{FC}/\delta_{ZFC} > 2.0$ passes the Moskowitz test and is considered to be an indicator of the presence of magnetosome chains, although partial oxidation and mixing can cause intact chains to fail the test (MOSKOWITZ et al., 1993; WEISS et al., 2004a). Magnetization retained through low-temperature cycling is expressed as the memory parameter $f_{LTC} = J_{LTC}/J_0$, where J_0 and J_{LTC} are respectively the room-temperature magnetization measured before and after cycling the samples to 10 K.

2.3.2 Ferromagnetic resonance spectroscopy

Ferromagnetic resonance spectra were acquired using an X-band Bruker ESP 300E EPR Spectrometer housed at Caltech. Except for particularly strong samples, microwave power was set at 640 μ W and spectra were integrated over three sweeps of the applied field from 0 to 600 mT. For the strongest samples, microwave power was set at 64 μ W and one sweep was performed. The spectra were measured at \sim 9.8 GHz. For 77 K measurements, samples were loaded in a quartz glass dewar filled with liquid nitrogen and spectra were measured at \sim 9.4 GHz.

FMR spectra are rich in detail; to extract all the information they convey, they must be examined individually. As a first order summary of spectral characteristics, we use three parameters (WEISS et al., 2004a): g_{eff} , A , and ΔB_{FWHM} (Figure 2-2). The effective g -factor, g_{eff} , is the g -factor associated with maximum absorption which is given by $g_{eff} = hv/\beta B_{eff}$, where B_{eff} is the field value of maximum absorption. The asymmetry ratio is defined as $A = \Delta B_{high}/\Delta B_{low}$, where $\Delta B_{high} = B_{high} - B_{eff}$, $\Delta B_{low} = B_{eff} - B_{low}$, and B_{high} and B_{low} are the fields of half maximum absorption at low-field and high-field sides of the absorption peak, respectively. The full width at half maximum, ΔB_{FWHM} , is defined as $\Delta B_{FWHM} = B_{high} + B_{low}$. Although all these parameters are derived from the integrated absorption spectrum, FMR spectra are generally displayed as derivative spectra, which reveal much greater detail upon

inspection. The empirical parameter α , generated by linear discriminant analysis (KEEPING, 1995) to maximize the difference between magnetosome chains and detrital magnetite in A vs. ΔB_{FWHM} space and discussed at length later, is defined as $\alpha = 0.17 A + 9.8 \times 10^{-4} \Delta B_{FWHM}/\text{mT}$.

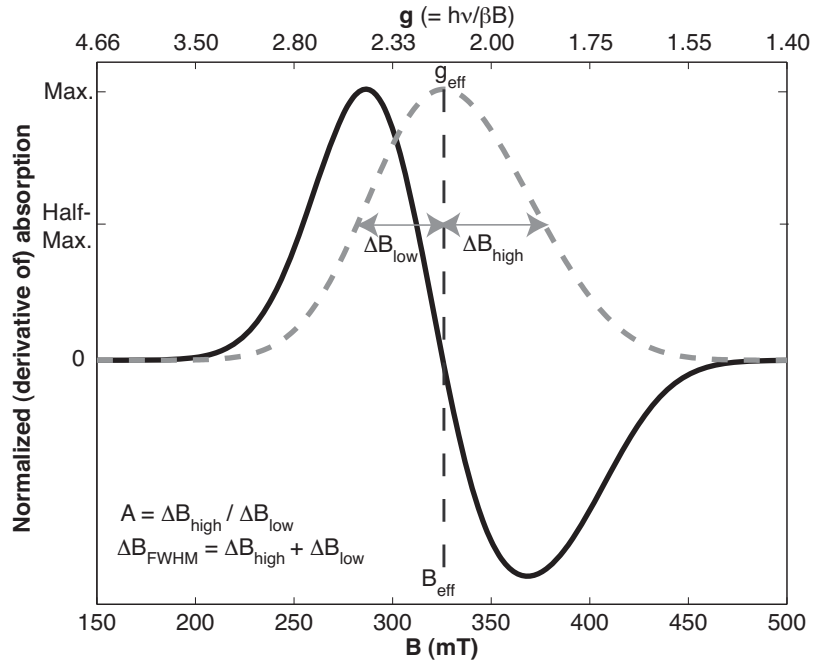


Figure 2-2: Definitions of basic FMR parameters. Illustrated on a synthetic FMR spectrum of non-interacting, equidimensional magnetite ($g = 2.12$, $\sigma = 30$ mT, cubic $B_{an} = -55$ mT, $K_2/K_1 = 0.21$). The solid curve shows the derivative spectrum and the dashed curve shows the integrated spectrum.

2.3.3 Simulation of ferromagnetic resonance spectra

We used MATLAB code, written following GRISCOM (1974; 1981), to simulate FMR spectra and thereby allow us to understand the relationship between the empirical parameters and physical parameters. We assume that the simulated material is a powder of dilute single-domain particles, small with respect to the microwave skin depth (~ 5 μm in magnetite (GRISCOM, 1974)), with the particles uniformly distributed in all orientations, and that, at resonance, the orientation of the moment vector approximates the field orientation. Magnetostatic interactions were neglected except as a source of anisotropy, and all anisotropy, whether arising from magnetocrystalline anisotropy, shape anisotropy, or particle arrangement, was treated through a single pair of anisotropy constants, K_1 and K_2 .

The orientation of an individual particle is defined by the angles θ and ϕ , where θ is the angle between the applied DC field and the axis of the particle and ϕ is the angle of the axis out of the plane defined by the microwave field and the applied DC field. For a particle with uniaxial anisotropy, the first-order resonance condition (derived from the anisotropy energy $E = K_1 \sin^2 \theta + K_2 \sin^4 \theta$ following the approaches of SCHLÖMANN, 1958 and GRISCOM, 1981) is given by

$$B_{res,uni}(\theta) = B_{true} - \frac{1}{2} B_{an} \times \left[3 \cos^2 \theta - 1 + (K_2/K_1)(8 \cos^2 \theta \sin^2 \theta - 2 \sin^4 \theta) \right],$$

where $B_{true} = hv/\beta g_{true}$ is the resonance field in the absence of anisotropy, B_{an} is the anisotropy field $2K_1/M_s$, K_1 and K_2 are the first-order and second-order uniaxial anisotropy constants, and M_s is the saturation magnetization. For cubic anisotropy, the resonance condition of GRISCOM (1981) was used.

To compute the powder absorption at applied field B_{app} , a Gaussian broadening function of linewidth σ is applied and spectra are numerically integrated over all solid angles:

$$A(B_{app}) = \int_{\theta=0}^{\pi/2} \int_{\phi=0}^{2\pi} \frac{\exp\left(-\left(B_{app} - B_{res}(\theta, \phi)\right)^2 / 2\sigma^2\right)}{\sqrt{2\pi}\sigma} d\phi \sin\theta d\theta.$$

Several physical effects are subsumed in the Gaussian broadening; in natural samples, a major cause of broadening is heterogeneity in particle size, shape, and arrangement (DRAIN, 1962).

While not capable of fitting our observed spectra perfectly, nonlinear least square fitting using these model spectra provides reasonably good approximations. For almost all our samples, second-order uniaxial fits were better than second-order cubic fits, and they never were significantly worse. We would expect this to be the case for samples in which magnetostatic interactions or shape anisotropy dominated the internal magnetic environment.

2.3.4 Transmission electron microscopy (TEM)

We prepared replicas, composed of a 1-2 nm thick metal thin film of 95% platinum and 5% carbon and a supporting carbon film 15-20 nm thick, of the synthetic magnetite dilutions to allow us to remove the sucrose dilutant while preserving the relationship between the dilutant and the magnetite. Ten μL of ~ 20 mg of powder dispersed in 99% pure methanol were transferred onto a freshly cleaved mica thin plate. As the powder settled, the fluid was removed by blotting with filter paper. The replica was prepared in a freeze-fracture unit (Baltec 60, Lichtenstein) at room temperature under high vacuum (10^{-6} torr), as described in (ZEILE, 2000), by depositing a fine granular Pt-C film from an evaporating source at an incident angle of 30° and a distance of 15 cm to the mica plate. Variable densities of Pt-C accumulate along the topographic slopes of the specimen that are facing, oblique to, or shielded from the source, emphasizing the topographic contrast for TEM imaging. To strengthen the ultra-thin Pt films and preserve their integrity during cleaning steps, a supporting carbon film was immediately condensed on the Pt film by a vertical electron beam gun sputtering a carbon rod perpendicular to and 12 cm away from the surface of the specimen. The replicas were cleaned with distilled water to remove the sucrose and transferred onto 200 mesh formvar-coated Cu grids.

Imaging was carried out in bright-field illumination with a JEOL JEM-2000FX transmission electron microscope, at an accelerating voltage of 80 kV and magnifications from 5000x-50,000x, and a Gatan 792 Bioscan 1k x 1k Wide Angle Multiscan CCD camera.

2.4 Results

2.4.1 Lysis of magnetotactic bacteria

When comparing different arrangements of similar particles, ARM susceptibility quantifies magnetostatic interactions. Three-dimensional magnetostatic interactions shield particles from the DC biasing field, which causes materials with greater interactions to exhibit lower ARM susceptibility. (This is not the case for materials with one-dimensional magnetostatic interactions, as in magnetosome chains.) As expected from these considerations, the ARM susceptibilities of the samples are ordered: intact AMB-1 (samples A1a and A1b) >

ultrasonically disrupted AMB-1 (samples A2a and samples A2b) > dispersed, SDS-treated AMB-1 (sample A3c) > concentrated, SDS-treated AMB-1 (samples A3b and A3a) (Figure 2-3a and Table 2-1).

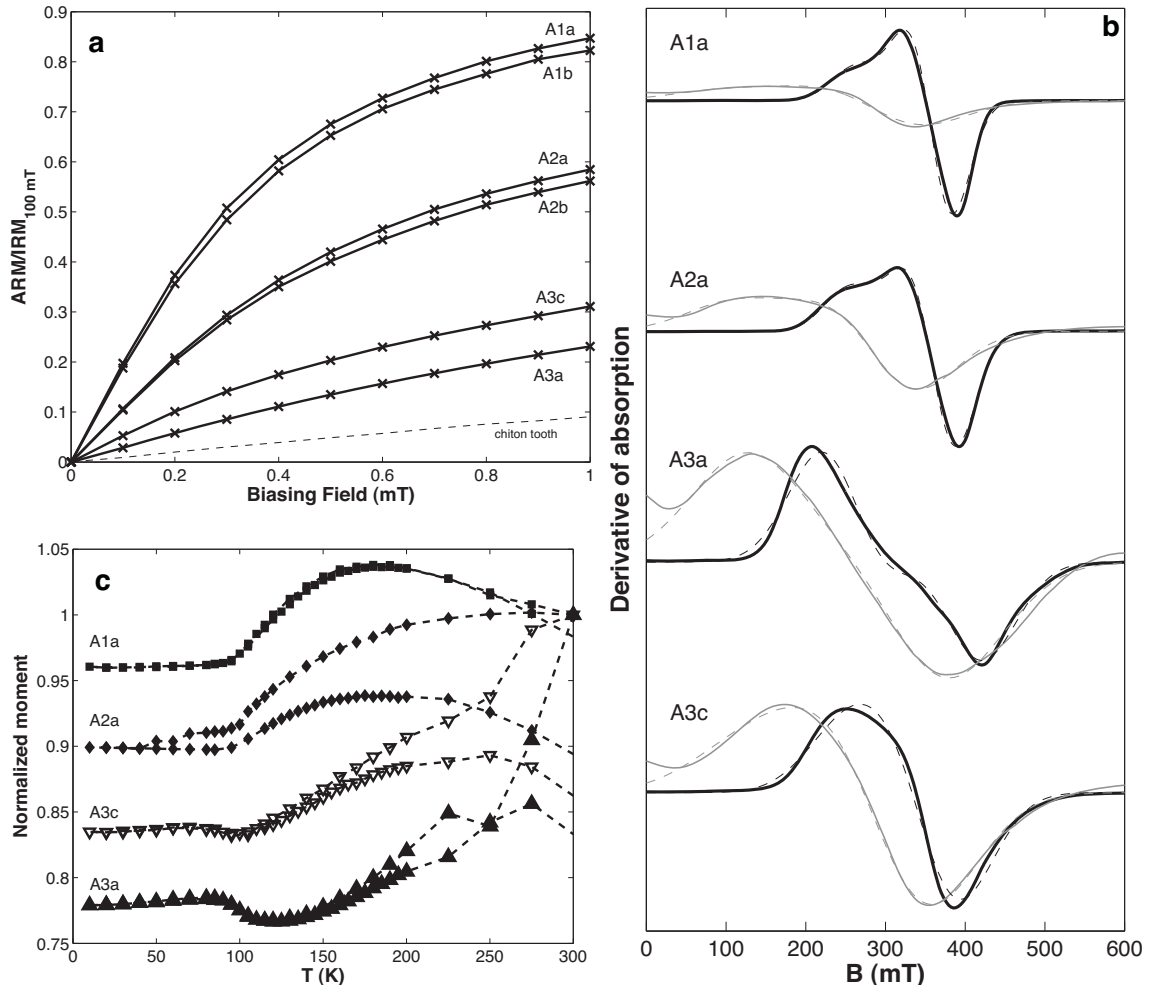


Figure 2-3: Measurements of intact and altered AMB-1. (a) ARM acquisition curves, (b) ferromagnetic resonance spectra, and (c) low-temperature cycling curves of cultures of AMB-1. In (a), the lower dashed line is a chiton tooth standard for highly interacting magnetite. In (b), thick lines represent room-temperature measurements, thin lines represent 77 K measurements (where performed), and dashed lines indicate spectral fits.

Ferromagnetic resonance spectra of the disrupted AMB-1 samples reflect a shift from linear chains to highly interacting clumps (Figure 2-3b, Table 2-1). The ultrasonically disrupted AMB-1 (sample A2a) exhibits little change in spectrum shape or in the spectral parameters compared to intact AMB-1 (sample A1a). This suggests that, although the magnetostatic

interactions as revealed by the ARM curves have increased relative to the intact cells, the local magnetic environment felt by each individual crystal remains dominated by head-to-tail axial interactions; the chains are still intact, although they are no longer separated from one another by cell material (see Figure 1 of KOBAYASHI et al., 2006). In contrast, the spectrum of the SDS-treated cells exhibits a high-field extended asymmetry and high g_{eff} (sample A3a), consistent with the observations of WEISS et al. (2004a).

Table 2-1. Summary of FMR and magnetic parameters of bacterial samples

Sample		FMR Spectrum				FMR Uniaxial Fit				Magnetic properties				
ID	Treatment	g_{eff}	A	ΔB (mT)	α	g_{fit}	B_{an} (mT)	K_2/K_1	σ (mT)	$k_{ARM}/$ IRM (mm/A)	δ_{ZFC}	δ_{FC}	f_{LTC}	δ_{ZFC}
A1a	intact	2.01	0.79	96	0.23	2.08	81	-0.13	27	2.48	0.14	2.44	0.98	
A1b	intact, pwd.	2.01	0.83	93	0.23	2.08	86	-0.20	29	2.36				
A2a	ultra.	2.01	0.73	112	0.23	2.10	84	-0.06	30	1.34	0.16	1.94	0.89	
A2b	ultra., pwd.	2.02	0.78	103	0.23	2.09	85	-0.14	31	1.31				
A3a	SDS, conc.	2.25	1.13	208	0.40	2.20	-81	0.43	48	0.36	0.37	1.21	0.83	
A3b	SDS, pwd. 1m	2.14	0.89	188	0.34	2.17	-60	0.65	48	0.36				
A3c	SDS, pwd. 5m	2.07	0.76	148	0.27	2.14	79	0.01	50	0.66	0.26	1.39	0.86	

The diluted SDS-treated cells (sample A3c) exhibit a spectrum that more closely resembles that of the intact and ultrasonicated samples, although the spectrum of A3c is a bit wider. One key trait of this spectrum that is not readily apparent from the parameterization is its degree of sharpness. The derivative spectra of intact and ultrasonicated AMB-1 (A1a and A2a) have two local maxima, which indicate a low degree of peak broadening caused by heterogeneous particle arrangements. Each particle experiences roughly the same magnetic anisotropy produced by particle interactions within the chain, because the magnetite chains are produced under biological control. In contrast, the dispersed, SDS-treated AMB-1 (A3c) has only one local maximum, likely because the particles are arranged in one-dimensional strings that form through physical processes and therefore have more heterogeneous magnetic anisotropy. The same effect is seen in comparing Figure 2-1c and Figure 2-1e.

All the AMB-1 spectra are fairly well fit by second-order uniaxial model spectra. The intact, ultrasonicated, and dispersed SDS-treated samples have B_{an} values around 80 mT. Following the method of Butler and Banerjee (BUTLER and BANERJEE, 1975; DIAZ-RICCI

and KIRSCHVINK, 1992), this value is equivalent to the shape anisotropy of an elongate magnetite crystal with a 2.2:1 length-to-width ratio. Since the crystals produced by AMB-1 are equidimensional, the apparent shape anisotropy must be due to linear magnetostatic interactions. The -81 mT B_{an} value of the concentrated SDS-treated sample is equivalent to a single crystal with a 1:1.1 length-to-width ratio, and may be due to planar magnetostatic interactions, as on the surface of a clump. All SDS-treated samples have larger σ values than intact and ultrasonicated samples, which likely reflect greater heterogeneity of particle arrangement.

Table 2-2. Summary of 77 K FMR parameters of bacterial and synthetic magnetite samples

ID	FMR Spectrum				FMR Uniaxial Fit			
	g_{eff}	A	ΔB (mT)	α	g_{fit}	B_{an} (mT)	K_2/K_1	σ (mT)
A1a	2.47	0.64	215	0.32	2.76	149	-0.04	64
A1b	2.46	0.64	201	0.31	2.75	144	-0.04	57
A2a	2.53	0.69	211	0.32	2.79	134	0.02	59
A2b	2.48	0.68	206	0.32	2.73	138	-0.02	59
A3a	2.59	0.97	266	0.43	2.63	97	0.46	75
A3c	2.45	0.83	214	0.35	2.59	134	-0.08	71
T1c	2.16	0.77	297	0.42	2.33	144	0.22	71
T2b	2.26	0.80	299	0.43	2.42	139	0.25	72
T3c	2.20	0.71	228	0.34	2.40	147	0.01	63

The FMR spectra measured at 77 K are consistent with these findings (Figure 2-3b, Table 2-2). Below the Verwey transition, which, as measured in the FC and ZFC curves (not shown; see also Weiss, 2004 #124), occurs at ~100 K in magnetite from AMB-1, magnetite shifts from a cubic crystal system to a monoclinic crystal system and experiences a large increase in magnetocrystalline anisotropy, with the anisotropy constants becoming positive (ABE et al., 1976; MUXWORTHY and MCCLELLAN, 2000). Thus, the spectra broaden considerably, g_{eff} shifts to higher values, and A becomes lower, reflecting the positive anisotropy. The last effect is strongest in sample A3a, which shifts from high-field asymmetry to mild low-field asymmetry, presumably as the anisotropy field comes to dominate magnetostatic interactions. A3a continues, however, to have higher g_{eff} , A , and ΔB_{FWHM} than the other samples.

Low-temperature data (Figure 2-3c; Table 2-3) exhibit increasing loss of remanence upon warming or cooling through the Verwey transition with increasing magnetostatic interactions (decreasing ARM susceptibility), consistent with KING and WILLIAMS (2000). In addition, the δ_{FC}/δ_{ZFC} ratio decreases with chain breakdown and only the intact AMB-1 cells pass a Moskowitz test with $\delta_{FC}/\delta_{ZFC} > 2$. Increased chain breakdown also increases the fraction of remanence loss on cooling and re-warming through the Verwey transition. Curiously, the SDS-treated cells, both concentrated and dispersed, experience a slight increase in remanence when they are cooled through the Verwey transition, while the samples with intact chains lose remanence across the Verwey transition.

Table 2-3. Summary of FMR and magnetic parameters of synthetic magnetite samples

Sample		FMR Spectrum				FMR Uniaxial Fit				
ID	Conc. (ppm) / Pwd Time (min)	g_{eff}	A	ΔB (mT)	α	g_{fit}	B_{an} (mT)	K_2/K_1	σ (mT)	$k_{\text{ARM}}/\text{IRM}$ (mm/A)
T1a	60,000 / 0	2.37	1.12	339	0.52262	2.31	114	0.59	78	0.11
T1b	60,000 / 1	2.21	0.96	282	0.43956	2.26	117	0.34	74	0.15
T1c	60,000 / 4	2.11	0.87	267	0.40956	2.19	123	0.25	69	0.40
T2a	6,000 / 0	2.17	0.91	274	0.42322	2.24	126	0.24	73	0.18
T2b	6,000 / 1	2.16	0.92	259	0.41022	2.23	123	0.20	73	0.24
T2c	6,000 / 4	2.10	0.85	228	0.36794	2.19	121	0.09	69	0.64
T3a	400 / 0	2.09	0.83	230	0.36650	2.19	131	0.06	67	0.59
T3b	400 / 1	2.09	0.83	222	0.35866	2.19	132	0.03	67	0.74
T3c	400 / 4	2.07	0.83	201	0.33808	2.17	131	-0.06	64	1.23

2.4.2 Dilutions of abiogenic magnetite

To test our hypothesis that the low-field extended asymmetry of the dispersed, lysed AMB-1 is a product of physical string formation, we performed analogous experiments using synthetic magnetite. As expected, dilution of the powder decreases three-dimensional magnetostatic interactions, which is reflected in increased ARM susceptibility (Figure 2-4a and Table 2-3). This pattern is consistent when comparing different ratios of magnetite to sucrose and when comparing shaken mixtures to mixtures ground with a mortar and pestle

for four minutes. The ARM susceptibility of the samples is ordered: 400 ppm ground mixture (sample T3c) > 0.6% ground mixture (sample T2c) > 400 ppm shaken mixture (sample T3a) > 6% ground mixture (sample T1c) > 0.6% shaken mixture (sample T2a) > 6% shaken mixture (sample T1a), although the ARM/IRM ratios of T1c cross above those of T3a and T2c at higher biasing fields.

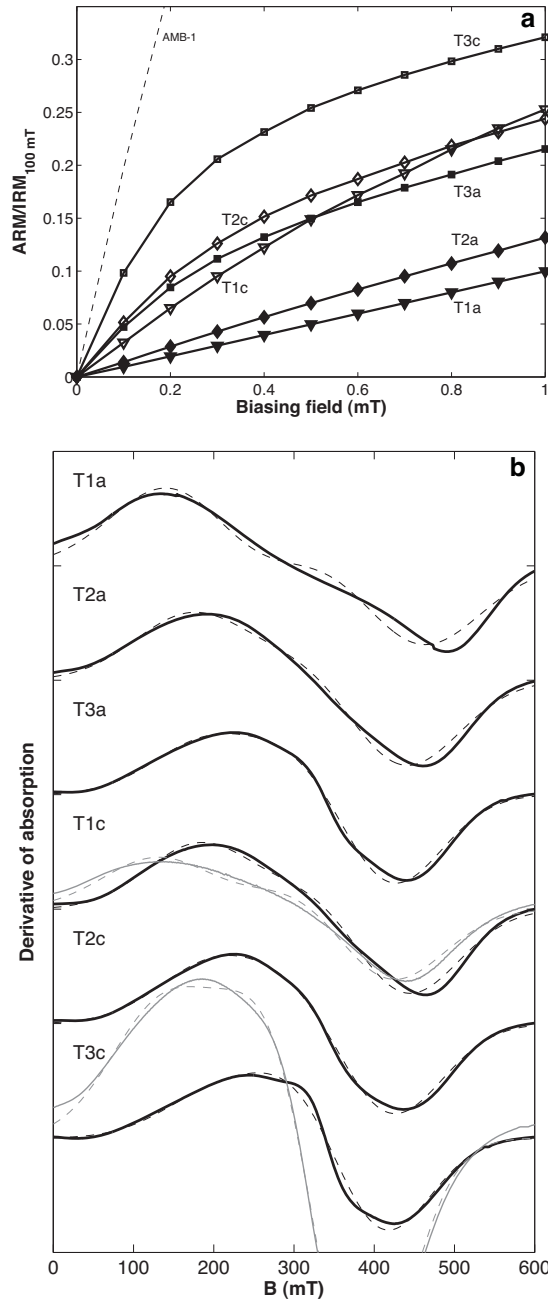


Figure 2-4: Measurements of synthetic magnetite. (a) ARM acquisition curves and (b) ferromagnetic resonance spectra of dilutions of synthetic magnetite powder TMB-100. In (a), the upper dashed line is intact AMB-1. The chiton tooth standard shown in Figure 2-3a closely follows the line for sample T1a. In (b), thick lines represent room-temperature measurements, thin lines represent 77 K measurements, and dashed lines indicate spectral fits.

The FMR spectra of these samples reveal the same trend, with g_{eff} and ΔB_{FWHM} decreasing in the same order that ARM susceptibilities decrease (Figure 2-4b, Figure 2-5 and Table 2-3). The 6% shaken mixture is markedly different from the other mixtures. It alone exhibits high-field extended asymmetry, rather than low-field extended asymmetry. The other mixtures exhibit low-field extended asymmetry, which we suggest is due to the formation of strings of particles. If the shift to low-field extended asymmetry were due to changes in crystal shape upon powdering, it would not be present in samples diluted only by shaking. The fitted B_{an} of the particles is equivalent to that of single magnetite crystals with length-to-width ratios of $\sim 3:1$, even though TEM images show largely equidimensional crystals. TEM images of sample T2c (Figure 2-6) indicate that, as predicted, many of the crystals are arranged in strings. While the strings are much more irregular than biogenic chains, they produce the appropriate magnetic anisotropy to generate FMR spectra with low-field extended asymmetry. Their heterogeneity, however, leads to a broader spectrum than those produced by bacterial magnetite chains; the strings of magnetite have only a single low-field derivative peak, in contrast to the double peak of the bacterial chains.

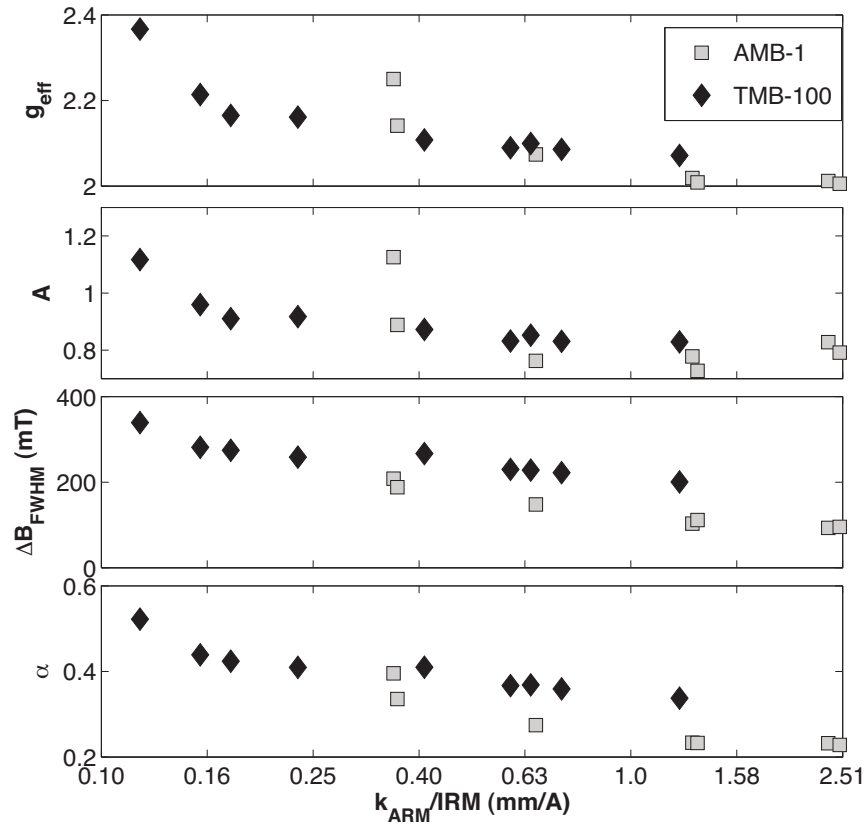


Figure 2-5: Semi-log plots of the FMR parameters of the synthetic magnetite and AMB-1 samples against k_{ARM}/IRM

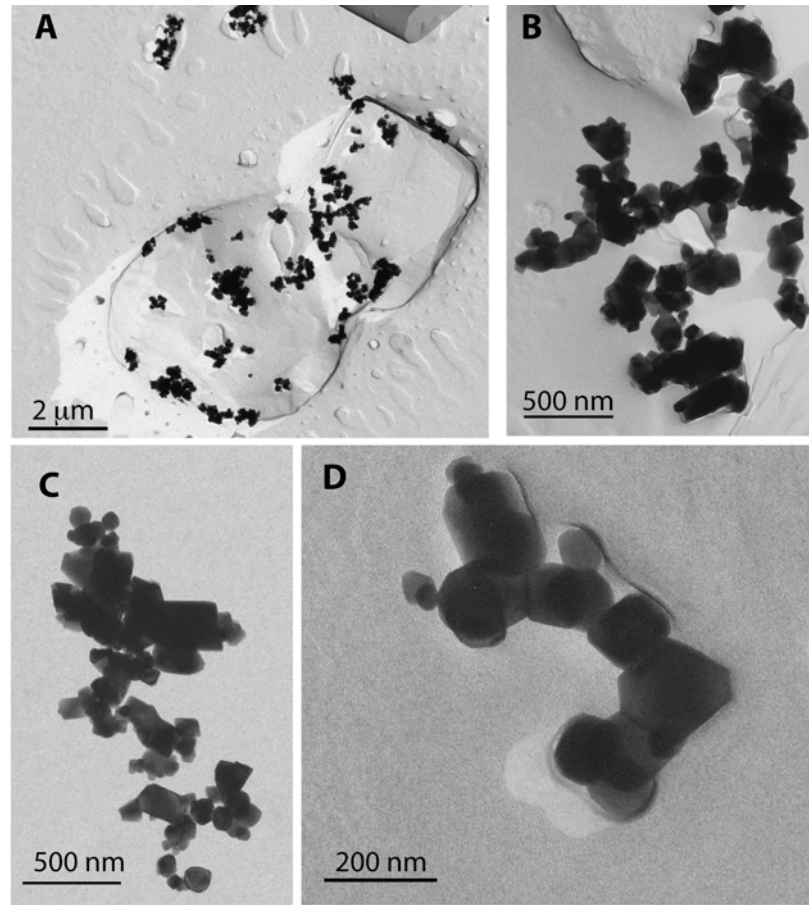


Figure 2-6: Transmission electron micrographs of Pt-C replica of synthetic magnetite powder TMB-100 diluted at 6,000 ppm in sucrose. The bright material is the Pt-C replica of the sucrose dilutant, while the dark crystals are magnetite. (a) shows the association between clumps and strings of magnetite particles and the surface of sucrose crystals. (b), (c), and (d) show higher-resolution images of the clumps and strings.

2.4.3 Sedimentary samples

The sedimentary samples studied come from three sources: the Bahamas, the southern Atlantic Ocean, and Mono Basin, CA. The range of FMR parameters from these samples are shown in Figure 2-7 and in Table 2-4. Although no samples from Andros Island have been previously studied using FMR, magnetic measurements and electron microscopy on a small number of samples from elsewhere in the Great Bahama Bank suggest that magnetotactic bacteria are common at the sediment/water interface (MCNEILL, 1990), and data from Pliocene-Pleistocene sediments on San Salvador Island and from the Clino core drilled through the Great Bahama Bank indicate that biogenic magnetite can be preserved in

sediments that have undergone diagenesis (MCNEILL et al., 1988; MCNEILL and KIRSCHVINK, 1993; WEISS et al., 2004a).

The spectra of the Bahamian samples all exhibit multiple derivative maxima and low-field extended asymmetry, with A between 0.71 and 0.86, g_{eff} between 2.01 and 2.11, and ΔB_{FWHM} between 109 and 192 mT (Figure 2-8a). Based on the criteria of WEISS et al. (2004a), these traits are all consistent with the presence of intact magnetosome chains (Figure 2-3). Although many of these parameters also characterize the strings of crystals from lysed cells described above (Figure 2-4), the secondary absorption peaks of these Bahamian samples resemble those observed for intact magnetosome chains. In addition, all samples have strong paramagnetic resonances from Fe^{+3} ($g = 4.3$) and Mn^{+2} ($g = 2.0$). The latter obscure the magnetite signal in the derivative curve, but due to the sharp peaks of the Mn^{+2} sextet, the Mn^{+2} signal is readily removed by curve smoothing (Figure 2-8a).

A close examination of core C51 reveals changes with depth suggestive of the progressive alteration of magnetosome chains. The first local maximum of the derivative spectrum in the 6 cm and 14 cm samples is well defined. In the 22 and 31 cm samples, it is present but diminished in strength relative to the second local maximum. In the 42 and 52 cm samples, the first local maximum is not present, and ARM susceptibility is markedly diminished compared to shallower samples (Figure 2-8, b and c). These changes suggest the progressive degradation of magnetosome chains with depth, although they could alternatively represent the mixing of two discrete magnetic materials in the upper sediments, and the loss of one of these with depth.

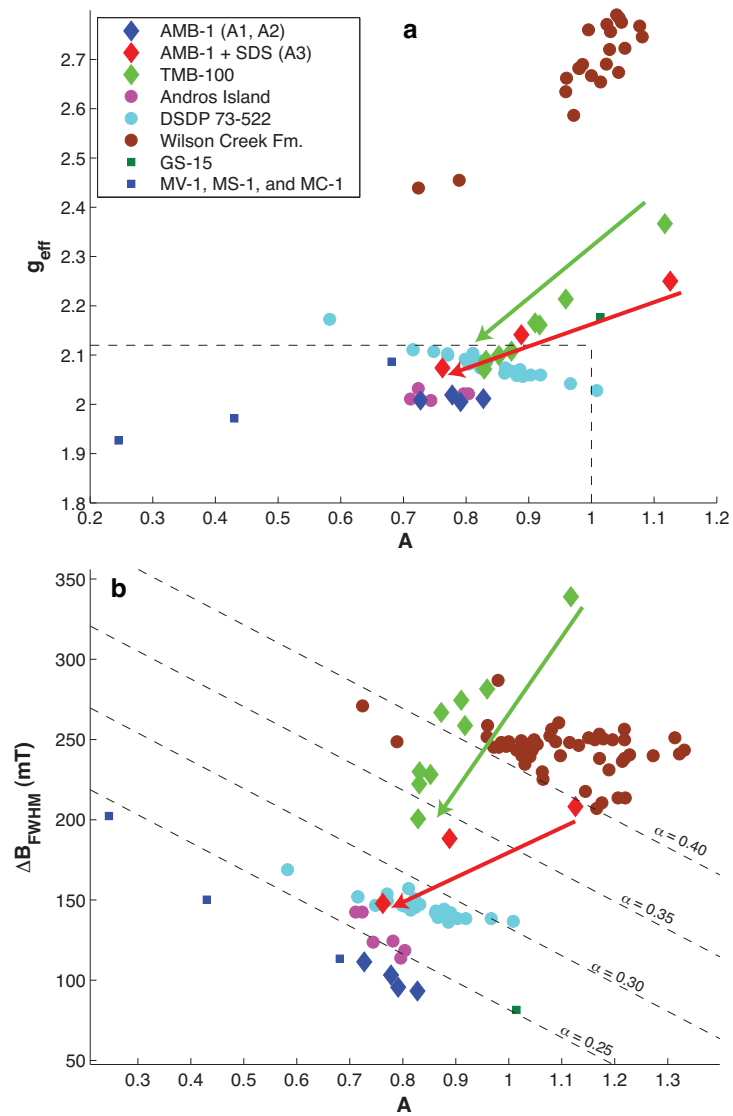


Figure 2-7: Summary of FMR parameters. Plots of (a) effective g -factor vs. asymmetry ratio A , in the manner of WEISS et al. (2004a), and (b) full width at half maximum (ΔB_{FWHM}) vs. A . In (a), the dashed lines demarcate the area defined by WEISS et al. (2004a) as being the domain of magnetosome chains, with $A < 1$ and $g_{\text{eff}} < 2.12$. In (b), the dashed lines are contours of constant α values, where α is defined in the text. Red and green arrows highlight the dilution trends for, respectively, SDS-treated AMB-1 and TMB-100. Parameters for *Geobacter metallireducens* GS-15, which precipitates extracellular superparamagnetic magnetite, and for the magnetotactic bacteria strains MV-1, MS-1, and MC-1 (arranged in order of increasing A) are derived from the data of WEISS et al. (2004a).

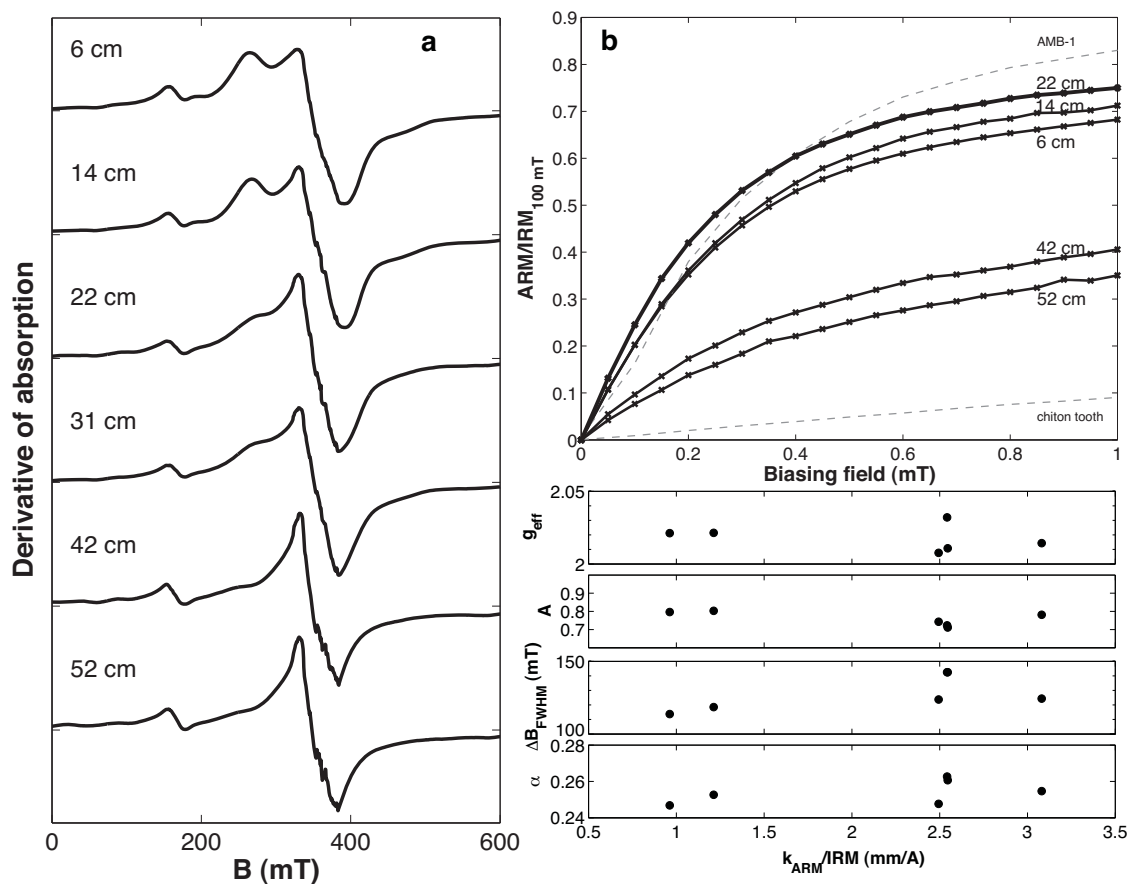


Figure 2-8. Measurements through Andros Island core C51. (a) Smoothed ferromagnetic resonance spectra, (b) ARM acquisition curves, and (c) plots of FMR parameters against k_{ARM}/IRM . In (a), the small peak at ~ 160 mT is the paramagnetic resonance of Fe^{+3} and the jaggedness at ~ 330 mT is the remanent of the Mn^{+2} resonance, most of which was removed by smoothing. On (b), the upper dashed line is the ARM acquisition curve of intact AMB-1, while the lower dashed line is that of the highly interacting chiton tooth standard. The 31 cm ARM curve, not shown, nearly follows the 14 cm curve.

Table 2-4. Summary of parameters of environmental samples

Sample	FMR Spectrum				$k_{\text{ARM}}/\text{IRM}$ (mm/A)
	g_{eff}	A	ΔB (mT)	α	
<i>Andros Island C51</i>					
6 cm	2.03	0.72	143	0.26	2.54
14 cm	2.01	0.71	143	0.26	2.55
22 cm	2.01	0.78	124	0.25	3.08
31 cm	2.01	0.74	124	0.25	2.49
42 cm	2.02	0.80	118	0.25	1.21
52 cm	2.02	0.80	114	0.25	0.96
<i>Andros Island</i>					
Mean	2.04	0.77	140	0.27	1.97
Min.	2.01	0.71	109	0.25	0.96
Max.	2.11	0.86	192	0.32	3.08
<i>DSDP 73-522</i>					
Mean	2.08	0.83	146	0.28	1.31
Min.	2.03	0.58	136	0.26	1.07
Max.	2.17	1.01	169	0.31	1.62
<i>Wilson Creek</i>					
Mean	2.88	1.11	242	0.43	0.25
Min.	2.58	0.96	207	0.40	0.25
Max.	3.34	1.33	287	0.47	0.38

The deep-sea sediments studied contain magnetofossils of a variety of morphologies, some partially dissolved (VALI and KIRSCHVINK, 1989). TEM images of magnetic extracts from these samples often produced interlocking meshes and linked strings more closely resembling those present in our dilutions of abiogenic magnetite than the chains present in intact bacteria. Excluding one outlier, all the DSDP Leg 73 samples have A of 0.72-1.01, g_{eff} of 2.03-2.11, and ΔB_{FWHM} of 136-157 mT. A typical spectrum is shown in Figure 2-9a. It is similar to that of the dispersed, SDS-treated AMB-1 (sample A3c; dashed line in Figure 2-9a). Like sample A3c, it lacks the second local maximum characteristic of intact bacterial cultures and the laminated Bahamian sediments. Instead, it is consistent with more heterogeneous sediments where the magnetization is dominated by bacterial magnetite in which many of the chains have been broken up but the particles have largely remained associated in roughly linear low-energy configurations—precisely what TEM images (VALI and KIRSCHVINK, 1989) reveal.

The samples from the Pleistocene Wilson Creek Formation (Figure 2-9b) were deposited in Lake Russell, the late Pleistocene predecessor of modern Mono Lake. Microbiological research in Mono Lake has revealed a variety of magnetotactic organisms (C. Z. Nash, unpublished results), but due to the basin's location in the Sierra Nevada, sedimentary flux into the basin and thus sediment magnetization is dominated by detrital material derived from Sierran intrusive bodies. These samples exhibit a broad range of A values (0.73-1.33; all but two compositionally anomalous samples, an ash and sand lens, have $A \geq 0.96$), have g_{eff} well above those of all other samples considered in this paper (2.44-3.34; all but the two anomalous samples have $g_{\text{eff}} \geq 2.58$), and ΔB_{FWHM} larger than the samples dominated by bacterial magnetite (207-287 mT).

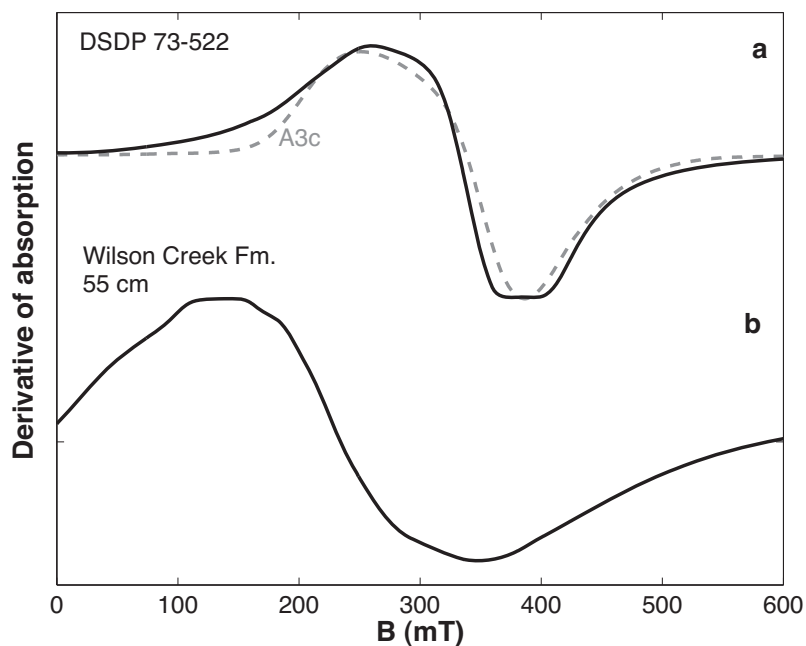


Figure 2-9. Representative FMR spectra of (a) Oligocene-Miocene deep-sea muds from DSDP Leg 73 Site 522, in which magnetofossils are a major remanence carrier and (b) silts from the Pleistocene Wilson Creek Formation of Mono Basin, which are magnetically dominated by detrital magnetite. In (a), the dashed line shows by way of comparison AMB-1 sample A3c, which was treated with SDS and diluted in sucrose by powdering for five minutes.

2.5 Discussion

WEISS et al. (2004a) suggested that the magnetosome chain structure led cultures of magnetotactic bacteria to produce FMR spectra with multiple derivative maxima, $A < 1$ and $g_{\text{eff}} < 2.12$ (the true g-factor for magnetite). Our results support these claims: Our bacterial samples with intact chains had multiple maxima, $A \leq 0.84$ and $g_{\text{eff}} \leq 2.02$. With two exceptions, our sedimentary samples in which magnetofossils are believed to be a major carrier of magnetization had $A \leq 0.97$ and $g_{\text{eff}} \leq 2.11$ (Figure 2-7a; Tables 2-1, 2-4), although not all had multiple maxima. Yet while $A < 1$ and $g_{\text{eff}} < 2.12$ may be necessary conditions for a FMR spectrum to be a spectrum of magnetofossils, they are not sufficient. We were able to produce abiogenic samples with $A \leq 0.87$ and $g_{\text{eff}} \leq 2.11$ by dispersing magnetite in a non-magnetic matrix, thus causing the crystals to string out in minimum energy head-to-tail configurations (Table 2-3). This finding strengthens the claim that $A < 1$ and $g_{\text{eff}} < 2.12$ reflect linear arrangements of crystals, but indicates that these criteria alone cannot uniquely identify magnetofossils.

Closer examination of the FMR spectra suggests alternative criteria that may better distinguish between biogenic and abiogenic magnetite. Increased ΔB_{FWHM} in a spectrum can have multiple causes, including increased anisotropy (increased $|B_{\text{an}}|$ in model spectra) and greater sample heterogeneity (increased σ in model spectra). Variability among magnetotactic bacteria is largely accounted for by the former: The magnetotactic bacteria strain MV-1, which produces elongate truncated hexaoctahedral crystals, has higher magnetic anisotropy than MS-1 or AMB-1, which produce chains of cubo-octahedral crystals (BAZYLINSKI and MOSKOWITZ, 1997). The higher anisotropy both increases ΔB_{FWHM} and decreases A . Similarly, MS-1 has lower A and higher ΔB_{FWHM} than AMB-1, possibly due to better-formed crystals and fewer gaps in their chains than AMB-1. In contrast, in abiogenic samples, heterogeneity plays a major role in controlling ΔB_{FWHM} , and ΔB_{FWHM} can vary significantly without corresponding decreases in A .

The parameter α , defined above, is useful in distinguishing between biogenic and abiogenic samples. All the bacterial samples with intact chains, including magnetotactic strains MV-1, MS-1 and MC-1 (measured by WEISS et al., 2004a), possess $\alpha < 0.25$, while almost all the lithogenic samples from the Wilson Creek Formation have $\alpha > 0.40$. With only two

exceptions, the DSDP and Bahamian samples, as well as the most dispersed SDS-treated AMB-1, have α between 0.25 and 0.30. The most dispersed synthetic magnetite sample we produced had $\alpha = 0.34$, and the trend from the most concentrated to the most dilute falls roughly upon a straight line in ΔB_{FWHM} vs. A space.

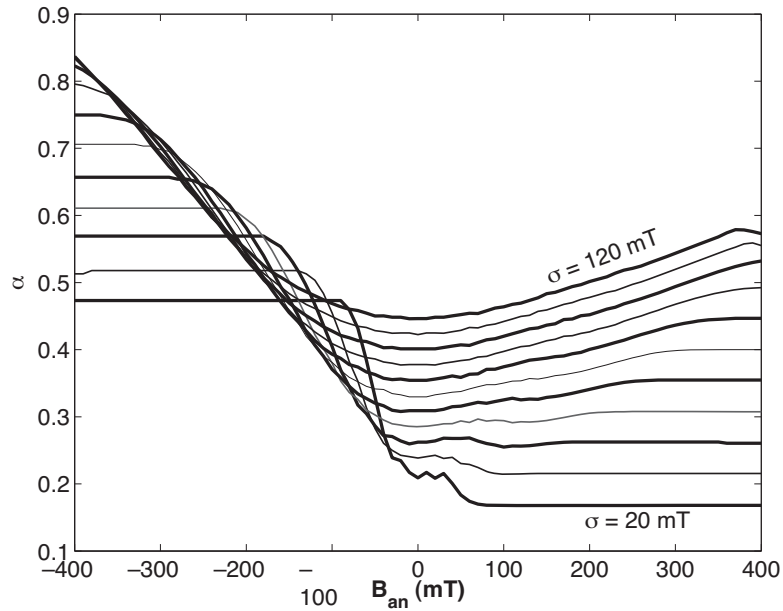


Figure 2-10. The factor α for model spectra. α is plotted for synthetic spectra with first-order uniaxial anisotropy specified by B_{an} . Contour lines show values of σ ranging from 20 mT to 120 mT in 10 mT steps. In the region occupied by measured magnetotactic bacteria and magnetofossil-bearing samples ($B_{an} \geq 75$ mT, $\alpha < 0.30$), α varies nearly linearly with σ .

Although α is an empirical parameter, it serves as a proxy for the physically meaningful Gaussian linewidth σ . In the domain of parameter space occupied by magnetotactic bacteria and magnetofossils, α of synthetic spectra varies almost linearly with σ , and for most values of B_{an} , α increases monotonically as σ increases (Figure 2-10). The intact magnetotactic bacteria have nearly constant α values, which suggests the differences among their spectra are predominantly caused by variations of B_{an} . The B_{an} and σ parameters obtained by fitting the bacterial and synthetic samples (Table 2-1 and Table 2-3) support this hypothesis; the intact and ultrasonicated AMB-1 have $\sigma \approx 30$ mT, while SDS-treated AMB-1 have $\sigma \approx 50$ mT and the synthetic magnetite powders have $\sigma \geq 64$ mT. We propose that $\alpha < 0.30$ suggests the presence of magnetofossils, with lower α values reflecting more intact chains.

At the moment, the data are not strong enough to support firm claims about the presence or absence of biogenic magnetite based on ferromagnetic resonance spectra alone, except perhaps in the case of bacteria that have undergone minimal diagenetic alteration. Nonetheless, FMR provides a useful guide in the search for magnetofossils, and in sediments in which biogenic magnetite is known to be a major contributor to magnetization, FMR allows rapid assessment of the degree to which the magnetite chains have been disrupted. Its speed may also make it a useful tool in unmixing the magnetic components of sediments, although further work in this area is needed. Furthermore, as TEM of sedimentary biogenic magnetite requires the extraction of magnetite from the sediments, FMR provides the only known technique for detecting the presence of linear arrangements of magnetite crystals in situ.

2.6 Conclusions

1. Linear arrangements of magnetite crystals generally yield FMR spectra with $g_{eff} < 2.12$ and $A < 1$. To date, all intact magnetosome chains and almost all sedimentary samples believed to have a significant magnetofossil component fall within this domain, as do physically generated magnetite strings produced by dilution of lysed bacterial magnetite or synthetic magnetite.
2. Intact, biogenic magnetite chains yield derivative spectra with multiple low-field local maxima because their constituent particles experience fairly uniform magnetic anisotropy. Physically generated magnetite strings, which have more heterogeneous magnetic anisotropy, do not exhibit multiple local maxima.
3. Among the magnetotactic bacteria, greater crystal anisotropy produces both higher ΔB_{FWHM} and lower A . MV-1, which produces chains of elongate truncated hexa-octahedral crystals, and MS-1 and AMB-1, which produce chains of cubo-octahedral crystals, have nearly identical values of $\alpha = 0.17 A + 9.8 \times 10^{-4} \Delta B_{FWHM}/\text{mT}$. The factor α is an empirical proxy for symmetric spectral broadening caused by factors such as sample heterogeneity. All magnetotactic bacteria measured have $\alpha < 0.25$, while almost all sedimentary samples believed to contain significant biogenic magnetite have α between 0.25 and 0.30. We

suggest that, in samples containing magnetofossils, increasing α reflects a lower magnetofossil content and/or increased diagenetic alteration.

4. FMR provides a powerful tool for searching for samples likely to contain magnetofossils and for assessing the degree of alteration of magnetofossils in samples known to contain them.

FERROMAGNETIC RESONANCE SPECTROSCOPY FOR ASSESSMENT OF MAGNETIC ANISOTROPY AND MAGNETOSTATIC INTERACTIONS*

An example using mutant magnetotactic bacteria

3.1 Introduction

Ferromagnetic resonance spectroscopy (FMR), a form of electron spin resonance spectroscopy, can serve as a rapid technique for assessing the magnetic anisotropy of and magnetostatic interactions between individual particles in a polycrystalline sample. It is based upon the Zeeman effect, which is the splitting between electron spin energy levels that occurs in the presence of a magnetic field. The Zeeman effect allows a ground-state electron to absorb a photon with energy equal to the splitting between the energy states. In a magnetic material, magnetic anisotropy (whether magnetocrystalline, shape, or stress-induced) and interparticle interactions contribute to the energy of the particles within a sample and thereby alter the resonance energy. As a result, FMR can be used to probe these parameters (Chapter 2 and GRISCOM, 1974; GRISCOM, 1981; KITTEL, 1948; SCHLÖMANN, 1958; WEISS et al., 2004a).

Techniques for measuring anisotropy and magnetostatic interactions have a number of applications in the field of rock magnetism. The example on which we will focus here is the identification of magnetite produced by magnetotactic bacteria, a topic of great interest for understanding the magnetization of sediments. Fossil magnetotactic bacteria may also serve as paleoenvironmental indicators of both strong magnetic fields and local redox gradients (CHANG and KIRSCHVINK, 1989; KIRSCHVINK and CHANG, 1984). These bacteria are a phylogenetically diverse group that biomineralize intracellular crystals of magnetic minerals (magnetite or greigite) which orient the bacteria passively in the geomagnetic field. Natural

* Adapted from R. E. Kopp, C. Z. Nash, A. Kobayashi, B. P. Weiss, D. A. Bazylinski, and J. L. Kirschvink (2006). Ferromagnetic resonance spectroscopy for assessment of magnetic anisotropy and magnetostatic interactions: A case study of mutant magnetotactic bacteria. *Journal of Geophysical Research* 111, B12S25, doi:10.1029/2006JB004529.

selection has led these bacteria to optimize the magnetic moment produced for the amount of iron used. Among the traits present in magnetite produced by many magnetotactic bacteria are a narrow distribution of particle sizes within the single-domain stability field, particle elongation, and the arrangement of particles in chains (THOMAS-KEPRTA et al., 2000). The biophysical problem of keeping strongly magnetic particles aligned in a chain may also have driven the evolution of a variety of cytoskeletal supporting mechanisms, including an intracellular “sheath” (KOBAYASHI et al., 2006), actin-like cytoskeletal filaments (SCHEFFEL et al., 2006) and/or direct attachments to the periplasmic membrane (KOMEILI et al., 2006).

The adaptive traits possessed by these biogenic magnetic particles at a microscopic level generate distinct magnetic properties that are identifiable with macroscopic techniques. The particles’ narrow distribution within the single-domain size range is typically observed in analyses of coercivity spectra, including the measurement of the acquisition of isothermal remanent magnetization and the demagnetization of remanent magnetizations (CHANG et al., 1989; PAN et al., 2005). EGLI (2004b) used the unmixing of coercivity spectra to determine the biogenic contribution to lacustrine sedimentary magnetization.

Anhyseritic susceptibility, which provides a qualitative measure of inverse interaction strength when comparing single-domain particles of similar volumes (DUNLOP et al., 1990; EGLI and LOWRIE, 2002), has also been used to distinguish bacterial magnetite chains from abiogenic magnetite (MOSKOWITZ et al., 1993). Anhyseritic magnetization is acquired by the application of a small biasing field in the presence of a decaying alternating field. In the absence of thermal effects, non-interacting single-domain particles would have infinite anhyseritic susceptibility; they should become magnetized in the direction of the biasing field as soon as the alternating field decreases below their microcoercivity (DUNLOP and ÖZDEMİR, 1997; EGLI and LOWRIE, 2002). In fact, thermal effects cause more elongate and smaller particles to have lower ARM susceptibility than less elongate or larger single-domain particles (EGLI and LOWRIE, 2002). The shielding effects of magnetostatic interactions operating in three dimensions also lower anhyseritic susceptibility.

In many strains of magnetotactic bacteria, however, linear magnetostatic interactions cause an entire chain of particles to behave in a magnetically coherent fashion (HANZLIK et al., 2002; PENNINGA et al., 1995). Intact cells of magnetotactic bacteria therefore have low three-dimensional magnetostatic interactions and thus relatively high anhysteritic susceptibility, so high anhysteritic remanent magnetization (ARM)/isothermal remanent magnetization (IRM) ratios are characteristic of the presence of magnetite chains. Collapsed magnetosome chains, with stronger three-dimensional magnetostatic interactions, have lower ARM/IRM ratios.

Another test that is indicative of the presence of chains is the delta-delta test of (MOSKOWITZ et al., 1993), which uses the ratio of magnetization lost upon warming through the ~90–120 K Verwey transition in saturated samples that have been cooled in a strong field to the magnetization lost after cooling in zero field. While previous data indicate that this test does identify chains of biogenic magnetite (MOSKOWITZ et al., 1993; WEISS et al., 2004a), it is susceptible to false negatives and the underlying physical mechanisms are incompletely understood (CARTER-STIGLITZ et al., 2004).

Ferromagnetic resonance spectroscopy is capable of rapidly distinguishing biogenic magnetite chains based on three traits: (i) a narrow range of particle size, shape, and arrangement, (ii) chain structure, and (iii) particle elongation (Chapter 2 and WEISS et al., 2004a). Samples with narrow distributions of size, shape, and arrangement have narrow FMR peaks. Chain structure and particle elongation produce positive uniaxial anisotropy, which can be distinguished from the negative cubic magnetocrystalline anisotropy that dominates isolated, equidimensional magnetite.

Bacterial mutagenesis is a central technique in molecular microbiology. By disabling regions of the genome, it probes the roles of different genes in the production of a phenotype. Our attempts to understand the molecular mechanism of magnetite biosynthesis (which will be described in a follow-up paper by Nash et al.) led us to create mutant strains of the magnetotactic bacterium *Magnetospirillum magneticum* strain AMB-1, whose wild-type creates chains of almost equidimensional cubo-octahedral crystals. Two of these mutants produce crystals that are usually isolated and are either approximately

equidimensional (mutant *mmm18*) or elongate (mutant *mmm13*). We used these mutants, along with cells of wild-type AMB-1 and the magnetotactic marine vibrio MV-1, which produces chains of elongate hexa-octahedral crystals, to investigate the contributions of magnetic anisotropy and magnetostatic interactions to ferromagnetic resonance spectra. These different strains allow us for the first time to separate directly the effects of chain structure on FMR and rock magnetic properties from those of single crystal traits.

3.2 Methods

3.2.1 Mutagenesis

To generate the mutants, transposon mutagenesis was performed on AMB-1 following previously described procedures (KOMEILI et al., 2004). Mutants were grown up on plates, and single colonies were then picked and grown up in 96-well plates in sealed jars with 2% oxygen/98% nitrogen atmospheres. After 3-5 days of growth, weakly magnetic and non-magnetic mutants were identified by placing the plates on an array of magnets. Mutants that were not drawn towards the side of the well were subcultured for further analysis. For mutant *mmm13*, sequencing of genomic DNA indicated that an interruption by the introduced transposon occurred in a gene encoding for a hypothetical protein. For *mmm18*, sequencing indicated that the interruption occurred in a pyruvate/ferredoxin oxidoreductase gene. Time course experiments indicate that *mmm18* is a growth defective mutant that takes 1–2 days longer to reach stationary phase than the wild-type.

3.2.2 Growth conditions and lysis

Cells of strain MV-1 were grown anaerobically with nitrous oxide as the terminal electron acceptor under heterotrophic conditions as previously described (DEAN and BAZYLINSKI, 1999). Cells were harvested at early stationary phase, at a cell density of about 1.5×10^9 cells/mL, by centrifugation at $5,000 \times g$ at 4°C for 10 min and then resuspended in ice-cold artificial seawater containing 20 mM Tris-HCl at pH 7.0. Cells were recentrifuged and the resultant pellet of cells was frozen and shipped on dry ice to Caltech, where it was thawed. A fraction of the cell mass was resuspended in Tris buffer, from which point it was subject to the same treatments as AMB-1.

Two liters each of AMB-1 wild-type and mutants *mmm13* and *mmm18* were grown up to early stationary phase, at a cell density of about 10^8 cells/mL, using standard culture conditions (KOMEILI et al., 2004). The cultures were divided into thirds (A1, A2, and A3 for the wild-type; B1, B2, and B3 for *mmm13*; C1, C2, and C3 for *mmm18*; V1, V2, and V3 for MV-1), spun down, and resuspended in ~5 mL 100 mM Tris buffer at pH 7. Five μ L of β -mercaptoethanol and ~250 mg of sodium dodecyl sulfate (SDS) were added to subsamples A3, B3, C3, and V3. Subsamples A2, A3, B2, B3, C2, C3, V2, and V3 were then subjected to ultrasonication with a Fisher Scientific Sonic Dismembrator 550 for about six minutes, with pulses of 0.5 seconds alternating with pauses of equal duration. Ultrasonication should destroy cell membranes while leaving magnetosome membranes intact. SDS treatment should destroy both cell membranes and magnetosome membranes, thereby freeing the magnetite particles from organic structures.

The samples were then spun down, frozen, and freeze-dried. In a set of experiments analogous to the dilution experiments described in Chapter 2, V2 was diluted at ~1 part per thousand in sucrose. It was initially measured as sample V2a, then was diluted by mixing with a mortar and pestle for 4 minutes to form subsample V2b. Sample V3 was similarly diluted at ~1 part per thousand as sample V3a, diluted by mixing for 1 minute to form sample V3b, and then mixed for four additional minutes to form sample V3c.

3.2.3 Electron microscopy

Specimens were dispersed on hydrophilic copper TEM grids, air-dried, and made electrically conductive by coating with a thin carbon film using conventional methods. The grids were inserted into a beryllium TEM specimen holder for EDS analysis. TEM and HAADF/STEM images were obtained with a Tecnai G2 F20 Twin (FEI, Holland), operating at 200 kV and equipped with Gatan energy filter GIF2001 and HAADF/STEM detecting unit. The HAADF/STEM/EDS analysis was performed by an EDX detecting unit (EDAX, Inc.). Histograms of particle size/shape distributions were made by measuring the maximum length and widths of magnetite crystals visible in the TEM images in a similar fashion to that of KIRSCHVINK and LOWENSTAM (1979) and DEVOUARD et al. (1998). Due to the sharp decay in field strength with distance ($1/r^3$), particles were grouped into chains if they were positioned within less than one grain diameter from an adjacent crystal.

3.2.4 Ferromagnetic resonance spectra

Ferromagnetic resonance spectra were acquired using an X-band Bruker ESP 300E EPR Spectrometer housed at Caltech. Except for particularly strong samples (V3a, V3b, and V3c), microwave power was set at 640 μW and spectra were integrated over three sweeps of the applied field from 0 to 600 mT. For strong samples, power was set at 64 μW and only one spectrum was acquired. To summarize spectral characteristics, we use the empirical parameters developed by WEISS et al. (2004a) and in Chapter 2: g_{eff} , A , ΔB_{FWHM} , and α . The effective g -factor, g_{eff} , is the g -factor associated with maximum absorption which is given by $g_{\text{eff}} = h\nu/\beta B_{\text{eff}}$, where B_{eff} is the field value of maximum absorption. The asymmetry ratio is defined as $A = \Delta B_{\text{high}}/\Delta B_{\text{low}}$, where $\Delta B_{\text{high}} = B_{\text{high}} - B_{\text{eff}}$, $\Delta B_{\text{low}} = B_{\text{eff}} - B_{\text{low}}$, and B_{high} and B_{low} are the fields of half maximum absorption at low-field and high-field sides of the absorption peak, respectively. The full width at half maximum, ΔB_{FWHM} , is defined as $\Delta B_{\text{FWHM}} = B_{\text{high}} + B_{\text{low}}$. Although all these parameters are derived from the integrated absorption spectrum, FMR spectra are generally displayed as derivative spectra, which magnify fine detail. The empirical parameter α , which serves as a proxy for the linewidth of symmetric Gaussian broadening caused by factors including heterogeneity of particle size, shape, and arrangement, is defined as $\alpha = 0.17 A + 9.8 \times 10^{-4} \Delta B_{\text{FWHM}}/\text{mT}$.

The empirical parameters defined above differ from the physical parameters that control the spectral shape (g , B_{an} , K_2/K_1 , and σ) and which we estimate using the models discussed in section 3.3.

3.2.5 Room-temperature remanent magnetization experiments

Room temperature remanent magnetization experiments were performed using a 2G Enterprises Superconducting Rock Magnetometer housing in a magnetically-shielded room at Caltech and equipped with in-line coils for degaussing, DC pulsing, and applying weak DC biasing fields. Starting with an AF-demagnetized sample, anhysteritic remanent magnetization (ARM) was acquired in a 100 mT alternating field (AF) and a DC biasing field that was raised in 0.05 mT steps to 1 mT. The ARM was then removed by step-wise AF demagnetization up to 250 mT in logarithmically-spaced steps (where the steps were multiples of $10^{0.1}$ mT). The sample was then imparted an isothermal remanent magnetization (IRM) by pulsing with a 100 mT field. This IRM was then removed by

stepwise AF demagnetization. Finally, an IRM was imparted stepwise in logarithmically-spaced steps up to 980 mT and then removed by AF demagnetization.

To produce coercivity spectra from the stepwise AF and IRM curves, we took the derivative of the curves with respect to the log of the applied field and smoothed the curves with a running average. We report the following parameters: the coercivity of remanence H_{cr} , the Cisowski crossover R value, the median acquisition field of IRM (MAF_{IRM}), the median destructive fields of IRM (MDF_{IRM}) and ARM (MDF_{ARM}), and the ARM ratio k_{ARM}/IRM .

The parameters H_{cr} and R are determined from the IRM stepwise acquisition and demagnetization curves. H_{cr} is the field value at which the two magnetization curves cross, and R is the ratio of magnetization to SIRM at that field (CISOWSKI, 1981). For non-interacting single-domain particles (or magnetically coherent chains of particles that do not interact with other chains), $R = 0.5$, while decreasing values indicate increasing magnetostatic interactions. The median acquisition and destructive fields are defined as the fields required to yield half of the maximum remanent magnetization, where the IRM value is taken from the stepwise IRM curve and the ARM value is taken from the ARM demagnetization curve. We report ARM susceptibility as k_{ARM}/IRM , the ARM acquired per A/m of biasing field (as measured in a biasing field of 0.1 mT (79.6 A/m) and an alternating field of 100 mT), normalized to the IRM acquired in a field of 100 mT.

3.2.6 Low temperature rock magnetic experiments

Low temperature rock magnetic experiments were performed using a Quantum Design Magnetic Properties Measurement System (MPMS) housed in the Molecular Materials Resource Center of the Beckman Institute at Caltech. Following the procedure of MOSKOWITZ et al. (1993), field-cooled and zero-field-cooled curves were acquired by cooling the sample either in a 3 T field or in zero field to 5 K, respectively, followed by pulsing with a 3 T field and then measuring the remanence magnetization during warming to room temperature in zero field. Low-temperature cycling curves were then acquired by pulsing the sample with a 3 T field at room temperature and then measuring the remanent magnetization as the sample was cooled to 10 K and then warmed to room temperature.

The results of the low-temperature experiments are reported as the parameters δ_{ZFC} , δ_{FC} , and f_{LTC} . The parameters $\delta = (J_{80K} - J_{150K})/J_{80K}$ were assessed for the zero-field-cooled and field-cooled curves respectively, where J_{80K} and J_{150K} are the moments measured at 80 K and 150 K, respectively. A ratio $\delta_{FC}/\delta_{ZFC} > 2.0$ passes the Moskowitz test and is considered to be an indicator of the presence of magnetosome chains, although partial oxidation and mixing can cause intact chains to fail the test (MOSKOWITZ et al., 1993; WEISS et al., 2004a). Magnetization retained through low temperature cycling is expressed as the memory parameter $f_{LTC} = J_{LTC}/J_0$, where J_0 and J_{LTC} are respectively the room-temperature magnetization measured before and after cycling the samples to 10 K.

3.3 Models

The models used to fit FMR spectra in this paper are a generalization of prior models (Chapter 2 and GRISCOM, 1974; GRISCOM, 1981). They derive from the resonance condition (Equation 7 of SMIT and BELJERS, 1955):

$$\left(\frac{h\nu}{g\beta}\right)^2 = \frac{1}{M_s^2 \sin^2 \vartheta} \left(\frac{\partial^2 G}{\partial \vartheta^2} \frac{\partial^2 G}{\partial \varphi^2} - \frac{\partial^2 G}{\partial \vartheta \partial \varphi} \right), \quad (3-1)$$

where $h\nu$ is the energy of the microwave photons, g is the spectroscopic g -factor of an isolated particle with all anisotropy effects removed, β is the Bohr magneton (9.37×10^{-24} A•m²), M_s is the saturation magnetization, G is the free energy of the system, and ϑ and φ are the polar coordinates of the magnetization vector in its minimum energy orientation.

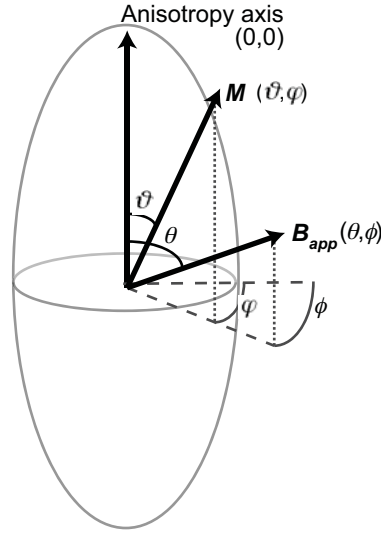


Figure 3-1: Angles used in the derivation of the resonance conditions. The origin of the reference frame is defined with respect to the anisotropy axis. The applied field \mathbf{B}_{app} is oriented at azimuthal angle θ and declination ϕ . The magnetization \mathbf{M} is oriented at azimuthal angle ϑ and declination φ .

Neglecting thermal energy, which is isotropic and therefore does not appear in Equation 3-1, the free energy G of a system composed of non-interacting, single-domain particles can be written as a sum of the magnetostatic energy $-\mathbf{M}\cdot\mathbf{B}$ and the anisotropy energy. When the reference frame is defined such that the anisotropy axis is directed along $(\vartheta, \varphi) = (0, 0)$ as shown in Figure 3-1, the free energy is given by

$$G = M_s \left\{ B_{app} [\sin \vartheta \sin \theta \cos(\phi - \varphi) + \cos \vartheta \cos \theta] + \frac{1}{2} B_{an} F(\vartheta, \varphi) \right\}, \quad (3-2)$$

where (θ, ϕ) are the polar coordinates of the experimentally applied field B_{app} with respect to the anisotropy axis, B_{an} is an effective anisotropy field, and $F(\vartheta, \varphi)$ is a geometric factor expressing the variation of the anisotropy energy as a function of the direction of the magnetization vector.

B_{an} and F vary depending on the source of the anisotropy. For magnetocrystalline anisotropy, B_{an} is $2K_1/M_s$, where K_1 is the first-order anisotropy constant (generally written as K'_1 for uniaxial anisotropy). For uniaxial shape anisotropy, B_{an} is $\mu_0 M_s \Delta N$, where μ_0 is the magnetic permeability of free space ($4\pi \times 10^{-7}$ N/A²) and ΔN is the difference between the

demagnetization factors N_{\parallel} and N_{\perp} parallel and perpendicular to the elongate axis. For uniaxial anisotropy, regardless of the source,

$$F(\vartheta) = \sin^2 \vartheta + \frac{K'_2}{K'_1} \sin^4 \vartheta , \quad (3-3)$$

while for cubic anisotropy,

$$F(\vartheta, \varphi) = \sin^4 \vartheta \sin^2 \varphi \cos^2 \varphi + \sin^2 \vartheta \cos^2 \vartheta + \frac{K_2}{K_1} \sin^4 \vartheta \cos^2 \vartheta \sin^2 \varphi \cos^2 \varphi , \quad (3-4)$$

where K_2 is the second-order anisotropy constant (generally written as K'_2 for uniaxial anisotropy) (DUNLOP and ÖZDEMİR, 1997).

By using a first-order approximation to calculate the equilibrium orientation of the magnetization vector and considering only terms that are first order in B_{an}/B_{res} , we arrive at Equation A.3 of SCHLÖMANN (1958):

$$\left(\frac{h\nu}{g\beta B_{res}} \right)^2 = 1 + \frac{B_{an}}{2B_{res}} a , \quad (3-5)$$

where B_{res} is the applied field at which a particle in an arbitrary orientation achieves resonance and

$$a = \frac{\partial^2 F}{\partial \vartheta^2} + \frac{\partial^2 F}{\partial \varphi^2} \cdot \frac{1}{\sin^2 \vartheta} + \frac{\partial F}{\partial \vartheta} \cot \vartheta . \quad (3-6)$$

Solving the quadratic expression in Equation 3-5 yields an expression for B_{res} as a function of orientation:

$$B_{res} = \sqrt{\left(\frac{h\nu}{g\beta} \right)^2 + \left(\frac{aB_{an}}{4} \right)^2} - \frac{aB_{an}}{4} . \quad (3-7)$$

For uniaxial anisotropy,

$$a_{uniaxial} = 6 \cos^2 \theta - 2 + \frac{K'_2}{K'_1} (16 \cos^2 \theta \sin^2 \theta - 4 \sin^4 \theta), \quad (3-8)$$

while for cubic anisotropy,

$$a_{cubic} = 4 \left(\begin{array}{l} 1 - 5(\cos^2 \theta \sin^2 \theta + \sin^4 \theta \sin^2 \phi \cos^2 \phi) \\ + \frac{K_2}{2K_1} \left(\cos^2 \theta \sin^2 \theta + \sin^4 \theta \sin^2 \phi \cos^2 \phi \right) \\ - 21 \sin^4 \theta \cos^2 \theta \sin^2 \phi \cos^2 \phi \end{array} \right). \quad (3-9)$$

When the second-order anisotropy terms in Equation 3-9 and the second term under the radical in Equation 3-7 are ignored, the resonance conditions thus computed are identical to those of GRISCOM (1974). When only the second term under the radical is ignored, the cubic anisotropy condition is identical to that of GRISCOM (1981), except that in Equation 3-9 we drop the third-order anisotropy term in K_3 introduced in that paper. The resonance conditions we have derived are strictly correct to first order in terms of B_{an}/B_{res} for dilute powders of single-domain particles.

To compute the powder absorption spectrum at B_{app} , we apply a Gaussian broadening function of linewidth σ and numerically integrate the spectra over all solid angles:

$$A(B_{app}) = \int_{\theta=0}^{\pi/2} \int_{\phi=0}^{2\pi} \frac{\exp\left(-\left(B_{app} - B_{res}(\theta, \phi)\right)^2 / 2\sigma^2\right)}{\sqrt{2\pi}\sigma} d\phi \sin\theta d\theta. \quad (3-10)$$

The Gaussian broadening incorporates a number of physical effects, including those associated with heterogeneity of size, shape, arrangement, and composition within the sample population. To reflect the physics more accurately, the spectroscopic g -factor and the anisotropy parameters ought to have population distributions associated with them individually. However, attempting to fit experimental spectra to a model that employed population distributions for each of these terms would almost always be a problem without a unique solution.

We fit measured spectra to simulated spectra using non-linear least squares fitting. For each magnetic component included, the models have four parameters that can be adjusted to fit

the spectra: g , B_{an} , K_2/K_1 , and σ . When appropriate, the spectra can be fit to two components, in which case K_2/K_1 is set to zero for both components in order to limit the number of additional degrees of freedom introduced.

For most of the samples, we attempted fits with both cubic and uniaxial models, as well as models combining two uniaxial components, two cubic components, or a uniaxial component and a cubic component. Except when $|B_{an}| \gg \sigma$, substituting a cubic component for a uniaxial component did not significantly improve or degrade the goodness of the fit. We suspect this is because the Gaussian broadening conceals the underlying physics in a fashion that makes it difficult to discriminate between samples best fit with a cubic component and those best fit with a uniaxial component.

The substitution often had only slight effects on the fitted parameters as well, but sometimes did vary the parameters outside the confidence intervals on the uniaxial fits. Because the anisotropy field expected from the cubic magnetocrystalline anisotropy of stoichiometric magnetite ($K_1 = -1.35 \times 10^4 \text{ J/m}^3$, $M_s = 480 \text{ kA/m}$) is about -56 mT (DUNLOP and ÖZDEMİR, 1997), we report the fitted parameters using cubic anisotropy for components with B_{an} between approximately -56 and 0 mT. (The dominant components of samples C1 and C2 are the only components that fit this criterion). The underlying physics in fact reflects neither purely uniaxial nor purely cubic anisotropy, but a more complicated combination of approximately uniaxial shape anisotropy and cubic magnetocrystalline anisotropy, which would be reflected in a more complete form of Equation 3-2. Some of the Gaussian broadening likely results from our simplified treatment of the anisotropy.

The decision as to whether to represent a measured spectrum with a one-component spectrum or the sum of two model spectra was made heuristically, based upon the level of the improvement of fit when a second spectrum was added, how physically realistic the two spectra identified by the fitting routine are, and the size of the confidence intervals around fit parameters. In interpreting the models, it is important to remember that, if properly modeled, multiple components in a fit reflect multiple end-members mixed together (e.g. isolated particles and particles in chains, or particles in chains and particles in clumps); they do not reflect multiple aspects of the anisotropy of a single end-member.

3.4 Results

3.4.1 Electron microscopy

Consistent with DEVOUARD et al. (1998), our TEM images indicate that MV-1 produces chains of magnetite crystals with a mean single crystal length of ~ 75 nm and a mean length-to-width ratio of ~ 1.8 (Figure 3-2). The untreated cells of MV-1 we measured experienced some chain collapse, perhaps due to the freezing of the sample. As can be seen in Figure 3-2a, some chains collapsed into zero stray field loop configurations, while in other chains some of the particles have fallen into side-by-side arrangements. About ten percent of the crystals appear sufficiently separated from other crystals to be magnetically isolated. Collapse features are greatly enhanced by ultrasonication (Figure 3-2b). Few of the chains in the ultrasonicated sample V2 are unaffected; most are bent or interwoven with other chains. Only a small number of crystals are magnetically isolated. Treatment with SDS (sample V3) led to near complete collapse of chains into clumps (Figure 3-2c).

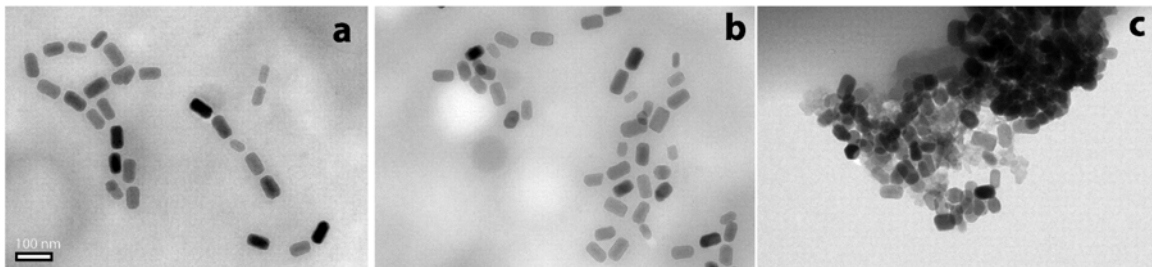


Figure 3-2: Transmission electron micrographs of MV-1. (a) Sample V1, untreated, (b) Sample V2a, ultrasonicated, and (c) Sample V3a, lysed with SDS. Scale bar is 100 nm.

There appears to be a greater tendency for chain collapse to occur in strain MV-1 than in *M. magnetotacticum* strain MS-1, a strain related to AMB-1 that produces more equidimensional particles than MV-1 (KOBAYASHI et al., 2006). In the case of MS-1, ultrasonication does not produce many side-by-side crystal pairs. Instead, ultrasonication of MS-1 tends to cause chains to string together in a head-to-tail fashion. The difference between the collapse styles of MV-1 and MS-1 is likely attributable to the energetic differences between elongate and equidimensional particles.

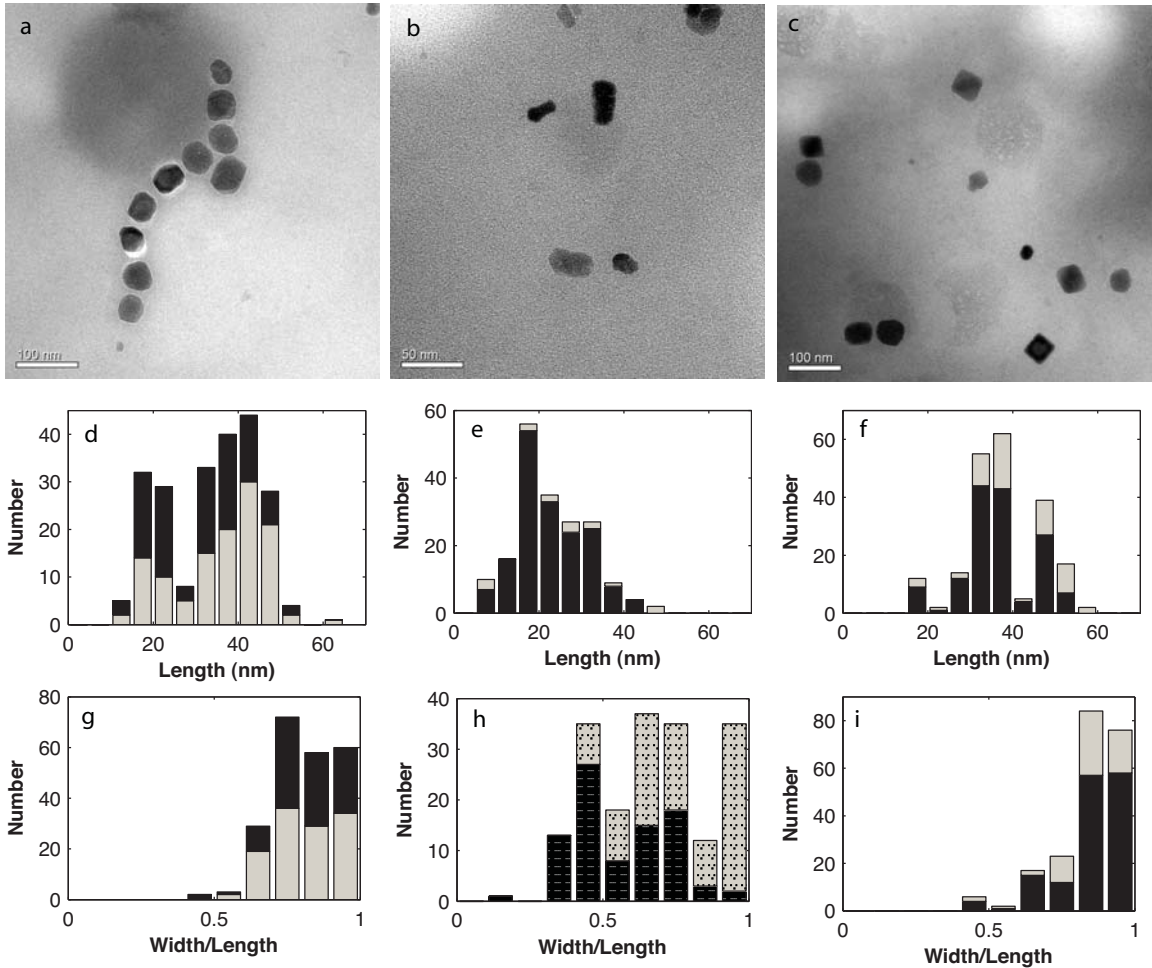


Figure 3-3: Transmission electron micrographs of and summary statistics for AMB-1 strains. (a-c) TEM images of freeze-dried powders of (a) wild-type, (b) *mmm13*, and (c) *mmm18*. In (a) and (c), scale bar is 100 nm; in (b), scale bar is 50 nm. (d-f) Histograms of particle length for magnetite produced by (d) wild-type, (e) *mmm13*, and (f) *mmm18*. (g-i) Histograms of particle width/length ratios for magnetite produced by (g) wild-type, (h) *mmm13*, and (i) *mmm18*. In (d-g) and (i), dark bars represent particles in chains and light bars represent isolated particles. In (h), dark bars represent particles with length ≥ 25 nm and light bars represent particles with length < 25 nm.

Cells of wild-type AMB-1 produce magnetite particles with a mean particle length of ~ 35 nm and length-to-width ratio ~ 1.2 (Figure 3-3 a,d,f). In powder A1, derived from freeze-dried wild-type AMB-1, $\sim 65\%$ by volume of the crystals we measured were in chains of at least 2 particles and $\sim 35\%$ were isolated. Previous observations of whole cells of wild-type AMB-1 indicate that single cells often produce chains with segments of anywhere between 1 and 21 crystals separated by gaps. The presence of isolated crystals in the freeze-dried

powder is likely due to a combination of gaps in chains produced by single cells and desegregation during the freeze-drying process.

Cells of the AMB-1 mutant *mmm13* produce elongated crystals, with a mean length of ~25 nm and a mean length-to-width ratio of ~1.5 (Figure 3-3 b,e,h). About 90% by volume of the crystals produced by *mmm13* are isolated and ~10% are in chains of 2 or more particles. Among particles with a length > 25 nm, which dominate by volume and control the magnetic properties, the mean length-to-width ratio is ~1.75. Some of the bias toward greater elongation in larger crystals is likely observational; an elongate particle, viewed down the axis of elongation, appears to have a width/length ratio of 1 and a shorter length than its true length.

Cells of the mutant *mmm18* produce more equidimensional crystals, similar to those produced by the wild-type, with a mean length of ~40 nm and a mean length-to-width ratio of ~1.2 (Figure 3-3 c,f,i). By volume, ~65% of the particles are isolated and ~35% are in chains. Though most of the chains consist of only two particles, they can grow significantly longer. The longest *mmm18* chain we observed consisted of seven particles, which suggests that a small fraction of *mmm18* cells exhibit the wild-type phenotype.

Table 3-1. Measured ferromagnetic resonance parameters

Sample	Strain	Treatment	g_{eff}	A	ΔB_{FWHM} (mT)	A
A1	AMB-1 wild-type	untreated	2.01	0.76	87	0.21
A2	AMB-1 wild-type	sonicated	2.02	0.79	84	0.22
A3	AMB-1 wild-type	SDS	2.31	1.17	206	0.40
B1	AMB-1 <i>mmm13</i>	untreated	2.02	0.88	91	0.24
B2	AMB-1 <i>mmm13</i>	sonicated	2.01	0.86	95	0.24
B3	AMB-1 <i>mmm13</i>	SDS	2.02	0.83	107	0.25
C1	AMB-1 <i>mmm18</i>	untreated	2.07	1.13	80	0.27
C2	AMB-1 <i>mmm18</i>	sonicated	2.07	1.16	79	0.27
C3	AMB-1 <i>mmm18</i>	SDS	2.07	0.78	151	0.28
V1	MV-1	untreated	1.78	0.35	127	0.18
V2a	MV-1	sonicated	1.84	0.29	219	0.26
V2b	MV-1	sonicated, 4m dilution	1.85	0.30	206	0.25
V3a	MV-1	SDS	2.58	1.77	244	0.54
V3b	MV-1	SDS, 1m dilution	2.54	1.62	218	0.49
V3c	MV-1	SDS, 5m dilution	1.86	0.25	208	0.25

3.4.2 Ferromagnetic resonance spectroscopy

Our measurements of the FMR spectra of intact MV-1 and wild-type AMB-1 agree with those of WEISS et al. (2004a), exhibiting distinctive asymmetric spectra that are extended in the low-field direction. MV-1 has a broader spectrum than AMB-1, which reflects the greater anisotropy of its magnetite chains, generated by particle elongation as well as chain alignment (Table 3-1; Figure 3-4; Figure 3-5a). MV-1 also has three characteristic maxima in the derivative spectrum, seen in samples V1, V2a, and V2b at ~ 180 mT, ~ 300 mT, and ~ 350 mT. Our one-component model spectra are unable to reproduce this trait. Our attempts to fit these three spectra with two-component models, however, yielded disparate secondary fit components with no clear physical interpretation. This disparity suggests the values thus determined were artifacts, and we therefore report the single-component fits in Table 3-2. A more complete physical model capable of including multiple sources of anisotropy might explain the distinctive triple maxima of MV-1 spectra.

Table 3-2. Ferromagnetic resonance spectral fits

Sample	Component weight	g	B_{an} (mT)	K_2/K_1	σ (mT)
A1	100%	2.07 \pm 0.00	69.1 \pm 0.8	-0.12 \pm 0.01	24.2 \pm 0.2
A2	100%	2.07 \pm 0.00	63.6 \pm 0.7	-0.13 \pm 0.01	23.5 \pm 0.2
A3	61%	2.15 \pm 0.03	87.4 \pm 10.1		55.5 \pm 2.4
	39%	2.38 \pm 0.01	-171.2 \pm 4.3		31.7 \pm 1.5
B1	100%	2.08 \pm 0.00	90.9 \pm 2.5	-0.32 \pm 0.02	31.1 \pm 0.3
B2	100%	2.09 \pm 0.00	104.3 \pm 2.5	-0.31 \pm 0.01	31.8 \pm 0.2
B3	100%	2.10 \pm 0.00	99.7 \pm 1.5	-0.23 \pm 0.01	34.2 \pm 0.2
C1	70%	2.05 \pm 0.00	-47.3 \pm 0.8		19.2 \pm 0.1
	30%	2.12 \pm 0.01	76.1 \pm 1.1		22.1 \pm 0.8
C2	57%	2.06 \pm 0.00	-43.0 \pm 0.6		18.4 \pm 0.2
	43%	2.09 \pm 0.01	64.1 \pm 3.1		28.2 \pm 0.6
C3	68%	2.05 \pm 0.01	50.2 \pm 5.4		43.1 \pm 0.8
	32%	2.34 \pm 0.01	-142.3 \pm 3.3		30.4 \pm 0.9
V1	100%	2.21 \pm 0.01	170.9 \pm 2.6	-0.03 \pm 0.01	17.3 \pm 0.3
V2a	100%	2.26 \pm 0.01	164.0 \pm 3.2	0.01 \pm 0.01	26.7 \pm 0.6
V2b	100%	2.24 \pm 0.01	160.4 \pm 2.7	0.00 \pm 0.01	24.9 \pm 0.4
V3a	100%	2.35 \pm 0.01	-120.0 \pm 2.3	0.23 \pm 0.02	56.9 \pm 0.8
V3b	84%	2.37 \pm 0.01	-129.9 \pm 2.6		58.3 \pm 0.9
	16%	2.24 \pm 0.01	157.4 \pm 2.5		21.2 \pm 0.7
V3c	100%	2.24 \pm 0.01	132.6 \pm 3.4	0.08 \pm 0.02	20.6 \pm 0.6

Dominant components of C1 and C2 are modeled using cubic anisotropy. All others are uniaxial.

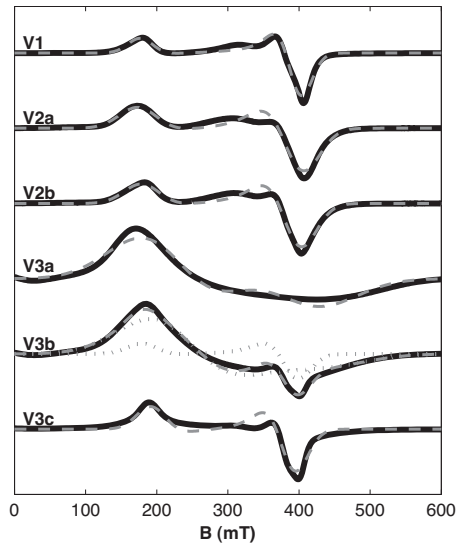


Figure 3-4: FMR spectra of MV-1. Solid lines show measured spectra, dashed lines show fitted spectra, and dotted lines show the spectra of the individual fit components for two-component fits.

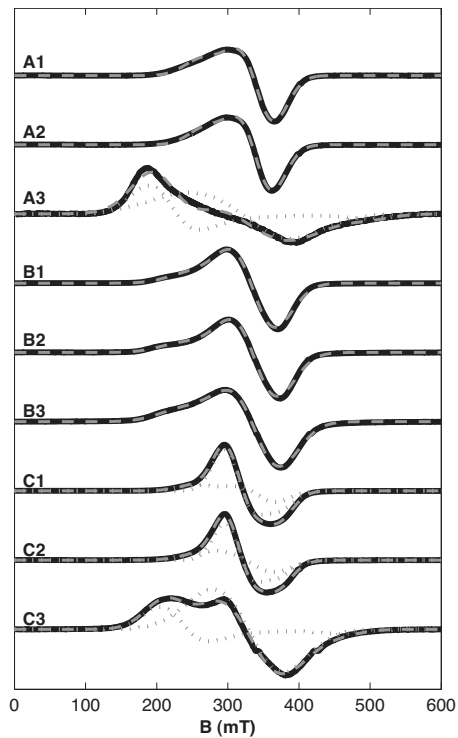


Figure 3-5: FMR spectra of AMB-1 wild-type (A1-A3), *mmm13* (B1-B3), and *mmm18* (C1-C3). Solid lines show measured spectra, dashed lines show fitted spectra, and dotted lines show the spectra of the individual fit components for two-component fits.

Based on the demagnetization factors derived by OSBORN (1945) and assuming that the anisotropy is dominated by uniaxial shape anisotropy, the B_{an} value of 171 mT fitted to the spectrum of intact MV-1 (sample V1) is that expected from prolate spheroids of stoichiometric magnetite ($M_s = 480$ kA/m) with length-to-width ratios of ~ 2.35 . The calculated ratio is significantly larger than that observed for individual particles under TEM and therefore likely reflects the joint contribution of particle elongation and chain structure. The large, positive B_{an} value indicates that the negative contribution of magnetocrystalline anisotropy is overwhelmed by the positive contributions of shape anisotropy and chain structure.

Ultrasonication of MV-1 broadens the FMR spectrum, with ΔB_{FWHM} increasing from 127 mT in sample V1 to 219 in sample V2a. This broadening, which is reflected in the spectral fits by an increase of σ from 17 mT to 27 mT despite a slight decline in B_{an} , suggests an increase in the heterogeneity of particle arrangement without the formation of strongly interacting clumps. Although dilution (sample V2b) produces a significant increase in anhysteritic susceptibility (see discussion below), it results in little change in the FMR spectrum.

In contrast, lysis of MV-1 cells with SDS produces a drastic change in the FMR spectrum, as it causes the particles to collapse into clumps. The FMR spectra of these clumps, like the FMR spectra of similarly treated AMB-1 observed by WEISS et al. (2004a) and in the present work, are broad and exhibit high-field extended asymmetry reflective of a negative effective anisotropy field. The negative anisotropy may reflect the anisotropy of the surface of particle clumps or the oblateness of the clumps. Although modeling clumps with expressions derived for isolated particles is far from ideal, the fitted B_{an} value of -120 mT corresponds to that predicted for oblate spheroids with a length-to-width ratio of ~ 0.62 . GRISCOM et al. (1988) observed similar traits in the spectra of powders of magnetite nanoparticles exhibiting planar interactions.

Subsequent dilution causes the gradual reappearance of positive anisotropy, again as in the case of AMB-1 (see Chapter 2). After one minute of dilution, the spectrum is best fit by a two-component model, with 84% of the absorption caused by a component with B_{an} of -130

mT and 16% caused by a component with B_{an} of 157 mT. The former component likely corresponds to particles in clumps, while the latter component likely corresponds to particles that are either isolated or in strings. After five minutes of dilution, the component with positive anisotropy dominates the spectrum (Figure 3-5).

The spectrum of untreated cells of *mnm13* is not markedly different from that of wild-type AMB-1 (Figure 3-5b). Although the empirical asymmetry parameter A for *mnm13* reflects a lesser degree of asymmetry than the wild-type, this represents a failure of the empirical parameter; the fitted spectra reveal that *mnm13* in fact has a somewhat stronger anisotropy field than the wild-type, which reflects the particle elongation. The wild-type has a fitted B_{an} of 69 mT, corresponding to a length-to-width ratio of ~ 1.35 , while *mnm13* has a fitted B_{an} of 91 mT, corresponding to a length-to-width ratio of ~ 1.50 . As with MV-1, the ratio calculated for the wild-type exceeds the value observed under TEM for individual particles, likely due to the effect of the chain structure in increasing B_{an} . In contrast, the ratio calculated for *mnm13* corresponds to that observed under TEM.

Both sonication and lysis with SDS cause a slight increase in the fitted anisotropy field of *mnm13*, which may reflect the formation of short strings of particles. In contrast, while sonication has only slight effect on the wild-type, treatment of the wild-type with SDS leads to a broader spectrum that is best fit by a two-component model in which 61% of particles have positive anisotropy ($B_{an} = 87$ mT) and 39% have negative anisotropy ($B_{an} = -171$ mT). The latter component may reflect clumping. The absence of clumps in SDS-treated *mnm13* suggests that the greater diluteness of the particles prevents them from clumping.

The mutant *mnm18* has an extremely distinctive spectrum (Figure 3-5c). It is the only untreated magnetotactic bacterium measured so far that has $A > 1$, which reflects the negative magnetocrystalline anisotropy of isolated particles of equidimensional magnetite. It provides the best example of a spectrum that can be fitted as a mixture, as it is the mixture of two components with clear physical interpretations corresponding to TEM observations. The intact *mnm18* is a mixture composed 70% of a component with negative anisotropy ($B_{an} = -47$ mT) and 30% of a positive anisotropy component with parameters closely resembling those of the wild-type ($B_{an} = 76$ mT). From the FMR data, we can predict that,

by volume, the sample consists 70% of isolated crystals and 30% of chains of at least 2 crystals in length. These proportions are in close agreement with the values (65% and 35%) estimated from the TEM images, which confirms the proposal by WEISS et al. (2004a) that the uniquely asymmetric FMR spectrum of magnetotactic bacteria results primarily from the alignment of crystals in chains. We can also use this composition to unmix the isolated crystals from the other rock magnetic parameters, taking the properties of the wild-type to represent those of the fraction in chains.

The isolated component has a narrower Gaussian linewidth ($\sigma = 20$ mT) than is typical of most magnetotactic bacteria, which may reflect that lesser degree of heterogeneity possible with isolated crystals than with arrangements of crystals. The anisotropy measured for isolated crystals of *mmm18* is slightly less than that expected for isolated crystals of stoichiometric magnetite dominated by cubic anisotropy, which would have B_{an} of about -56 mT. The reduced anisotropy constant ($K_1 \approx 1.1 \times 10^4$ J/m³) may result from minor non-stoichiometry (~0.4% cation depletion) (KAKOL and HONIG, 1989), which is consistent with the reduced Verwey transition temperature of ~100 K observed in AMB-1 magnetite (Figure 3-6e) (MUXWORTHY and MCCLELLAN, 2000).

Sonication of *mmm18* cells leads to a slight increase in the proportion in chains, while treatment with SDS drastically alters the spectrum. SDS-treated cells of *mmm18* come to resemble those of the wild-type more closely, because the sample becomes dominated by short linear strings of particles, the anisotropy of which is controlled primarily by particle arrangement. The fitted spectrum consists 68% of a component with positive anisotropy ($B_{an} = 50$ mT) and 32% of a component with strong negative anisotropy ($B_{an} = -142$ mT) comparable to those of clumps formed in SDS treatment of wild-type AMB-1 and MV-1. Thus, the comparison of the unmixed components of intact and SDS-treated *mmm18* provides powerful insight into the role of chain formation in controlling the magnetic properties of magnetotactic bacteria.

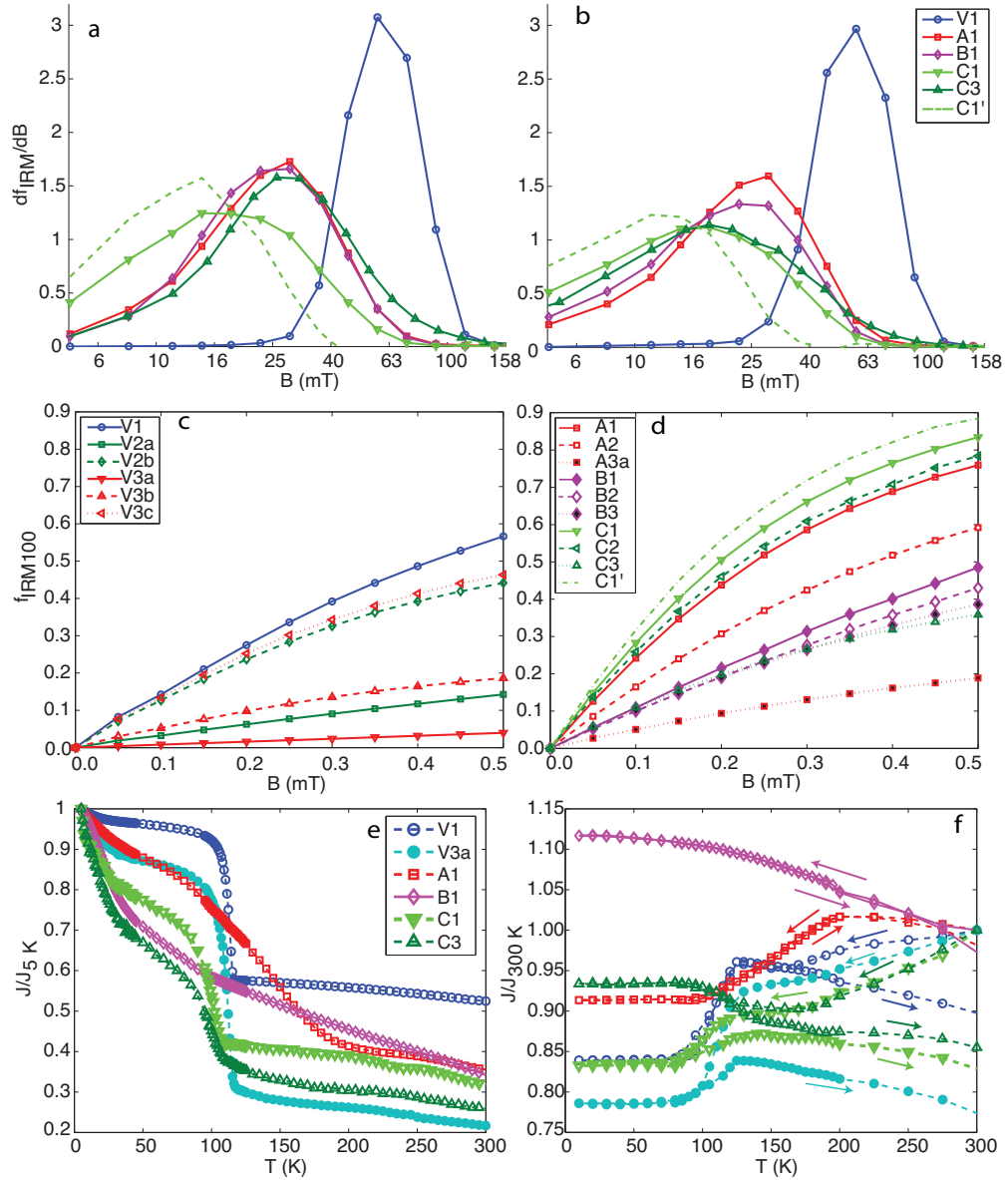


Figure 3-6: Rock magnetic measures of selected samples. (a-b) Coercivity spectra determined from (a) stepwise IRM acquisition and (b) stepwise AF demagnetization of IRM. The dashed line C1' in (a), (b), and (d) indicates the unmixed isolated particle component of C1, produced using the proportions of isolated and chain components determined from the FMR spectra to remove the chain component. (c-d) ARM acquisition curves of (c) MV-1 and (d) AMB-1 wild-type and mutants. (e-f) Low-temperature demagnetization curves. (e) shows the demagnetization upon warming of a magnetization acquired by saturation at 5 K of samples cooled in a 3 T field. Magnetization values are shown normalized to the magnetization at 5 K. (f) shows the demagnetization upon cooling and subsequent warming of a magnetization acquired by saturation at 300 K. Magnetization values are shown normalized to the initial room-temperature magnetization.

3.4.3 Isothermal remanent magnetization

The room-temperature IRM acquisition coercivity spectra for cells of wild-type AMB-1 and MV-1, regardless of treatment, agree in general shape, though not in precise parameterization, with the biogenic soft and biogenic hard components recognized by EGLI (2004a) (Figure 3-6a; Table 3-3). MV-1 has a narrow peak centered at a median field of 55 mT, while AMB-1 has a broader peak centered at 27 mT. The mutant *mnm13* is slightly softer than the wild-type (median field of 23 mT), which may be due to the smaller volume of *mnm13* particles. The mutant *mnm18* is both softer and has a broader spectrum than the other strains (median field of 16 mT). When FMR analyses and TEM observations are used to guide the unmixing of the chains and solitary particles in *mnm18*, the solitary particles are revealed to have a spectrum with a median coercive field of 11 mT. The drastic difference between the isolated, equidimensional particles produced by *mnm18* and the elongate particles of *mnm13*, as well as the chains of equidimensional particles in the wild-type cells, highlights the role of these traits in stabilizing the magnetic moments of magnetotactic bacteria.

Table 3-3. Room temperature rock magnetic parameters

Sample	H_{cr} (mT)	R	MAF of IRM (mT)	MDF of IRM (mT)	MDF of ARM (mT)	k_{ARM}/IRM (mm/A)	Predicted switching field (mT)
A1	24.0	0.44	26.5	21.6	22.2	2.93	30.3
A2	22.0	0.43	24.0	19.8	21.1	2.07	27.8
A3	16.6	0.29	24.1	10.2	17.4	0.64	59.8
B1	21.3	0.42	23.4	19.3	19.3	1.37	31.0
B2	23.9	0.42	26.6	22.2	22.3	1.26	35.7
B3	26.0	0.39	30.7	21.8	24.2	1.29	38.2
C1	14.5	0.47	15.7	13.8	13.7	3.55	26.7
C1'	10.7	0.44	10.6	9.9	10.5	3.99	22.3
C2	14.7	0.44	16.6	13.8	13.8	3.25	24.4
C3	21.7	0.35	26.7	16.6	21.9	1.38	39.8
V1	57.8	0.42	55.3	61.2	65.8	1.79	82.9
V2a	55.1	0.27	63.3	45.9	58.1	0.41	82.8
V2b	48.4	0.31	55.0	41.7	49.8	1.59	80.2
V3a	28.4	0.14	43.2	17.0	24.7	0.10	73.8
V3b	n.d.	n.d.	n.d.	n.d.	52.7	0.66	67.2
V3c	52.3	0.34	52.5	46.5	56.3	1.68	71.6

C1' is the unmixed end member of C1 composed of isolated particles. Step-wise IRM curves were not measured for V3b. Predicted switching field is calculated from the FMR fit parameters as described in the text.

For all samples of unlysed cells of AMB-1, both wild-type and mutant, acquisition and demagnetization curves align fairly closely (Figure 3-6, a and b); Cisowski R values are all ≥ 0.42 , and the median destructive field falls within 5 mT of the median acquisition field. This is not the case for the SDS-treated mutants and both the SDS-treated and the ultrasonicated wild-types, which reflects greater interparticle magnetostatic interactions in the wild-types than in the mutants. Notably, the IRM acquisition curve of SDS-treated *mnm18* closely resembles that of the wild-type (median field of 27 mT), while the demagnetization curve remains closer to that of the untreated *mnm18*. As FMR data indicate the formation of linear strings of particle in the SDS-treated *mnm18*, the observation may suggest that IRM acquisition coercivity is more strongly affected by chain structures than is demagnetization coercivity.

3.4.4 Anhyseritic remanent magnetization

The ARM acquisition curves for wild-type AMB-1 and MV-1 are consistent with previous measurements (MOSKOWITZ et al., 1993; MOSKOWITZ et al., 1988) (Figure 3-6, c and d; Table 3-3). MV-1 has markedly lower anhyseritic susceptibility than AMB-1. Two factors likely contribute to this difference. First, as seen in the TEM images, untreated MV-1 has undergone a greater degree of chain collapse than untreated AMB-1, due to the intrinsic instability of chains of elongate particles. The increased three-dimensional magnetostatic interactions in collapsed chains serve to lower ARM susceptibility. Second, elongate particles have a higher switching field and thus lower intrinsic ARM susceptibility than more equidimensional particles of the same volume (see Figure 1 of EGLI, 2003).

The pattern of variation of ARM susceptibility of lysed MV-1 shows some notable differences from parallel experiments previously reported for AMB-1 (see Chapter 2). For both strains, ultrasonicated bacteria exhibit a lower susceptibility than untreated bacteria and a higher susceptibility than SDS-treated bacteria. But whereas dilution of ultrasonicated AMB-1 produced little change in ARM susceptibility, dilution of ultrasonicated MV-1 produces significant change. Undiluted ultrasonicated MV-1 exhibits a similar susceptibility to SDS-treated MV-1 diluted for 1 minute, and ultrasonicated MV-1 diluted for 4 minutes

exhibits a similar susceptibility to SDS-treated MV-1 diluted for five minutes. The difference between the strains again likely reflects differences in collapse style between equidimensional particles and elongate particles; the strings produced by ultrasonication of AMB-1 are less likely to be reconfigured during dilution than the meshes produced by ultrasonication of MV-1.

The crystals produced by *mmm13* have even lower anhysteritic susceptibility than MV-1, a reflection of the combined influence of their elongation and their smaller size. In fact, their ARM susceptibility lies significantly above what would be predicted based on TEM measurements. EGLI and LOWRIE (2002) calculate that a particle with a length-to-width ratio of 1.9 and a cube root of volume of ~ 20 nm should have a k_{ARM}/IRM ratio of about 0.5 mm/A, whereas the measured value is 1.4 mm/A. Given the measured median destructive field, the ARM susceptibility measured would be expected for particles with a length of 45 nm and a length-to-width ratio of 1.3.

The isolated particles in untreated cells of *mmm18* produce one of the highest ARM susceptibilities that we have ever observed. With a k_{ARM}/IRM of 4.0 mm/A, they lie among the highest sediment values tabulated by EGLI (2004a), and above previously measured magnetotactic bacteria (MOSKOWITZ et al., 1993). Given the similarity of the crystals produced by *mmm18* to those produced by the wild-type, the high k_{ARM}/IRM is likely due to the absence of magnetostatic interactions. Although they have less effect than three-dimensional interactions, even the linear interactions in wild-type AMB-1 appear to lower ARM susceptibility slightly.

At biasing fields below 300 μ T, the ARM/IRM curves of ultrasonicated *mmm13* (B2), SDS-treated *mmm13* (B3), and SDS-treated *mmm18* (C3) are almost identical, whereas above 300 μ T they diverge, with $B2 > B3 > C3$. The divergence may reflect the presence of a greater proportion of more strongly interacting particles (which acquire ARM in higher biasing fields) in the more severely treated samples.

Table 3-4. Low temperature magnetic properties

Sample	δ_{ZFC}	δ_{FC}/δ_{ZFC}	f_{LTC}
A1	0.13	2.53	0.98
B1	0.17	1.07	0.97
C1	0.16	2.57	0.83
C3	0.35	1.24	0.86
V1	0.29	1.40	0.90
V2a	0.29	1.42	0.94
V3a	0.61	1.10	0.77

3.4.5 Low-temperature magnetic properties

Regardless of treatment, the MV-1 samples have low δ_{FC}/δ_{ZFC} : The untreated and ultrasonicated samples have δ_{FC}/δ_{ZFC} of 1.4, while the SDS-treated MV-1 has δ_{FC}/δ_{ZFC} of 1.1 (Figure 3-6e; Table 3-4). Based on the criterion of MOSKOWITZ et al. (1993), $\delta_{FC}/\delta_{ZFC} > 2$ indicates the presence of chains. The reason why our untreated MV-1 fails this test is unclear, although such low values have previously been observed for some fresh cultures of MV-1 (B. Moskowitz, pers. comm.). The low values may be related to the partial chain collapse previously described, but they stand in contrast to FMR data indicating the presence of chains. They are not a product of accidental sample oxidation; the absolute values of δ_{FC} and δ_{ZFC} are relatively large.

The untreated cells of mutant *mnm13* fail the Moskowitz test, with $\delta_{FC}/\delta_{ZFC} = 1.9$, consistent with the absence of chains in this sample. Inspection of its low-temperature demagnetization curves indicates that the sample's low-temperature properties are dominated by the unblocking of superparamagnetic grains, in agreement with the smaller grain size observed in the TEM images. In contrast, the untreated cells of *mnm18* have $\delta_{FC}/\delta_{ZFC} = 2.6$, which slightly exceeds the wild-type value of 2.5 even though less than half of the crystals present are in chains. The unexpected result cannot be explained by non-stoichiometry, which would increase δ_{FC}/δ_{ZFC} while at the same time decreasing δ_{FC} and δ_{ZFC} (CARTER-STIGLITZ et al., 2004). No such drop in δ_{FC} and δ_{ZFC} is observed. Furthermore, whereas SDS-treatment of *mnm18* produces an FMR spectrum reflecting the presence of linear particle arrangements, it also causes δ_{FC}/δ_{ZFC} to drop to 1.2, comparable to the SDS-

treated wild-type (see Chapter 2). The elevated δ_{FC}/δ_{ZFC} ratios of *mmm18* may occur because the chain component within the sample has a higher δ_{FC}/δ_{ZFC} than the wild-type AMB-1 that we measured; previously observed δ_{FC}/δ_{ZFC} ratios for AMB-1 range as high as 5.9 (WEISS et al., 2004a). Alternatively, the distinctive δ_{FC}/δ_{ZFC} ratios of magnetotactic bacteria may be due, at least in part, to some factor other than chain structure and non-stoichiometry.

Consistent with prior measurements of wild-type AMB-1, reported in Chapter 2, SDS-treated *mmm18* exhibits an increase in remanence on cooling through the Verwey temperature, while intact *mmm18* exhibits a decrease in remanence. In contrast, both intact and SDS-treated MV-1, like intact AMB-1, exhibit a decrease in remanence upon cooling through the Verwey transition (Figure 3-6f). We have no explanation for this phenomenon.

3.5 Discussion

As measures of magnetic anisotropy and magnetostatic interaction, FMR parameters should be related to other magnetic properties that are a function of these characteristics. In so far as it is possible to fit spectra well and thus obtain an accurate measurement of the anisotropy field of a sample, it is possible to use FMR spectra to estimate the switching field distribution of a sample. Neglecting thermal energy, the median coercive field of a sample is given by $B_c \approx \frac{1}{2} |B_{an} (1 + K_2/K_1)|$ (DUNLOP and ÖZDEMİR, 1997). A plot of the calculated B_c against the median acquisition field of IRM acquisition is shown in Figure 3-7a.

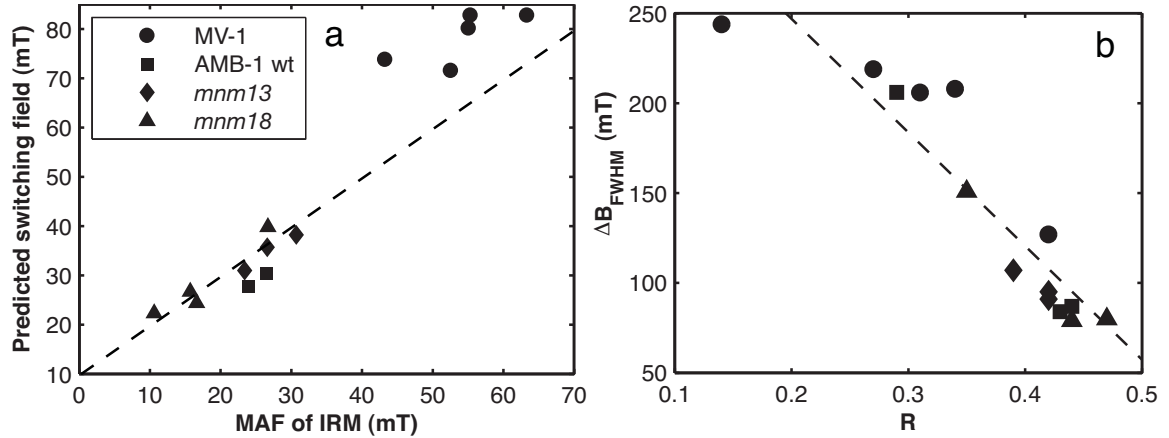


Figure 3-7: FMR parameters compared to rock magnetic parameters for the samples discussed in this paper. (a) Predicted switching field, determined from the weighted average of B_c of fit components for each sample, plotted against the median acquisition field of IRM. The dashed line represents a line fitted through the points for *mnm13* and *mnm18* with slope fixed at 1. The line has a y-intercept of 9.7 mT and a coefficient of determination $r^2 = 0.89$. (b) ΔB_{FWHM} plotted against the Cisowski R parameter, which measures magnetostatic interactions. The dashed line represents a line fitted to all samples and is given by $\Delta B_{FWHM} = 373 \text{ mT} - 632 \text{ mT} \times R$. It has a coefficient of determination $r^2 = 0.84$.

There is a good correlation between the two parameters, although the estimates derived from the FMR spectra are significantly higher than the measured values. The discrepancy is largely accounted for by the thermal fluctuation field, which for 100 nm cubes of magnetite at room temperature is approximately $50\sqrt{B_c}$, or about 10 mT for particles with $B_c = 30$ mT (DUNLOP and ÖZDEMİR, 1997). Linear regression of the B_c values for *mnm13* and *mnm18*, with the slope of the line fixed at 1 because of the expected theoretical relationship between B_c and MAF, yields the line $B_c = \text{MAF} + 9.7 \text{ mT}$, with a coefficient of determination $r^2 = 0.89$. Removing the constraint on the slope does not significantly improve the fit. The y-intercept thus calculated is in agreement with the expected thermal fluctuation field.

Cells of mutant AMB-1 and intact cells of wild-type AMB-1 have B_c close to those predicted from the regression line, but SDS-treated cells of AMB-1 and all MV-1 samples fall well off the line. This difference may be due to a combination of imperfect fitting of the

FMR spectra and the presence of additional factors not treated in the simple physical model used to predict B_c .

There is no single parameter that perfectly reflects interaction field strength (DUNLOP et al., 1990), but the crossover R value of CISOWSKI (1981) is commonly used. The strength of three-dimensional magnetostatic interactions affects two parameters employed in modeling FMR spectra: the anisotropy field B_{an} and the Gaussian linewidth σ . Local anisotropy in magnetostatic interactions, such as that which occurs on the surface of a clump of particles, alters the anisotropy field, while the heterogeneity of local magnetic environments produced by interactions results in an increase in Gaussian linewidth. Other factors also contribute to both these terms, however, so neither provides a good measure of interaction field strength. The empirical linewidth parameter ΔB_{FWHM} appears to provide a better measure, as it correlates reasonably well with the Cisowski R parameter (Figure 3-7b). Linear regression yields the relationship $\Delta B_{FWHM} = 373 \text{ mT} - 632 \text{ mT} \times R$, with a coefficient of determination $r^2 = 0.84$. When present, strong three-dimensional interactions overwhelm other factors controlling ΔB_{FWHM} , such as single-particle anisotropy and linear interactions.

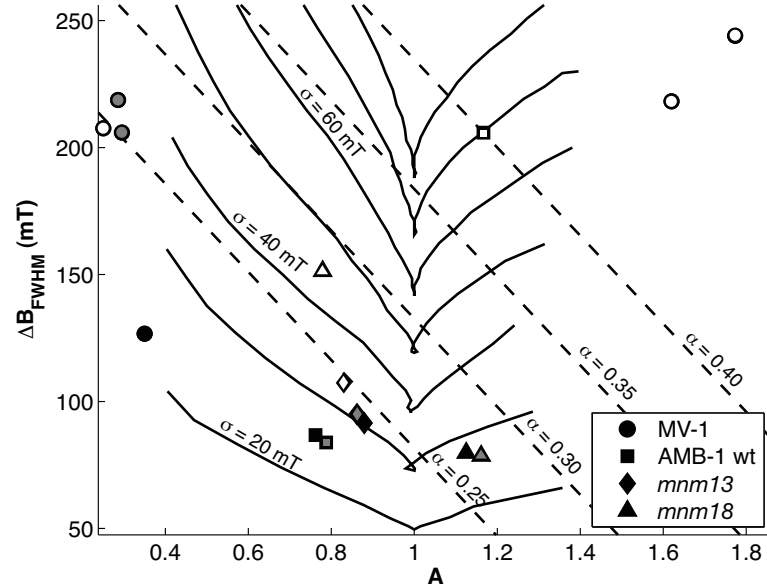


Figure 3-8: Plot of ΔB_{FWHM} against A for the samples discussed in this paper. Solid symbols represent untreated samples, symbols with grey interiors represent ultrasonicated samples, and samples with white interiors represent SDS-treated samples. The dilution trend for ultrasonicated MV-1 goes slightly from the upper-left to the bottom-right, while the dilution trend for SDS-treated MV-1 goes from right to left. Dashed lines are contours of constant values of α . Solid lines represent simulated spectra with fixed Gaussian linewidth σ and variable B_{an} .

The bacterial samples measured in this work continue to support the use of the empirical discriminant factor α (see Chapter 2) to distinguish biogenic magnetite chains (Figure 3-8). Of all the intact cells of magnetotactic bacteria we measured, only those of the mutant *mnm18* have $\alpha > 0.24$. This exception arises because *mnm18* has $A > 1$ and, while α serves as a proxy for Gaussian linewidth σ when σ is around 30 mT and $A < 1$, it does not when $A > 1$, as can be seen from the α contours plotted on Figure 3-8. As can be seen on Figure 3-8, *mnm18* falls within the domain of intact magnetotactic bacterial cells when σ values of synthetic spectra are used to delineate boundaries.

Ultrasonication in general results in a slight increase in α , which confirms prior results (see Chapter 2). SDS treatments of the wild-type cells of both MV-1 and AMB-1 result in drastic shifts in α as highly interacting clumps come to dominate the sample. The increase in α that occurs with SDS-treatment of cells of the AMB-1 mutants, in which the magnetite is more dilute, is present but subtle. SDS-treated cells of both wild-type strains, when

diluted by mixing for five minutes, experience a significant reduction in α to values characteristic of the domain previously identified as being the magnetofossil domain, namely $\alpha < 0.30$ (see Chapter 2).

In agreement with the results of WEISS et al. (2004a) and Chapter 2, these data support the use of ferromagnetic resonance spectroscopy as a technique for identifying potential magnetofossils in the sedimentary record. Because it can provide a rapid way of estimating the biogenic contribution to sedimentary magnetism, FMR has the potential to be a highly useful tool for environmental magnetism and magnetic paleobiology.

3.6 Conclusion

We have generated mutant strains of magnetotactic bacteria that allow us to start to untangle the contributions of chain arrangement and particle elongation to the ferromagnetic resonance and rock magnetic properties of magnetotactic bacteria. The four strains we have analyzed represent all four possible combinations of chain and solitary particles, and elongate and equidimensional particles. In addition, the SDS-treated cells of *mmm18* allow us to investigate the changes that occur as solitary equidimensional particles assemble into linear structures. Our findings indicate that ferromagnetic resonance spectroscopy provides an effective technique for estimating the switching field distribution and interaction effects within a sample and continue to support the use of ferromagnetic resonance spectroscopy as a way of identifying magnetotactic bacteria and magnetofossils. Since it takes only a few minutes to acquire a FMR spectrum, which is significantly faster than most rock magnetic techniques being used for similar purposes, we hope that our work will spur the broader adoption of ferromagnetic resonance spectroscopy by the rock magnetic community.

3.7 Selected notation

FMR: Empirical Parameters

A	Asymmetry ratio = $\Delta B_{high}/\Delta B_{low}$
B_{eff}	Applied field at peak of integrated absorption spectrum, mT
ΔB_{FWHM}	Full-width at half-maximum, $\Delta B_{high} + \Delta B_{low}$
ΔB_{high} (ΔB_{low})	Half-width at half-maximum of integrated spectrum on high-field (low-field) side of peak, mT
g_{eff}	g value at absorption peak, $h\nu/\beta B_{eff}$
α	Empirical discriminant factor, $0.17 A + 9.8 \times 10^{-4} \text{ mT}^{-1} \cdot \Delta B_{FWHM}$

FMR: Physical Parameters

B_{an}	Effective anisotropy field: $2K_1/M$ for magnetocrystalline anisotropy, $\mu_0 M_s \Delta N$ for shape anisotropy
g	True spectroscopic g -factor (equivalent to g_{eff} when $B_{an} = 0$)
K_2/K_1	Ratio of second-order and first-order anisotropy constants
σ	Standard deviation of Gaussian broadening function

Rock magnetic parameters

H_{cr}	Coercivity of remanence, determined here from intersection point of IRM acquisition and demagnetization curves, mT
f_{LTC}	Fraction of room-temperature SIRM retained after cycling to low temperature and back
k_{ARM}/IRM	ARM susceptibility normalized to IRM (measured here with 0.1 mT ARM biasing field, 100 mT ARM alternating field, and 100 mT IRM pulse field), mm/A
MAF (MDF)	Median acquisition (destructive) fields, at which half of a total remanence is acquired (destroyed), mT
R	Cisowski R parameter, reflecting magnetostatic interactions: fraction of IRM remaining at H_{cr}
δ_{FC} (δ_{ZFC})	$(J_{80K} - J_{150K})/J_{80K}$ for field-cooled (zero-field-cooled) low-temperature SIRM thermal demagnetization curves

*Chapter 4*SEDIMENTARY IRON CYCLING AND THE ORIGIN AND PRESERVATION OF
MAGNETIZATION IN PLATFORM CARBONATE MUDS, ANDROS ISLAND,
BAHAMAS***4.1 Introduction**

Like all sediments, platform carbonates provide, in their stratigraphy and sedimentology, a local record of changing environmental conditions. However, as chemical sediments, carbonates also carry a record of regional and global ocean chemistry and biogeochemical cycling.

Coupling the environmental and geochemical record available in carbonates to paleomagnetic data places proxy data in a richer global context by providing paleolatitude information, and enabling paleogeographic reconstructions and magnetostratigraphic correlations. In the Neoproterozoic (~800 Ma) Akademikerbreen Group of Svalbard, Norway, for instance, stratigraphic, geochemical and paleomagnetic data from platform carbonate sediments provide the best evidence to date for rapid true polar wander (MALOOF et al., 2006). Coupled measurements also provide a way of studying the influence of climate on sedimentary magnetism (EVANS and HELLER, 2003), as well as testing hypotheses about the influence of geomagnetic intensity on climate (COURTILLOT et al., 2007).

Where clastic input is low, carbonate platform sediments are often magnetically weak and extraction of their primary paleomagnetic signals requires special care (MALOOF et al., 2006; MCNEILL, 1997; MONTGOMERY et al., 1998). In the absence of significant clastic flux, iron cycling in the stratigraphic column should leave a strong imprint on sediment magnetic properties. Processes expected to be important in the iron cycle include the production of magnetite and iron sulfides as a byproduct of bacterial metabolism, the reductive dissolution of magnetic particles by iron-reducing bacteria, and the intracellular

* Co-authored with Adam C. Maloof, John P. Grotzinger, David A. Fike, Tanja Bosak, Hojotollah Vali, Pascale M. Poussart, Benjamin P. Weiss, and Joseph L. Kirschvink.

precipitation of magnetite and greigite by magnetotactic bacteria (BAZYLINSKI et al., 1994; SAKAGUCHI et al., 2002; SIMMONS et al., 2004). Fossil magnetotactic bacteria, called magnetofossils, have previously been identified as a major magnetic constituent in sediments in Holocene (e.g., KIRSCHVINK and CHANG, 1984; MCNEILL, 1990), Neogene (e.g., MCNEILL et al., 1988; SAKAI and JIGE, 2006), Cretaceous (MONTGOMERY et al., 1998), and perhaps older (BELKAALLOUL and AISSAOUI, 1997; CHANG and KIRSCHVINK, 1989; CHANG et al., 1989) shallow marine carbonates.

Prior studies of primary magnetic remanence preservation in platform carbonates have focused on (1) the consequences of dolomitization in subtidally-deposited Neogene rocks from cores through the Bahamas platform (MCNEILL, 1997; MCNEILL et al., 1988; MCNEILL and KIRSCHVINK, 1993) and (2) secondary magnetite growth in orogenic pore fluids in Lower Paleozoic carbonates of the midcontinental United States (JACKSON, 1990; JACKSON et al., 1992; MCCABE and ELMORE, 1989; MCCABE et al., 1989; MCCABE et al., 1983; VAN DER VOO, 1989). The interpretation of magnetic records in ancient carbonates would be strengthened by a detailed understanding of the sedimentary iron cycle and its role in altering magnetic mineralogy during early diagenesis. Furthermore, understanding the relationship between sedimentological sequences and magnetism could provide a magnetic signature useful for the interpretation of cyclostratigraphy. In this paper we present sedimentological, geochemical, magnetic, and ferromagnetic resonance analyses of carbonates from a Recent shoaling-upward subtidal-to-supertidal parasequence in the Triple Goose Creek region of northwest Andros Island, Bahamas, and evaluate the origin and preservation of primary magnetic remanence.

4.2 Geological Setting

The Bahamas archipelago is a carbonate depositional environment consisting of several isolated platforms at the southern extremity of North America's eastern continental margin. Andros is the largest island in the Bahamas, located on the raised eastern rim of the western half of the Great Bahama Bank, and bounded by seaways to the east (Tongue of the Ocean) and west (Straits of Florida). The positive relief of Andros island is composed of Pleistocene carbonate dunes overlying karsted and cemented coral reef (Figure 4-1).

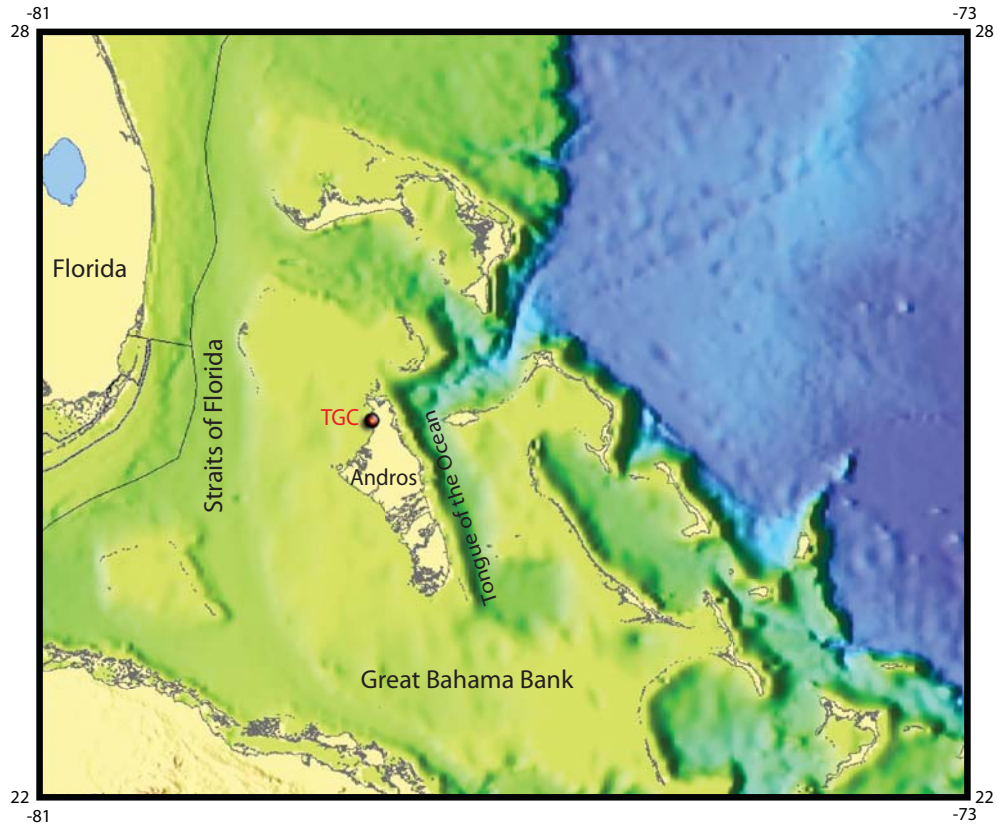


Figure 4-1: Bathymetry of the Great Bahama Bank from NOAA's ETOPO2 (USGS CMG InfoBank Atlas). TGC-Triple Goose Creek

Andros Island has a tropical-maritime climate, with wet summers, dry winters, and fairly uniform monthly average temperatures of $\sim 25^{\circ}\text{C}$ (HARDIE, 1977). Annual average rainfall is ~ 130 cm/yr (HARDIE, 1977), making Andros significantly wetter than other Holocene carbonate platforms such as Abu Dhabi (annual average rainfall ~ 12 cm/yr). Prevailing northeasterly trade winds are strongest and most variable in the winter, and often dominate the semi-diurnal lunar-solar tide.

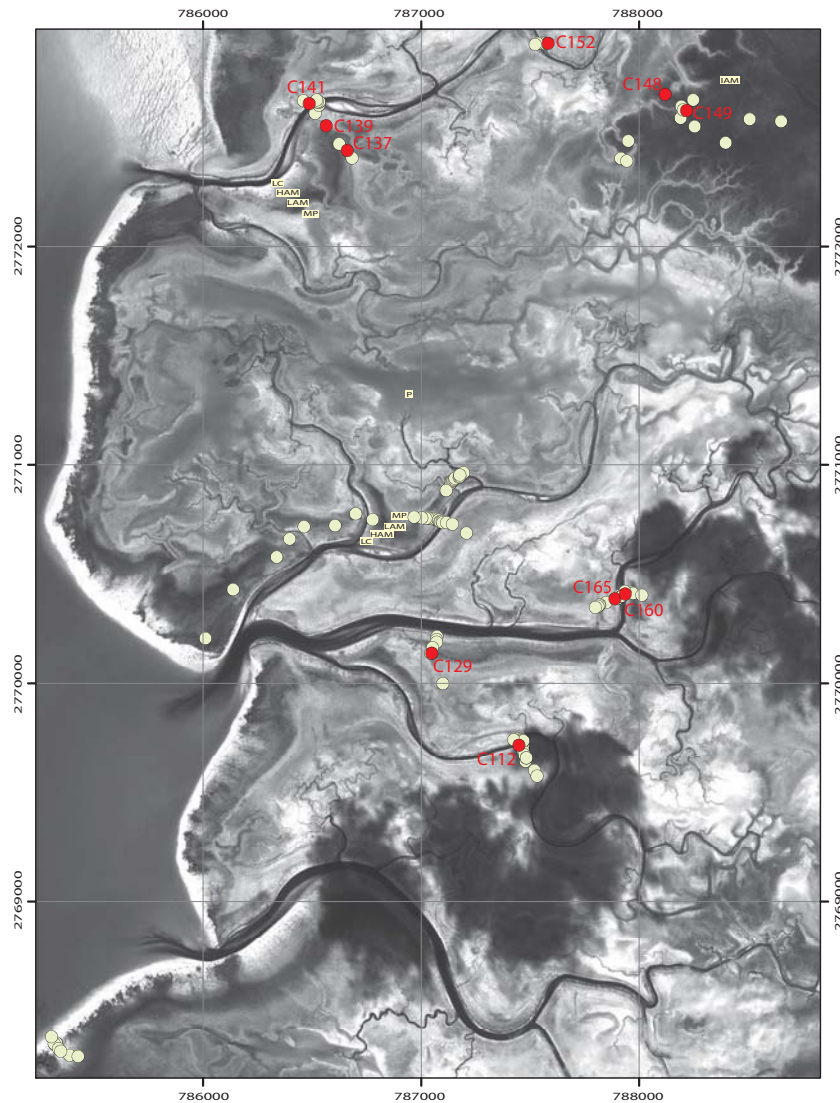


Figure 4-2: Panchromatic Quickbird image of Triple Goose Creek. Core locations are marked with light green circles. Sample locations are marked with red circles and red labels. Some characteristic geobiological facies are labeled (LC-levee crest, HAM-high algal marsh, LAM-low algal marsh, MP-shallow mangrove pond, P-deep pond, IAM-inland algal marsh).

Triple Goose Creek (TGC) is located on the northwestern edge of Andros Island (Figure 4-1). TGC has long captured the imaginations of carbonate sedimentologists because it is a rare Holocene example of a wet carbonate platform with a well-developed intertidal zone characterized by meandering channels (Figure 4-2). Virtually all carbonate sediment

delivered to the intertidal and supratidal zones of TGC is derived from aragonite-producing green algae such as *Halimeda*, *Penicillus* and *Udotea*. Without a fluvial flux of siliciclastic sediment, the only significant iron in the TGC system is derived from plumes of dust originating in Saharan West Africa (MOORE et al., 2002).

SHINN et al. (1969) and HARDIE (1977) first documented the major physiographic elements of TGC. On the landward eastern side, a flat, mostly supratidal 3–8 km wide inland algal marsh (IAM) is characterized by luxuriant *Scytonema* filamentous cyanobacterial mat communities and desiccated carbonate mud flats left by hurricane surges. The stratigraphic thickness of Holocene mud increases seaward, from emergent cemented Pleistocene dune sands in the east to 1 m of Holocene mud along the western fringe of the IAM.

A central intertidal zone, 1–4 km wide, is characterized by tidal channels with bars and, from high elevation to low elevation, levee crests (LC), high (HAM) and low (LAM) algal marshes on the levee backslopes, and shallow mangrove ponds (MP). The LCs are draped with thin mats formed by filamentous *Schizothrix* cyanobacteria, display a low diversity of grasses, and are rarely bioturbated. LCs are rippled and mudcracked when overbank silts and sands accumulate on the mats after large tides. HAMs and LAMs are dominated by *Scytonema* mats, have a higher diversity of grasses and a greater abundance of mangroves, and are only weakly bioturbated by *Marphysa* worms. MPs contain abundant mangroves and are colonized by a low diversity assemblage of *Cerithid* gastropods, *Geloina* bivalves, *Peneroplis* foraminifera, and burrowing worms and crabs. The stratigraphic thickness of Holocene mud in this belt ranges from 1 m on the landward edge to 2.5 m at the beach. Radiocarbon ages from foraminifera tests from seven widely-spaced stratigraphic cores indicate that carbonate mud at TGC has accumulated over the last ~1000 years (MALOOF and GROTZINGER, in prep.).

The topographic relief that defines the geobiological zonation in the intertidal zone ranges from 0.5 m above mean tide level (MTL) for high LCs to 0.2 m above MTL for high MPs, to 0.5 m below MTL for some of the deeper ponds, to 1.5 m below MTL for some of the deeper channel bottoms. The mean high tide level (MHTL) corresponds approximately to the intersection between LAM facies and MP facies. Sediment above MHTL is nearly

always white and usually laminated, while sediment below MHTL is bioturbated and nearly always dark grey. The mean annual tidal range at TGC dampens quickly as the tidal wave flows up-channel, with tidal ranges of 46 cm at the channel mouths, 29 cm in the western ponds, 18 cm at 2–3 km up-channel, and ~0 cm at 4–5 km up-channel (HARDIE, 1977).

As part of a larger project studying the nature and time scale of channel migration in the intertidal zone of TGC (MALOOF and GROTZINGER, in prep.), we conducted five weeks of cm-scale topographic surveying coupled to surface geologic observations of sediment composition, sedimentary structures, and microbial and plant ecology. We also took more than 200 piston-cores (Figure 4-2) and developed a Holocene stratigraphy of TGC referenced to approximate MTL, as determined by observations of water level. All the geochemical, rock magnetic, and paleomagnetic samples we discuss in this paper were collected in the context of this larger topographic, geobiologic and stratigraphic survey and are presented here to demonstrate the role of sedimentary iron cycling in the origin and fidelity of magnetic remanence in peritidal carbonates.

4.3 Methods

4.3.1 Sample Collection

We took over 500 samples during two field seasons in March and December 2005. We collected oriented surface samples (upper 2 cm) by pressing open 7 cm³ plastic boxes (Natsuhara Gaiken, Osaka, Japan) vertically down into the mud until the boxes were full. The sharp edges of the boxes allowed us to retrieve undeformed samples. We oriented the samples using a magnetic compass and employed a sun compass to calculate local magnetic declination and check for orientation errors.

For subsurface samples, we extracted 5 cm diameter oriented cores ranging from 0.5–2.5 m in length using a stainless steel and aluminum Livingstone piston corer from the University of Minnesota Limnology laboratory. We kept vertical orientation marks on the corer aligned with an orientation mark on the ground surface. When we extruded each core, we used a plastic tool attached to the end of the corer to etch a line parallel to the orientation marks. Cores were sampled with respect to this orientation line using plastic boxes. Using this coring method, we were able to take consistently vertical cores, but azimuthal core

orientations were less reliable. We tape-sealed plastic boxes to prevent desiccation during transport, and kept samples refrigerated whenever possible.

We group cores based on the surface facies. Five cores were used for rock magnetic and FMR measurements: C129 (LAM), C139 (HAM), C149 (IAM), C160 (LC), and C165 (MP). Five cores were used for paleomagnetic measurements: C112 (MP), C137 (LAM), C141 (LC), C148 (IAM), and C152 (MP), along with subsamples of C160 and C165. C130 and C148 were studied in the field using microelectrodes. We measured the acid-insoluble fraction of C139 and C149 (see Figure 4-2 for core locations).

4.3.2 Geochemical measurements

Oxygen and hydrogen sulfide concentrations were determined using OX100 and H2S500 microelectrodes (Unisense, Aarhus, Denmark). The microelectrodes were calibrated following manufacturer's instructions using solutions of the same salinity and temperature as the porewaters examined (35‰ and ~29°C). For the oxygen microelectrode, we calibrated between an aerobic end member (vigorously aerated seawater at ambient temperature) and an anaerobic end-member (0.25 M NaCl, 0.1 M Na-ascorbate, and 0.1 M NaOH with tetrafluoroethane in the headspace). [O₂] for water saturated at 1 bar total pressure, 29°C, and ~35‰ salinity is 194 μM. The lower detection limit for [O₂] is ~2 μM. The sulfide microelectrode was calibrated using serial dilutions (1-100 μM) of a 1 mM stock solution of sodium sulfide. The stock solution was made in pH 2 buffer reduced by bubbling with tetrafluoroethane and the addition of 1 mM Ti(III)Cl. pH was measured with each sulfide measurement to convert measured H₂S to total sulfide (TS = H₂S + HS⁻ + S²⁻). In addition to C130 and C148, we made microelectrode measurements through ~3 cm of *Scytonema* mat near C130 and *Schizothrix*-bearing LC surface sediments.

The acid-insoluble fraction of sediments was determined by air-drying ~500-1500 mg of sediment, dissolving the sample by drop-wise addition of 6 N HCl, allowing the sample to sit for ~12 hours, centrifuging the remaining pellet of material and washing it twice, then air-drying the pellet and measuring its mass.

4.3.3 *Paleomagnetic and Rock Magnetic Measurements*

Paleomagnetic measurements and room-temperature rock magnetic experiments were conducted using a 2G SQUID Magnetometer equipped with in-line alternating field (AF) demagnetization coils, isothermal remanent magnetization (IRM) pulse coils, and an anhysteritic remanent magnetization (ARM) biasing field coil housed in a magnetically shielded room. Paleomagnetic measurements were made on samples in plastic core boxes. A subset was then subjected to three-axis AF demagnetization in logarithmic steps to a maximum field strength of 85 mT. Magnetic components were analyzed for each sample in Paleomag 3.1 (JONES, 2002) using principal component analysis (KIRSCHVINK, 1980b).

Rock magnetic experiments were conducted on ~300-500 mg of freeze-dried sediment powders in quartz glass EPR tubes using procedures described in Chapter 2. Starting with an AF-demagnetized sample, vertical ARMs were imparted in 100 mT alternating fields with DC biasing fields increased in 50 μ T steps up to 1 mT and then demagnetized. ARM susceptibility was determined from the ARM acquired in a 100 μ T biasing field. For comparison with the ARM, the sample was given an IRM in a 100 mT pulse field, and then demagnetized. Finally, the sample was given IRMs progressively up to 350 mT, and the final, nearly saturated IRM was demagnetized stepwise. To produce coercivity spectra from the stepwise IRM data, we take the derivative of moment with respect to the logarithm of the applied field.

We report the following parameters: IRM, determined at the maximum applied field strength of 350 mT; the coercivity of remanence B_{cr} and crossover interaction indicator R , determined from the intersection of the stepwise IRM acquisition and AF demagnetization curves (Cisowski:1981); and the ratio of ARM susceptibility to IRM measured in a 100 mT field, χ_{ARM}/IRM .

4.3.4 *Ferromagnetic resonance spectroscopy*

Ferromagnetic resonance (FMR) spectra were acquired from freeze-dried sediment samples using the technique described in Chapters 2 and 3. For all samples, enough powder was placed in the EPR tubes to fill the spectrometer sample cavity; thus, all absorption strengths measured are effectively normalized to volume. To summarize spectral characteristics, we

use the following empirical parameters of WEISS et al. (2004a): the effective g-factor of maximum absorption g_{eff} , the asymmetry ratio A , and the full-width at half-maximum ΔB_{FWHM} .

FMR spectra also carry information about electron paramagnetic resonance (EPR). Following CROOK et al. (2002), we assess the relative abundance of paramagnetic Fe(III) in different samples by measuring the height of the $g=4.3$ (~ 160 mT) peak above a baseline, which we approximated by linear interpolation between the 120 mT and 230 mT points in the derivative absorption spectra. To assess the relative abundance of Mn(II), we measure the height between the maximum and the minimum of the sixth line of the Mn(II) sextet.

To guide detailed interpretation of spectral shapes, we modeled the data as described in Chapter 3. To reduce the impact of paramagnetic components on the fits, we eliminated the Fe(III) peak by linear interpolation between 120 and 230 mT and smoothed out Mn(II) peaks and other narrow peaks using the robust LOWESS method (CLEVELAND, 1979) with a 30 mT window. Each fit component can be described by three parameters: the true g-factor g , the anisotropy field B_{an} , and a Gaussian broadening factor σ . Because of the complexity of natural samples, we used only components with first-order uniaxial anisotropy and varied the number of fit components. To determine whether we were reaching global or local fit optima, we also varied the initial fit parameters. Different initial parameters generally produced different fit optima, so we employ the fit solutions as qualitative guides to spectrum interpretation rather than as true indicators of underlying physical parameters.

4.3.5 *Electron microscopy*

Samples were prepared for analysis with a transmission electron microscope (TEM) using two methods. The first method involved separating magnetic materials with a strong magnet following the procedure of PETERSEN et al. (1986). Separates were transferred onto carbon film supported Cu TEM grids. In the second method, core samples were fixed with 2.5% glutaraldehyde in 0.1 M sodium cacodylate buffer and washed with 100% ethyl alcohol. Thin slices from the cores were embedded in epoxy resin to preserve biological components associated with magnetic material. Ultrathin sections (70-80 nm thick) were cut using a

diamond knife and transferred to carbon film supported Cu TEM grids (Valietal04). Samples were imaged and analyzed using a JEOL JEM-2000FX TEM with a Quartz XOne microanalytical system.

4.4 Results

4.4.1 Ferromagnetic resonance and rock magnetic data

Both IRM and total FMR absorption measure the total amount of ferromagnetic material in a sample. Variability in these parameters through a core reveals first-order changes in magnetic mineralogy. Changes in the ratio of IRM to FMR absorption reflect the differing sensitivities of the two techniques. IRM strength excludes particles with coercivities greater than the maximum applied field and, more importantly in these samples, superparamagnetic particles with an unblocking time shorter than the ~30 second measurement time. FMR, in contrast, detects particles with sub-nanosecond unblocking times, reflecting the 9.8 GHz frequency of the microwave source.

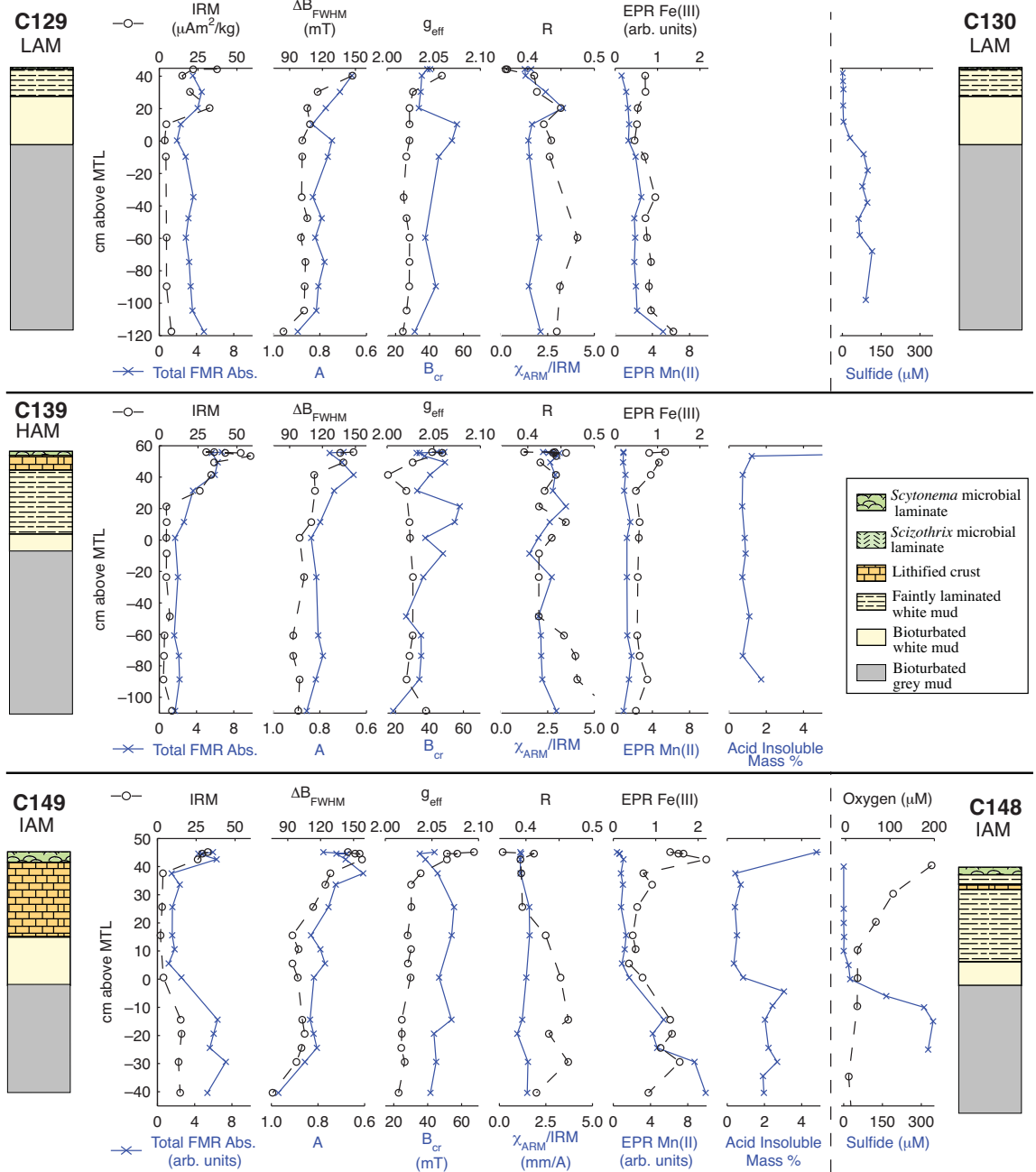


Figure 4-3: Stratigraphic columns and profiles of magnetic and ferromagnetic resonance parameters through algal marsh cores C129, C139, and C149, and microelectrode data from C130, adjacent to C129, and C148, near C149

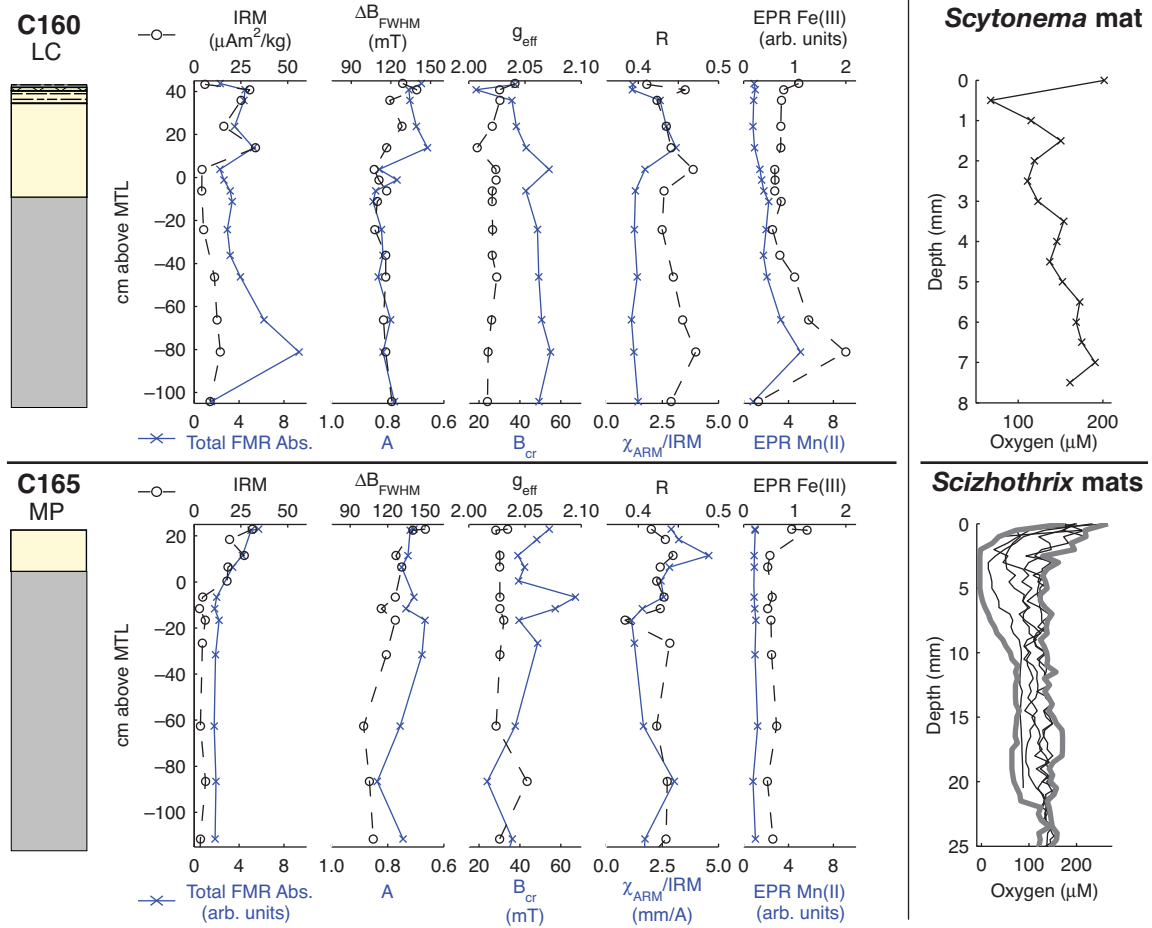


Figure 4-4: Stratigraphic columns and profiles of magnetic and ferromagnetic resonance parameters through levee crest core C160 and mangrove pond core C165, and mm-scale oxygen profiles through *Scytonema* and *Schizothrix* mats. The *Scytonema* profile was measured near C130. The *Schizothrix* profiles were measured at different patches of a single levee crest site. The thick grey lines in the *Schizothrix* plot represent the upper and lower bounds of measured oxygen levels. Facies legend as in Figure 4-3

All cores, regardless of facies, experience a significant decrease in ferromagnetic material at a depth near or above the mean tide level (Figure 4-3 and Figure 4-4). Above the drop-off, IRM strengths range from 15-53 $\mu\text{Am}^2/\text{kg}$, while below the drop-off, IRM plunges to 2-6 $\mu\text{Am}^2/\text{kg}$. Total FMR absorption also decreases at this transition, but by a lesser degree, which reflects an increase in the proportion of superparamagnetic and/or high coercivity particles.

In three of the five cores analyzed (C129, C149, and C160), all from algal marsh or levee crest facies, total FMR absorption and IRM strength exhibit a moderate increase in the

lower portion of the submerged and bioturbated depths of the cores. In C149 and C160, IRM reaches values of 11-16 $\mu\text{Am}^2/\text{kg}$. In C129, recovery in IRM is modest. In all three cores, the recovery is more pronounced in total FMR absorption, which reflects an IRM/FMR absorption ratio similar to or slightly higher than that in the magnetic minimum zone. The magnetic recovery is therefore fueled by a process that produces predominantly superparamagnetic grains.

In all cores, the magnetic drop-off coincides with a $\sim 10\text{-}20$ mT increase in B_{cr} , to $\sim 50\text{-}60$ mT. Despite the coercivity increase, coercivity remains too low to indicate a significant role for high-coercivity phases such as hematite or goethite. Rather, it suggests that the decrease in magnetization is due to a preferential loss of the lowest coercivity portion of the particles. As the change in IRM/FMR absorption ratios indicate that this loss occurs simultaneously with the precipitation of new superparamagnetic particles, the return to lower coercivity farther down core may reflect the growth of these new superparamagnetic particles into the low coercivity region of the single-domain field.

ARM/IRM ratios vary considerably between cores. In three of the cores (C129, C160, and C165), ARM/IRM ratios peak just above the magnetic drop-off. In C139, ARM/IRM ratios are high throughout, while in C149, they are more subdued.

Particulate Mn(II), presumably present as a constituent of carbonate and sulfide phases, is consistently low above the magnetic drop-off. Though the change in raw Mn(II) concentrations at the drop-off is generally slight, the drop-off itself produces a 2-3 fold increase in Mn(II)/Total FMR Absorption ratios. This enhanced Mn(II)/Absorption ratio remains nearly constant throughout the lower portion of the core, which suggests that the process producing a magnetic recovery in some of the cores is also producing particulate Mn(II). The precipitation of iron sulfide minerals, including the ferrimagnetic mineral greigite, with Mn(II) as a trace element is a likely candidate (ARAKAKI and MORSE, 1993).

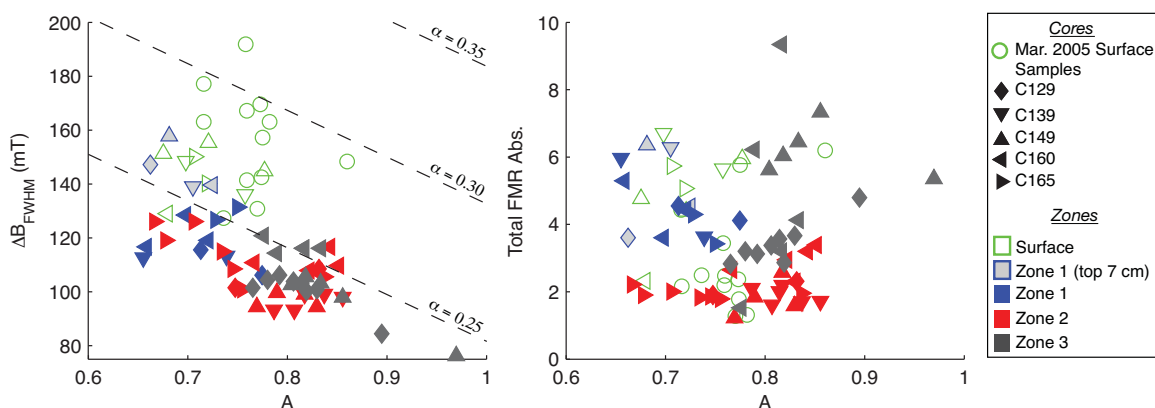


Figure 4-5: Crossplots of FMR spectral full-width at half-maximum (ΔB_{FWHM} , left) and total ferromagnetic resonance absorption (right) against the FMR asymmetry parameter A , defined as the ratio of the high-field half-width at half-maximum to the low-field half-width at half-maximum. Symbol shapes represent different cores, while colors represent sample depth, described with reference to the zones defined in the text. Dashed diagonal lines on the left plot contour constant values of the α parameter of Chapter 2. Depths of the zones in each core are shown in Figure 4-10.

For surface samples, the empirical FMR asymmetry parameter A and width parameter ΔB_{FWHM} define a broad field, with A from 0.68 to 0.86 and ΔB_{FWHM} from 129 to 191 mT (Figure 4-5). Samples from the top 7 cm of the cores fall at the low ΔB_{FWHM} end of this range, but almost all the surface samples have broader spectra than deeper core samples. Deeper samples fall in a more narrow field of ΔB_{FWHM} vs. A space, with samples from the oxic sediments above the magnetic drop off generally slightly broader and more asymmetric than deeper samples. The magnetically depleted samples span a fairly broad range of asymmetry values, while samples from the lower magnetically enriched zone are less asymmetric than those from the upper magnetically enriched zone and overlap with the less asymmetric samples from the magnetically depleted zone.

4.4.2 Geochemical Data

The formation of magnetic minerals in sediments is linked to stratigraphic redox gradients set by oxygen and sulfide. Oxygen microelectrode measurements taken in daylight at 500 μm intervals through *Scytonema* mats at the top of algal marsh sediments and *Schizothrix*-bearing laminated levee crest sediments indicate the presence of oxygen-depleted microenvironments within the uppermost sediments (Figure 4-4). In one example,

Schizothrix-bearing sediments became fully anoxic ($[O_2] < 5 \mu\text{M}$) 2 mm below the surface, while returning to only moderately depleted oxygen levels by 11 mm depth. Other transects through *Schizothrix*-bearing sediments in the same area found $[O_2] \geq 110 \mu\text{M}$ at all depths, which highlights the small-scale spatial variability. Our transect through a *Scytonema* mat found $[O_2]$ varying between ~ 70 and $\sim 200 \mu\text{M}$. We emphasize that all our measurements were taken during the day; at night, when photosynthetic oxygen production in the mats ceases, oxygen levels should be significantly lower (JØRGENSEN et al., 1979).

We performed microelectrode measurements of sulfide on C130, immediately adjacent to C129, and C148, located proximal to C149. We also made microelectrode O_2 measurements and litmus paper pH measurements of C148. In C130, sulfide concentrations are $< 1 \mu\text{M}$ in the upper 30 cm (> 12 cm above MTL), then increase between 12 cm above MTL and 8 cm below MTL to about $80 \mu\text{M}$. The concentration remains between 60 and $120 \mu\text{M}$ throughout the remainder of the core. The start of the increase in sulfide concentrations coincides with the magnetic drop-off in C129, while the stabilization of sulfide concentrations at high levels coincides with the magnetic recovery.

In C148, $[O_2]$ falls below $30 \mu\text{M}$ over the upper 20 cm (> 20 cm above MTL), while sulfide concentrations first exceed $10 \mu\text{M}$ at 5 cm above MTL and climb to values in excess of $200 \mu\text{M}$ by 10 cm below MTL. pH values are ~ 7.2 in the top 20 cm, fall to 7.0 between 25 and 30 cm, and stabilize around 7.5 farther down the core. These data suggest that the recovery of magnetization starting around MTL in C149 correlates with the onset of sulfidic conditions.

Due to absence of clastic materials, measurements of the fraction of sediment mass composed of acid-insoluble material provide estimates of the amount of organic matter. We measured the acid-insoluble fraction in sediments from two algal marsh cores: C149, which has a lower zone of relatively high magnetization, and C139, which does not. In both cores, the uppermost samples, containing visible mat material, were organic rich, consisting of 4–13% by mass acid-insoluble material. The amount of organic matter rapidly decays with depth, and is generally $< 1\%$ in C139 and in C149 above the lower zone of relatively high magnetization. In the lower zone of relatively high magnetization in C149, the acid-

insoluble content is 2–3% by weight. Throughout C149 and in C139 below 65 cm, mangrove root fragments are a visually identifiable component of the acid-insoluble fraction.

4.4.3 FMR and coercivity spectra

Component analysis of FMR and coercivity spectra help identify different major magnetic components in sediments. Both visual inspection and non-linear least squares fitting reveal the presence of two paramagnetic components and at least three ferromagnetic components in the FMR spectra of the carbonate muds (Figure 4-6). Two ferromagnetic components and both paramagnetic components are present in all samples; the third ferromagnetic component is present above the magnetic drop-off.

The two paramagnetic components are a singlet peak centered at $g = 4.3$ (~160 mT) and a complicated set of peaks between ~320 and ~380 mT, centered at $g = 2.00$. The peak at $g = 4.3$ represents paramagnetic Fe(III), likely present primarily in clay minerals. The set of peaks around $g = 2.00$ primarily represents Mn(II), although it may also include contributions from the singlet peaks of free radicals in organic carbon and free electron centers in carbonates.

A narrow, slightly high-field extended ferromagnetic component, centered at ~350 mT and with g_{eff} of ~1.99 and ΔB_{FWHM} of ~60 mT, is present in varying degrees in all spectra (Figure 4-6, comp. SP). It is generally possible to obtain well-constrained fit parameters for this component; typical best-fit parameters are $g = 1.97$, $B_{an} = -33$ mT, and $\sigma = 17$ mT. Anisotropy fields of this magnitude suggest room-temperature remanent coercivities less than 10 mT (see Chapter 3) and are consistent with those expected for very fine-grained, predominantly superparamagnetic, ferrimagnetic particles.

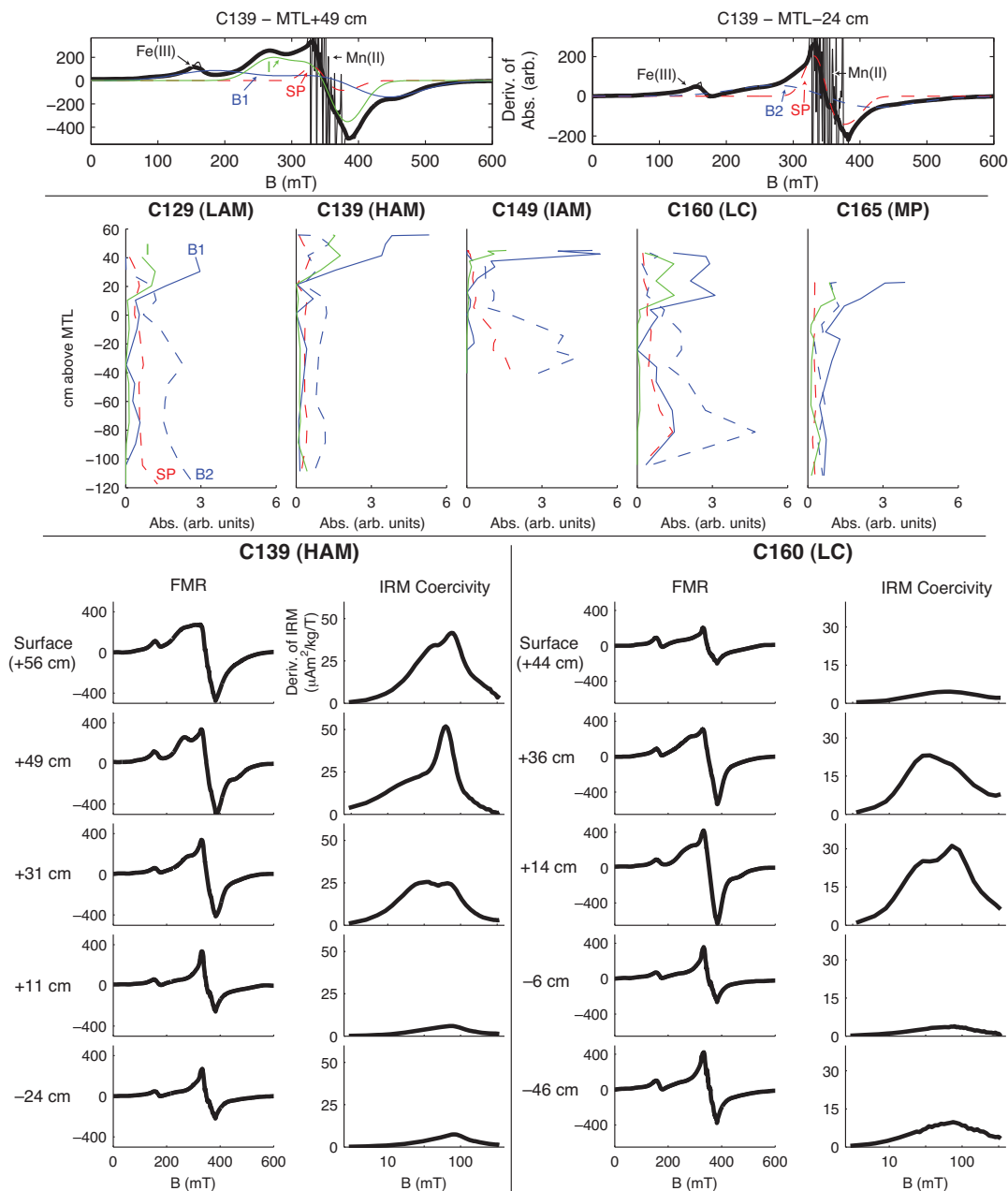


Figure 4-6: (Top) Smoothed (heavy line) and unsmoothed (thin line) FMR derivative absorption spectra for C139 samples from 49 cm above and 24 cm below MTL. Colored lines show fitted components: a narrow ferromagnetic peak associated with superparamagnetic particles (SP), an intermediate width component attributable to magnetotactic bacteria (I), a broad component with asymmetry suggesting a contribution from magnetotactic bacteria (B1), and a broad symmetric component (B2). Paramagnetic absorptions are also labeled. (Middle) Profiles showing approximate contributions of each component to total FMR absorption in each core, calculated by fitting each spectrum to a linear combination of end-members with spectral parameters fixed in the center of the range typical for each component. (Bottom) Selected FMR spectra and IRM acquisition coercivity spectra from cores C139 and C160

A broad ferromagnetic component, with ΔB_{FWHM} of ~ 200 mT and generally centered between ~ 330 and ~ 370 mT, is also present in varying degrees in all spectra. The nature of this broad component varies between samples, however. In samples taken above the magnetic drop-off, it is usually possible to obtain consistent fit parameters; typical values are $g = 2.15-2.25$, $B_{an} = 100-200$ mT, and $\sigma = 50-100$ mT (Figure 4-6, comp. B1). Thus, in the upper sediments, the broad component has a slight low-field extended asymmetry. This asymmetry suggests that elongate magnetite particles produced by magnetotactic bacteria may contribute to the broad signal (see Chapter 3). In contrast, the broad signal below the magnetic drop-off is more nearly symmetric and therefore consistent with ferrimagnetic particles capable of carrying a stable remanence and exhibiting only limited magnetostatic interactions (Figure 4-6, comp. B2). Typical fit parameters are $g = 1.90-2.10$, $|B_{an}| < 30$ mT, and $\sigma = 70-90$ mT.

A ferromagnetic component of intermediate width is usually present in sediments above the magnetic drop-off (Figure 4-6, comp. I). The intermediate component exhibits low-field extended asymmetry and ΔB_{FWHM} of ~ 100 mT. This component generally yields fit parameters with g between 2.05 and 2.16, B_{an} between 50 and 75 mT, and σ between 20 and 30 mT. These characteristics resemble those of chains of nearly equidimensional magnetite particles produced by magnetotactic bacteria (see Chapters 2 and 3).

The coercivity spectra in general take the form of broad, approximately Gaussian peaks with maxima between ~ 35 and ~ 75 mT (Figure 4-6). However, a few samples have two clearly distinct coercivity peaks, one centered around 30 mT and another centered around 60-75 mT. These samples (20-30 cm above MTL in C129, 31-49 cm above MTL in C139, 14-24 cm above MTL in C160, and at MTL in C165) all come from sediments above the magnetic drop-off. The clarity and median values of the dual peaks suggest magnetic carriers with narrowly defined population characteristics, as would be expected from magnetite produced by magnetotactic bacteria. The locations of the two peaks is consistent with the lower peak representing equidimensional magnetosomes and the higher peak representing elongate magnetosomes (see Chapter 3). We caution that this interpretation is by no means unique, and it is unlikely that magnetosomes would be the only source of magnetite in these sediments. Nonetheless, in agreement with a previous electron

microscopy and rock magnetic study of a single surface sample from northwest Andros Island (MCNEILL, 1990), both the coercivity spectra and the FMR spectra support a major role for magnetotactic bacteria in producing magnetite in the upper portion of the sediment columns.

4.4.4 Electron microscopy

The most abundant magnetic component in imaged samples is superparamagnetic (SP) magnetite (Figure 4-7a). SP magnetite was predominantly associated with Fe-rich clay minerals or with biomass containing remnant cellular structures. In both cases, the SP magnetite is similar to magnetite produced extracellularly by microbial Fe reduction (e.g., LI et al., 2004). Aggregates of euhedral single-domain (SD) magnetite, similar in size and aspect-ratio to that produced by magnetotactic bacteria, were found in some surface samples but were not abundant (Figure 4-7b). In ultrathin sections prepared from core samples 20 cm below MTL in C149, aggregates of iron sulfides were present (Figure 4-7c). The aggregates contain nanosized crystals (Figure 4-7c) that chemically and morphologically resemble soil greigite (STANJEK et al., 1994). We found no hematite, goethite or multi-domain magnetite.

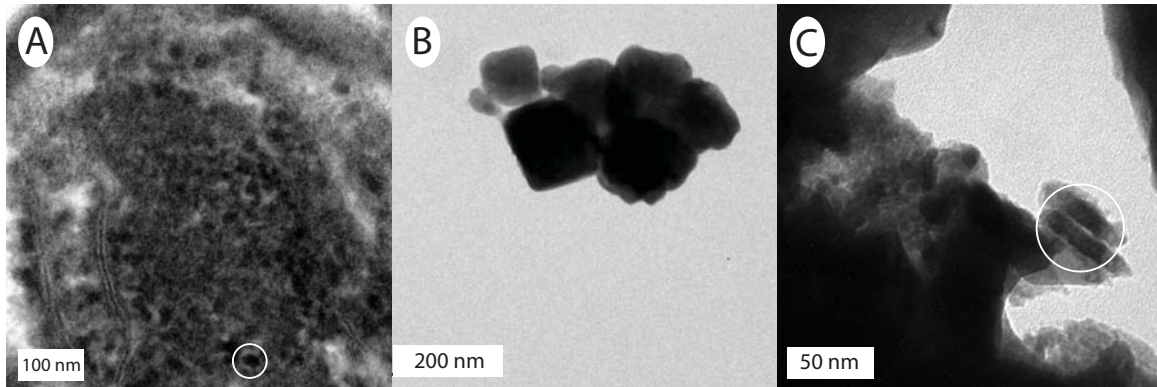


Figure 4-7: TEM images of (A) superparamagnetic magnetite particles within an organic matrix from above MTL in C139 (HAM), (B) single-domain stoichiometric magnetite particles from surface samples at C6 (LC), and (C) elongate magnetic iron sulfide particles resembling greigite from 20 cm below MTL in C149 (IAM). White circles in (A) and (C) show representative particles of SP magnetite and iron sulfide, respectively. White areas in ultrathin sections are holes where primary aragonite has dissolved when exposed to water during sample preparation.

4.4.5 *Paleomagnetic data*

We measured paleomagnetic direction in oriented carbonate samples to determine how different magnetic facies record the geomagnetic field. All 87 surface samples collected during the first field season preserved a natural remanent magnetization (NRM) indistinguishable from the local geomagnetic field (5-year IGRF). Stepwise AF-demagnetization of a 17 sample subset from this preliminary collection showed consistent linear decay to the origin and a high-AF direction indistinguishable from the NRM.

Most of the 154 samples (53 surface, 101 core) collected during the second field season did not have NRM directions colinear with the local geomagnetic field. 59% required AF demagnetizing fields as large as 11 mT to remove a fairly stable overprint direction before decaying linearly to the origin with further demagnetization (Figure 4-8). Stable overprint directions form a random stereonet distribution (Figure 4-9) and may have been acquired during airport security screening. High-AF directions from surface samples form a tight cluster with Fisher means overlapping the local IGRF (Figure 4-9). High-AF directions from core samples form clouds with greater scatter. Core Fisher means display inclinations indistinguishable from the local IGRF, but tend to show a counterclockwise declination offset from the local IGRF of 10-60°. We attribute the systematic declination offset to difficulties keeping the azimuth of the circular corer aligned during each drive. Comparing NRM intensities after AF removal of the low-AF overprint to SIRM intensities after similar AF cleaning yields SIRM/NRM ratios of 30 to 300, consistent with a chemical, rather than detrital, origin of the high-AF remanence (FULLER et al., 2002).

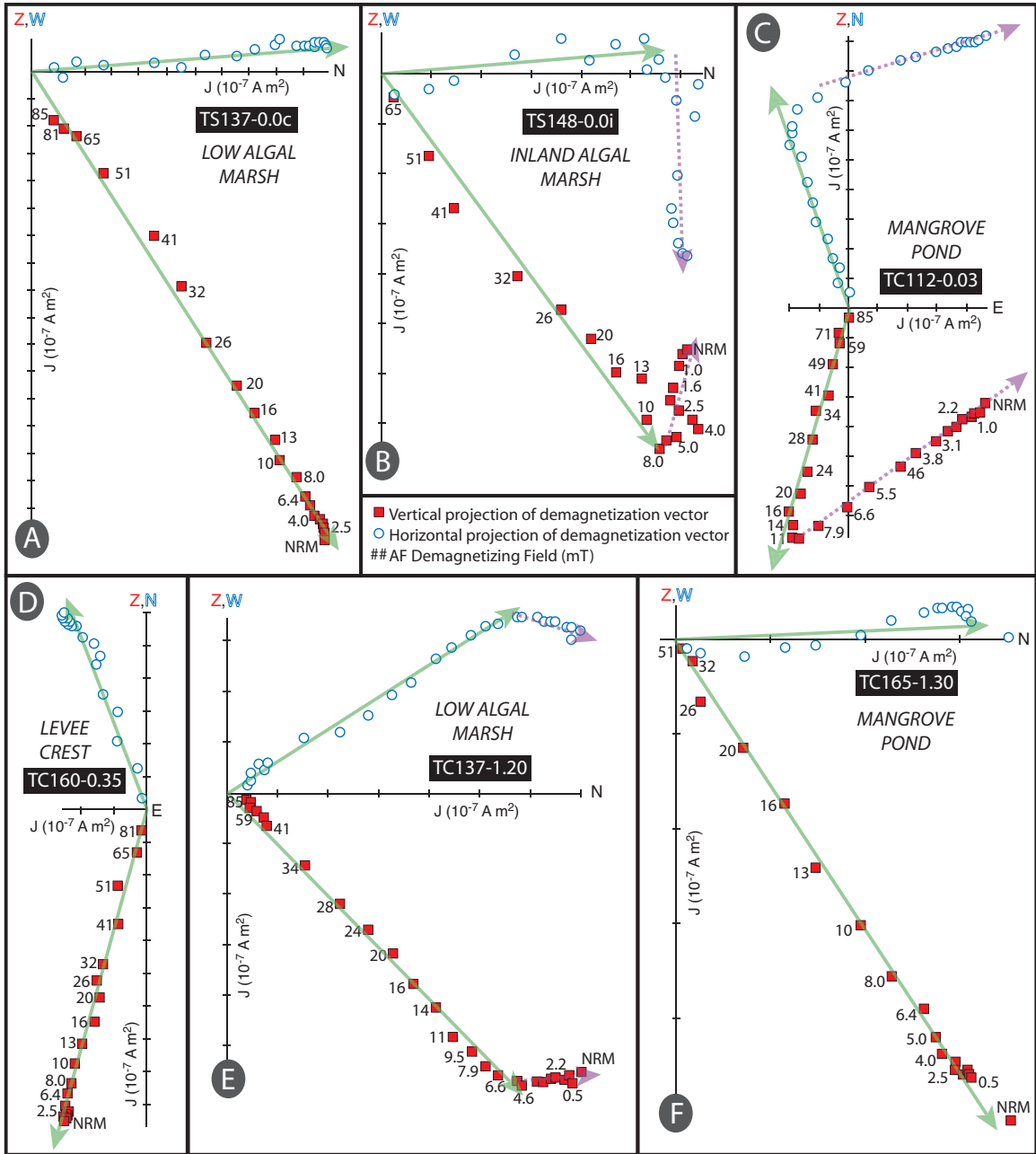


Figure 4-8: Representative vector component diagrams showing AF-demagnetization behavior of TGC carbonate samples. A, E and F show single-component behavior, where the high-AF magnetic component decays linearly to the origin during progressive AF-demagnetization from 0 to 85 mT. B, C and E show two-component behavior, where a low-AF overprint direction is removed between 5 and 10 mT, before the high-AF component decays linearly to the origin.

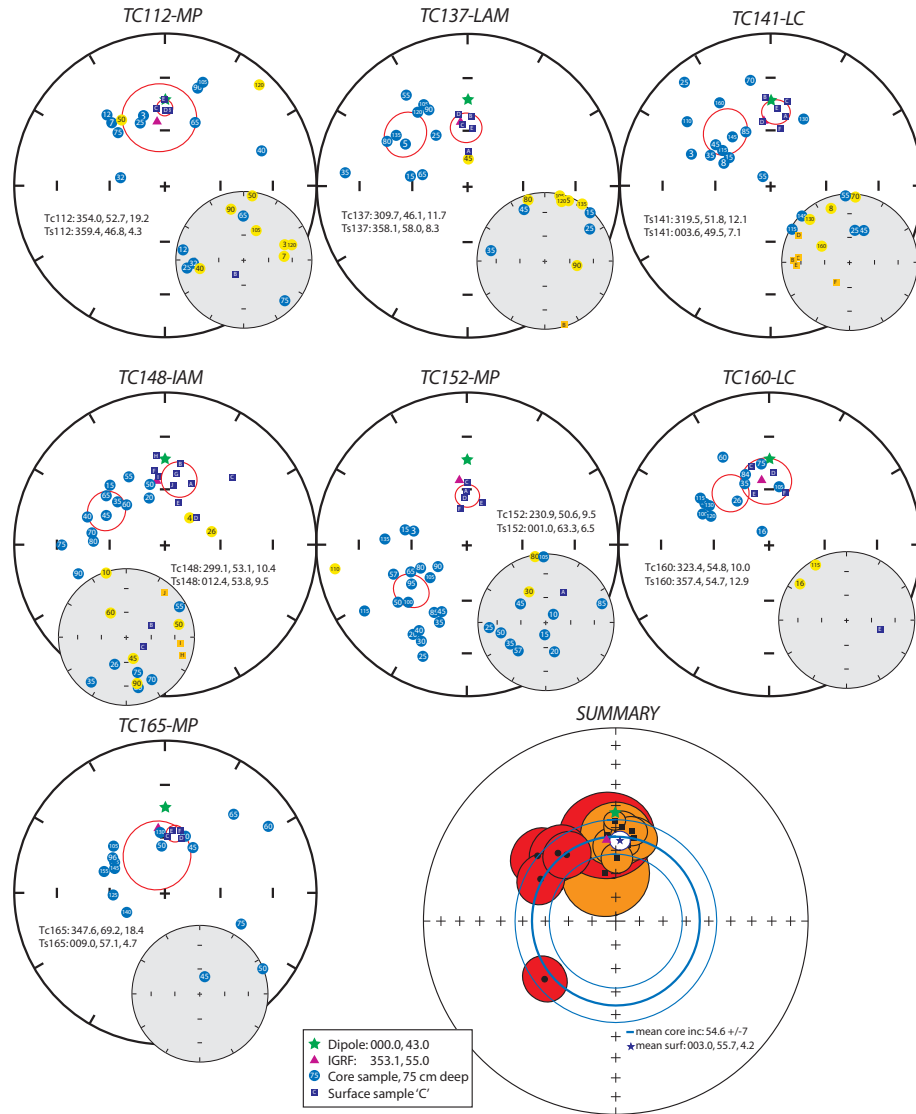


Figure 4-9: Equal-area stereonet projections of paleomagnetic directions from surface (S) and core (C) samples. Small grey stereonets collect overprint directions, and large white stereonets collect primary remanent magnetization directions. Blue/orange squares represent lower/upper hemisphere directions for surface samples from the facies and location of the associated core. Light blue/yellow circles represent lower/upper hemisphere directions for core samples, with the stratigraphic depth labeled in white/black text. The green star and purple triangle indicate the direction of the dipole field and the International Geomagnetic Reference Field (IGRF) for Triple Goose Creek, respectively. In the summary stereonet, Fisher means for surface/core primary remanence directions are depicted with black squares/circles, and α_{95} uncertainties are depicted with orange/red circles. The Fisher mean of the surface site means is drawn as a purple star with a white α_{95} uncertainty ellipse. Mean inclination for core site means is represented with a thick blue small circle, with α_{95} uncertainty depicted as bracketing thin blue small circles. The declination offsets in core samples, generally $\sim 10\text{-}60^\circ$ and reaching a maximum of $\sim 125^\circ$ in C-152, are likely related to vertical-axis orientation error during the coring process.

Direct observations of the geographic position of the magnetic north pole since 1904 suggest that magnetic inclination at TGC should have reached values as high as $\sim 60^\circ$ in 1904 (compared to 55° today). Archeomagnetic reconstructions spanning the last 2000 years suggest that magnetic inclination should have attained values as low as 32° during the onset of carbonate sedimentation at TGC, ~ 1000 CE (OHNO and HAMANO, 1992). Assuming a general sedimentation rate of 2 mm/yr for a typical levee crest, consistent with our ^{14}C data and measured accumulation rates of 1-3 mm/yr during dye experiments on levee crests (HARDIE, 1977), we would expect to see an increase in inclination between 0 and 20 cm depth in an LC core and a steady decline in inclination from 20 to 200 cm depth.

Inclination data from the cores yield a mean of $\sim 54.6^\circ$ and are, in general, too variable to discern secular trends with depth. It is not surprising that the inclination peak in 1904 is not observed, as $\sim 5^\circ$ is within the range of the scatter we observe in our directions. However, if carbonate muds near the base of the sedimentary column were recording the syndepositional geomagnetic field, we would expect to see $> 20^\circ$ shallowing with depth. The lack of a trend toward shallower inclinations likely indicates that physical and biogeochemical reworking of magnetic particles below MTL continues until the carbonates are actually cemented, and therefore carbonate muds deposited at 1000 CE have aligned themselves with the modern geomagnetic field. The stratigraphic changes with depth in bioturbation, geochemistry and rock magnetics described above do not have a discernible effect on magnetic direction, further supporting the idea that the entire Holocene sedimentary column is magnetized in the present local field.

4.5 Discussion

The magnetic and FMR data divide the sediment cores into three main zones: an upper zone of relatively high magnetization (Zone 1), a zone of low magnetization (Zone 2), and, in some cores, a lower zone of relatively high magnetization (Zone 3). In concert with the geochemical analyses, these data suggest that three major processes control the magnetic mineralogy of Triple Goose Creek sediments: (1) the deposition or precipitation of magnetite in the upper sediments, (2) the reductive dissolution of magnetite, and (3) in some areas, the reduction of marine sulfate and subsequent precipitation of magnetic iron sulfides.

The depth of the transitions between the zones vary among the cores. The boundary between the zones are defined by two horizons, a magnetite dissolution horizon (MDH) between Zones 1 and 2 and a sulfide precipitation horizon (SPH) between Zones 2 and 3 (Figure 4-10 and Figure 4-11).

Surface samples exhibit a broad range of FMR properties and strength of magnetization, likely reflecting the diversity of processes operating at the surface. These processes include the deposition of aeolian dust, both directly and after aqueous reworking, other aqueous transport processes, and biological processes including microbial metabolism and shallow burrowing.

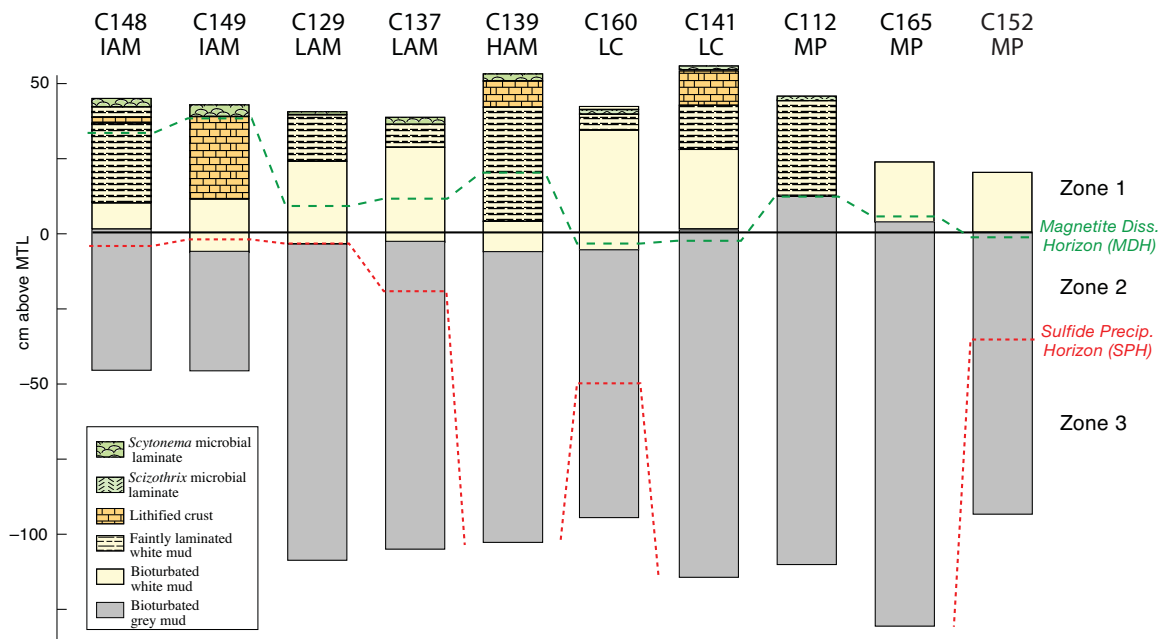


Figure 4-10: Redox zones of cores determined from changes in ferromagnetic material, as measured by total FMR absorption, IRM strength, and/or NRM intensity. The boundaries between zones are defined by the magnetite dissolution horizon (MDH) between Zones 1 and 2, which corresponds to a drop-off in the concentrations of ferromagnetic material, and the sulfide precipitation horizon (SPH) between Zones 2 and 3, which corresponds to a return to higher concentrations of ferromagnetic material.

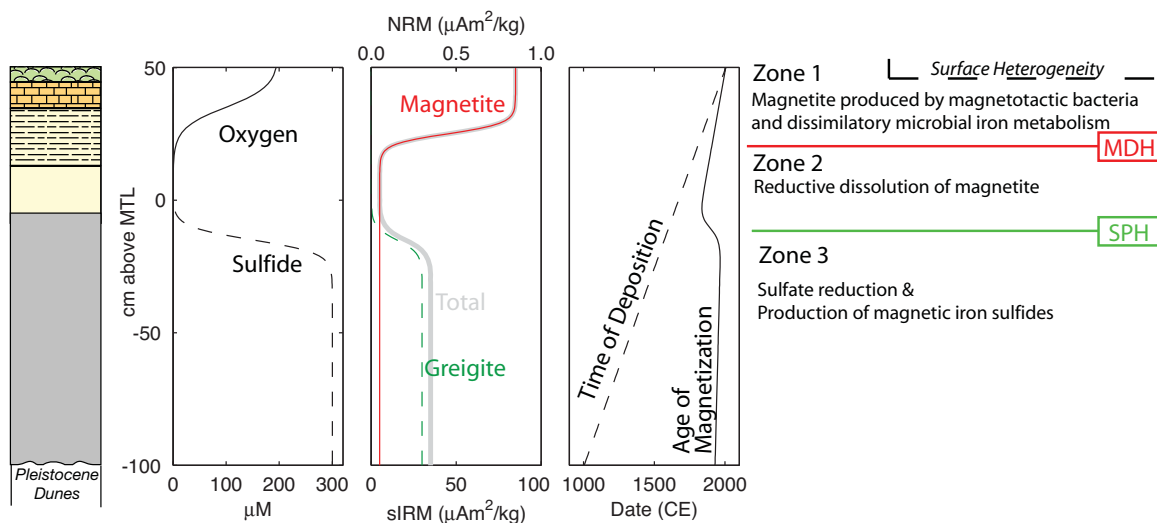


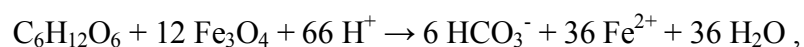
Figure 4-11: Schematic representation of the biogeochemical processes affecting the magnetic properties of Triple Goose Creek sediments

The coercivities of the surface sediments, which range between 32 and 77 mT, are consistent with magnetite as the main magnetic carrier. We find no magnetic evidence for a significant contribution of high coercivity antiferromagnetic minerals such as hematite or goethite, nor can we find such minerals in TEM/EDS experiments. As hematite and goethite are the major iron oxides in North African dust (BALSAM et al., 1995; LARRASOANA et al., 2003), this suggests that iron minerals in aeolian dust are not significantly preserved even in the surface sediment. Aeolian-transported paramagnetic Fe(III)-bearing clay minerals may, however, contribute to the Fe(III) peak observed in the FMR spectra.

The heterogeneity displayed by the surface sediments is diminished greatly in the top ~7 cm of the cores, which may reflect biological redox cycling of iron. Superparamagnetic magnetite or maghemite, the presence of which is indicated in the FMR spectra, may be produced in the upper zone of the sediment cores as a byproduct of microbial Fe(III) reduction or Fe(II) oxidation. The FMR spectra also suggest a major role for magnetotactic bacteria in this zone. In culture, magnetite-producing magnetotactic bacteria preferentially produce magnetite under oxygen partial pressures of ~10 mbar, corresponding to dissolved O_2 concentrations of ~10-15 μM (BAZYLINSKI and FRANKEL, 2004). The microelectrode data through *Schizothrix* and *Scytonema* mats suggest that oxygen-depleted microenvironments, hospitable to magnetotactic bacteria, occur in the mats. Such

microenvironments are likely more abundant at night, when photosynthesis ceases, than during the day, when we performed our measurements (JØRGENSEN et al., 1979). A broader sub-zone of appropriate oxygen concentrations occurs in the sediment cores, and we suggest that the regions with clear double peaks in the coercivity spectra and often ARM/IRM maxima reflect the greatest abundance of magnetite produced by magnetotactic bacteria.

Just below the magnetotactic bacteria-enriched subzone is the MDH and the transition into Zone 2. At the MDH, oxygen and nitrate levels are sufficiently low that Fe(III) becomes the main electron acceptor for microbial respiration. Magnetite is reduced to Fe²⁺ in reactions such as

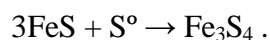
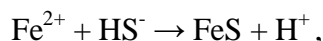
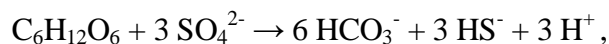


as has been demonstrated in pure cultures of *Shewanella* (DONG et al., 2000; KOSTKA and NEALSON, 1995). This reaction consumes protons and would promote carbonate cementation. This metabolic process is thermodynamically favorable at environmental pH levels so long as Fe²⁺ concentrations remain below ~100 μM (KOSTKA and NEALSON, 1995), which suggests an important role for carbonate and/or sulfide precipitation in limiting the accumulation of ferrous iron. The mildly elevated particulate Mn(II) levels in this zone reflect the parallel reduction of oxidized Mn and the precipitation of Mn(II) in carbonate or sulfide minerals.

The MDH dissolution horizon is present in all the sediment cores (Figure 4-10). It occurs near MTL in LC and MP environments and above MTL in algal marsh environments. The depth is controlled by the oxygen consumption rate, which is a function of biological productivity. In the algal marsh environment, the surface and near-surface sediments are rich in organic carbon, with the acid-insoluble content reaching as high as 13% by weight. Differences in biological productivity in other settings may alter the thickness of the oxic zone.

In some cores, sulfate reduction leads to the presence of Zone 3. At and below the SPH, microbial sulfate reduction produces dissolved sulfide, which can then react with dissolved

Fe^{2+} to produce first iron monosulfide minerals and then the ferrimagnetic mineral greigite in reactions such as:



By acidifying porewaters, this reaction also promotes dissolution of carbonate and might lead to the destruction of magnetic remanence carried in lithified carbonate crusts formed at or above the MDH. Particulate Mn(II) concentrations increase in parallel with the increase in total FMR absorption, which suggests the precipitation of Mn(II) as a cation in sulfide minerals.

Zone 3 is not present in two MP cores, one LC core, and one HAM core. In two IAM and one LAM cores, it occurs near MTL, while in one LAM core, one LC core, and one MP core, it occurs ~20-50 cm below MTL (Figure 4-10). The sulfidic sediments in Zone 3 are richer in organic carbon than the sediments that overlie them. Visual inspection indicates that mangrove root hairs are richer in the acid-insoluble component of C149, which has a Zone 3, than in the acid-insoluble component of C139, which does not. This difference suggests that organic matter from decaying mangrove roots may exert an important control over the presence and depth of Zone 3.

The iron cycle model described above predicts that the remanent magnetization in Zone 1 is predominantly a chemical remanent magnetization produced near the time of deposition, while the remanent magnetization in Zone 3 is a chemical remanent magnetization produced significantly after deposition (Figure 4-11). The absence of the depth trends in inclination expected from syndepositional remanent magnetizations supports this model. However, the accuracy of the paleomagnetic data is limited by the orientation system used in this study.

Our analyses of the Andros Island sediments have implications for the interpretation of paleomagnetic data from weakly magnetic carbonate platform sediments with limited to

non-existent clastic input. Magnetic data from a single shoaling-upward meter-scale parasequence will not carry a record of magnetization synchronous with cm-scale sediment accumulation; rather, the most strongly magnetic parts of the parasequence will all carry a magnetic record formed at the time of carbonate cementation/lithification. At Triple Goose Creek, cementation occurs syndepositionally in the intertidal-to-supratidal top of the parasequence. Most compaction and cementation of the lower portion of the parasequence that was deposited subtidally and currently resides below the MTL occurs intracyclically, either after (1) a sea-level drop leaves the entire parasequence above MTL, or (2) the parasequence is deeply buried. Therefore, it is the laminated, early-cemented top of the parasequence that is most likely to preserve a syndepositional magnetic direction, and is also the region most likely to preserve a fossil record of magnetotactic bacteria.

If sedimentation in the Triple Goose Creek region were controlled by purely autocyclic processes, sediments would continue to aggrade until no accommodation space remained and a weathering horizon or hiatal surface developed. Early lithification would likely protect some of the magnetite in the upper, laminated sediments and thereby preserve both a nearly syndepositional record of remanent magnetization and fossil magnetotactic bacteria. If sea level were to fall drastically in response to the onset of the next ice age, the Holocene parasequence would be left high and dry, and deep oxidative weathering might destroy the primary magnetic signal in the carbonates. In the more likely short-term scenario that anthropogenic climate warming leads to a rapid rise in eustatic sea level, the fast rise might overtake the rate of carbonate accumulation, flood the TGC area, and allow iron respiration to erase the magnetic record in all but the impermeable, cemented portions of the upper part of the Holocene parasequence.

4.6 Conclusions

Our study of ~1–2 m thick late Holocene peritidal carbonate sediments from the Triple Goose Creek region of Andros Island reveals an iron biogeochemical cycle divided, from a magnetic perspective, into three parts. We find evidence for a prominent role for magnetotactic bacteria in a zone constituting the upper ~5–30 cm of the sediments. Below this zone, at a boundary that lies near or above mean tide level, iron reduction leads to a 5–

10-fold drop in the magnetic strength of the sediments. Where decaying mangrove root fibers supplement the levels of organic carbon, a zone of sulfate reduction and a co-occurring increase in magnetization due to greigite precipitation can develop deeper in the subtidally deposited, bioturbated sediments.

Our results suggest that the lower portion of shoaling-upward peritidal carbonate parasequences are likely to be magnetically weaker than the tops of the parasequences and, where not weaker, likely record a slightly post-depositional magnetization contemporary with the magnetization of the top of the parasequence. The best target for recovering paleomagnetic signals with high temporal resolution from ancient peritidal carbonates, as well as the best target for finding ancient peritidal magnetofossils, are therefore the early-cemented, laminated tops of shoaling-upward parasequences.

A MAGNETOFOSSIL SPIKE DURING THE PALEOCENE/EOCENE THERMAL MAXIMUM*

5.1 Introduction

The Paleocene-Eocene boundary is followed by a ~5°C global warming event, the Paleocene/Eocene Thermal Maximum (PETM), most likely driven by increased atmospheric greenhouse gas concentrations (PAGANI et al., 2006). In sediments from the northeastern and northwestern North Atlantic margin (BOLLE and ADATTE, 2001; GAWENDA et al., 1999; GIBSON et al., 2000; SCHMITZ et al., 2001), New Zealand (KAIHO et al., 1996), and the Antarctic (ROBERT and KENNETT, 1994), the PETM is associated with enhanced deposition of kaolinite, a clay mineral typically formed during chemical weathering under hot, humid conditions. KENT et al. (2003) found that PETM sediments from the northern US Atlantic Coastal Plain, New Jersey, also had anomalous magnetic properties indicating enrichment of fine-grained magnetite. The production of a similarly anomalous magnetic nanophase, albeit one composed of ferric oxyhydroxides, as fallout condensate from the end-Cretaceous impact (WDOWIAK et al., 2001) led Kent et al. to speculate that the PETM was a “bolide summer” triggered by cometary impact (CRAMER and KENT, 2005; KENT et al., 2003). Here, we reexamine the PETM clay with ferromagnetic resonance (FMR) spectroscopy and transmission electron microscopy (TEM) and find magnetite nanoparticles bearing signature traits of crystals produced by magnetotactic bacteria. This result, the first identification of ancient biogenic magnetite using FMR, indicates that the anomalous magnetic properties of the PETM sediments are not produced by an impact. They instead reflect environmental changes along the western North Atlantic margin during the extreme warming of the PETM that led to enhanced production and/or preservation of magnetofossils.

* Co-authored with Timothy D. Raub, Dirk Schumann, Hojatollah Vali, and Joseph L. Kirschvink.

Magnetotactic bacteria synthesize intracellular chains of single-domain, frequently elongate crystals of magnetite or greigite, which can be preserved in sediments as magnetofossils. Common in both freshwater and marine environments, the bacteria are most abundant under suboxic conditions, both in sediments and in the water column. Although magnetofossils are common magnetic components of Quaternary sediments (PETERSEN et al., 1986), reports of magnetofossils from older rocks are scarce (see Chapter 1). KENT et al. (2003) considered the possibility that the magnetic properties of the New Jersey PETM clay were produced by magnetofossils but imaged only isolated, equidimensional magnetite under TEM and therefore dismissed the possibility.

5.2 Samples

Ocean Drilling Program Leg 174AX, a land-based leg, recovered cores from two sections containing shallow water deposits of late Paleocene and early Eocene age, at Bass River and Ancora, New Jersey (MILLER et al.) (Figure 5-1). Paleocene-Eocene sediments from Bass River were deposited at ~105–140 m depth, while sediments from Ancora were deposited at ~45–70 m depth (VAN SICKEL et al., 2004). The United States Geological Survey drilled a core through shallower sediments at Clayton, New Jersey (GIBSON et al., 1993), and later supplemented this core with another at the adjacent Wilson Lake locality, ~5 km east of Clayton (ZACHOS et al., 2006b).

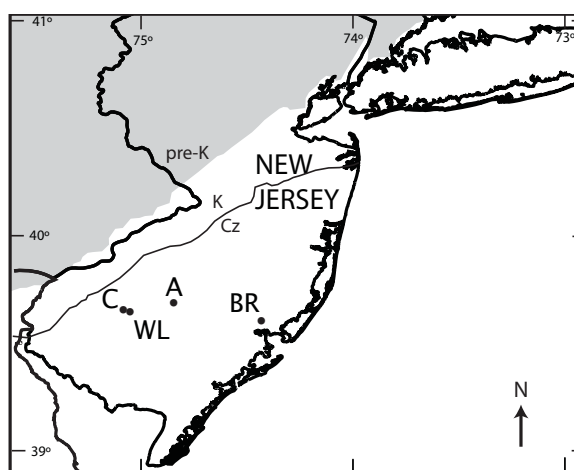


Figure 5-1: Map of New Jersey drill sites. From west to east, sites are Clayton (C), Wilson Lake (WL), Ancora (Anc) and Bass River (BR). Cenozoic (Cz), Cretaceous (K), and pre-Cretaceous (pre-K) outcrop limits are shown (VAN SICKEL et al., 2004).

The four cores record a ~5‰ negative carbon isotopic excursion (CIE) in ~5 to ~9 m of kaolinite-rich clay with low quartz content. The clay layer, which interrupts otherwise quartzose and glauconitic sandy, silty clay and clayey silt and sand, provides a high deposition-rate record of the PETM. The clay exhibits high ratios of saturation-remanent magnetization to saturation magnetization (M_r/M_s) that reach values exceptional for sedimentary rocks and close to the theoretical uniaxial, single-domain magnetite limit of 0.50. The highest M_r/M_s ratios are exhibited in the shallower cores. M_r/M_s during the PETM is nearly uniformly ~0.40 at Clayton and ~0.35 at Ancora. At more distal Bass River, M_r/M_s varies within the clay between ~0.10 and ~0.30.

Saturation magnetization measurements indicate that the PETM sediments with high M_r/M_s ratios contain ~120–200 ppm of predominantly single-domain magnetite, whereas underlying and overlying sediments contain ~30–70 ppm predominantly detrital magnetite (KENT et al., 2003). Magnetic and carbon isotopic data from the Ancora core (KENT et al., 2003) record the onset of the magnetic anomaly over the ~40 cm above the onset of CIE (KENT et al., 2003). The lag indicates that the magnetic response of the New Jersey PETM sediments was delayed by < ~8% of the total ~110–220 ky duration of PETM (FARLEY and ELTGROTH, 2003; ROHL et al., 2000), ~9–18 ky. Since kaolinite fraction decreases upward through the PETM clay at Clayton while magnetic parameters remain effectively constant, and since Bass River preserves magnetic variation throughout the lithologically homogeneous clay interval, the anomalous magnetic properties do not appear to be produced by lithological changes.

Samples of the Ancora drill core (IODP Leg 174AX) were retrieved from the storage facility at the Rutgers/New Jersey Geological Survey Rift-Drift Core Repository. Thirty-one samples were collected between 164.33 m (539.14 ft) and 172.46 m (565.83 ft). The CIE in Ancora is present from ~171.3 m to ~165.5 m. FMR, rock magnetic, and TEM measurements were made as described in Chapter 4.

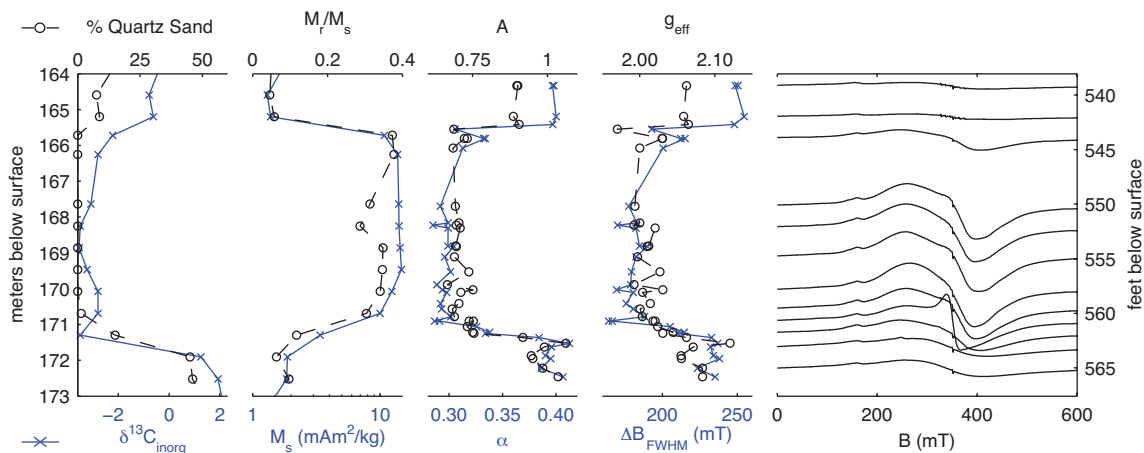


Figure 5-2: Fine quartz sand fraction, $\delta^{13}\text{C}_{\text{inorganic}}$, ratio of saturation remanence magnetization to saturation magnetization, saturation magnetization (all from KENT et al., 2003), FMR parameters α , A , ΔB_{FWHM} , and g_{eff} , and example FMR spectra for upper Paleocene to lower Eocene strata, ODP Leg 174AX, Ancora, New Jersey. Left edges of example spectra align with drill core depth.

5.3 Characterization of magnetic particles

Ferromagnetic resonance (FMR) spectroscopy is an electron spin resonance technique capable of assessing the magnetic anisotropy, magnetic interactions, and morphological heterogeneity of magnetic particles in bulk samples (see Chapters 2 and 3). It is thus ideally suited for distinguishing among (1) detrital magnetite, (2) isolated particles of equidimensional magnetite, and (3) magnetofossils, which are frequently elongate and often preserved in intact chains. FMR can therefore readily check the observation that magnetite in the PETM sediments occurs as isolated, equidimensional particles: the finding that spurred the “bolide summer” hypothesis (KENT et al., 2003).

Using FMR, rock magnetic, and transmission electron microscopy (TEM) techniques, we examined latest Paleocene to early Eocene sediments from the Ancora drill core, which preserves a complete record of the CIE onset and recovery. FMR parameters (Table S1) confirm that pre-CIE and post-CIE siltstones are dominated by presumably detrital magnetic particles with broad size distributions and indicate that the PETM clay hosts fairly homogeneous magnetic populations of elongate particles and/or chains, consistent with magnetofossils rather than isolated, equidimensional particles (Figure 5-2 and Figure 5-3).

A sand lens within the upper portion of the clay (at 165.81 m) has nearly identical FMR properties to the surrounding clay, which supports the hypothesis that grain size is not controlling the change in magnetic properties.

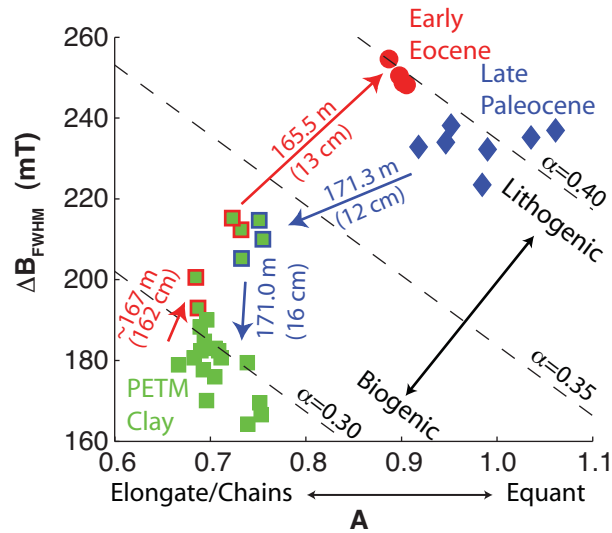


Figure 5-3: FMR parameters ΔB_{FWHM} and A for PETM clay (green squares; lowermost outlined in blue; uppermost outlined in red) and underlying (blue diamonds) and overlying (red circles) sediments. Arrows, showing transitions between populations, are labeled with transition depth and unsampled interval thickness. Detrital-dominated sediments generally have $\alpha > 0.40$, while previously studied pelagic magnetofossil-rich sediments have $\alpha < 0.30$ (see Chapter 2).

Consistent with prior results from hysteresis experiments (Table 5-1), the isothermal remanent magnetization (IRM) strength of samples from the PETM clay are ~10-60 times higher than those of samples from underlying and overlying sediments (Figure 5-4). The coercivity of remanence of the PETM clay, which ranges from 53 to 69 mT, is lower than that of underlying and overlying samples (72-78 mT). Examination of the coercivity spectra (Figure 5-5) indicates that the increase in bulk coercivity is due to the influence of a high coercivity component, such as goethite or hematite. The PETM clay also exhibits high values of anhysteritic susceptibility, consistent with those of magnetotactic bacteria (Figure 5-6).

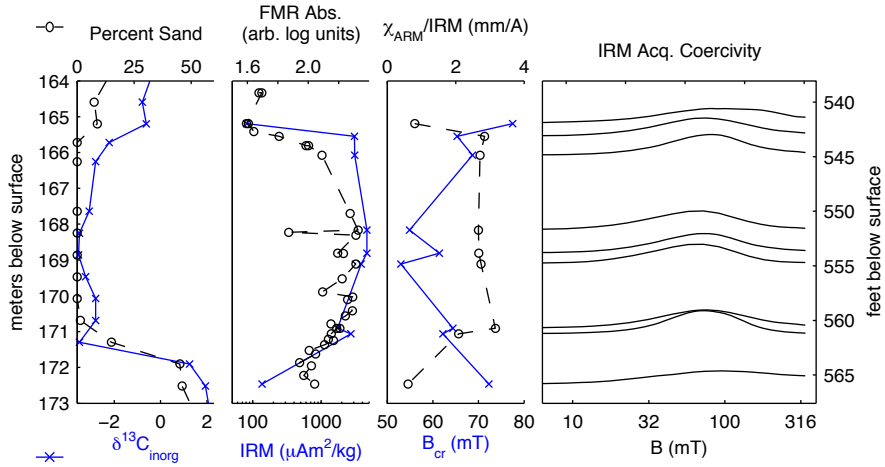


Figure 5-4: Fine quartz sand fraction, $\delta^{13}C_{inorganic}$, total FMR absorption, rock magnetic parameters, and IRM acquisition coercivity spectra for upper Paleocene to lower Eocene strata, ODP Leg 174AX, Ancora, New Jersey. Maximum IRM was imparted in a 350 mT field. Coercivity of remanence B_{cr} was determined from the intersection of IRM acquisition and demagnetization curves (CISOWSKI, 1981). χ_{ARM}/IRM is the ratio of ARM susceptibility determined in a 100 mT alternating field and a 0.1 mT DC biasing field to IRM acquired in 100 mT field. Left edges of coercivity spectra align with drill core depth.

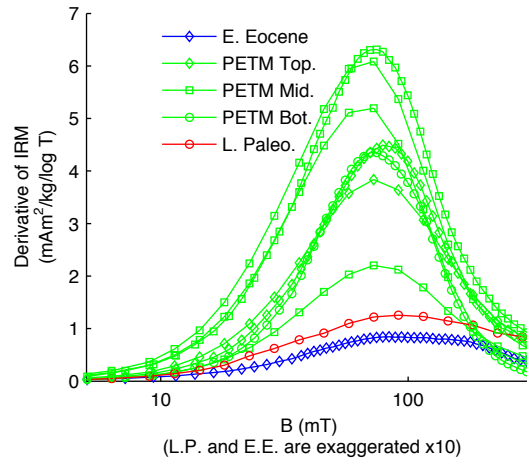


Figure 5-5: Coercivity spectra from Ancora samples in late Paleocene silty clay, PETM clay, and early Eocene silty clay, determined from the derivative of IRM acquisition curves. Coercivity spectra for late Paleocene and early Eocene silty clay samples are exaggerated by a factor of 10.

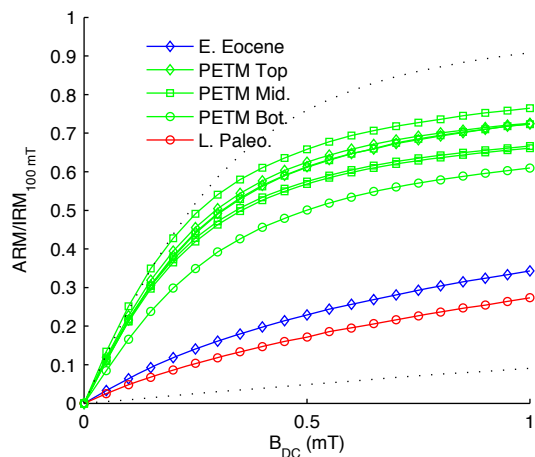


Figure 5-6: ARM acquisition curves for Ancora samples in late Paleocene silty clay, PETM clay, and early Eocene silty clay, determined in a 100 mT alternating field. The upper dotted line shows the reference curve of the magnetotactic bacterium *Magnetospirillum magneticum* AMB-1, while the lower dotted line shows the reference curve for highly interacting single-domain magnetite in a chiton tooth.

Transmission electron microscopy and energy dispersive X-ray spectroscopy analysis of magnetic separates (PETERSEN et al., 1986) from suspended clay reveals abundant elongate prismatic and bullet-shaped, single-domain size crystals of stoichiometric magnetite (Figure 5-7 and Figure 5-8) that resemble magnetite present within a variety of bacteria (see Chapter 1). Equidimensional cuboidal particles are also present, but less common than elongate particles. The bullet-shaped particles reach sizes that, to our knowledge, exceed the size of previously-reported magnetofossils but are consistent with the largest bullet-shaped particles observed in living bacteria (VALI and KIRSCHVINK, 1991). Some particles show irregular shapes that suggest minor dissolution. In the magnetic separates, particles with similar morphologies occasionally form short chains of 3-5 crystals, possibly remnants of biologically-generated chain structures. Consistent with FMR and rock magnetic data, magnetic separates from non-CIE siltstones did not include putative magnetofossils.

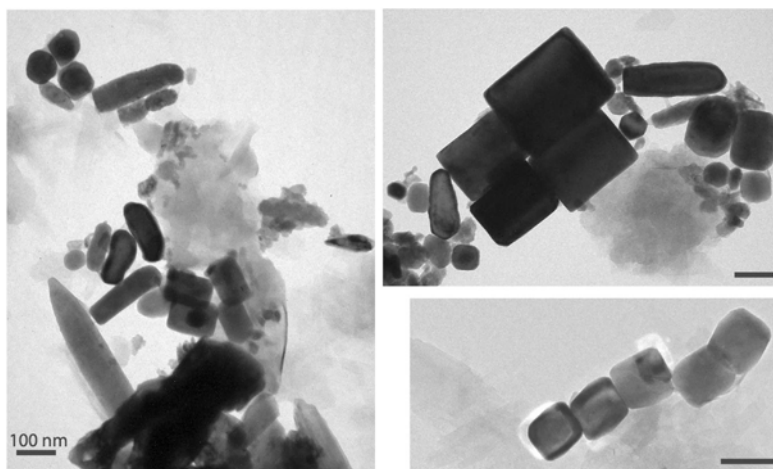


Figure 5-7: TEM images of well-preserved single-domain magnetite crystals from the PETM clay with shapes characteristic of bacterial magnetite. Contrast differences in the images are due to crystal orientations with respect to the electron beam.

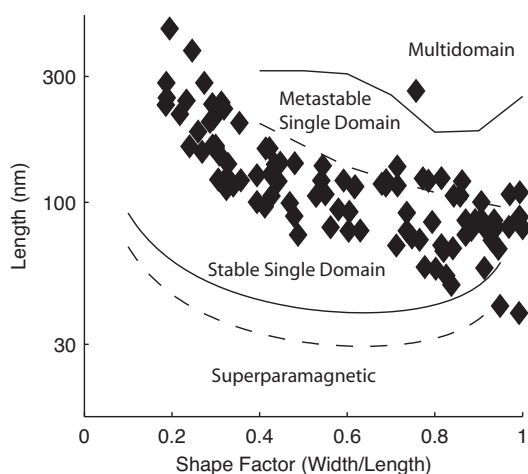


Figure 5-8: Length and shape factor (width/length ratio) of magnetite particles from magnetic separates of Ancora sample at 168.81 m depth. The lower, SD/superparamagnetic boundary is determined for rectangular parallelepipeds with unblocking times of 100 s (dashed line) and 4.5 Gy (solid line) following BUTLER and BANERJEE (1975) and DIAZ-RICCI and KIRSCHVINK (1992). The upper solid line and upper dashed line show the upper boundary of the metastable single-domain field and stable single-domain field, respectively (WITT et al., 2005).

5.4 Environmental implications

Similar, though shorter duration and less pronounced, climate-linked increases in magnetofossil abundance have been observed in Quaternary pelagic and hemipelagic

sediments (DINARÈS-TURELL et al., 2003; HESSE, 1994; LEAN and MCCAVE, 1998). In these settings, magnetofossil abundance is generally lower in glacial sediments and higher in interglacial sediments. Observations of degree of bioturbation, sediment color, and organic carbon content suggest that increased porewater oxygen during interglacial glacial stages drives the change. Elevated porewater oxygen, which at a constant sedimentation rate could result from a reduced flux of organic carbon to sediments or enhanced bottom water oxygen content (VAN DER LOEFF, 1990), will increase the depth at which anoxia occurs within the sediments. The suboxic zone of the sediments, in which most magnetotactic bacteria live, will expand and cause the total population of magnetotactic bacteria to grow. Moreover, because fine-grained magnetite dissolves readily under fully anoxic conditions, an expanded suboxic zone will foster better magnetofossil preservation, a taphonomic bias that exaggerates the ecological effect.

We therefore suggest that the initial Eocene enrichment of magnetofossils in shallow-water sediments is linked to expanded sedimentary suboxia. Potential contributors to this biogeochemical transformation include changes in sedimentation rate, biological productivity, and oxygen solubility. By diluting sedimentary organic carbon, an increase in the ratio of sedimentation rate to productivity would increase the depth and thickness of the suboxic zone. A decrease in oxygen solubility would allow suboxic and anoxic conditions to develop at shallower depths.

The sedimentation rate on the Atlantic Coastal Plain during the PETM was high. The best estimate for the late Paleocene and early Eocene background sedimentation rate in Ancora is ~5–10 m/My (VAN SICKEL et al., 2004), while the average sedimentation rate during the CIE was ~20–50 m/My. The kaolinitic character of the PETM clay also indicates enhanced continental weathering. If biological productivity and organic carbon preservation were constant, the ~4 fold increase in sedimentation rate would be expected to produce a comparable decrease in organic carbon content.

At Wilson Lake, the organic carbon content predominantly remains ~0.3% to ~0.4% before, during, and after the CIE, although it reaches a nadir of ~0.0% to ~0.2% in the lower third of the CIE (ZACHOS et al., 2006a). However, particles with high surface area-to-volume

ratios, like clay-sized particles, generally preserve organic carbon better than coarser particles (HEDGES and KEIL, 1995). Thus, the clay sediments deposited during the CIE should more effectively preserve organic carbon than the underlying and overlying siltstones. The absence of the expected increase in carbon content likely reflects dilution caused by an increase in the ratio of sedimentation rate to biological production. Although changes in nannofossil assemblages at Wilson Lake during the PETM indicate a shift from oligotrophic to mesotrophic nanoplankton taxa (GIBBS et al., 2006) and are generally interpreted as reflecting increased nutrient input and productivity, both the abundance of magnetofossils and the consistently low organic carbon content limit the magnitude of the enhanced productivity and preclude an increase large enough to drive bottom water anoxia.

The temperature increase during the PETM could also have contributed to the magnetofossil enrichment. Measurements of crenarcheotal lipids from Wilson Lake indicate that the sea surface temperature of the Atlantic Coastal Plain warmed from $\sim 25^{\circ}\text{C}$ to $\sim 33^{\circ}\text{C}$ (ZACHOS et al., 2006a) during the PETM. The warming would have decreased oxygen solubility by $\sim 12\%$ ($\sim 25\ \mu\text{M}$) (DREVER, 1997) and thereby facilitated the development of suboxic conditions.

5.5 Conclusions

The discovery of the most continuously magnetofossil-rich sediments yet recognized in the stratigraphic record, deposited at low- to mid-latitude within the northwestern Atlantic Coastal Plain, validates the use of ferromagnetic resonance spectroscopy for magnetofossil identification in ancient sediments and offers an alternative explanation for the only unique evidentiary plank of the PETM comet-trigger hypothesis (KENT et al., 2003). Building upon work that links magnetofossil populations and Quaternary climate change, it constrains chemical oceanographic effects of the severe initial Eocene climate change.

Table 5-1. FMR and rock magnetic parameters for upper Paleocene to lower Eocene strata, ODP Leg 174AX, Ancora, New Jersey

Lithology	Depth (ft)	Depth (m)	Total Abs. (arb. units)	g _{eff}		A		ΔB_{FWHM} (mT)		α	sIRM ($\mu\text{Am}^2/\text{kg}$)	Bcr (mT)	χ_{ARM}/IRM (mm/A)
Eocene silty clay/clayey silt	539.14	164.33	47	2.062	0.90	250	0.40						
			50	2.062	0.90	249	0.40						
	541.98	165.20	39	2.059	0.89	255	0.40	82	77.5	0.8			
			40	2.059	0.89	255	0.40						
	542.70	165.41	44	2.065	0.91	248	0.40						
Transitional	543.14	165.55	64	1.970	0.69	193	0.31	3050	65.3	2.8			
	543.99	165.81	97	2.030	0.73	212	0.33						
	543.99	165.81	101	2.030	0.72	215	0.33						
	544.87	166.08	123	2.000	0.68	201	0.31	3090	68.7	2.7			
PETM clay	550.20	167.70	189	1.993	0.69	178	0.29						
	551.73	168.17	212	2.000	0.70	183	0.30	4650	54.9	2.7			
	551.93	168.23	74	1.993	0.70	170	0.28						
	552.94	168.54	205	2.020	0.71	182	0.30						
	553.84	168.81	156	2.012	0.69	185	0.30	4660	61.4	2.7			
	553.87	168.82	171	2.010	0.70	190	0.30						
	554.83	169.11	206	1.997	0.69	182	0.30	3830	53.0	2.7			
	556.19	169.53	167	2.027	0.74	179	0.30						
	557.39	169.89	124	1.993	0.67	179	0.29						
	557.85	170.03	196	2.031	0.75	170	0.29						
	558.10	170.11	182	2.004	0.71	181	0.30						
	559.10	170.41	195	2.014	0.70	176	0.29						
	559.59	170.56	176	2.000	0.68	181	0.29						
	560.32	170.79	141	2.004	0.69	188	0.30						
560.72	170.91	162	2.017	0.74	164	0.29	1740	64.4	3.2				
		154	2.020	0.75	167	0.29							
Transitional	561.22	171.06	142	2.024	0.73	205	0.33	2710	62.2	2.1			
	561.73	171.22	135	2.044	0.75	215	0.34						
	561.83	171.25	147	2.031	0.75	210	0.33						
Paleocene silty clay/clayey silt	562.22	171.36	128	2.062	0.92	233	0.38						
	562.75	171.53	102	2.120	1.06	237	0.41						
	563.07	171.62	112	2.071	0.99	232	0.40						
	563.88	171.87	88	2.055	0.95	234	0.39						
	564.15	171.95	105	2.055	0.95	238	0.40						
	565.03	172.22	94	2.084	0.98	223	0.39						
	565.83	172.46	110	2.084	1.04	235	0.41	137	72.3	0.6			

EPILOGUE

Iron is the fourth most abundant element in the Earth's crust, trailing oxygen, silicon, and aluminum. Uniquely among these four elements, it is a redox-sensitive metal, capable of existing under surface conditions in both reduced (ferrous, Fe^{2+}) and oxidized (ferric, Fe^{3+}) forms. Because life is, in large part, redox chemistry, the behavior of iron in sediments bears a heavy fingerprint of biological activity, particularly microbial metabolism.

Iron is special for another reason, too. With its partially filled *d* orbital, it is the main cation in the most common magnetic minerals. Its behavior in sediments can therefore be tracked with the highly sensitive techniques of rock magnetism and with related approaches, such as ferromagnetic resonance spectroscopy. Thus, not only do iron abundance, iron speciation, and the size, shape, and arrangement of particles reflect the handiwork of life, but these properties can also be assessed with magnetic tools. Because magnetic techniques are generally rapid and non-destructive, they are ideal for the development of high-resolution sedimentary records.

In the last five chapters, we have taken a few glimpses through an iron lens into the world of biogeomagnetism, with studies ranging from microbial magnetism in laboratory-grown cultures (Chapters 2 and 3), to microbial iron cycling in Recent sediments (Chapter 4), to the magnetofossil signature of an ancient extreme climate change event (Chapter 5). The laboratory work has tested a new technique capable of detecting microbial magnetic signatures, while the work in Recent sediments provides a guide to the ancient, and the work in the ancient provides tantalizing hints of the relationship between climate and microbial iron cycling.

Many questions remained unanswered, at all three levels. In the controlled environment of the laboratory, we have only begun to understand the ferromagnetic resonance spectra of the sorts of materials that exist in the natural world. Many more measurements need to be made of minerals other than magnetite and maghemite, such as hematite, goethite, and pyrrhotite. The database of igneous and metamorphic magnetite is also fairly limited. Our models currently employ a Gaussian broadening factor to accommodate a range of physical

processes that would be better modeled in more concrete terms, even though they would make the model far too complex to use for fitting natural samples. More detailed modeling might also explain peculiarities such as the characteristic triple-humped spectra of MV-1.

In the Recent, future studies should take greater advantage of the opportunity to study microbes in the act of weaving the magnetic fabric of sediments by combining sedimentological, geochemical, and magnetic studies like those we conducted in the Bahamas with studies of microbial ecology. Furthermore, carbonate platforms are but one of many environments in which an understanding of modern biogeomagnetic processes would shed light on the past; similar studies are needed in a variety of lacustrine and marine settings.

The discovery of a magnetofossil lagerstaate in the initial Eocene, a time of great relevance for those interested in future climate change as well as for students of the past, impels further studies of the linkages between climate and biogeomagnetism. The question of whether magnetofossil lagerstaaten truly reflect expanded suboxia could be addressed by transforming temporal variability into spatial variability through comparative biogeomagnetic studies of marine sediments deposited under different levels of carbon flux and different bottom water oxygen concentrations. Expansion of the ancient magnetofossil record would also reveal whether such lagerstaaten are genuine oddities or whether they have been hidden by sparse sampling of pre-Quaternary sediments.

CHANG and KIRSCHVINK (1984)'s hope that the changes in the magnetofossil record might serve as a proxy for ancient environmental oxygen levels remains uncertain but alive. Insights into the evolution and metabolism of magnetotactic bacteria gained by testing the magnetosome battery hypothesis (Chapter 1) might strengthen the linkages between magnetotactic bacteria and specific redox conditions. Ultimately, though, the test of the idea will come as thorough sedimentological, geochemical, and magnetic studies of ancient rocks extend the magnetofossil record from the Cretaceous back toward the start of the Proterozoic, when oxygen may have been making its first appearances (Appendix I).

THE PALEOPROTEROZOIC SNOWBALL EARTH*

A climate disaster triggered by the evolution of oxygenic photosynthesis

I.1 Introduction

After the rise of life itself, the most radical transformation of Earth's biogeochemical cycles occurred in the transition from an anoxic to an oxic world. This transformation took place in three phases. First, oxygenic photosynthesis evolved and brought into the world locally oxic environments. Second, oxygen became a major component of the atmosphere; some authors (ANBAR and KNOLL, 2002; CANFIELD, 1998) have suggested this period was a protracted phase during which the ocean became euxinic. Finally, the whole ocean-atmosphere system took on its modern oxygen-dominated cast.

Though the timing of and relationship between the three stages have been topics of active research for many decades, there is still a wide divergence of opinion. Evidence from organic biomarkers (BROCKS et al., 2003b; BROCKS et al., 1999; SUMMONS et al., 1999) and arguments concerning trace element mobility (ROSING and FREI, 2004) and biological productivity (DES MARAIS, 2000) have convinced many that O₂-generating cyanobacteria and aerobic eukaryotes evolved no later than ~2.78 Ga and perhaps as long ago as 3.7 Ga. Meanwhile, the developing record of mass-independent fractionation of sulfur isotopes in the sedimentary record, as well as some other geochemical tracers, has been interpreted as supporting a protracted atmospheric oxygenation over the period of ca. 2.5-2.2 Ga (FARQUHAR and WING, 2003).

An early origin for oxygenic photosynthesis demands an explanation of how surface oxidation was muted for perhaps as long as 1500 My, until cyanobacteria finally

* Adapted from R. E. Kopp, J. L. Kirschvink, I. A. Hilburn, and C. Z. Nash (2005). The Paleoproterozoic Snowball Earth: A climate disaster triggered by the evolution of oxygenic photosynthesis. *Proceedings of the National Academy of Sciences* 102: 11131-11136, doi:10.1073/pnas.0504878102.

surmounted some geochemical, environmental, or ecological barrier and successfully oxidized the planet. Perhaps this scenario is correct, and some abiotic change, such as the long-term escape of hydrogen to space (CATLING et al., 2001), was the direct cause of planetary oxygenation. We suggest, however, that the data are also consistent with scenarios without oxygenic photosynthesis in the Archean. Herein we discuss an alternate hypothesis: one in which the evolution of cyanobacteria destroyed a methane greenhouse and thereby directly and rapidly triggered a planetary-scale glaciation, the ~2.3–2.2 Ga Makganyene Snowball Earth.

I.2 Geological setting

The earliest evidence for glaciation comes from the late Archean and early Proterozoic, which suggests Earth at this time experienced global temperatures not much different from those today. The oldest known mid-latitude glaciation, recorded in the Pongola Supergroup diamictite, occurred at 2.9 Ga (NHELKO, 2004). The period from 2.45 Ga until some point before 2.22 Ga saw a series of three glaciations recorded in the Huronian Supergroup, Canada (YOUNG et al., 1998) (Figure I-1). The final glaciation in the Huronian, the Gowganda, is overlain by several kilometers of sediments in the Lorrain, Gordon Lake, and Bar River Fms. The entire sequence is penetrated by the 2.22 Ga Nipissing diabase (CORFU and ANDREWS, 1986); the Gowganda Fm. is therefore significantly older than 2.22 Ga.

In its eastern domain, the Transvaal Supergroup, South Africa, contains two glacial diamictites, in the Duitschland and Boshhoek Fms. The base of the Timeball Hill Fm., which underlies the Boshhoek Fm., has a Re-Os date of 2316 ± 7 Ma (HANNAH et al., 2004). The Boshhoek Fm. correlates with the Makganyene diamictite in the western domain of the Transvaal Basin, the Griqualand West region. The Makganyene diamictite interfingers with the overlying Ongeluk flood basalts, which are correlative to the Hekpoort volcanics in the eastern domain and have a paleolatitude of $11^\circ \pm 5^\circ$ (EVANS et al., 1997). In its upper few meters, the Makganyene diamictite also contains basaltic andesite clasts, interpreted as being clasts of the Ongeluk volcanics. The low paleolatitude of the Ongeluk volcanics implies that the glaciation recorded in the Makganyene and Boshhoek Fms. was planetary in extent: a Snowball Earth event (TAJKA, 2003). Consistent with earlier whole-rock Pb-Pb

measurements of the Ongeluk Fm. (CORNELL et al., 1996), the Hekpoort Fm. contains detrital zircons as young as 2225 ± 3 Ma (DORLAND, 2004), an age nearly identical to that of the Nipissing diabase in the Huronian Supergroup. As the Makganyene glaciation begins some time after 2.32 Ga and ends at 2.22 Ga, the three Huronian glaciations predate the Makganyene Snowball.

In contrast to the Makganyene Fm., the three Huronian diamictites are unconstrained in latitude. Poles from the Matachewan dyke swarm, at the base of the Huronian sequence, do indicate a latitude of $\sim 5.5^\circ$ (BATES and HALLS, 1990), but about 2 km of sedimentary deposits separate the base of the Huronian from the first glacial unit (YOUNG et al., 2001), which makes it difficult to draw conclusions about the latitude of the glacial units based on these poles. Low-latitude poles in the Lorrain Fm. (SCHMIDT and WILLIAMS, 1999; WILLIAMS and SCHMIDT, 1997), which conformably overlies the Gowganda diamictite, are post-depositional overprints (HILBURN et al., 2005).

I.3 Mass-independent fractionation of sulfur

The recent discovery of mass independent fractionation (MIF) of S isotopes in Archean and early Proterozoic rocks has provided a major constraint on atmospheric O_2 . Large MIF of S (up to several hundred per mil) is produced by photolysis of SO_2 to S by light of wavelengths < 200 nm, which would have been unable to penetrate to the lower atmosphere had O_2 levels been above a few percent of the present atmospheric level (PAL) (FARQUHAR et al., 2001). To preserve MIF, multiple atmospheric S species must be maintained as partially isolated reservoirs, rather than being homogenized by oxidation of reduced species like hydrogen sulfide and polysulfur, as would occur at $> \sim 10^{-5}$ PAL O_2 (PAVLOV and KASTING, 2002). Mixing and dilution of the atmospherically-fractionated component, both in the atmosphere and in the oceans, presumably yields the observed Archean MIF values of up to $\sim 10\%$ (ONO et al., 2003). An active oceanic S cycle, as would exist at moderately high O_2 levels, would also likely prevent the preservation of MIF.

Prior to the deposition of the ~ 2.32 Ga Rooihogite and Timeball Hill Fms. in the Transvaal Supergroup (BEKKER et al., 2004; HANNAH et al., 2004) and the McKim Fm. in the Huronian Supergroup (WING et al., 2002), sedimentary sulfides often display MIF (BEKKER

et al., 2004; FARQUHAR et al., 2000; FARQUHAR and WING, 2003) over an order of magnitude larger than the largest values observed in modern sulfate aerosols (ONO et al., 2003; SAVARINO et al., 2003). One plausible interpretation of the diminished MIF observed in the Rooihogite, Timeball Hill, and McKim Fms. is a rise in atmospheric O₂. At present, only glaciers record the MIF sometimes present in sulfate aerosols; in the marine environment, with fluvial input composing about 90% of sulfate input and aerosols about 10%, MIF is not preserved (ONO et al., 2003). The small range of MIF could reflect an environment in which atmospheric chemistry began to approach modern conditions, decreasing the magnitude of MIF, but in which aerosols formed the major component of marine sulfate input, allowing its preservation.

The small range of MIF also permits an opposite interpretation. Rather than a decrease in atmospheric fractionation, the diminution could be a product of increased continental input and ocean/atmosphere mixing driven by glacial conditions. The period of 2.5–2.2 Ga was a time of glaciations. Enhanced glacial weathering could have made unfractionated sulfur from igneous sources a larger part of the marine sulfur budget, while sharper thermal gradients would have driven homogenization of the sulfur pool. Both effects would have decreased sedimentary MIF. If this interpretation is correct, only the final decrease of MIF after ~2.09 Ga may reflect the rise of atmospheric O₂, and the oxygenation event may have been more rapid than the length of FARQUHAR and WING's (2003) MIF Stage II (2.45–2.09 Ga) indicates.

I.4 The appearance of local oxygen

Both the Huronian and the Transvaal Supergroups contain features suggestive of but not demanding the first appearance of O₂ in the period between the Gowganda and Makganyene glaciations. As noted previously (WING et al., 2002), MIF in the Huronian rocks examined so far is at diminished values compatible with either increased atmospheric O₂ or enhanced glacial weathering and ocean/atmosphere mixing. The Lorrain Fm. contains red beds, as well as a hematitic paleosol at Ville-Marie, Quebec, and the Bar River Fm. contains pseudomorphs after gypsum, consistent with an increase in sulfate levels from oxidative

weathering of sulfide minerals on land. In the Transvaal Supergroup, the upper Timeball Hill Fm., like the Lorrain Fm., contains red beds.

Table I-1. Midpoint potentials of relevant redox couplets

Redox couplet	E (mV)	
	pH 7	pH 8
CO ₂ / CH ₄ (a,b)	-230	-289
SO ₄ ²⁻ / HS ⁻ (c)	-217	-284
Fe(OH) ₃ (ferrhydrite) / Fe ²⁺ (c)	-5	-183
UO ₂ (CO ₃) ₂ ²⁻ / UO ₂ (uraninite) + CO ₂ (a,d)	-18	-137
NO ₃ ⁻ / NH ₄ ⁺ (c)	+366	+292
P ₈₇₀ /P ₈₇₀ ⁺ (purple bacteria)	~+450	
MnO ₂ (pyrolusite) / Mn ²⁺ (c)	+490	+372
NO ₃ ⁻ / N ₂ (c)	+717	+646
O ₂ / H ₂ O	+815	+756
P ₆₈₀ /P ₆₈₀ ⁺ (Photosystem II)	~+1100	

a. Calculated for pCO₂ = 100 mbar. b. Calculated for pCH₄ = 1 mbar. c. Calculated with all aqueous reactants at 1 mM. d. Calculated with dissolved U species at 20 nM. (All reactants not specifically noted are at standard state. Thermodynamic constants from (DREVER, 1997; LANGMUIR, 1978). Photosystem potentials from (WHITE, 2000).)

Stronger evidence for O₂ appears after the Makganyene glaciation. The Ongeluk Fm. is overlain by the Hotazel Fm., which consists predominantly of banded iron formation (BIF). The basal half meter of the Hotazel Fm. contains dropstones (KIRSCHVINK et al., 2000) (see Supporting Information), which suggests it was deposited toward the end of the glacial period. The Hotazel Fm. hosts a massive Mn member (KIRSCHVINK et al., 2000): a blanket of Mn deposition unmatched by any other known in the world, ~50 m thick and with an erosional remnant, the Kalahari Mn Field, measuring ~11x50 km in extent (CAIRNCROSS et al., 1997).

The Kalahari Mn Field indicates the release of large quantities of O₂ into the ocean and therefore suggests a highly active post-glacial aerobic biosphere. In seawater at circumneutral pH, only NO₃⁻ and O₂ can chemically oxidize soluble Mn²⁺ to produce insoluble Mn(IV) (GAIDOS et al., 1999) (Table I-1). Though a Mn²⁺ oxidizing phototroph could also produce Mn(IV), no such organism has ever been identified. Given the high

redox potential of the Mn(IV)/Mn(II) couplet, it is likely no such organism exists. The unexcited P_{870} reaction center in purple bacteria has a redox potential too low to accept electrons from Mn(II) (Table 1), but no known photosystem reaction center aside from the P_{670} reaction center of photosystem II has a higher redox potential. Photosynthetic reduction of Mn(IV) would therefore likely require a two-part photosystem akin to that involved in oxygenic photosynthesis.

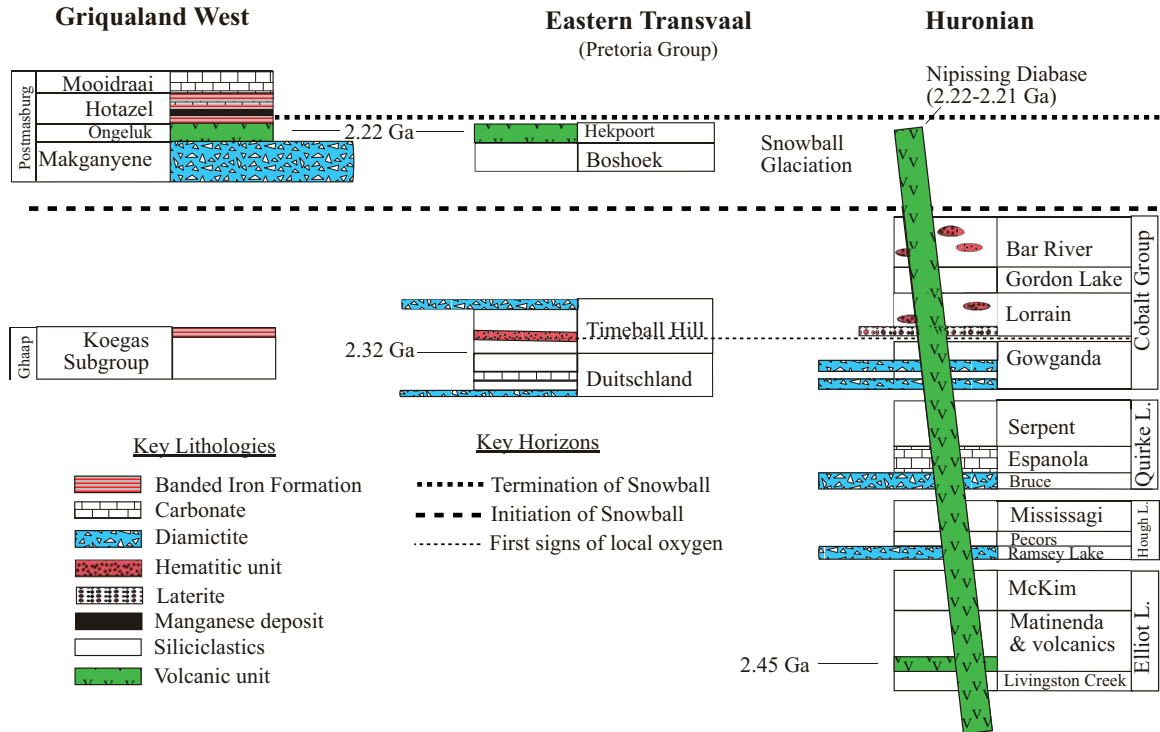


Figure I-1: Proposed correlation of the Huronian Supergroup and the upper Transvaal Supergroup. The three Huronian glacial units, penetrated and capped by the Nipissing diabase, predate the Makganyene diamictite in the Transvaal. The uppermost Huronian glacial unit, the Gowganda Fm., is overlain by hematitic units, perhaps reflecting a rise in O_2 . The basal Timeball Hill Fm. contains pyrite with minimal MIF (BEKKER et al., 2004), while the upper Timeball Hill Fm., which we suggest is correlative to the Lorrain or Bar River Fms., contains red beds. The Makganyene diamictite records a low-latitude, Snowball glaciation (KIRSCHVINK et al., 2000), perhaps triggered by the destruction of a CH_4 greenhouse. It is overlain by the Kalahari Mn Field in the Hotazel Fm., the deposition of which requires free O_2 . Transvaal stratigraphy is based on (DORLAND, 2004); Huronian stratigraphy is based on (YOUNG et al., 2001).

One plausible interpretation of the sequence of events leading up to the Paleoproterozoic Snowball Earth is shown in Figure I-1 and is as follows:

- 1) Three glaciogenic units were deposited in the Huronian. The extent of the glaciations is not constrained, but they generally lack the lithographic features associated with Snowball Earths, such as a sharp transition from a diamictite to a cap carbonate (HOFFMAN and SCHRAG, 2002). While the Espanola carbonate (BERNSTEIN and YOUNG, 1990) could be a cap for the Bruce glaciation, without paleomagnetic data or additional lithographic features, its presence alone is insufficient to conclude that the Bruce glaciation was a Snowball event.
- 2) Some of the earliest continental red beds were deposited in the Firstbrook member of the Gowganda Fm. and in the Lorrain and Bar River Fms. in Canada, as well as in the upper Timeball Hill Fm. in South Africa. The basal Timeball Hill Fm. has recently been dated at 2316 ± 7 Ma (HANNAH et al., 2004). In our proposed correlation, all the red bed-bearing units were deposited after the last Huronian glaciation and before the Makganyene glaciation. The formation of the red beds could involve local O_2 , although it does not demand it (WALKER, 1987). Syngenetic pyrite from the basal Timeball Hill Fm. shows only slight MIF of S (BEKKER et al., 2004), consistent with the initiation of planetary oxygenation or enhanced glacial activity.
- 3) The low-latitude glaciation that formed the Makganyene and Boshhoek diamictites (EVANS et al., 1997) was initiated when the production of O_2 triggered the collapse of a methane greenhouse. Although PAVLOV et al. (2001) proposed a similar trigger, they assumed a delay of at least ~ 400 My between the onset of oxygenic photosynthesis and its surficial expression. We suggest a more immediate linkage.
- 4) The Nipissing diabase intruded into the Huronian sequence (NOBLE and LIGHTFOOT, 1992), and the Ongeluk and Hekpoort volcanics were deposited (CORNELL et al., 1996).
- 5) The Hotazel Fm., which includes BIF and Mn members, was deposited in oxygenated waters in the aftermath of the Snowball.
- 6) The upper siderite facies of the Hotazel Fm. and perhaps also part of the overlying Moodraai dolomite were deposited as cap carbonates in the process of removing CO_2 from a thick post-Snowball greenhouse (KIRSCHVINK et al., 2000).

I.5 An ecological stoichiometry model of planetary oxygenation

In order for cyanobacteria to be directly responsible for triggering a planetary glaciation, they must have been able to produce enough O₂ to destroy the methane greenhouse before the carbonate-silicate weathering cycle could compensate. On sufficiently long timescales, global cooling would slow silicate weathering and carbonate precipitation, thereby allowing CO₂ to build up in the atmosphere (WALKER et al., 1981). The response time of the carbonate-silicate weathering cycle is generally estimated at ~1 My (BERNER et al., 1983), although the time to replace the greenhouse capacity lost in a methane greenhouse collapse may be longer. To estimate the timescale for destruction of the methane greenhouse, we constructed a steady-state ocean biogeochemistry model based upon the assumptions that biological productivity was controlled by P and N and that Fe(II) oxidation was the main inorganic oxygen sink. We took the minimum of the productivity calculated assuming P limitation and the productivity calculated assuming N limitation as our model productivity. Results are shown in Figure I-2.

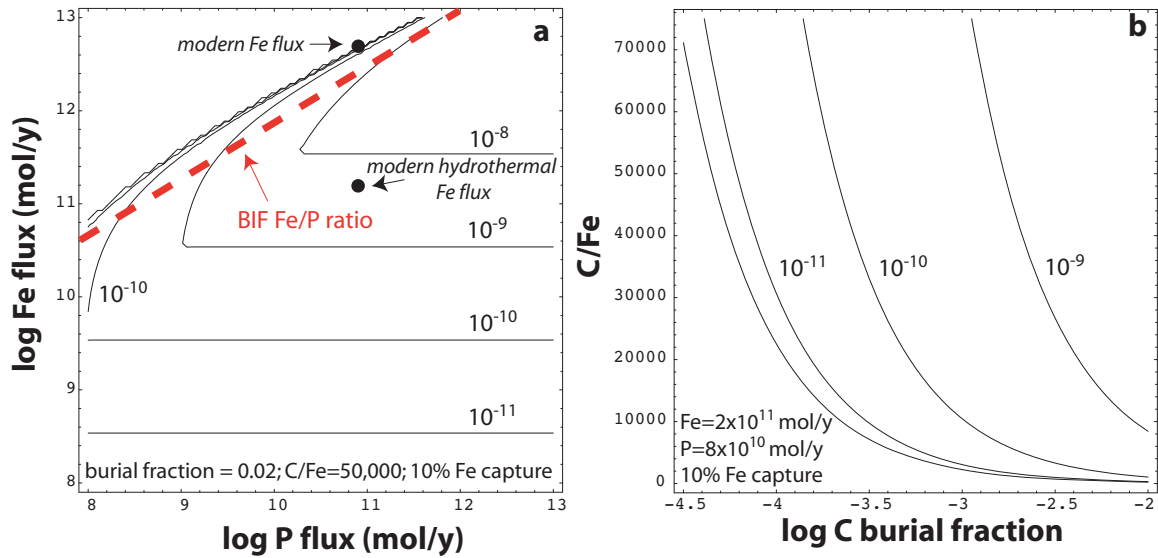


Figure I-2: (a) Modeled O_2 production at different levels of P and Fe flux into the photic zone. Contours are labeled in bar net O_2/y . Following BJERRUM and CANFIELD (2002), we assumed a carbon burial efficiency of 0.019, a C/P ratio of 185, a P adsorption onto Fe(III) constant of $0.07 \mu M^{-1}$, and mixing velocity of $1.26 \times 10^{18} L/y$. All the P flux and 10% of the Fe flux were assumed available for biological use. The upper, diagonal portions of the contours represent P limitation, while the lower, horizontal portions represent Fe limitation. (b) Modeled O_2 production at varying C burial efficiency and C/Fe ratio. Except for carbon burial efficiency, parameters are as in part a, with P and Fe flux fixed. Observed C/Fe ratios for modern field populations of *Trichodesmium* range from $< 2,000$ to $50,000$.

P-limited ocean model. Following BJERRUM and CANFIELD (2002), we assumed in the P-limited case that P was removed from the ocean either adsorbed onto Fe(III) particles or in organic matter and organic-derived carbonate fluoroapatite. We also assumed P fluxes into and out of the photic zone were balanced and iterated toward a steady state solutions of the equations

$$F_{P,out} = F_{P,in} = \gamma \eta_{C:P} P_{CH_2O} + K_{ads} F_{FeIII,out} [P_d], \quad (I-1)$$

$$P_{CH_2O,anoxy} = \text{Min}[\eta_{C:P} u [P_d] f_{anoxy}, \frac{1}{4} F_{Fe,in}], \quad (I-2)$$

$$P_{CH_2O,oxy} = \eta_{C:P} u [P_d] - P_{CH_2O,anoxy}, \quad (I-3)$$

$$F_{\text{FeIII,out}} = \alpha \text{Min}[F_{\text{Fe,in}}, 4\gamma P_{\text{CH}_2\text{O,oxy}} + P_{\text{CH}_2\text{O,anoxy}}] , \quad (\text{I-4})$$

$$P_{\text{O}_2} = \gamma(P_{\text{CH}_2\text{O,oxy}} + P_{\text{CH}_2\text{O,anoxy}}) - \frac{1}{4}F_{\text{FeIII,out}} , \quad (\text{I-5})$$

where γ is the ratio of organic C production to organic C burial, $\eta_{\text{C:P}}$ is the ratio of carbon to phosphate in buried organic matter, K_{ads} is equilibrium constant for the adsorption of P onto Fe(III) particles, u is the velocity of upwelling bringing nutrient-rich waters into the surface oceans, f_{anoxy} is the maximum fraction of C production for which anoxygenic, Fe(II)-oxidizing photosynthesis can be accountable, and α is the maximum fraction of Fe buried as Fe(III). $F_{\text{Fe,in}}$ is the flux of Fe into the oceans, $F_{\text{FeIII,out}}$ is the flux of Fe(III) out of the oceans, $F_{\text{P,in}}$ is the flux of P into the oceans, $F_{\text{P,out}}$ is the flux of P out of the oceans, $P_{\text{CH}_2\text{O}}$ is the rate of primary productivity, $P_{\text{CH}_2\text{O}}$ is the net rate of surface ocean oxidation in O₂ equivalents, and $[\text{P}_d]$ is the concentration of dissolved P in the oceans.

N-limited ocean model. In a locally aerobic environment, denitrification may have compelled cyanobacteria to engage in the Fe-demanding process of N₂ fixation (FALKOWSKI, 1997). We modeled this using C/Fe ratios observed in field populations of *Trichodesmium* (KUSTKA et al., 2002). We assumed the upwelling flux of Fe to be removed from the photic zone either as ferric particles or in organic matter, through the following modifications:

$$P_{\text{CH}_2\text{O,oxy}} = \eta_{\text{C:Fe}}\beta F_{\text{Fe,in}} - P_{\text{CH}_2\text{O,anoxy}} , \quad (\text{I-6})$$

$$F_{\text{FeIII,out}} = \text{Min}[(1 - \beta)F_{\text{Fe,in}}, 4\gamma P_{\text{CH}_2\text{O,oxy}} + P_{\text{CH}_2\text{O,anoxy}}] , \quad (\text{I-7})$$

where $\eta_{\text{C:Fe}}$ is the ratio of carbon to iron and β is the efficiency of the cyanobacteria in capturing iron.

I.6 Timescale for methane greenhouse collapse

The critical P/Fe flux ratio for net oxidation of the surface ocean increases with the burial rate of C (Figure I-22a). For a P flux similar to today's value of about 8×10^{10} mol/y (BJERRUM and CANFIELD, 2002) and a burial fraction of 2×10^{-2} , similar to modern anoxic

environments, the model results indicate that the critical value is $\sim 1/50$. The current ratio of P flux to hydrothermal Fe flux is $\sim 1/2$, while the ratio of P flux to hydrothermal and terrigenous Fe flux is $\sim 1/64$ (CANFIELD, 1998). Rare earth element patterns of BIFs (KLEIN and BEUKES, 1992) and the stability of terrestrial ferrous sulfides in an anoxic atmosphere suggest that the main source of reactive Fe in the Archean was hydrothermal, so the P/Fe ratio may have been closer to $1/2$ than $1/64$.

When the P/Fe ratio falls below the critical value, essentially all O_2 produced is captured by Fe^{2+} . Above the critical P/Fe value, there is a net release of O_2 (Figure I-2a). Other dissolved O_2 sinks, such as Mn^{2+} , H_2 , and CH_4 , will consume some O_2 , but hydrothermal fluxes of these reductants are up to an order of magnitude less than the flux of Fe^{2+} (ELDERFIELD and SCHULTZ, 1996). At today's levels, these are capable of consuming $\sim 7 \times 10^{10}$ mol O_2/y , equivalent to 4×10^{-10} bar/y. While the flux of H_2S from vent fluids in today's high-sulfate oceans is comparable to that of Fe^{2+} , in an ocean where Fe^{2+} is the main electron donor, H_2S levels would be lower. A formaldehyde rainout flux of $\sim 10^{12}$ mol/y (PAVLOV and KASTING, 2002) would be the largest O_2 sink, capable of adsorbing $\sim 6 \times 10^9$ bar O_2/y , but would be nullified by H_2O_2 rainout once even a small amount of O_2 accumulated in the atmosphere. O_2 production in excess of about 6×10^9 bar/y would therefore be sufficient to initiate CH_4 oxidation, and, once begun, net O_2 production in excess of about 4×10^{-10} bar/y would suffice to continue it. At the rates predicted by our model, destruction of a 1 mbar methane greenhouse, if it occurred at all, would likely occur within a few My, a timescale comparable to the carbonate-silicate weathering cycle. Therefore, either cyanobacteria did not evolve until shortly before the oxygenation event, or the nutrient flux did not reach sufficiently high levels at any point after the evolution of cyanobacteria until then.

If cyanobacteria were present during the Huronian glaciations, the increased P flux into the oceans generated by glacial weathering (FÖLLMI, 1995) should have triggered the oxygenation event. Instead, the oxygenation event seems to correlate with the later Makganyene glaciation; this finding suggests the evolution of cyanobacteria occurred in the interval between the Huronian glaciations and the Makganyene glaciation.

Whether N limitation could have delayed the destruction of a methane greenhouse (FALKOWSKI et al., 2003) depends upon the Fe demand of the N₂ fixers and the ability of cyanobacteria to capture Fe before it reacted with O₂ and sank beneath the photic zone as a ferric precipitate. With anoxic deep waters providing a large source of Fe to the photic zone, life for an early Proterozoic diazotroph would have been easier than for modern diazotrophs that must subsist off of Fe transported from the continents. C/Fe ratios in N₂-fixing populations of *Trichodesmium* range from < 2,000 to 50,000 (KUSTKA et al., 2002). If early cyanobacteria were inefficient at both capturing and utilizing Fe (e.g., C/Fe=2000, capture efficiency=1%), then N limitation could have protected the methane greenhouse, but under more optimistic assumptions (either a higher capture efficiency or a higher C/Fe ratio), it would not have done so (Figure I-2b). The geologic record, not computational models, must ultimately decide.

I.7 Implications of the possible late evolution of cyanobacteria

The interpretation presented here suggests planetary oxygenation began in the interval between the end of the Huronian glaciations and the onset of the Makganyene glaciation, and that the Paleoproterozoic Snowball Earth was the direct result of a radical change in the biosphere. In the Archean and earliest Proterozoic oceans, life may have been fueled predominantly by Fe, with Fe(II) used as the electron donor for photosynthesis and Fe(III) as the main electron acceptor for respiration. The sediments would therefore be moderately oxidizing and the surface waters reduced (WALKER, 1987). Because the redox potential for Mn²⁺ oxidation is much higher than that of Fe²⁺, Mn would have to be removed from the oceans in reduced form. The carbonates precipitated at this time contain up to about 2% Mn (CAIRNCROSS et al., 1997), indicating that Mn²⁺ reached shallow waters and co-precipitated with Ca⁺²; oxidized Mn is extremely rare. The atmosphere was likely reducing. Astrophysical models predict the Sun was substantially dimmer than today, but a CH₄ greenhouse (PAVLOV et al., 2000) produced by methanogens living in a reduced upper ocean would have kept the planet warm enough to allow for the presence of liquid water without leading to massive siderite precipitation (RYE et al., 1995).

This world would have been overthrown when cyanobacteria capable of oxygenic photosynthesis evolved, which molecular phylogenies indicate occurred later than the main bacterial radiation (OLSEN et al., 1994). The surface waters became oxidizing and more productive. Reduced carbon accumulated in the sediments; methanogenesis moved from the surface ocean to the deep ocean, where it was isolated from the atmosphere. Methanotrophy in the ocean and photochemistry in the atmosphere used O_2 to transform atmospheric CH_4 to CO_2 , a less effective greenhouse gas. The rise of O_2 might thus have triggered a glacial interval without the ~400 My delay assumed by others (PAVLOV et al., 2001).

Phosphate flux into the oceans correlates with increased continental weathering during glacial intervals (FÖLLMI, 1995), so increased continental weathering produced by the glaciations may have increased nutrient availability above the threshold for net O_2 release into the atmosphere. Due to the relatively low global temperature, it would have taken only a trace of OH radicals from the oxygenic bloom produced when cyanobacteria appeared in a high-P ocean to damage the CH_4 greenhouse enough to bring average global temperatures below $0^\circ C$. During the at least ~35 My (KIRSCHVINK et al., 2000; PIERREHUMBERT, 2004) it took to build up a sufficient CO_2 greenhouse to escape from the Snowball, hydrothermal fluxes would have built up a rich supply of nutrients in the oceans. When the planet finally warmed, the oceans were ripe for a cyanobacterial bloom. The O_2 produced by the bloom cleared out tens of My of accumulated reductants and thus produced the Kalahari Mn field (KIRSCHVINK et al., 2000).

I.8 Biomarker counterevidence for Archean oxygen

Despite the parsimony of cyanobacterial evolution occurring within a few My before the onset of the Paleoproterozoic Snowball Earth, some organic biomarker evidence and indirect sedimentological and geochemical arguments have been used to suggest that the origin of cyanobacteria dates to far earlier times: at least 2.78 Ga, and maybe as long ago as 3.7 Ga.

The critical piece of evidence placing the origin of cyanobacteria and locally oxic environments in the Archean is the discovery in bitumens from rocks as old as 2.78 Ga of organic biomarkers apparently derived from lipids employed by cyanobacteria and

eukaryotes in their cell membranes. While BROCKS et al. (2003a) concluded that the bitumens were likely syngenetic, they could not exclude the possibility that they were post-depositional contaminants. Even if the biomarkers are as old as their host rocks, however, the uniformitarian extrapolation of modern lipid distributions to the Archean should be viewed cautiously.

Hopanes. Among modern organisms, 2-methyl-bacteriohopanepolyol (2-methyl-BHP) is produced predominantly by cyanobacteria and in trace quantities by methylotrophs like *Methylobacterium organophilum* (SUMMONS et al., 1999). Hopanes derived from 2-methyl-BHP can be preserved in sedimentary rocks, where they have been used as tracers for cyanobacteria (SUMMONS et al., 1999). Hopanol synthesis has traditionally been assumed, based upon the understood modern distribution of hopanols, to occur only in aerobic organisms. FISCHER et al. (2004) recently demonstrated, however, that *Geobacter sulfurreducens* can synthesize diverse hopanols, though not 2-methyl-hopanols, when grown under strictly anaerobic conditions. Thus, fossil hopanes do not necessarily imply the presence of O₂-producing organisms, and nothing about 2-methyl-hopanols suggests that they are any different in this respect. Archean 2-methyl-hopanes might also have been produced by ancestral cyanobacteria that predated oxygenic photosynthesis.

Steranes. Produced by eukaryotes for use in the cell membrane, sterols are preserved in the rock record as steranes. BROCKS et al. (2003b; 1999) recovered steranes, along with 2-methyl-BHP, from 2.78 Ga Pilbara Craton shales. Because there is no known anaerobic sterol synthesis pathway, they used their discovery to argue for the presence of O₂.

Cholesterol biosynthesis in modern organisms is a long biochemical pathway that employs four O₂-dependent enzymes: (1) squalene epoxidase, (2) lanosterol 14 α -methyl demethylase cytochrome P450, (3) sterol-4 α -methyl oxidase, and (4) lathosterol oxidase (RISLEY, 2002). These O₂-dependent enzymes perform reactions that, though not currently known to occur biochemically in anaerobic organisms, could feasibly occur without O₂. Moreover, the substitution of an O₂-dependent enzyme for an anaerobic step in a biosynthetic pathway appears to be a common evolutionary occurrence. RAYMOND and BLANKENSHIP (2004) found that, of the 473 O₂-dependent enzymatically catalyzed reactions in the BioCyc

database, twenty have at least one O₂-independent counterpart that performs the same reaction. For instance, AcsF catalyzes an O₂-dependent cyclization step in the synthesis of chlorophyll and bacteriochlorophyll, a pathway that must have existed prior to the evolution of oxygenic photosynthesis. The O₂-independent enzyme BchE performs the same reaction as AcsF but uses vitamin B12 in place of O₂ (2004). The assumption that sterol synthesis is always O₂-dependent and always has been therefore merits close inspection.

Indeed, the Hamersley bitumens include their own cautionary message about the application of uniformitarian assumptions to fossil lipids. Dinosterane is generally accepted to be characteristic of dinoflagellates and is interpreted as a dinoflagellate biomarker in Phanerozoic rocks (MOLDOWAN and JACOBSON, 2000). Yet even though an Archean origin for dinoflagellates seems implausible, as it would indicate the Archean origin of modern eukaryotic group not known in the fossil record until at least the Paleozoic (FALKOWSKI et al., 2004), BROCKS et al. (2003b) found dinosterane. They interpreted the molecule as the product of eukaryotes of unknown affinities, though an alternative explanation is that these modern-style putative Archean biomarkers are contaminants.

I.9 Indirect counterevidence for Archean oxygen

While organic biomarkers may be difficult to interpret, they are a significant improvement upon several other geological tracers that have been used to argue for the presence of cyanobacteria and environmental oxygen: microfossils, stromatolites, BIFs, and assorted isotopic fractionations.

Microfossils. Before 2 Ga, when diversified assemblages with affinities to major groups of cyanobacteria first appear in the fossil record, the microfossil record is murky (AMARD and BERTRAND-SARFATI, 1997). Some have interpreted filamentous forms in earlier rocks as cyanobacterial remains (AWRAMIK et al., 1983; SCHOPF, 1993; SCHOPF and PACKER, 1987), but BRASIER et al. (2002) have recently questioned the biogenic nature of these objects. Moreover, cyanobacteria cannot be identified solely by a filamentous form. Many non-oxygenic bacteria are also filamentous, including some mat-forming green non-sulfur and purple sulfur bacteria (D'AMELIO et al., 1987; PIERSON, 1994) and a methanogenic archeon (JOULIAN et al., 2000). The wide variety of filamentous prokaryotes highlights a problem in

identifying fossil microbes lacking clear evidence of cell differentiation based on morphology: any given form has probably arisen many times in Earth history, both in extant and extinct organisms.

Stromatolites and BIFs. Two types of late Archean rock formations have often been interpreted as indicating cyanobacterial activity: stromatolites and BIFs. DES MARAIS (2000) argued that large stromatolite reefs indicate the presence of cyanobacteria and therefore a locally aerobic environment, but large reefs can also form under anaerobic conditions. Populations of anaerobic methane oxidizers, for instance, have built massive reefs at methane seeps in the Black Sea (MICHAELIS et al., 2002). In addition, the Archean and Paleoproterozoic oceans were likely more supersaturated with respect to calcite and aragonite than the modern oceans (GROTZINGER and KASTING, 1993), which would have facilitated the precipitation of large reefs even without biological participation. Indeed, abiotic processes may have played a major role in the formation of many Precambrian stromatolites (GROTZINGER and KNOLL, 1999). Moreover, while the deposition of ferric iron in BIFs has traditionally been taken to imply the presence of free O₂ (CLOUD, 1973; HOLLAND, 1973; KLEIN and BEUKES, 1992), BIFs could also have formed in a O₂-free environment, either by photo-oxidation (CAIRNS-SMITH, 1978) or by Fe(II)-oxidizing phototrophic bacteria (KAPPLER and NEWMAN, 2004; WIDDEL et al., 1993).

Isotopic evidence. ROSING and FREI (2004) argued based on isotopic evidence that > 3.7 Ga meta-shale from West Greenland preserves signs of an aerobic ecosystem. They found organic carbon with $\delta^{13}\text{C}$ values of -25.6‰ in the same sediments as Pb with isotopic ratios indicating that the samples were originally enriched in U with respect to Th and interpreted this as reflecting an environment in which U could be cycled between its reduced, insoluble U(IV) form and its oxidized, soluble U(VI) form. They concluded the light C was produced by oxygenic phototrophs and that biogenic O₂ had permitted the redox cycling of U. However, all biological C fixation pathways and some abiotic mechanisms can produce light C, and, just like the Fe(III) in BIFs, U(VI) can form in the absence of O₂. At circumneutral pH values, the midpoint potential of the U(VI)/U(IV) couplet is ~0 V, similar to the Fe(III)/Fe(II) couplet and considerably less oxidizing than Mn(IV)/Mn(II), NO₃⁻/N₂, or O₂/H₂O (see Table I-1).

A strong negative $\delta^{13}\text{C}$ excursion in organic C at ~2.7 Ga has been interpreted as evidence for the evolution of aerobic methanotrophy (HAYES, 1994). Such light C suggests repeated fractionation: first in the production of CH_4 subsequently oxidized to CO_2 , then in re-reduction by a primary producer. Similar fractionations are observed today in environments with methanotrophs. But while CH_4 oxidation was once thought to require O_2 , geochemical measurements (BARNES and GOLDBERG, 1976) and recent microbiological work (BOETIUS et al., 2000; ORPHAN et al., 2002) have demonstrated that CH_4 oxidation can also occur with alternative electron acceptors, so O_2 is not needed to explain the isotopic excursions. Though the anaerobic methane oxidizing bacteria studied today rely upon sulfate, which is unlikely to have been available in a high-Fe Archean ocean, thermodynamics permits a variety of electron acceptors, including Fe(III), to be used for CH_4 oxidation.

Sulfur isotope data indicate local spikes in sulfate concentration starting ~3.45 Ga (CANFIELD et al., 2000; SHEN et al., 2001). CANFIELD et al. (2000) argued these spikes were produced in high- O_2 environments. But given the low redox potential of the sulfide/sulfate couplet, local sulfate spikes can be explained by scenarios that do not involve O_2 . Moreover, sedimentary sulfate deposits, which disappear in the rock record after ~3.2 Ga (HUSTON and LOGAN, 2004), do not reappear until after the Huronian glaciations, which suggests high-sulfate conditions were rare.

None of these indirect lines of evidence necessitate oxygenic photosynthesis. The case for cyanobacteria and locally oxic environments existing before the disappearance of MIF of S isotopes and the massive deposition of Mn in the Kalahari Mn Field rests, at the moment, solely on steranes.

I.10 Future directions

Our model for a Paleoproterozoic origin of cyanobacteria is testable by several methods. It suggests that sterols in Archean rocks, if they are original, were synthesized by anaerobic reactions. It therefore should be possible to find or engineer enzymes capable of synthesizing cholesterol under anaerobic, biochemically-plausible conditions. In addition, a continuous biomarker record that stretches back from time periods when O_2 is definitely

present into the Archean might reveal transitions in community composition. Current work with samples from recent drilling programs targeting the late Archean and the Paleoproterozoic has begun this task. An intensive search for biomarkers with definite relationships to metabolism, such as those derived from the pigment molecules of phototrophic bacteria, would also produce a more convincing record. A search for cyanobacterial or eukaryotic fossils that predate 2.0 Ga yet have affinities to modern groups would complement the geochemical approaches.

With respect to the record of MIF of sulfur, the timeline we propose for a rapid oxygenation scenario suggests that decreased fractionation during the interval of the Huronian glaciations may be a byproduct of enhanced glacial weathering and ocean/atmosphere mixing. If this scenario is correct, a similar phenomenon should have occurred in association with the Pongola glaciation at ~2.9 Ga. Investigation of the Huronian deposits where low-MIF sulfur is found should reveal these deposits to be sedimentologically immature, reflecting glacial input. Additionally, the syngenicity of the MIF values should be tested through techniques such as the paleomagnetic search for significantly post-depositional formation of sulfides.

Finally, our model predicts that the Makganyene Snowball Earth was a singular event. Convincing paleomagnetic evidence (including positive synsedimentary field tests) that demonstrated the Huronian glaciations were low-latitude would contradict our model and instead support a protracted episode of planetary oxygenation with multiple Snowball events not directly triggered by a singular event, the evolution of cyanobacteria.

I.11 Summary

Due to the importance of the evolution of cyanobacteria and the planetary oxygenation event in Earth history, it is particularly useful to consider multiple working hypotheses about these events. We propose a model that takes a skeptical attitude toward the evidence for Archean cyanobacteria and a protracted early Proterozoic planetary oxygenation. In our alternative scenario, an evolutionary accident, the genesis of oxygenic photosynthesis, triggered one of the world's worst climate disasters, the Paleoproterozoic Snowball Earth. Intensive investigation of the time period of the Paleoproterozoic glaciations may reveal

whether a novel biological trait is capable of radically altering the world and nearly bringing an end to life on Earth.

*Appendix II***AN AUTOMATIC SAMPLE CHANGER FOR RAPID, PRECISE, AND HIGH-SENSITIVITY ACQUISITION OF PALEOMAGNETIC AND ROCK MAGNETIC DATA*****II.1 Introduction**

Most samples collected for paleomagnetic analysis possess multiple magnetic components of differing stability, which could potentially have been acquired during any part of their geological history. Nearly half a century ago, AS and ZIJDERVELD (1958) recognized that progressive demagnetization analysis could sometimes preferentially remove some of these components relative to others. A variety of thermal, chemical, magnetic, and even microwave demagnetization techniques have been developed for this purpose. Principal component analysis (KIRSCHVINK, 1980b) provides a systematic method for deducing a set of component magnetization vectors from the results of demagnetization experiments.

A long-standing challenge in paleomagnetism is conducting the large number of demagnetization experiments needed to determine accurately the magnetic history of a given specimen. Since paleomagnetism is a statistical science, paleomagnetic studies necessarily involve the analysis of large numbers of specimens, each one of which must be demagnetized completely. Although the introduction of superconducting moment magnetometers in the early 1970s increased the speed of individual measurements (GOREE and FULLER, 1976), the advance required researchers or their students to change samples by hand every few minutes. The labor involved with conducting detailed demagnetization experiments has often led to inappropriate short-cuts, such as demagnetizing only a pilot group of specimens and then batch-processing the remaining samples at the "best" step. These methods are now recognized as statistically invalid (KIRSCHVINK, 1980b; VAN DER VOO, 1990).

* Co-authored with Joseph L. Kirschvink.

During the past three decades, numerous groups have attempted to reduce the labor intensity of paleomagnetic studies. Alan Cox introduced computer-controlled alternating field demagnetization in the late 1970s. His instrument allowed individual specimens to be loaded once for a complete three-axis demagnetization. However, his system did not automate the task of changing specimens several times per hour nor was it easy to adapt for thermal demagnetization.

The subsequent development of superconducting magnetometers for long-core measurements (e.g., NAGY and VALET, 1993) allowed the acquisition of high-resolution data from soft-sediment drill cores (e.g., VEROSUB, 1998). The long-core systems are not adaptable to the traditional discrete paleomagnetic specimen, however, and often suffer from problems with spatial resolution and noise. The magnetization of the sample holding tray is often larger than that of many important but weakly magnetized sediments.

Automating parts of the mechanical process of measuring discrete specimens enables higher-throughput paleomagnetic measurements and frees researchers to focus on the tasks of data analysis and scientific interpretation. In this article, we describe an automatic sample changer for paleomagnetic and rock magnetic measurements built upon a vertical-access superconducting rock magnetometer (SRM), such as that marketed for many years by 2G EnterprisesTM in Menlo Park, California. In addition to reducing the physical labor required for paleomagnetic measurements, the sample changer also increases the fraction of time the magnetometer can be used and provides a low magnetization sample holder.

The system described here is currently in use at four universities in the United States (the California Institute of Technology, Occidental College, Yale University, and the Massachusetts Institute of Technology). In its current form, it has been in use at Caltech since 2004, and a predecessor system was first used in 1997. Several other facilities, both in the United States and around the world, are in the process of or are planning to install systems based on this design.

II.2 Hardware and software

One limitation of most superconducting moment magnetometers now in use is the noise introduced by the sample holders used to move samples into and out of the measurement region of the magnetometers. Sample holders typically have magnetic moments two to three orders of magnitude greater than the root-mean-square instrument noise level with of modern DC SQUID sensors ($\sim 2 \times 10^{-13} \text{ Am}^2$). Straightforward back-of-the-envelope calculations indicate that meaningful information about the magnetic field can be preserved at levels down to $\sim 10^{-16} \text{ Am}^2$ (KIRSCHVINK, 1982; WEISS et al., 2001), comparable to the magnetic moment of a single magnetotactic bacterium. We have found that many industrial plastics (including virgin Teflon) contain ppb-levels of ferromagnetic contaminants with rock-magnetic properties similar to that of fine-grained magnetite (e.g., KOBAYASHI et al., 1995). Although it is possible to demagnetize a sample holder to measure the remanence moment of weakly magnetized rocks, many rock-magnetic experiments require exposing both the sample and the holder to strong magnetizing fields.

The least-magnetic material we have yet encountered is ultra-high-purity quartz glass, which is prohibitively expensive. However, regular purity quartz glass tubing with 1 mm thick walls can be soaked in concentrated HCl for extended periods (hours to days) to reduce ferromagnetic contamination. We employ ~ 1 m long quartz glass tubes in the sample changer system (Figure II-1). The tube hangs from a chassis connected to two microprocessor-controlled DC servo motors (QuickSilver Controls, San Dimas, CA). The motors are located above the magnetic shielding of the room containing the SRM. One servo motor, the “turner” motor, allows the tube to rotate, while the other, the “up/down” motor moves the tube vertically. In the present configuration, the motors run on a 48 V DC supply. The positions of the rotors are encoded optically to a precision of 1 part in 4000.

Within the shielded room, a Teflon-coated tray is suspended flat above the SRM, with one 3 cm hole in the tray aligned above the magnetometer cavity. A belt of two hundred 3 cm diameter cylindrical Delran plastic cups, labeled with consecutive numbers, runs along the top of the tray, connected by a pulley system to a μ metal-shielded DC servo motor, dubbed the “changer motor.” As shown on Figure 2, the cups are tapered along the top to minimize jamming problems and are held together by brass pins into a continuous ‘snake chain.’ The

brass pins also provide an orienting mark for sample alignment relative to the magnetometer axes. O-rings made from rubber with self-adhesive backing are attached to the interior bottom of each cup and provide friction for holding samples in place. A thin strip of adhesive weather-stripping foam (like that used to insulate window sills or door frames) is attached to the back side of every sample cup to prevent the specimens from becoming misaligned when the snake-chain belt moves. Every tenth cup in the belt is lacking a bottom, so that the magnetometer cavity is exposed when such a cup is on top of the hole on the tray.

The quartz glass sample holder tube, which hangs directly above the magnetometer cavity, is stabilized by a plastic guide 7.5 cm above the sample tray. The up/down motor allows the quartz glass rod to move vertically in a range between a position 7.5 cm above the tray (the “home” position) and the SRM sense region (the “measure” position). The top of the tube is connected to a brushless 600W vacuum blower motor regulated by relay switches.

The servo motors, the SRM SQUID control boxes, and the vacuum relay switches communicate with the controlling computer by the RS-232 protocol. In addition, the computer can optionally be connected to controllers for alternating field (AF) demagnetization, isothermal remanent magnetization (IRM), anhysteritic remanent magnetization (ARM) biasing field, and susceptibility coils. The current control software for the sample changer system, Paleomag 2007, is written in Visual Basic 6 (Microsoft, Redmond, WA).

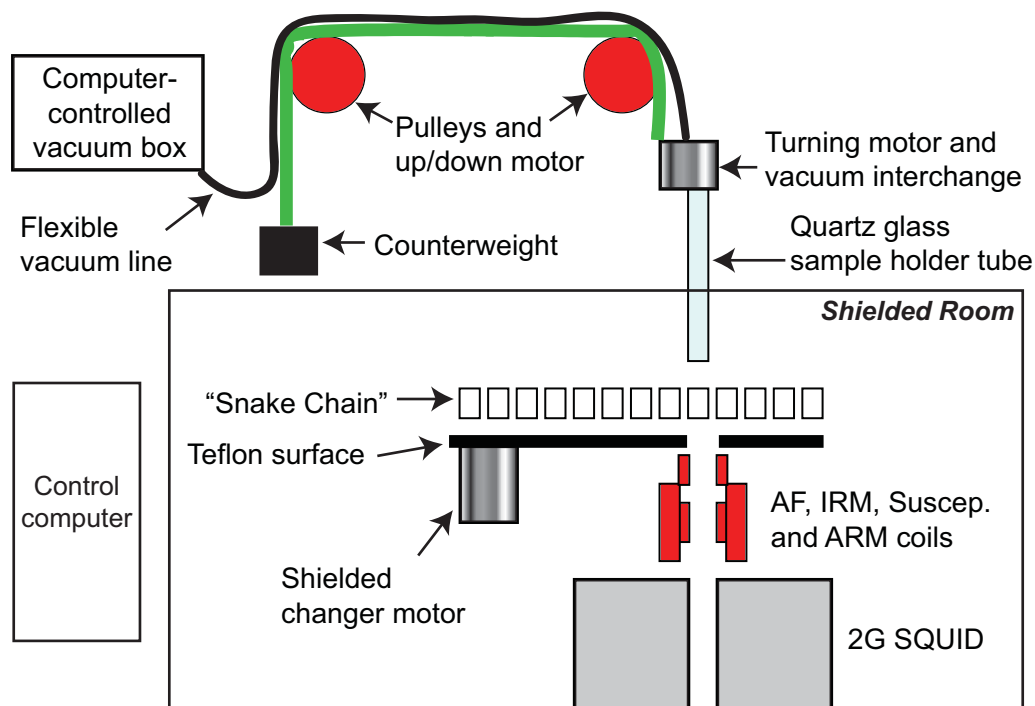


Figure II-1: Block diagram of the sample changer system

II.3 Operations

Samples for use in the sample changer system are cut into cylindrical cores. The cores are usually 2.5 cm in diameter and 1 cm tall, although the sample changer can measure cores as tall as 4 cm. The up direction of the core is marked with an arrow perpendicular to the top and bottom surfaces. To ensure proper orientation of the sample when it is retrieved by the sample changer, it is crucial that the top and bottom surfaces of each core are parallel.

Before users begin making measurements, they set up sample data files using a Microsoft Excel script. Paleomag 2007 uses the Caltech file format for paleomagnetic data. Each sample set is contained within its own directory. A SAM index file in the directory lists the individual samples within the set and records locality latitude, longitude, and magnetic declination, and optionally the plunge and azimuth of a fold axis. Each sample has its own file, which initially provides a sample name, core and bedding strikes and dips, and optionally core volume or mass. As paleomagnetic data is acquired, it is recorded in the sample file. In the rock magnetic mode of operation, measurement data as well as

experimental parameters are also recorded in a comma-separated rock magnetic data file created in the course of the measurements.

Once the files are created, the users identify the sample sets to be measured. For each sample set, a tag describing the current demagnetization step is associated with the set (e.g., “NRM” for the initial measurement, “TT 300” for a 300°C thermal treatment). The user can alternatively instruct the software to perform AF demagnetization treatments or rock magnetic experiments on a sample set.

In the normal operation mode, the user then places oriented samples in the plastic cups on the sample changer tray and informs the software of the range of numbers assigned to the cups in which the samples sit. The automatic measurements then commence.

The software begins by measuring the magnetic moment of the quartz glass sample holder. It turns the changer motor to slide the belt of plastic cups until the nearest empty-bottomed cup is over the hole in the tray. Then, it turns the up/down motor to move the bottom of the glass tube into the “zero” position, ~15 cm above the center of the sense region, and records the measurements from the SQUID read-outs. Next, it lowers the tube into the sense region, measures it, and repeats the measurements after 90°, 180°, and 270° rotations of the tube. It then does a second “zero” position measurement, averages the rotation-corrected measurements of the tube, and subtracts from them the averaged “zero” measurement. This corrected measurement is stored as the most recent holder measurement.

The up/down motors then lift the tube above the sample tray. The changer motors place a sample underneath the tube, and the up/down motors lower the tube until it is touching the sample. The vacuum relays connect the tube to the vacuum motor, thereby enabling the tube to pick up the sample. The sample is lifted above the tray, the sample belt slides so that an empty-bottomed cup is underneath the tube, and the sample is measured in the same fashion as the holder. The software can optionally average together multiple blocks of measurements of the sample. In positioning the sample, the software corrects for the sample height. The average measured sample moment, less the measured holder moment, is recorded in the sample data file, and the sample is returned to its cup. The software records

the orientation of the moment in bedding-corrected and fold-corrected orientations, as well as in the original core coordinates.

By default, the software expects to run measurements on samples oriented in the down direction after running the measurements in the up direction. Therefore, after completing the up measurements, the software prompts the user, both on screen and by email, to flip the samples. (A script on a monitoring computer announces the text of the message, as well as any error messages, to users in the lab.) It then repeats the measurements in the down direction and averages together the rotation-corrected up and down measurements. The user is notified when the samples are completed. The sample changer is capable of processing ~50 samples per hour in one direction. Data analysis can then be performed using software such as Paleomag (JONES, 2002) or PaleoMac (COGNE, 2003). Numerous publications report data acquired using the sample changer system or the predecessor system at the California Institute of Technology.

II.4 Automatic error checking

The software checks for measurements errors at two opportunities. First, for samples with moments stronger than 500 pAm^2 , the software checks several statistics after completing a measurement block. It computes a circular standard deviation for the measurement block by calculating the Fischer standard deviation of the unit-normalized measurement vectors. It automatically repeats the measurement block if the circular standard deviation is above a user-specified threshold (by default 8°), the mean rotation-corrected moment is less than the standard deviation of the rotation-corrected measurements, or the mean rotation-correction moment is less than the norm of the induced moment (the portion of the moment that is rotation-invariant).

In addition, after completing the measurements on all samples, the software scans for samples with circular standard deviations above a user-specified threshold, displays their IDs, Fischer standard deviations, total moment, and the ratio of the moment as measured in the up direction to the moment as measured in the down direction, and prompts the user to re-measure those samples. Performing both up and down direction measurements allows the second error check to identify any samples that were poorly aligned in their sample cups.

II.5 Measuring weak samples

The Caltech magnetometer and sample changer system has been successfully used to measure carbonates with moments as weak as few pAm^2 (Figure II-2a, b). The sample changer system supports measuring such weak samples by averaging together multiple measurement blocks on a single sample and by re-measuring and AF demagnetizing the quartz glass sample tube after every nine samples and by re-measuring and AF demagnetizing the quartz glass sample tube after every nine samples. Periodic washing of the quartz glass rod in concentrated HCl and more frequent washing of the rod with alcohol, occasional cleaning of the plastic guide for the rod, and handling samples wearing particle-free plastic gloves also increase sensitivity.

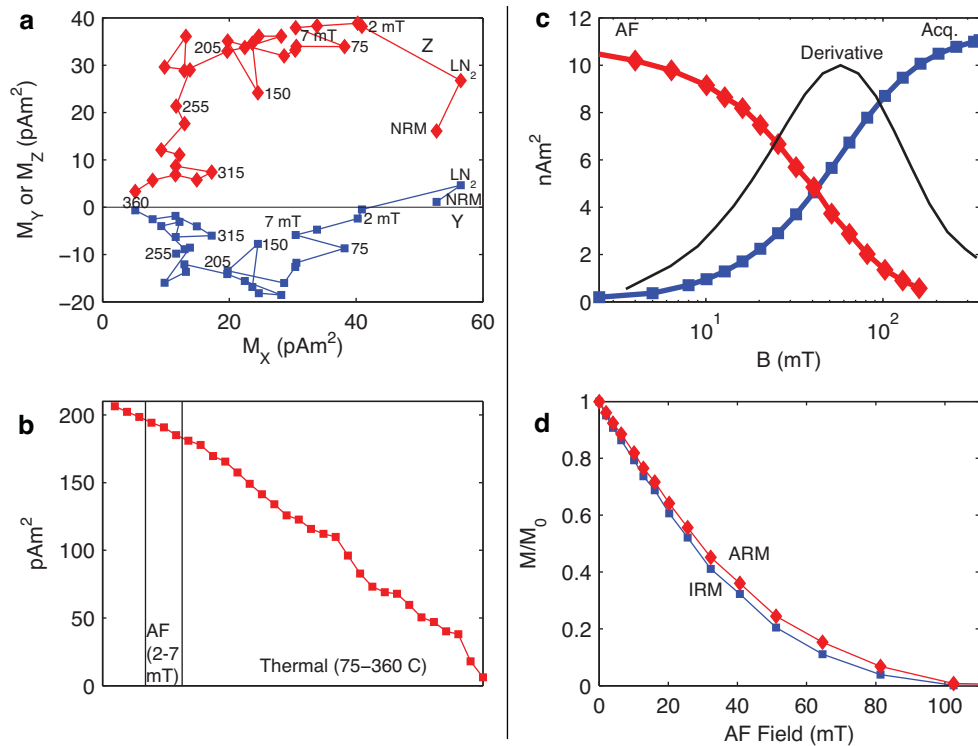


Figure II-2: Paleomagnetic and rock magnetic data from a weakly magnetic Permian carbonate specimen, Kyushu. (a) Vector diagram showing liquid nitrogen (LN_2), alternating field, and thermal demagnetization. A subset of points are labeled; AF steps are labeled with field strength and thermal steps are labeled with temperature ($^{\circ}\text{C}$). (b) Plot of total moment demagnetized over the course of the demagnetization sequence. (c) IRM acquisition (Acq.) and AF-demagnetization (AF) curves. Thin line shows coercivity spectra, determined from the derivative of the acquisition curve with respect to the log of applied field strength. (d) Modified Lowrie-Fuller plot, comparing the AF demagnetization of ARM acquired in 1 mT biasing field and 100 mT AF field to the AF demagnetization of IRM acquired in a 100 mT field

II.6 Alternating field demagnetization and rock magnetic experiments

As set up at Caltech, the sample changer system has a susceptibility coil and coils for AF, IRM, and ARM experiments installed between the top of the SRM and the sample tray. These permit routine susceptibility measurements in the course of paleomagnetic measurements and automated AF demagnetization and rock magnetic experiments. AF demagnetization experiments can be run in the same fashion as standard paleomagnetic measurements, with the system running a single three-axis AF demagnetization step on each sample before the up-direction measurement. Alternatively, the system can perform and measure multiple AF demagnetization steps sequentially on each sample. This approach permits time-intensive, high-resolution AF demagnetization experiments without user supervision but loses the error check provided by running up-direction and down-direction measurements after each demagnetization.

The system can similarly impart and measure ARMs and IRMs to samples. By spinning samples in transverse alternating fields, the system can also impart rotational remanence magnetizations. End chips can be run using the automated sample pickup system. Other sample shapes, such as powders in narrow quartz glass tubes, can be manually loaded and fitted to the sample tube using plastic adapters.

A typical rock magnetic measurement run consists of 20 ARMs imparted in biasing field increasing stepwise to 1 mT, an ~20-step demagnetization of the final ARM, the imparting and ~20-step demagnetization of an IRM acquired in field equivalent to the AF field using in the ARM experiments, the acquisition of ~20 IRMs in a stepwise increasing field, and the stepwise demagnetization of the maximum IRM. This set of experiments allows the construction of moderately high-resolution coercivity spectra, as well as the determination of parameters including IRM and ARM strength, B_{cr} , the Cisowski magnetostatic interaction parameter R , and χ_{ARM} . The total ~100-step experiment takes ~2 hours per sample and, barring unexpected errors, runs without user supervision. The user is notified of any errors requiring his or her attention by email. MATLAB scripts are then used to analyze rock magnetic data. Examples of rock magnetic data produced by the system are shown in Chapters 2 and 3. Example IRM acquisition and demagnetization data and a modified Lowrie-Fuller test using IRM and ARM demagnetization are shown in Figure II-2, c and d.

II.7 Assessment of systematic errors

To assess the errors associated with the sample changer system, we identified all samples run in 2006 on one of the two Caltech magnetometers, the Eugene Shoemaker Memorial Magnetometer, based on the last modification date of sample files. According to that metric, 1,216 samples were run on the Shoemaker Magnetometer in 2006. The system made 25,858 measurements of NRMs and thermally treated samples, and performed and measured 4,619 AF demagnetization steps.

We typically perform all AF treatments of a sample in series, measuring the sample between each treatment but not averaging together up-direction and down-direction measurements. Therefore, the errors associated with AF measurements should reflect the precision of the system. They arise from differences between the sample magnetization as measured in each of the four rotational orientations. The circular standard deviations of all AF measurements are fit by a log-normal distribution centered at 0.5 degrees and with a standard deviation of 0.3 log units (Figure 3a).

NRMs and thermally treated samples, in contrast, are always measured in both up and down orientations. The errors associated with the measurements therefore primarily reflect the accuracy of the system and are dominated by the effects of sample orientation. The circular standard deviation of all such measurements are fit by a log-normal distribution centered at 1.7 degrees and with a standard deviation of 0.5 log units. The distribution has a kink at 8 degrees associated with the error checking routines described above (Figure II-3a). 91.6% of the measurements have standard deviations less than 8 degrees; only 1.7% have standard deviations greater than 15 degrees.

Of the NRM and thermal treatment steps, 9.6% had to be re-measured at least once. 80.8% of the steps requiring re-measurement had standard deviations greater than 8 degrees, and the large majority of these would have been rerun after the software prompted the user. 45.3% had standard deviations greater than 15 degrees. After remeasurement, only 24.0% had standard deviations greater than 8 degrees, and only 10.1% had standard deviations greater than 15 degrees.

Fischer standard deviations increase with declining sample moment (Figure II-3b). The median moment of all NRM and thermal treatment measurements with circular standard deviations less than 8 degrees was 370 pAm^2 , while the median moment of all such measurements with circular standard deviations greater than 15 degrees was 28 pAm^2 .

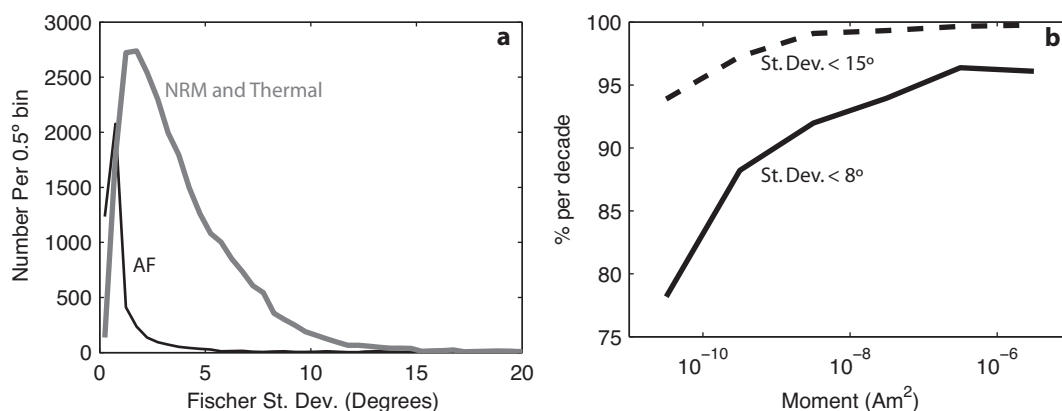


Figure II-3: (a) Distribution of circular standard deviations of measurements run on the Eugene Shoemaker Memorial Magnetometer in 2006, either obtained in the course of AF treatments (and generally measured only in the up direction) or NRM and thermal treatment measurements (averaged from measurements in both the up and down directions). Measurements are binned in 0.5 degree steps. (b) Percentage of measurements with circular standard deviations less than 8 and less than fifteen degrees as a function of moment. Measurements are binned by decade.

II.8 Conclusions

Under normal operating conditions, the automatic sample changer described here averages ~25 samples per hour, measured in both up and down directions. Thus, for a typical 50-specimen sample set, the measurement portion of a high-resolution 40-step thermal demagnetization process can be completed within four days of continuous operation. Automation frees the researcher from the role of handmaiden to the magnetometer and permits the creation of rich paleomagnetic data sets while liberating considerable time for data analysis.

*Appendix III*NOTES ON THE USAGE OF THE BRUKER EMX-300 FOR FERROMAGNETIC
RESONANCE SPECTROSCOPY

The Bruker EMX-300 is a reflection spectrometer (WEBER et al., 1998). Microwaves from the X-band (~9.0-9.9 GHz) source are directed through an attenuator then down a waveguide to the sample cavity, where an iris regulates the fraction of the microwaves allowed to enter the cavity. In the cavity, the sample absorbs some of the microwaves. The remaining microwaves are reflected back up the waveguide, at the end of which a circulator directs them to a detector diode. To keep the detector diode operating at the optimal power level, a reference arm taps some of the microwave source and provides what is called a “bias.” A phase shifter keeps the biasing microwaves in phase with the reflected microwaves. The parameters the user controls during the tuning process are the frequency of the microwave source, the level of the bias, the phase of the bias, the degree of attenuation, and the size of the iris.

Different cavities have different signal-to-noise ratios and quality factors (Q factor, which measures the ratio of energy stored to energy dissipated). The measurements described in this dissertation were made using the ER 4119HS high-sensitivity cavity.

The detector uses phase-sensitive detection to increase sensitivity. The applied field is modulated at some specified modulation amplitude and modulation frequency, which causes any absorption signal to be modulated in amplitude at the same frequency. The detector is sensitive only to signals modulated at this frequency, which leads to the filtering of extraneous signals, such as those produced by electrical noise. The user adjusts the modulation amplitude, the modulation frequency, and a time constant that affects the detector response time. The user also sets the conversion time, which determines how long the spectrometer measures at each specific field.

Typical rules of thumb for electron paramagnetic response (EPR) spectroscopy suggest that the modulation amplitude should be similar to the width of the EPR signal and that the total time to scan through a signal (the product of the conversion time and the number of points measured within the width of the absorption peak) should be at least ten times the time constant.

For most of the measurements described in Chapters 2-5, the field was swept for 0 to 6000 G in 1024 points. Modulation frequency was 100 kHz, modulation amplitude was 5 G, and modulation phase and offset were set to 0. The time constant was 21.48 ms and the conversion time was 81.92 ms. For weak samples, the attenuation was set at 25 dB (equivalent to a microwave power of $\sim 640 \mu\text{W}$), and the signal was summed over three field sweeps. For strong samples, the attenuation was set at 35 or 45 dB (~ 64 or $\sim 6 \mu\text{W}$ power) and the field was swept once.

Appendix IV

GUIDE TO ELECTRONIC MATERIAL

Three electronic software packages accompany this dissertation. matFMR provides MATLAB functions for analyzing ferromagnetic resonance spectra. matRockmag provides MATLAB functions, including a graphical interface, for analyzing rock magnetic data produced by the magnetometer system described in Appendix II. Paleomag 2007 is a Visual Basic 6 program for running the magnetometer system. In addition, the raw rock magnetic and ferromagnetic resonance data files for Chapters 2 through 5 are also included.

BIBLIOGRAPHY

- Abe, K., Miyamoto, Y. and Chikazumi, S., 1976. Magnetocrystalline anisotropy of low-temperature phase of magnetite. *Journal of the Physical Society of Japan* 41, 1894–1902.
- Aissaoui, D. M., McNeill, D. F. and Kirschvink, J. L., 1990. Magnetostratigraphic dating of shallow-water carbonates from Mururoa Atoll, French Polynesia—implications for global eustasy. *Earth and Planetary Science Letters* 97, 102–112.
- Akai, J., Iida, A., Akai, K. and Chiba, A., 1997. Mn and Fe minerals of possible biogenic origin from two Precambrian stromatolites in western Australia. *Journal of the Geological Society of Japan* 103, 484–488.
- Amard, B. and Bertrand-Sarfati, J., 1997. Microfossils in 2000 Ma old cherty stromatolites of the Franceville Group, Gabon. *Precambrian Research* 81, 197–221.
- Anbar, A. D. and Knoll, A. H., 2002. Proterozoic ocean chemistry and evolution: A bioinorganic bridge? *Science* 297, 1137–1142.
- Arakaki, T. and Morse, J. W., 1993. Coprecipitation and adsorption of Mn(II) with mackinawite (FeS) under conditions similar to those found in anoxic sediments. *Geochimica et Cosmochimica Acta* 57, 9–14.
- Arató, B., Szányi, Z., Flies, C., Schüller, D., Frankel, R. B., Buseck, P. R. and Pósfai, M., 2005. Crystal-size and shape distributions of magnetite from uncultured magnetotactic bacteria as a potential biomarker. *American Mineralogist* 90, 1233–1241.
- As, J. A. and Zijdeveld, J. D. A., 1958. Magnetic cleaning of rocks in palaeomagnetic research. *Geophysical Journal of the Royal Astronomical Society* 1, 308–319.
- Awramik, S. M., Schopf, J. W. and Walter, M. R., 1983. Filamentous fossil bacteria from the archean of Western Australia. *Precambrian Research* 20, 357–374.
- Balsam, W. L., Ottobliesner, B. L. and Deaton, B. C., 1995. Modern and Last Glacial Maximum eolian sedimentation patterns in the Atlantic Ocean interpreted from sediment iron oxide content. *Paleoceanography* 10, 493–507.
- Barnes, R. O. and Goldberg, E. D., 1976. Methane production and consumption in anoxic marine sediments. *Geology* 4, 297–300.
- Bates, M. P. and Halls, H. C., 1990. Regional variation in paleomagnetic polarity of the Matachewan Dyke Swarm related to the Kapuskasing Structural Zone, Ontario. *Canadian Journal of Earth Sciences* 27, 200–211.
- Bazylinski, D. A. and Frankel, R. B., 2004. Magnetosome formation in prokaryotes. *Nature Reviews Microbiology* 2, 217–230.
- Bazylinski, D. A., Frankel, R. B., Heywood, B. R., Mann, S., King, J. W., Donaghay, P. L. and Hanson, A. K., 1995. Controlled biomineralization of magnetite (Fe₃O₄) and greigite (Fe₃S₄) in a magnetotactic bacterium. *Applied and Environmental Microbiology* 61, 3232–3239.
- Bazylinski, D. A., Garratt-Reed, A. J., Abedi, A. and Frankel, R. B., 1993. Copper association with iron sulfide magnetosomes in a magnetotactic bacterium. *Archives of Microbiology* 160, 35–42.

- Bazylinski, D. A., Garratt-Reed, A. J. and Frankel, R. B., 1994. Electron microscopic studies of magnetosomes in magnetotactic bacteria. *Microscopy Research and Technique* 27, 389–401.
- Bazylinski, D. A. and Moskowitz, B. M., 1997. Microbial biomineralization of magnetic iron minerals: Microbiology, magnetism and environmental significance. *Reviews in Mineralogy and Geochemistry* 35, 181–223.
- Bekker, A., Holland, H. D., Wang, P.-L., Rumble III, D., Stein, H. J., Hannah, J. L., Coetsee, L. L. and Beukes, N. J., 2004. Dating the rise of atmospheric oxygen. *Nature* 427, 117–120.
- Belkaaloul, N. K. and Aissaoui, D. M., 1997. Nature and origin of magnetic minerals within the Middle Jurassic shallow-water carbonate rocks of the Paris Basin, France: Implications for magnetostratigraphic dating. *Geophysical Journal International* 130, 411–421.
- Berg, H. C., 1993. *Random Walks in Biology*. Princeton University Press, Princeton, NJ.
- Berner, R. A., 1967. Thermodynamic stability of sedimentary iron sulfides. *American Journal of Science* 265, 773–785.
- Berner, R. A., Lasaga, A. C. and Garrels, R. M., 1983. The carbonate-silicate geochemical cycle and its effect on atmospheric carbon dioxide over the past 100 million years. *American Journal of Science* 283, 641–683.
- Bernstein, L. and Young, G. M., 1990. Depositional environments of the early Proterozoic Espanola Formation, Ontario, Canada. *Canadian Journal of Earth Sciences* 27, 539–551.
- Bickford, L. R., Jr., 1950. Ferromagnetic resonance absorption in magnetite single crystals. *Physical Review* 78, 449–457.
- Bjerrum, C. J. and Canfield, D. E., 2002. Ocean productivity before about 1.9 Gyr ago limited by phosphorus adsorption onto iron oxides. *Nature* 417, 159–162.
- Blakemore, R., 1975. Magnetotactic bacteria. *Science* 190, 377–379.
- Boetius, A., Ravenschlag, K., Schubert, C. J., Rickert, D., Widdel, F., Gieseke, A., Amann, R., Jorgensen, B. B., Witte, U. and Pfannkuche, O., 2000. A marine microbial consortium apparently mediating anaerobic oxidation of methane. *Nature* 407, 623–626.
- Bolle, M. P. and Adatte, T., 2001. Palaeocene early Eocene climatic evolution in the Tethyan realm: Clay mineral evidence. *Clay Minerals* 36, 249–261.
- Brasier, M. D., Green, O. R., Jephcoat, A. P., Kleppe, A. K., Van Kranendonk, M. J., Lindsay, J. F., Steele, A. and Grassineau, N. V., 2002. Questioning the evidence for Earth's oldest fossils. *Nature* 416, 76–81.
- Brocks, J. J., Buick, R., Logan, G. A. and Summons, R. E., 2003a. Composition and syngeneity of molecular fossils from the 2.78 to 2.45 billion-year-old Mount Bruce Supergroup, Pilbara Craton, Western Australia. *Geochimica et Cosmochimica Acta* 67, 4289–4319.
- Brocks, J. J., Buick, R., Summons, R. E. and Logan, G. A., 2003b. A reconstruction of Archean biological diversity based on molecular fossils from the 2.78 to 2.45 billion-year-old Mount Bruce Supergroup, Hamersley Basin, Western Australia. *Geochimica et Cosmochimica Acta* 67, 4321–4335.
- Brocks, J. J., Logan, G. A., Buick, R. and Summons, R. E., 1999. Archean molecular fossils and the early rise of eukaryotes. *Science* 285, 1033–1036.

- Buseck, P. R., Dunin-Borkowski, R. E., Devouard, B., Frankel, R. B., McCartney, M. R., Midgley, P. A., Posfai, M. and Weyland, M., 2001. Magnetite morphology and life on Mars. *Proceedings of the National Academy of Sciences* 98, 13490–13495.
- Butler, R. F. and Banerjee, S. K., 1975. Theoretical single-domain grain size range in magnetite and titanomagnetite. *Journal of Geophysical Research* 80, 4049–4058.
- Butler, R. W. H., McClelland, E. and Jones, R. E., 1999. Calibrating the duration and timing of the Messinian salinity crisis in the Mediterranean: Linked tectonoclimatic signals in thrust-top basins of Sicily. *Journal of the Geological Society* 156, 827–835.
- Cairncross, B., Beukes, N. and Gutzmer, J., 1997. *The Manganese Adventure: The South African Manganese Fields*. The Associated Ore & Metal Corporation Limited, Johannesburg.
- Cairns-Smith, A. G., 1978. Precambrian solution photochemistry, inverse segregation, and banded iron formations. *Nature* 276, 807–808.
- Calas, G., 1988. Electron Paramagnetic Resonance. *Reviews in Mineralogy* 18, 513–571.
- Canfield, D. E., 1998. A new model for Proterozoic ocean chemistry. *Nature* 396, 450–453.
- Canfield, D. E., Habicht, K. S. and Thamdrup, B., 2000. The Archean sulfur cycle and the early history of atmospheric oxygen. *Science* 288, 658–661.
- Carter-Stiglitz, B., Jackson, M. and Moskowitz, B., 2002. Low-temperature remanence in stable single domain magnetite. *Geophysical Research Letters* 29, 1129.
- Carter-Stiglitz, B., Moskowitz, B. and Jackson, M., 2004. More on the low-temperature magnetism of stable single domain magnetite: Reversibility and non-stoichiometry. *Geophysical Research Letters* 31, L06606.
- Catling, D. C., Zahnle, K. J. and McKay, C. P., 2001. Biogenic methane, hydrogen escape, and the irreversible oxidation of the early Earth. *Science* 293, 839–843.
- Chang, S. B. R., 1988. Bacterial magnetite in sedimentary deposits and its geophysical and paleological implication. Ph.D. Thesis, California Institute of Technology.
- Chang, S. B. R. and Kirschvink, J. L., 1984. Bacterial magnetofossils as probes of Precambrian ecological and biochemical evolutionary events. 97th annual meeting, Geological Society of America.
- Chang, S. B. R. and Kirschvink, J. L., 1985. Possible biogenic magnetite fossils from the Miocene marine clay of Crete. In: Kirschvink, J. L., Jones, D. S., and McFadden, B. (Eds.), *Magnetite Biomineralization and Magnetoreception in Organisms: A New Biomagnetism*. Plenum Press, New York, NY.
- Chang, S. B. R. and Kirschvink, J. L., 1989. Magnetofossils, the magnetization of sediments, and the evolution of magnetite biomineralization. *Annual Review of Earth and Planetary Sciences* 17, 169–195.
- Chang, S. B. R., Kirschvink, J. L. and Stolz, J. F., 1987. Biogenic magnetite as a primary remanence carrier in limestone deposits. *Physics of the Earth and Planetary Interiors* 46, 289–303.
- Chang, S. B. R., Stolz, J. F., Kirschvink, J. L. and Awramik, S. M., 1989. Biogenic magnetite in stromatolites. 2. Occurrence in ancient sedimentary environments. *Precambrian Research* 43, 305–315.
- Cisowski, S., 1981. Interacting vs. non-interacting single-domain behavior in natural and synthetic samples. *Physics of the Earth and Planetary Interiors* 26, 56–62.
- Cleveland, W. S., 1979. Robust Locally Weighted Regression and Smoothing Scatterplots. *Journal of the American Statistical Association* 74, 829–836.

- Cloud, P., 1973. Paleocological significance of banded iron-formation. *Economic Geology* 68, 1135–1143.
- Cogne, J. P., 2003. PaleoMac: A Macintosh (TM) application for treating paleomagnetic data and making plate reconstructions. *Geochemistry, Geophysics, Geosystems* 4, 1007, doi:10.1029/2001GC000227.
- Corfu, F. and Andrews, A. J., 1986. A U-Pb Age for mineralized Nipissing Diabase, Gowganda, Ontario. *Canadian Journal of Earth Sciences* 23, 107–109.
- Cornell, D. H., Schutte, S. S. and Eglington, B. L., 1996. The Ongeluk basaltic andesite formation in Griqualand West, South Africa—submarine alteration in a 2222 Ma Proterozoic sea. *Precambrian Research* 79, 101–123.
- Courtillot, V., Gallet, Y., Le Mouel, J.-L., Fluteau, F. and Genevey, A., 2007. Are there connections between the Earth's magnetic field and climate? *Earth and Planetary Science Letters* 253, 328–339.
- Cox, B., 2002. Organization and elemental analysis of P-, S-, and Fe-rich inclusions in a population of freshwater magnetococci. *Geomicrobiology Journal* 19, 387–406.
- Cramer, B. S. and Kent, D. V., 2005. Bolide summer: The Paleocene/Eocene thermal maximum as a response to an extraterrestrial trigger. *Palaeogeography Palaeoclimatology Palaeoecology* 224, 144–166.
- Crook, N. P., Hoon, S. R., Taylor, K. G. and Perry, C. T., 2002. Electron spin resonance as a high sensitivity technique for environmental magnetism: Determination of contamination in carbonate sediments. *Geophysical Journal International* 149, 328–337.
- D'Amelio, E. D., Cohen, Y. and Des Marais, D. J., 1987. Association of a new type of gliding, filamentous, purple phototrophic bacterium inside bundles of *Microcoleus chthonoplastes* in hypersaline cyanobacterial mats. *Archives of Microbiology* 147, 213–220.
- Davis, B. L., Rapp, G. and Walawender, M. J., 1968. Fabric and structural characteristics of the martitization process. *American Journal of Science* 266, 482–496.
- Dean, A. J. and Bazylinski, D. A., 1999. Genome analysis of several marine, magnetotactic bacterial strains by pulsed-field gel electrophoresis. *Current Microbiology* 39, 219–225.
- Dearing, J. A., Boyle, J. F., Appleby, P. G., Mackay, A. W. and Flower, R. J., 1998. Magnetic properties of recent sediments in Lake Baikal, Siberia. *Journal Of Paleolimnology* 20, 163–173.
- DeLong, E. F., Frankel, R. B. and Bazylinski, D. A., 1993. Multiple evolutionary origins of magnetotaxis in bacteria. *Science* 259, 803–806.
- Denham, C. R. and Cox, A., 1971. Evidence that the Laschamp polarity event did not occur 13,300–30,400 years ago. *Earth and Planetary Science Letters* 13, 181–190.
- Des Marais, D. J., 2000. When did photosynthesis emerge on Earth? *Science* 289, 1703–1705.
- Devouard, B., Posfai, M., Hua, X., Bazylinski, D. A., Frankel, R. B. and Buseck, P. R., 1998. Magnetite from magnetotactic bacteria: Size distributions and twinning. *American Mineralogist* 83, 1387–1398.
- Diaz-Ricci, J. C. and Kirschvink, J. L., 1992. Magnetic domain state and coercivity predictions for biogenic greigite (Fe₃S₄)—a comparison of theory with magnetosome observations. *Journal of Geophysical Research* 97, 17309–17315.

- Dinarès-Turell, J., Hoogakker, B. A. A., Roberts, A. P., Rohling, E. J. and Sagnotti, L., 2003. Quaternary climatic control of biogenic magnetite production and eolian dust input in cores from the Mediterranean sea. *Palaeogeography, Palaeoclimatology, Palaeoecology* 190, 195–209.
- Dong, H., Fredrickson, J. K., Kennedy, D. W., Zachara, J. M., Kukkadapu, R. K. and Onstott, T. C., 2000. Mineral transformation associated with the microbial reduction of magnetite. *Chemical Geology* 169, 299–318.
- Dorland, H., 2004. Provenance, Ages, and Timing of Sedimentation of Selected Neoproterozoic and Paleoproterozoic Successions on the Kaapvaal Craton. D.Phil. Thesis, Rand Afrikaans University.
- Drain, L. E., 1962. The broadening of magnetic resonance lines due to field inhomogeneities in powdered samples. *Proceedings of the Physical Society* 80, 1380–1382.
- Drever, J. L., 1997. *The Geochemistry of Natural Waters*. Prentice Hall, Upper Saddle River, NJ.
- Dunin-Borkowski, R. E., McCartney, M. R., Posfai, M., Frankel, R. B., Bazylnski, D. A. and Buseck, P. R., 2001. Off-axis electron holography of magnetotactic bacteria: Magnetic microstructure of strains MV-1 and MS-1. *European Journal of Mineralogy* 13, 671–684.
- Dunlop, D. J. and Özdemir, Ö., 1997. *Rock Magnetism: Fundamentals and Frontiers*. Cambridge University Press, Cambridge.
- Dunlop, D. J., Westcottlewis, M. F. and Bailey, M. E., 1990. Preisach diagrams and anhysteresis: do they measure interactions? *Physics of the Earth and Planetary Interiors* 65, 62–77.
- Egli, R., 2003. Analysis of the field dependence of remanent magnetization curves. *Journal of Geophysical Research* 108, 2081.
- Egli, R., 2004a. Characterization of individual rock magnetic components by analysis of remanence curves, 1. Unmixing natural sediments. *Studia Geophysica et Geodaetica* 48, 391–446.
- Egli, R., 2004b. Characterization of individual rock magnetic components by analysis of remanence curves. 3. Bacterial magnetite and natural processes in lakes. *Physics and Chemistry of the Earth* 29, 869–884.
- Egli, R. and Lowrie, W., 2002. Anhysteretic remanent magnetization of fine magnetic particles. *Journal of Geophysical Research* 107, 2209.
- Elderfield, H. and Schultz, A., 1996. Mid-ocean ridge hydrothermal fluxes and the chemical composition of the ocean. *Annual Review of Earth and Planetary Sciences* 24, 191–224.
- Evans, D. A., Beukes, N. J. and Kirschvink, J. L., 1997. Low-latitude glaciation in the Paleoproterozoic. *Nature* 386, 262–266.
- Evans, M. E. and Heller, F., 2003. *Environmental Magnetism*. Academic Press, San Diego.
- Falkowski, P. G., 1997. Evolution of the nitrogen cycle and its influence on the biological sequestration of CO₂ in the ocean. *Nature* 387, 272–275.
- Falkowski, P. G., Follows, M. and Fennel, K., 2003. The co-evolution of the nitrogen and oxygen cycles on Earth. *Eos Trans. AGU* 84, Fall Meet. Suppl., Abstract U52C–01.
- Falkowski, P. G., Katz, M. E., Knoll, A. H., Quigg, A., Raven, J. A., Schofield, O. and Taylor, F. J. R., 2004. The evolution of modern eukaryotic phytoplankton. *Science* 305, 354–360.

- Farina, M., Kachar, B., Lins, U., Broderick, R. and Debarros, H. L., 1994. The observation of large magnetite (Fe_3O_4) crystals from magnetotactic bacteria by electron and atomic force microscopy. *Journal of Microscopy* 173, 1–8.
- Farley, K. A. and Eltgroth, S. F., 2003. An alternative age model for the Paleocene-Eocene thermal maximum using extraterrestrial He-3. *Earth and Planetary Science Letters* 208, 135–148.
- Farquhar, J., Bao, H. and Thiemens, M., 2000. Atmospheric Influence of Earth's Earliest Sulfur Cycle. *Science* 289, 756–758.
- Farquhar, J., Savarino, J., Airieau, S. and Thiemens, M. H., 2001. Observation of wavelength-sensitive mass-independent sulfur isotope effects during SO_2 photolysis: Implications for the early atmosphere. *Journal of Geophysical Research* 106, 32829–32839.
- Farquhar, J. and Wing, B. A., 2003. Multiple sulfur isotopes and the evolution of the atmosphere. *Earth and Planetary Science Letters* 213, 1–13.
- Fischer, W. W., Summons, R. E. and Pearson, A., 2004. Anaerobic biosynthesis of hopanoids by a microbe prevalent in anoxic environments. *Geological Society of America Abstracts with Programs* 36, 88.
- Föllmi, K. B., 1995. 160 m.y. record of marine sedimentary phosphorus burial: Coupling of climate and continental weathering under greenhouse and icehouse conditions. *Geology* 23, 503–506.
- Frankel, R. B. and Blakemore, R. P., 1989. Magnetite and magnetotaxis in microorganisms. *Bioelectromagnetics* 10, 223–237.
- Friedmann, E. I., Wierzchos, J., Ascaso, C. and Winklhofer, M., 2001. Chains of magnetite crystals in the meteorite ALH84001: Evidence of biological origin. *Proceedings of the National Academy of Sciences* 98, 2176–2181.
- Fuller, M., Kidane, T. and Ali, J., 2002. AF demagnetization characteristics of NRM, compared with anhysteretic and saturation isothermal remanence: An aid in the interpretation of NRM. *Physics and Chemistry of the Earth* 27, 1169–1177.
- Gaidos, E. J., Nealson, K. H. and Kirschvink, J. L., 1999. Life in ice-covered oceans. *Science* 284, 1631–1633.
- Gawenda, P., Winkler, W., Schmitz, B. and Adatte, T., 1999. Climate and bioproductivity control on carbonate turbidite sedimentation (Paleocene to earliest Eocene, Gulf of Biscay, Zumaia, Spain). *Journal of Sedimentary Research* 69, 1253–1261.
- Gibbs, S. J., Bralower, T. J., Bown, P. R., Zachos, J. C. and Bybell, L. M., 2006. Shelf and open-ocean calcareous phytoplankton assemblages across the Paleocene-Eocene Thermal Maximum: Implications for global productivity gradients. *Geology* 34, 233–236.
- Gibson, T. G., Bybell, L. M. and Mason, D. B., 2000. Stratigraphic and climatic implications of clay mineral changes around the Paleocene/Eocene boundary of the northeastern US margin. *Sedimentary Geology* 134, 65–92.
- Gibson, T. G., Bybell, L. M. and Owens, J. P., 1993. Latest Paleocene lithologic and biotic events in neritic deposits of southwestern New Jersey. *Paleoceanography* 8, 495–514.
- Glasauer, S., Langley, S. and Beveridge, T. J., 2002. Intracellular iron minerals in a dissimilatory iron-reducing bacterium. *Science* 295, 117–119.
- Golden, D. C., Ming, D. W., Morris, R. V., Brearley, A., Lauer, H. V., Treiman, A. H., Zolensky, M. E., Schwandt, C. S., Lofgren, G. E. and McKay, G. A., 2004.

- Evidence for exclusively inorganic formation of magnetite in Martian meteorite ALH84001. *American Mineralogist* 89, 681–695.
- Gorby, Y. A., Beveridge, T. J. and Blakemore, R. P., 1988. Characterization of the bacterial magnetosome membrane. *Journal of Bacteriology* 170, 834–841.
- Goree, W. S. and Fuller, M., 1976. Magnetometers using RF-driven SQUIDs and their applications in rock magnetism and paleomagnetism. *Reviews of Geophysics* 14, 591–608.
- Griscom, D. L., 1974. Ferromagnetic resonance spectra of lunar fines: Some implications of line shape analysis. *Geochimica et Cosmochimica Acta* 38, 1509–1519.
- Griscom, D. L., 1981. Ferromagnetic resonance condition and powder pattern analysis for dilute, spherical, single-domain particles of cubic crystal structure. *Journal of Magnetic Resonance* 45, 81–87.
- Griscom, D. L., Krebs, J. J., Perez, A. and Treilleux, M., 1988. Ferromagnetic resonance studies of iron-implanted silica. *Nuclear Instruments & Methods in Physics Research Section B* 32, 272–278.
- Grotzinger, J. P. and Kasting, J. F., 1993. New constraints on Precambrian ocean composition. *Journal of Geology* 101, 235–243.
- Grotzinger, J. P. and Knoll, A. H., 1999. Stromatolites in Precambrian carbonates: Evolutionary mileposts or environmental dipsticks? *Annual Review of Earth and Planetary Sciences* 27, 313–358.
- Hannah, J. L., Bekker, A., Stein, H. J., Markey, R. J. and Holland, H. D., 2004. Primitive Os and 2316 Ma age for marine shale: Implications for Paleoproterozoic glacial events and the rise of atmospheric oxygen. *Earth and Planetary Science Letters* 225, 43–52.
- Hanzlik, M., Winklhofer, M. and Petersen, N., 2002. Pulsed-field-remnance measurements on individual magnetotactic bacteria. *Journal of Magnetism and Magnetic Materials* 248, 258–267.
- Hardie, L. A., 1977. Sedimentation on the modern carbonate tidal flats of northwest Andros Island, Bahamas. Johns Hopkins University Press, Baltimore.
- Hayes, J. M., 1994. Global methanotrophy at the Archean-Proterozoic transition. In: Bengtson, S. (Ed.), *Early Life on Earth*. Columbia Univ. Press, New York.
- Hedges, J. I. and Keil, R. G., 1995. Sedimentary organic matter preservation: an assessment and speculative synthesis. *Marine Chemistry* 49, 81–115.
- Hesse, P. P., 1994. Evidence for bacterial paleoecological origin of mineral magnetic cycles in oxic and sub-oxic Tasman Sea sediments. *Marine Geology* 117, 1–17.
- Heywood, B. R., Bazylinski, D. A., Garrattreed, A., Mann, S. and Frankel, R. B., 1990. Controlled biosynthesis of greigite (Fe_3S_4) in magnetotactic bacteria. *Naturwissenschaften* 77, 536–538.
- Hilburn, I. A., Kirschvink, J. L., Tajika, E., Tada, R., Hamano, Y. and Yamamoto, S., 2005. A negative fold test on the Lorrain Formation of the Huronian Supergroup: Uncertainty on the paleolatitude of the Paleoproterozoic Gowganda glaciation and implications for the great oxygenation event. *Earth and Planetary Science Letters* 232, 315–332.
- Hilgenfeldt, K., 2000. Diagenetic dissolution of biogenic magnetite in surface sediments of the Benguela upwelling system. *International Journal of Earth Sciences* 88, 630–640.
- Hoffman, P. F. and Schrag, D. P., 2002. The snowball Earth hypothesis: Testing the limits of global change. *Terra Nova* 14, 129–155.

- Holland, H. D., 1973. Oceans—possible source of iron in iron-formations. *Economic Geology* 68, 1169–1172.
- Hounslow, M. W. and Maher, B. A., 1996. Quantitative extraction and analysis of carriers of magnetization in sediments. *Geophysical Journal International* 124, 57–74.
- Housen, B. A. and Moskowitz, B. M., 2006. Depth distribution of magnetofossils in near-surface sediments from the Blake/Bahama Outer Ridge, western North Atlantic Ocean, determined by low-temperature magnetism. *Journal of Geophysical Research* 111, G01005.
- Hsü, K. J., LaBrecque, J. L., Carman, M. F., Gombos, A. M., Karpoff, A., McKenzie, J. A., Percival, S. F., Petersen, N. P., Pisciotto, K. A., Poore, R. Z., Schreiber, E., Tauxe, L., Tucker, P. and Weissert, H. J., 1984. Initial Reports of the Deep Sea Drilling Project, 73. U.S. Govt. Printing Office, Washington.
- Huston, D. L. and Logan, G. A., 2004. Barite, BIFs and bugs: Evidence for the evolution of the Earth's early hydrosphere. *Earth and Planetary Science Letters* 220, 41–55.
- Jackson, M., 1990. Diagenetic sources of stable remanence in remagnetized Paleozoic cratonic carbonates: A rock magnetic study. *Journal of Geophysical Research* 95, 2753–2761.
- Jackson, M., Sun, W.-W. and Craddock, J. P., 1992. The rock magnetic fingerprint of chemical remagnetization in midcontinental Paleozoic carbonates. *Geophysical Research Letters* 19, 781–784.
- Jones, C. H., 2002. User-driven integrated software lives: "PaleoMag" paleomagnetism analysis on the Macintosh. *Computers and Geosciences* 28, 1145–1151.
- Joulian, C., Patel, B. K. C., Ollivier, B., Garcia, J. L. and Roger, P. A., 2000. *Methanobacterium oryzae* sp. nov., a novel methanogenic rod isolated from a Philippines ricefield. *International Journal of Systematic and Evolutionary Microbiology* 50, 525–528.
- Jørgensen, B. B. and Gallardo, V. A., 1999. *Thioploca* spp.: Filamentous sulfur bacteria with nitrate vacuoles. *FEMS Microbiology Ecology* 28, 301–313.
- Jørgensen, B. B., Revsbech, N. P., Blackburn, T. H. and Cohen, Y., 1979. Diurnal cycle of oxygen and sulfide microgradients and microbial photosynthesis in a cyanobacterial mat sediment. *Applied and Environmental Microbiology* 38, 46–58.
- Kaiho, K., Arinobu, T., Ishiwatari, R., Morgans, H. E. G., Okada, H., Takeda, N., Tazaki, K., Zhou, G. P., Kajiwara, Y., Matsumoto, R., Hirai, A., Niitsuma, N. and Wada, H., 1996. Latest Paleocene benthic foraminiferal extinction and environmental changes at Tawanui, New Zealand. *Paleoceanography* 11, 447–465.
- Kąkol, Z. and Honig, J. M., 1989. Influence of deviations from ideal stoichiometry on the anisotropy parameters of magnetite $\text{Fe}_{3(1-\delta)}\text{O}_4$. *Physical Review B* 40, 9090–9097.
- Kappler, A. and Newman, D. K., 2004. Formation of Fe(III)-minerals by Fe(II)-oxidizing photoautotrophic bacteria. *Geochimica et Cosmochimica Acta* 68, 1217–1226.
- Keeping, E. S., 1995. *Introduction to Statistical Inference*. Dover, New York.
- Keim, C. N., Solórzano, G., Farina, M. and Lins, U., 2005. Intracellular inclusions of uncultured magnetotactic bacteria. *International Microbiology* 8, 111–117.
- Kent, D. V., Cramer, B. S., Lanci, L., Wang, D., Wright, J. D. and Van der Voo, R., 2003. A case for a comet impact trigger for the Paleocene/Eocene thermal maximum and carbon isotope excursion. *Earth and Planetary Science Letters* 211, 13–26.

- Kim, B. Y., Kodama, K. P. and Moeller, R. E., 2005. Bacterial magnetite produced in water column dominates lake sediment mineral magnetism: Lake Ely, USA. *Geophysical Journal International* 163, 26–37.
- King, J. G. and Williams, W., 2000. Low-temperature magnetic properties of magnetite. *Journal of Geophysical Research* 105, 16427–16436.
- Kirschvink, J. L., 1980a. South-seeking magnetic bacteria. *Journal of Experimental Biology* 86, 345–347.
- Kirschvink, J. L., 1980b. The least-squares line and plane and the analysis of paleomagnetic data. *Geophysical Journal of the Royal Astronomical Society* 62, 699–718.
- Kirschvink, J. L., 1982. Paleomagnetic evidence for fossil biogenic magnetite in western Crete. *Earth and Planetary Science Letters* 59, 388–392.
- Kirschvink, J. L., 2001. A seventh criterion for the identification of bacterial magnetofossils. *Eos Trans. AGU* 82, S131.
- Kirschvink, J. L. and Chang, S. B. R., 1984. Ultrafine-grained magnetite in deep-sea sediments—possible bacterial magnetofossils. *Geology* 12, 559–562.
- Kirschvink, J. L., Gaidos, E. J., Bertani, L. E., Beukes, N. J., Gutzmer, J., Maepa, L. N. and Steinberger, R. E., 2000. Paleoproterozoic snowball Earth: Extreme climatic and geochemical global change and its biological consequences. *Proceedings of the National Academy of Sciences* 97, 1400–1405.
- Kirschvink, J. L., Kopp, R. E., Vali, H. and Tikoo, S., in prep. Rock magnetic characterization of the late Archean Ghaap Group, Transvaal Supergroup, from Agouron drill core GKP01: No signs of life, but a magnetic paleothermometer for siderite metamorphism. *Precambrian Research*.
- Kirschvink, J. L. and Lowenstam, H. A., 1979. Mineralization and magnetization of chiton teeth: Paleomagnetic, sedimentologic, and biologic implications of organic magnetite. *Earth and Planetary Science Letters* 44, 193–204.
- Kirschvink, J. L. and Rozanov, A. Y., 1984. Magnetostratigraphy of lower Cambrian strata from the Siberian Platform: A paleomagnetic pole and a preliminary polarity time-scale. *Geological Magazine* 121, 189–203.
- Kittel, C., 1948. On the theory of ferromagnetic resonance absorption. *Physical Review* 73, 155–161.
- Klein, C. and Beukes, N. J., 1992. Models for iron-formation deposition. In: Klein, C. (Ed.), *The Proterozoic Biosphere*. Cambridge University Press, Cambridge.
- Kobayashi, A., Kirschvink, J. L., Nash, C. Z., Kopp, R. E., Sauer, D. A., Bertani, L. E., Voorhout, W. F. and Taguchi, T., 2006. Experimental observation of magnetosome chain collapse in magnetotactic bacteria: Sedimentological, paleomagnetic, and evolutionary implications. *Earth and Planetary Science Letters* 245, 538–550.
- Kobayashi, A. K., Kirschvink, J. L. and Nesson, M. H., 1995. Ferromagnetism and EMFs. *Nature* 374, 123–123.
- Komeili, A., Li, Z., Newman, D. K. and Jensen, G. J., 2006. Magnetosomes are cell membrane invaginations organized by the actin-like protein MamK. *Science* 311, 242–245.
- Komeili, A., Vali, H., Beveridge, T. J. and Newman, D. K., 2004. Magnetosome vesicles are present before magnetite formation, and MamA is required for their activation. *Proceedings of the National Academy of Sciences* 101, 3839–3844.
- Kopp, R. E. and Humayun, M., 2003. Kinetic model of carbonate dissolution in Martian meteorite ALH84001. *Geochimica et Cosmochimica Acta* 67, 3247–3256.

- Kostka, J. E. and Nealson, K. H., 1995. Dissolution and Reduction of Magnetite by Bacteria. *Environmental Science & Technology* 29, 2535–2540.
- Kustka, A., Carpenter, E. J. and Sanudo-Wilhelmy, S. A., 2002. Iron and marine nitrogen fixation: Progress and future directions. *Research in Microbiology* 153, 255–262.
- Langmuir, D., 1978. Uranium solution-mineral equilibria at low temperatures with applications to sedimentary ore deposits. *Geochimica et Cosmochimica Acta* 42, 547–569.
- Larrasoana, J. C., Roberts, A. P., Rohling, E. J., Winkhofer, M. and Wehausen, R., 2003. Three million years of monsoon variability over the northern Sahara. *Climate Dynamics* 21, 689–698.
- Lean, C. M. B. and McCave, I. N., 1998. Glacial to interglacial mineral magnetic and palaeoceanographic changes at Chatham Rise, SW Pacific Ocean. *Earth and Planetary Science Letters* 163, 247–260.
- Lehtoranta, J., 2003. Dissolved iron:phosphate ratio as an indicator of phosphate release to oxic water of the inner and outer coastal Baltic Sea. *Hydrobiologia* 492, 69.
- Li, Y.-L., Vali, H., Sears, S. K., Yang, J., Deng, B. and Zhang, C. L., 2004. Iron reduction and alteration of nontronite NAU-2 by sulfate-reducing bacterium. *Geochimica et Cosmochimica Acta* 68, 3251–3260.
- Lowenstam, H. A., 1981. Minerals formed by organisms. *Science* 211, 1126.
- Maher, B. A., Thompson, R. and Hounslow, M. W., 1999. Introduction. In: Maher, B. A. and Thompson, R. (Eds.), *Quaternary Climates, Environments, and Magnetism*. Cambridge University Press, Cambridge.
- Majzlan, J., Grevel, K.-D. and Navrotsky, A., 2003. Thermodynamics of Fe oxides: Part II. Enthalpies of formation and relative stability of goethite (α -FeOOH), lepidocrocite (γ -FeOOH), and maghemite (γ -Fe₂O₃). *American Mineralogist* 88, 855–859.
- Maloof, A. C. and Grotzinger, J. P., in prep. The origin of meter-scale parasequences in platformal carbonates—Holocene stratigraphy Triple Goose Creek, Andros Island, Bahamas. *Geological Society of America Bulletin*.
- Maloof, A. C., Halverson, G. P., Kirschvink, J. L., Schrag, D. P., Weiss, B. P. and Hoffman, P. F., 2006. Combined paleomagnetic, isotopic, and stratigraphic evidence for true polar wander from the Neoproterozoic Akademikerbreen Group, Svalbard, Norway. *Geological Society of America Bulletin* 118, 1099–1124.
- Mann, S., Sparks, N. H. C. and Blakemore, R., 1987. Structure, morphology, and crystal growth of anisotropic magnetite crystals in magnetotactic bacteria. *Proceedings of the Royal Society of London Series B* 231, 477–487.
- Maratea, D. and Blakemore, R. P., 1981. *Aquaspirillum magnetotacticum* sp. nov., a magnetic spirillum. *International Journal of Systematic Bacteriology* 31, 452–455.
- Matsunaga, T. and Okamura, Y., 2003. Genes and proteins involved in bacterial magnetite particle formation. *Trends in Microbiology* 11, 536–541.
- McCabe, C. R. and Elmore, R. D., 1989. The occurrence and origin of Late Paleozoic remagnetization in the sedimentary rocks of North America. *Reviews of Geophysics* 27, 471–494.
- McCabe, C. R., Jackson, M. and Saffer, B., 1989. Regional patterns of magnetite authigenesis in the Appalachian Basin: Implications for the mechanism of Late Paleozoic remagnetization. *Journal of Geophysical Research* 94, 10429–10443.

- McCabe, C. R., Van der Voo, R., Peacor, D. R., Scotese, C. R. and Freeman, R., 1983. Diagenetic magnetite carries ancient yet secondary remanence in some Paleozoic sedimentary carbonates. *Geology* 11, 221–223.
- McKay, D. S., Gibson, E. K., Thomas-Keprta, K. L., Vali, H., Romanek, C. S., Clemett, S. J., Chillier, X. D. F., Maechling, C. R. and Zare, R. N., 1996. Search for past life on Mars: Possible relic biogenic activity in Martian meteorite ALH84001. *Science* 273, 924–930.
- McNeill, D. F., 1990. Biogenic magnetite from surface Holocene carbonate sediments, Great Bahama Bank. *Journal of Geophysical Research* 95, 4363–4371.
- McNeill, D. F., 1997. Facies and early diagenetic influence on the depositional magnetization of carbonates. *Geology* 25, 799–802.
- McNeill, D. F., Ginsburg, R. N., Chang, S. B. R. and Kirschvink, J. L., 1988. Magnetostratigraphic dating of shallow-water carbonates from San Salvador, Bahamas. *Geology* 16, 8–12.
- McNeill, D. F. and Kirschvink, J. L., 1993. Early dolomitization of platform carbonates and the preservation of magnetic polarity. *Journal of Geophysical Research* 98, 7977–7986.
- Meert, J. G., Eide, E. A. and Torsvik, T. H., 1997. The Nama Group revisited. *Geophysical Journal International* 129, 637–650.
- Meldrum, F. C., Mann, S., Heywood, B. R., Frankel, R. B. and Bazylinski, D. A., 1993a. Electron microscopy study of magnetosomes in 2 cultured vibrioid magnetotactic bacteria. *Proceedings of the Royal Society of London Series B* 251, 237–242.
- Meldrum, F. C., Mann, S., Heywood, B. R., Frankel, R. B. and Bazylinski, D. A., 1993b. Electron microscopy study of magnetosomes in a cultured coccoid magnetotactic bacterium. *Proceedings of the Royal Society of London Series B* 251, 231–236.
- Meulenkamp, J. E., 1979. Lithostratigraphy and relative chronostratigraphic position of the sections Apostoli and Potamidha 1 and 2. *Utrecht Micropaleontology Bulletin* 21, 9–21.
- Michaelis, W., Seifert, R., Nauhaus, K., Treude, T., Thiel, V., Blumenberg, M., Knittel, K., Gieseke, A., Peterknecht, K., Pape, T., Boetius, A., Amann, R., Jorgensen, B. B., Widdel, F., Peckmann, J., Pimenov, N. V. and Gulin, M. B., 2002. Microbial reefs in the Black Sea fueled by anaerobic oxidation of methane. *Science* 297, 1013–1015.
- Miller, K. G., Sugarman, P. J., Browning, J. V., Olsson, R. K., Pekar, S. F., Reilly, T. J., Cramer, B. S., Aubry, M.-P., Lawrence, R. P., Curran, J., Stewart, M., Metzger, J. M., Uptegrove, J., Bukry, D., Burckle, L. H., Wright, J. D., Feigenson, M. D., Brenner, G. J. and Dalton, R. F., 1998. *Proceedings of the Ocean Drilling Program, Initial Reports, Vol. 174AX*. U.S. Govt. Printing Office, Washington.
- Moench, T. T., 1988. *Bilophococcus magnetotacticus* gen. nov. sp. nov., a motile, magnetic coccus. *Antonie van Leeuwenhoek, International Journal of General and Molecular Microbiology* 54, 483–496.
- Moldowan, J. M. and Jacobson, S. R., 2000. Chemical signals for early evolution of major taxa: Biosignatures and taxon-specific biomarkers. *International Geology Review* 42, 805–812.
- Montgomery, P., Hailwood, E. A., Gale, A. S. and Burnett, J. A., 1998. The magnetostratigraphy of Coniacian–late Campanian chalk sequences in southern England. *Earth and Planetary Science Letters* 156, 209–224.

- Moore, J. K., Doney, S. C., Glover, D. M. and Fung, I. Y., 2002. Iron cycling and nutrient-limitation patterns in surface waters of the World Ocean. *Deep Sea Research* 49, 463–507.
- Morrish, A. H., 1965. *The Physical Principles of Magnetism*. J. Wiley, New York.
- Morse, J. W., Millero, F. J., Cornwell, J. C. and Rickard, D., 1987. The chemistry of the hydrogen sulfide and iron sulfide systems in natural waters. *Earth Science Reviews* 24, 1–42.
- Moskowitz, B. M., Frankel, R. B. and Bazylinski, D. A., 1993. Rock magnetic criteria for the detection of biogenic magnetite. *Earth and Planetary Science Letters* 120, 283–300.
- Moskowitz, B. M., Frankel, R. B., Flanders, P. J., Blakemore, R. P. and Schwartz, B. B., 1988. Magnetic properties of magnetotactic bacteria. *Journal of Magnetism and Magnetic Materials* 73, 273–288.
- Muxworthy, A. R. and McClellan, E., 2000. Review of the low-temperature magnetic properties of magnetite from a rock magnetic perspective. *Geophysical Journal International* 140, 101–114.
- Nagy, E. A. and Valet, J. P., 1993. New advances for paleomagnetic studies of sediment cores using U-channels. *Geophysical Research Letters* 20, 671–674.
- Nhelko, N., 2004. *The Pongola Supergroup in Swaziland*. D.Phil. Thesis, Rand Afrikaans University.
- Niitsuma, S., Kakegawa, T., Nagasu, T. and Nedachi, M., 2005. Discovery of greigite from Archean rock? Japan Earth and Planetary Science Joint Meeting. Japan Geoscience Union, Makuhari, Japan.
- Niitsuma, S., Nedachi, M., Hoashi, M., Sukanuma, Y., Sugita, T., Ohno, K., Hisamitsu, T., Kodama, K. and Niitsuma, N., 2004. Rock magnetism of the black shale in the Mt. Roe Basalt, Pilbara Craton, Western Australia. Japan Earth and Planetary Science Joint Meeting. Japan Geoscience Union, Makuhari, Japan.
- Noble, S. R. and Lightfoot, P. C., 1992. U-Pb baddeleyite ages of the Kerns and Triangle Mountain intrusions, Nipissing Diabase, Ontario. *Canadian Journal of Earth Sciences* 29, 1424–1429.
- O'Sullivan, D. W., Hanson, J. A. K. and Kester, D. R., 1997. The distribution and redox chemistry of iron in the Pettaquamscutt Estuary. *Estuarine, Coastal and Shelf Science* 45, 769–788.
- Ohno, M. and Hamano, Y., 1992. Geomagnetic poles over the past 10,000 years. *Geophysical Research Letters* 19, 1715–1718.
- Oldfield, F., Wake, R., Boyle, J., Jones, R., Nolan, S., Gibbs, Z., Appleby, P., Fisher, E. and Wolff, G., 2003. The late-Holocene history of Gormire Lake (NE England) and its catchment: A multiproxy reconstruction of past human impact. *Holocene* 13, 677–690.
- Olsen, G. J., Woese, C. R. and Overbeek, R., 1994. The winds of (evolutionary) change: Breathing new life into microbiology. *Journal of Bacteriology* 176, 1–6.
- Ono, S., Eigenbrode, J. L., Pavlov, A. A., Kharecha, P., Rumble, D., Kasting, J. F. and Freeman, K. H., 2003. New insights into Archean sulfur cycle from mass-independent sulfur isotope records from the Hamersley Basin, Australia. *Earth and Planetary Science Letters* 213, 15–30.

- Orphan, V. J., House, C. H., Hinrichs, K. U., McKeegan, K. D. and DeLong, E. F., 2002. Multiple archaeal groups mediate methane oxidation in anoxic cold seep sediments. *Proceedings of the National Academy of Sciences* 99, 7663–7668.
- Osborn, J. A., 1945. Demagnetizing factors of the general ellipsoid. *Physical Review* 67, 351–357.
- Özdemir, Ö., Dunlop, D. J. and Moskowitz, B. M., 1993. The effect of oxidation on the Verwey transition in magnetite. *Geophysical Research Letters* 20, 1671–1674.
- Pagani, M., Caldeira, K., Archer, D. and Zachos, J. C., 2006. An ancient carbon mystery. *Science* 314, 1556–1557.
- Pan, Y. X., Petersen, N., Davila, A. F., Zhang, L. M., Winklhofer, M., Liu, Q. S., Hanzlik, M. and Zhu, R. X., 2005. The detection of bacterial magnetite in recent sediments of Lake Chiemsee (southern Germany). *Earth and Planetary Science Letters* 232, 109–123.
- Pavlov, A. A., Brown, L. L. and Kasting, J. F., 2001. UV shielding of NH₃ and O₂ by organic hazes in the Archean atmosphere. *Journal of Geophysical Research* 106, 23267–23287.
- Pavlov, A. A. and Kasting, J. F., 2002. Mass-independent fractionation of sulfur isotopes in Archean sediments: Strong evidence for an anoxic Archean atmosphere. *Astrobiology* 2, 27–41.
- Pavlov, A. A., Kasting, J. F., Brown, L. L., Rages, K. A. and Freedman, R., 2000. Greenhouse warming by CH₄ in the atmosphere of early Earth. *Journal of Geophysical Research* 105, 11981–11990.
- Peck, J. A. and King, J. W., 1996. Magnetofossils in the sediment of Lake Baikal, Siberia. *Earth and Planetary Science Letters* 140, 159–172.
- Penninga, I., Dewaard, H., Moskowitz, B. M., Bazylinski, D. A. and Frankel, R. B., 1995. Remanence measurements on individual magnetotactic bacteria using a pulsed magnetic field. *Journal of Magnetism and Magnetic Materials* 149, 279–286.
- Petersen, N., von Döbeneck, T. and Vali, H., 1986. Fossil bacterial magnetite in deep-sea sediments from the South Atlantic Ocean. *Nature* 320, 611–615.
- Philipse, A. P. and Maas, D., 2002. Magnetic colloids from magnetotactic bacteria: Chain formation and colloidal stability. *Langmuir* 18, 9977–9984.
- Pierrehumbert, R. T., 2004. High levels of atmospheric carbon dioxide necessary for the termination of global glaciation. *Nature* 429, 646–649.
- Pierson, B. K., 1994. The emergence, diversification, and role of photosynthetic eubacteria. In: Bengtson, S. (Ed.), *Early Life on Earth*. Columbia U. Press., New York.
- Pósfai, M., Buseck, P. R., Bazylinski, D. A. and Frankel, R. B., 1998a. Iron sulfides from magnetotactic bacteria: Structure, composition, and phase transitions. *American Mineralogist* 83, 1469–1481.
- Pósfai, M., Buseck, P. R., Bazylinski, D. A. and Frankel, R. B., 1998b. Reaction sequence of iron sulfide minerals in bacteria and their use as biomarkers. *Science* 280, 880–883.
- Pósfai, M., Cziner, K., Marton, E., Marton, P., Buseck, P. R., Frankel, R. B. and Bazylinski, D. A., 2001. Crystal-size distributions and possible biogenic origin of Fe sulfides. *European Journal of Mineralogy* 13, 691–703.
- Pósfai, M., Moskowitz, B. M., Arato, B., Schüller, D., Flies, C., Bazylinski, D. A. and Frankel, R. B., 2006. Properties of intracellular magnetite crystals produced by

- Desulfovibrio magneticus strain RS-1. *Earth and Planetary Science Letters* 249, 444–455.
- Purcell, E. M., 1997. The efficiency of propulsion by a rotating flagellum. *Proceedings of the National Academy of Sciences* 94, 11307–11311.
- Reitner, J., Peckmann, J., Blumenberg, M., Michaelis, W., Reimer, A. and Thiel, V., 2005. Concretionary methane-seep carbonates and associated microbial communities in Black Sea sediments. *Palaeogeography, Palaeoclimatology, Palaeoecology* 227, 18–30.
- Reynolds, R. L., Tuttle, M. L., Rice, C. A., Fishman, N. S., Karachewski, J. A. and Sherman, D. M., 1994. Magnetization and geochemistry of greigite-bearing Cretaceous strata, North Slope basin, Alaska. *American Journal of Science* 294, 485–528.
- Risley, J. M., 2002. Cholesterol biosynthesis: Lanosterol to cholesterol. *Journal of Chemical Education* 79, 377–384.
- Robert, C. and Kennett, J. P., 1994. Antarctic subtropical humid episode at the Paleocene-Eocene Boundary—clay mineral evidence. *Geology* 22, 211–214.
- Rohl, U., Bralower, T. J., Norris, R. D. and Wefer, G., 2000. New chronology for the late Paleocene thermal maximum and its environmental implications. *Geology* 28, 927–930.
- Rosing, M. T. and Frei, R., 2004. U-rich Archaean sea-floor sediments from Greenland—indications of > 3700 Ma oxygenic photosynthesis. *Earth and Planetary Science Letters* 217, 237–244.
- Rye, R., Kuo, P. H. and Holland, H. D., 1995. Atmospheric carbon dioxide concentrations before 2.2 billion years ago. *Nature* 378, 603–605.
- Sakaguchi, T., Arakaki, A. and Matsunaga, T., 2002. *Desulfovibrio magneticus* sp. nov., a novel sulfate-reducing bacterium that produces intracellular single-domain-sized magnetite particles. *International Journal of Systematic and Evolutionary Microbiology* 52, 215–221.
- Sakaguchi, T., Burgess, J. G. and Matsunaga, T., 1993. Magnetite formation by a sulphate-reducing bacterium. *Nature* 365, 47–49.
- Sakai, S. and Jige, M., 2006. Characterization of magnetic particles and magnetostratigraphic dating of shallow-water carbonates in the Ryukyu Islands, northwestern Pacific. *The Island Arc* 15, 468–475.
- Savarino, J., Romero, A., Cole-Dai, J., Bekki, S. and Thiemens, M. H., 2003. UV induced mass-independent sulfur isotope fractionation in stratospheric volcanic sulfate. *Geophysical Research Letters* 30, 2131.
- Scheffel, A., Gruska, M., Faivre, D., Linaroudis, A., Plitzko, J. M. and Schuler, D., 2006. An acidic protein aligns magnetosomes along a filamentous structure in magnetotactic bacteria. *Nature* 440, 110–114.
- Schlömann, E., 1958. Ferromagnetic resonance in polycrystal ferrites with large anisotropy: General theory and application to cubic materials with a negative anisotropy constant. *Journal of Physics and Chemistry of Solids* 6, 257–266.
- Schmidt, P. and Williams, G., 1999. Paleomagnetism of the Paleoproterozoic hematitic breccia and paleosol at Ville-Marie, Quebec: Further evidence for the low paleolatitude of Huronian glaciation. *Earth and Planetary Science Letters* 172, 273–285.

- Schmitz, B., Pujalte, V. and Nunez-Betelu, K., 2001. Climate and sea-level perturbations during the Initial Eocene Thermal Maximum: Evidence from siliciclastic units in the Basque Basin (Ermua, Zumaia and Trabakua Pass), northern Spain. *Palaeogeography, Palaeoclimatology, Palaeoecology* 165, 299–320.
- Schopf, J. W., 1993. Microfossils of the Early Archean Apex Chert—New evidence of the antiquity of life. *Science* 260, 640–646.
- Schopf, J. W. and Packer, B. M., 1987. Early Archean (3.3-billion to 3.5-billion-year-old) microfossils from Warrawoona Group, Australia. *Science* 237, 70–73.
- Schüler, D. and Baeuerlein, E., 1998. Dynamics of iron uptake and Fe₃O₄ biomineralization during aerobic and microaerobic growth of *Magnetospirillum gryphiswaldense*. *Journal of Bacteriology* 180, 159–162.
- Schulz, H. N. and Jørgensen, B. B., 2001. Big bacteria. *Annual Review of Microbiology* 55, 105–137.
- Seong, S. and Park, T. H., 2001. Swimming characteristics of magnetic bacterium, *Magnetospirillum* sp. AMB-1, and implications as toxicity measurement. *Biotechnology and Bioengineering* 76, 11–16.
- Shen, Y. A., Buick, R. and Canfield, D. E., 2001. Isotopic evidence for microbial sulphate reduction in the early Archean era. *Nature* 410, 77–81.
- Shinn, E. A., Ginsburg, R. N. and Lloyd, R. M., 1969. Anatomy of a modern carbonate tidal-flat, Andros Island, Bahamas. *Journal of Sedimentary Petrology* 39, 1202–1228.
- Simmons, S. L., Bazylinski, D. A. and Edwards, K. J., 2006. South-seeking magnetotactic bacteria in the northern hemisphere. *Science* 311, 371–374.
- Simmons, S. L., Sievert, S. M., Frankel, R. B., Bazylinski, D. A. and Edwards, K. J., 2004. Spatiotemporal distribution of marine magnetotactic bacteria in a seasonally stratified coastal salt pond. *Applied and Environmental Microbiology* 70, 6230–6239.
- Skinner, B. J., Grimaldi, F. S. and Erd, R. C., 1964. Greigite, the thio-spinel of iron; a new mineral. *American Mineralogist* 49, 543–555.
- Smit, J. and Beljers, H. G., 1955. Ferromagnetic Resonance Absorption in BaFe₁₂O₁₉, a Highly Anisotropic Crystal. *Philips Research Reports* 10, 113–130.
- Snowball, I. F., 1994. Bacterial magnetite and the magnetic properties of sediments in a Swedish lake. *Earth and Planetary Science Letters* 126, 129–142.
- Spring, S., Amann, R., Ludwig, W., Schleifer, K. H., Van Gemerden, H. and Petersen, N., 1993. Dominating role of an unusual magnetotactic bacterium in the microaerobic zone of a freshwater sediment. *Applied and Environmental Microbiology* 59, 2397–2403.
- Spring, S. and Schleifer, K. H., 1995. Diversity of magnetotactic bacteria. *Systematic and Applied Microbiology* 18, 147–153.
- Stanjek, H., Fassbinder, J. W. E., Vali, H., Wägele, H. and Graf, W., 1994. Evidence of biogenic greigite (ferrimagnetic Fe₃S₄) in soil. *European Journal Of Soil Science* 45, 97–103.
- Stolz, J. F., Chang, S. B. R. and Kirschvink, J. L., 1986. Magnetotactic bacteria and single-domain magnetite in hemipelagic sediments. *Nature* 321, 849–851.
- Stolz, J. F., Chang, S. B. R. and Kirschvink, J. L., 1989. Biogenic magnetite in stromatolites. 1. Occurrence in modern sedimentary environments. *Precambrian Research* 43, 295–304.

- Summons, R. E., Jahnke, L. L., Hope, J. M. and Logan, G. A., 1999. 2-methylhopanoids as biomarkers for cyanobacterial oxygenic photosynthesis. *Nature* 400, 554–557.
- Tajika, E., 2003. Faint young Sun and the carbon cycle: Implication for the Proterozoic global glaciations. *Earth and Planetary Science Letters* 214, 443–453.
- Tarduno, J. A., 1994. Temporal trends of magnetic dissolution in the pelagic realm—gauging paleoproductivity. *Earth and Planetary Science Letters* 123, 39–48.
- Tauxe, L., Tucker, P., Petersen, N. P. and LaBrecque, J. L., 1984. Magnetostratigraphy of Leg 73 Sediments. In: Hsü, K. J. and LaBrecque, J. L. (Eds.), *Initial Reports of the Deep Sea Drilling Project*. U.S. Govt. Printing Office, Washington.
- Taylor, A. P. and Barry, J. C., 2004. Magnetosomal matrix: Ultrafine structure may template biomineralization of magnetosomes. *Journal of Microscopy* 213, 180–197.
- Taylor, A. P., Barry, J. C. and Webb, R. I., 2001. Structural and morphological anomalies in magnetosomes: Possible biogenic origin for magnetite in ALH84001. *Journal of Microscopy* 201, 84–106.
- Thomas-Keprta, K. L., Bazylinski, D. A., Kirschvink, J. L., Clemett, S. J., McKay, D. S., Wentworth, S. J., Vali, H., Gibson, E. K. and Romanek, C. S., 2000. Elongated prismatic magnetite crystals in ALH84001 carbonate globules: Potential Martian magnetofossils. *Geochimica et Cosmochimica Acta* 64, 4049–4081.
- Thomas-Keprta, K. L., Clemett, S. J., Bazylinski, D. A., Kirschvink, J. L., McKay, D. S., Wentworth, S. J., Vali, H., Gibson, E. K., McKay, M. F. and Romanek, C. S., 2001. Truncated hexa-octahedral magnetite crystals in ALH84001: Presumptive biosignatures. *Proceedings of the National Academy of Sciences* 98, 2164–2169.
- Thomas-Keprta, K. L., Clemett, S. J., Bazylinski, D. A., Kirschvink, J. L., McKay, D. S., Wentworth, S. J., Vali, H., Gibson, E. K. and Romanek, C. S., 2002. Magnetofossils from ancient Mars: A robust biosignature in the Martian meteorite ALH84001. *Applied and Environmental Microbiology* 68, 3663–3672.
- Thomas-Keprta, K. L., Clemett, S. J., Schwartz, C., Mophew, M., McIntosh, J. R., Bazylinski, D. A., Kirschvink, J. L., Wentworth, S. J., McKay, D. S., Vali, H., Gibson, E. K. and Romanek, C. S., 2004. Determination of the three-dimensional morphology of ALH84001 and biogenic MV-1 magnetite: Comparison of results from electron tomography and classical transmission electron microscopy (abstract). *Lunar and Planetary Science XXXV*, 2030.
- Thornhill, R. H., Burgess, J. G., Sakaguchi, T. and Matsunaga, T., 1994. A morphological classification of bacteria containing bullet-shaped magnetic particles. *FEMS Microbiology Letters* 115, 169–176.
- Ullman, W. J. and Aller, R. C., 1982. Diffusion coefficients in nearshore marine sediments. *Limnology and Oceanography* 27, 552–556.
- Valet, J.-P. and Laj, C., 1981. Paleomagnetic record of two successive Miocene geomagnetic reversals in western Crete. *Earth and Planetary Science Letters* 54, 53–63.
- Vali, H., Forster, O., Amarantidis, G. and Petersen, N., 1987. Magnetotactic bacteria and their magnetofossils in sediments. *Earth and Planetary Science Letters* 86, 389–400.
- Vali, H. and Kirschvink, J. L., 1989. Magnetofossil dissolution in a paleomagnetically unstable deep-sea sediment. *Nature* 339, 203–206.
- Vali, H. and Kirschvink, J. L., 1991. Observations of magnetosome organization, surface structure, and iron biomineralization of undescribed magnetic bacteria: Evolutionary

- speculations. In: Frankel, R. B. and Blakemore, R. P. (Eds.), *Iron biominerals*. Plenum Press, New York.
- van der Loeff, M. M. R., 1990. Oxygen in pore waters of deep-sea sediments. *Philosophical Transactions of the Royal Society of London Series A* 331, 69–84.
- van der Voo, R., 1989. Paleomagnetism of continental North America: The craton, its margins, and the Appalachian belt. In: Pakiser, L. C. and Mooney, W. D. (Eds.), *Geophysical Framework of the Continental United States*. Geological Society of America Memoir.
- van der Voo, R., 1990. The reliability of paleomagnetic data. *Tectonophysics* 184, 1–9.
- van Hinsbergen, D. J. J. and Meulenkamp, J. E., 2006. Neogene supradachment basin development on Crete (Greece) during exhumation of the South Aegean core complex. *Basin Research* 18, 103–124.
- Van Sickel, W. A., Kominz, M. A., Miller, K. G. and Browning, J. V., 2004. Late Cretaceous and Cenozoic sea-level estimates: Backstripping analysis of borehole data, onshore New Jersey. *Basin Research* 16, 451–465.
- Verosub, K. L., 1998. Paleomagnetism—faster is better. *Science* 281, 1297–1298.
- Wächtershäuser, G., 1990. The case for the chemoautotrophic origin of life in an iron-sulfur world. *Origins of Life and Evolution of the Biosphere* 20, 173–176.
- Walker, J. C. G., 1987. Was the Archaean biosphere upside down? *Nature* 329, 710–712.
- Walker, J. C. G., Hays, P. B. and Kasting, J. F., 1981. A negative feedback mechanism for the long-term stabilization of Earth's surface temperature. *Journal of Geophysical Research* 86, 9776–9782.
- Wdowiak, T. J., Armendarez, L. P., Agresti, D. G., Wade, M. L., Wdowiak, S. Y., Claeys, P. and Izett, G., 2001. Presence of an iron-rich nanophase material in the upper layer of the Cretaceous-Tertiary boundary clay. *Meteoritics and Planetary Science* 36, 123–133.
- Weber, R. T., Jiang, J. and Barr, D. P., 1998. *EMX User's Manual*, Manual Version 2.0. Bruker Instruments, Billerica, MA.
- Weiss, B. P., Baudenbacher, F. J., Wikswo, J. P. and Kirschvink, J. L., 2001. Magnetic microscopy promises a leap in sensitivity and resolution. *Eos Trans. AGU* 82, 513 & 518.
- Weiss, B. P., Kim, S. S., Kirschvink, J. L., Kopp, R. E., Sankaran, M., Kobayashi, A. and Komeili, A., 2004a. Ferromagnetic resonance and low temperature magnetic tests for biogenic magnetite. *Earth and Planetary Science Letters* 224, 73–89.
- Weiss, B. P., Kim, S. S., Kirschvink, J. L., Kopp, R. E., Sankaran, M., Kobayashi, A. and Komeili, A., 2004b. Magnetic tests for magnetosome chains in Martian meteorite ALH84001. *Proceedings of the National Academy of Sciences* 101, 8281–8284.
- White, D., 2000. *The Physiology and Biochemistry of Prokaryotes*. Oxford University Press, New York.
- Widdel, F., Schnell, S., Heising, S., Ehrenreich, A., Assmus, B. and Schink, B., 1993. Ferrous iron oxidation by anoxygenic phototrophic bacteria. *Nature* 362, 834–836.
- Williams, G. E. and Schmidt, P. W., 1997. Paleomagnetism of the Paleoproterozoic Gowganda and Lorrain Formations, Ontario—low paleolatitude for Huronian glaciation. *Earth and Planetary Science Letters* 153, 157–169.
- Wing, B. A., Brabson, E., Farquhar, J., Kaufman, A. J., Rumble III, D. and Bekker, A., 2002. $\Delta^{33}\text{S}$, $\delta^{34}\text{S}$ and $\delta^{13}\text{C}$ constraints on the Paleoproterozoic atmosphere during the earliest Huronian glaciation. *Geochimica et Cosmochimica Acta* 68, A840.

- Witt, A., Fabian, K. and Bleil, U., 2005. Three-dimensional micromagnetic calculations for naturally shaped magnetite: Octahedra and magnetosomes. *Earth and Planetary Science Letters* 233, 311–324.
- Xu, W. X., Peacor, D. R., Dollase, W. A., Van Der Voo, R. and Beaubouef, R., 1997. Transformation of titanomagnetite to titanomaghemite: A slow, two-step, oxidation-ordering process in MORB. *American Mineralogist* 82, 1101–1110.
- Yamazaki, T. and Ioka, N., 1997. Environmental rock magnetism of pelagic clay: Implications for Asian eolian input to the North Pacific since the Pliocene. *Paleoceanography* 12, 111–124.
- Yamazaki, T., Katsura, I. and Marumo, K., 1991. Origin of stable remanent magnetization of siliceous sediments in the central equatorial Pacific. *Earth and Planetary Science Letters* 105, 81–93.
- Yamazaki, T. and Kawahata, H., 1998. Organic carbon flux controls the morphology of magnetofossils in marine sediments. *Geology* 26, 1064–1066.
- Young, G. M., Long, D. G. F., Fedo, C. M. and Nesbitt, H. W., 2001. Paleoproterozoic Huronian basin: product of a Wilson cycle punctuated by glaciations and a meteorite impact. *Sedimentary Geology* 141, 233–254.
- Young, G. M., von Brunn, V., Gold, D. J. C. and Minter, W. E. L., 1998. Earth's oldest reported glaciation: Physical and chemical evidence from the Archean Mozaan Group (~2.9 Ga) of South Africa. *Journal of Geology* 106, 523–538.
- Zachos, J. C., Schouten, S., Bohaty, S., Quattlebaum, T., Sluijs, A., Brinkhuis, H., Gibbs, S. J. and Bralower, T. J., 2006a. Extreme warming of mid-latitude coastal ocean during the Paleocene-Eocene Thermal Maximum: Inferences from TEX86 and isotope data. *Geology* 34, 737–740.
- Zachos, J. C., Schouten, S., Bohaty, S., Quattlebaum, T., Sluijs, A., Brinkhuis, H., Gibbs, S. J. and Bralower, T. J., 2006b. Extreme warming of mid-latitude coastal ocean during the Paleocene-Eocene Thermal Maximum: Inferences from TEX86 and isotope data. *Geology* 34, 737–740.
- Zeile, U., 2000. Fundamentals of cryo preparation and replica technique. 7th Asia-Pacific Electron Microscopy Conference, Singapore.